Author:
Manzano, Francisco

Title:
Penetration depth study of high temperature and other novel superconductors.

Penetration Depth Study of High Temperature and Other Novel Superconductors

By

Francisco Manzano

SUBMITTED TO THE UNIVERSITY OF BRISTOL

IN ACCORDANCE WITH THE REQUIREMENTS

OF THE DEGREE OF DOCTOR OF PHILOSOPHY

IN THE FACULTY OF SCIENCE

January 2002

Acknowledgements and Declaration

I would like to thank my supervisor Dr. Antony Carrington for the constant help. guidance and encouragement throughout the course of my PhD.

I would like to thank John Turton, Pete Harrison, Bob Wiltshire and Ray Cattle for the technical support over the three years. Special thanks also goes to John Hart for assistance with the SEM images. I would like to thank my collaborators Dr. R. Prozorov, Dr. R.W. Giannetta and Dr. N.E. Hussey for providing samples. complementary data and advice on sushi.

I would like to thank all my friends in the Low Temperature Group at the University of Bristol for making my time there so enjoyable. I would like to especially thank Steve Yates, Ben Powell and Matt McBrien for the many stimulating, yet strangely difficult to remember next day, conversations that the we shared on numerous occasions, along with the new additions to the group, Dr. Pierre Rodiere and Jon Fletcher.

I would like to thank my family who have provided me with love and support, not just over the last three years, but throughout my life.

Finally I would like to thank Maria for her patience, love and support, without which this thesis may never have been started, let alone finished.

I declare that the work in this thesis was carried out in accordance with the Regulations of the University of Bristol. The work is original except where indicated by special reference in the text and no part of the thesis has been submitted for any other degree. Any views expressed in the thesis are those of the author and in no way represent those of the University of Bristol. This thesis has no been presented to any other University for examination either in the United Kingdom or overseas.

Signed

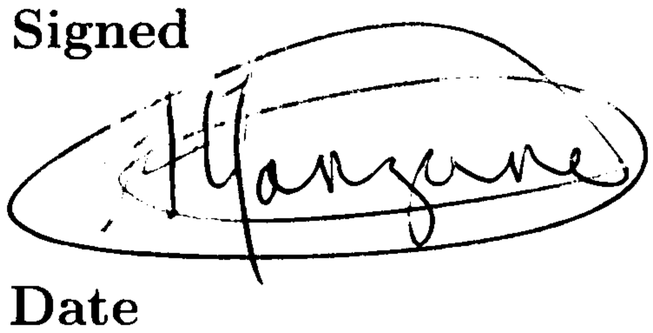

Date

1|5|02

Abstract

A high stability LC-oscillator technique was used to perform penetration depth measurements on optimally doped $YBa_2Cu_3O_7$ single crystals, naturally underdoped $YBa_2Cu_4O_8$ single crystals and the novel, newly discovered superconductor MgB_2 in both polycrystalline and single crystal form.

The study of optimally doped $YBa_2Cu_3O_7$ single crystals identified a low temperature increase in the temperature dependence of the penetration depth. This behaviour was attributed to the formation of Andreev boundstates (ABS) at the Fermi level along certain crystal surfaces. The ABS form as a direct consequence of the π-phase change around subsequent lobes of the $d_{x^2-y^2}$ order parameter. The field dependence of the ABS differentiates between possible origins of the extra penetration depth contribution. Small dc magnetic fields were seen to suppress the boundstate contribution. Measuring the field scale for the ABS suppression allowed an accurate value for the Fermi velocity to be inferred.

The penetration depth was measured in four MgB_2 samples to investigate the pairing symmetry of this material. All four samples showed an exponential $\lambda(T)$ associated with fully gapped BCS superconductivity. Values of the superconducting gap were yielded and compared with values from other techniques. A polycrystalline MgB_2 sample was prepared in order to measure $\lambda(0)$ for the material. An inplane zero temperature penetration depth of $\lambda_a(0) = (1100 \pm 200)$Å was yielded.

$YBa_2Cu_4O_8$ single crystals were measured to observe any contribution from Andreev boundstates. No evidence for this was found. The penetration depth was seen to decrease at low temperature rather than follow the linear temperature dependence associated with $d_{x^2-y^2}$ superconductivity. This low temperature decrease was seen to be increasingly suppressed for magnetic fields above ~ 5 mT. The effect was attributed to the suppression of superconductivity along the CuO chains. An attempt was made to separate each of the penetration depth ($\Delta\lambda_a(T)$, $\Delta\lambda_b(T)$ and $\Delta\lambda_c(T)$) components using geometrical arguments.

Contents

Chapter 1

Introduction

1.1 Motivation

Penetration depth measurements provide unambiguous information regarding the symmetry of the order parameter in both conventional and unconventional superconductors. New physics is still emerging from the study of high temperature superconductors due to the high sensitivity measurement techniques and high quality samples available today. The aim of the project was to accurately measure the magnetic penetration depth of high temperature superconductors as a function of temperature and magnetic field to better understand the mechanism of superconductivity. To this end studies have been performed on $YBa_2Cu_3O_{6.97}$ and $YBa_2Cu_4O_8$ single crystals. Measurements were not only performed on high T_c cuprates however. The vast majority of work on superconductivity, both experimental and theoretical, over the past 15 years has focused almost exclusively on the high temperature superconductors. Recently that exclusivity has been re-addressed slightly with the discovery of superconductivity in MgB_2 at 39K by Nagamutsu [1] *et al.* This material has stimulated a large amount of theoretical and experimental study into the mechanism of superconductivity and the symmetry of the order parameter. The commercial availability of MgB_2 powder has meant that work has been performed on the material in many laboratories throughout the world and has lead to a large amount of published data

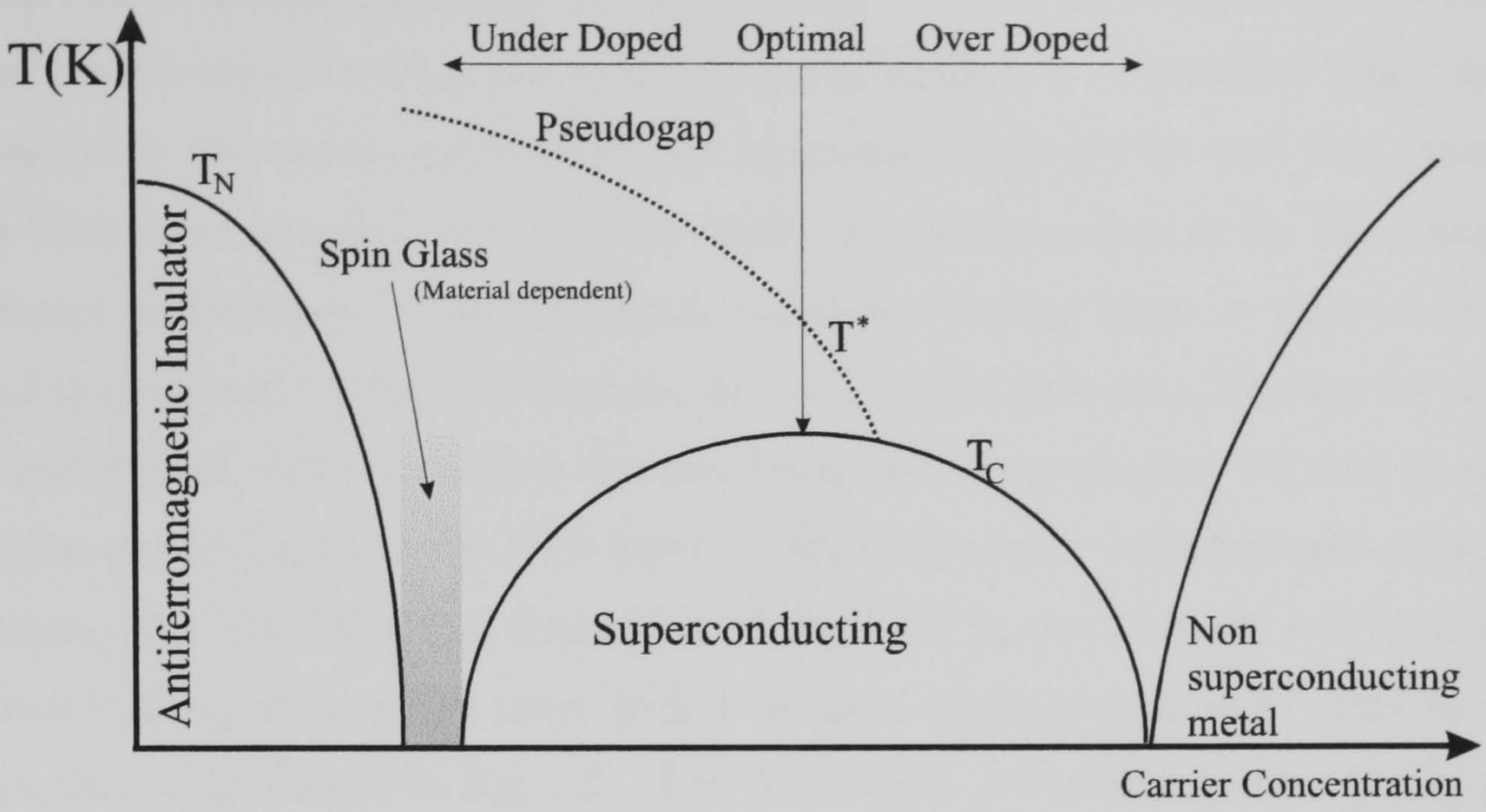

Figure 1.1: Generic phase diagram of HTS.

with some ambiguity between the results. The same high sensitivity technique as used to study high T_c single crystals has been used to study this compound and provide high quality data in order to better understand this material.

1.2 Introduction to High Temperature Superconductivity

The first High Temperature Superconductor (HTS) was discovered in 1986 by Bednorz and Müller [2] with the synthesis of the Lanthanum-Barium cuprate $La_{1.85}Ba_{0.15}CuO_4$. A year later the discovery of a similar Yttrium-Barium cuprate $YBa_2Cu_3O_{6+x}$ (Y123) by Wu *et al.* [3] (T_c=93 K) marked the arrival of arguably the most studied HTS to date. Subsequent discoveries of HTS have involved these layered cuprate stuctures. The highest recorded transition temperature at present is in $HgBa_2Ca_2Cu_3O_{8-\delta}$ (Hg1223) under pressure with T_c=164 K.

The hole doped HTS share a generic phase diagram as in Fig.1.1. Different materials can occupy different portions of the phase diagram although general trends

are observed in all the HTS families. By varying the hole concentration it is possible to alter the transition temperature of the compounds. As the carrier concentration is increased in the parent compound the transition temperature will rise. Materials with a transition temperature which is lower than the maximum for the compound are termed underdoped. The maximum transition temperature is said to occur at optimal doping with a further increase in carrier concentration leading to an over-doped compound with a less than optimal transition temperature. As well as sharing a common phase diagram, the HTS have a similar structure with features common to all compounds. The following discussion of the HTS in this chapter will concentrate on $YBa_2Cu_3O_{6+x}$ as it is the most widely studied of these materials. The structure of $YBa_2Cu_3O_7$ is shown in Fig.1.2. The Y123 unit cell contains two CuO_2 planes oriented within the *ab*-crystal direction which is a general feature of HTS. Superconductivity and many of the normal state properties of the HTS are attributed to the 2-dimensional CuO_2 planes; the reason for them popularly being termed 'cuprates'. The CuO_2 planes contain mobile charge carriers which are separated by charge reservoirs. These charge reservoirs are responsible for the carrier concentration within the planes. The parent compound $YBa_2Cu_3O_{6+x}$ is an antiferromagnetic insulator with $T_N \approx 400$ K for $x = 0$. At this doping the structure of the compound is tetragonal. Superconductivity occurs at a doping of x ~0.4 which is approximately the same point that the structure changes from tetragonal to orthorhombic. As the carrier concentration is increased T_c increases also. The variation of T_c with doping varies slightly from the parabolic temperature dependence shown in Fig.1.1. The transition temperature initially increases rapidly with doping. At intermediate doping levels the critical temperature as a function of doping varies more slowly and stabilizes at a value of $\sim$ 60 K [5]. This region is commonly termed the 60 K plateau. Optimal doping is achieved for $x = 0.97$ and can be slightly overdoped until $x \simeq 1$. Y123 also contains CuO chains running along the b direction but these are not a general feature of HTS. The presence of the CuO chains means that Y123 also has considerable

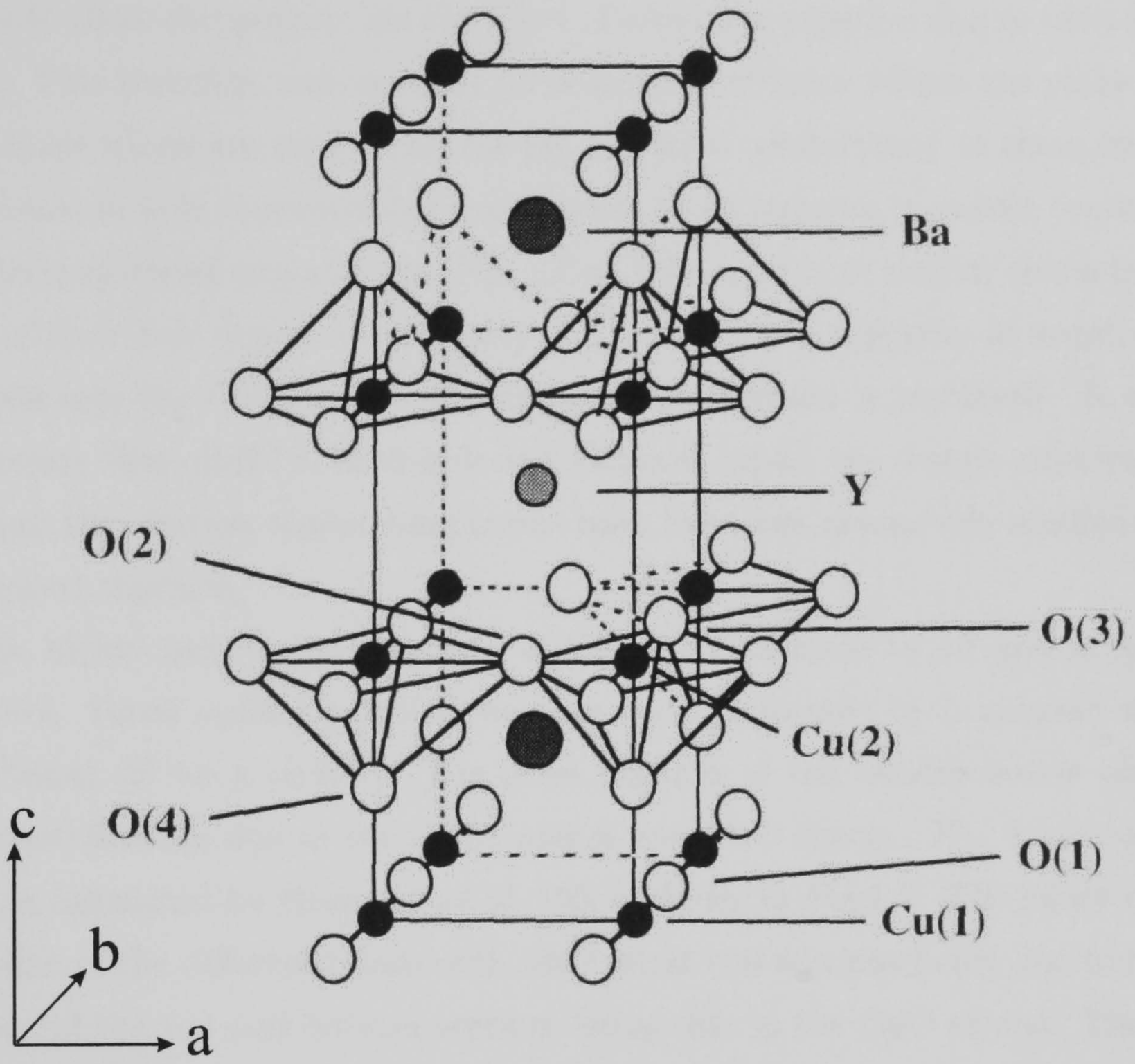

Figure 1.2: The structure of Y123. The Cu(2), O(2) and O(3) atoms are situated within the CuO_2 plane. The chains along the crystal b-direction consist of the Cu(1) and O(1) atoms. Taken from [4]

in-plane anisotropy which has been observed experimentally in resistivity [6] and penetration depth [7, 8] measurements. A similar phase diagram exists for electron doped HTS. Cuprates such as Y123 and Hg1223 have hole-like Fermi surfaces since the electron dispersions are closed around hole-like regions of the Brillouin zone. Following a simple valence argument, and recalling that oxygen is highly electronegative, adding oxygen to these compounds has the effect of removing negative charge from the CuO_2 planes. This therefore increases the concentration of holes within the plane. Since it is the holes which are responsible for the electrical conductivity in these compounds an increase in hole concentration corresponds to an increase in carrier concentration. The electron doped cuprates (eg. $Nd_{1.85}Ce_{0.15}CuO_{4-y}$) have similar characteristics to those of their hole doped counterparts but, as the name suggests, as negative charge is doped into the CuO_2 planes the carrier concentration is increased. A consensus is emerging that all HTS, both hole and electron doped, are *d*-wave superconductors although the electron doped compounds have been less extensively studied than the hole doped cuprates.

The highly anisotropic structure of the cuprates leads to an anisotropic bandstructure. Fermi surface calculations have been performed by a number of authors (see Pickett [9] for a review). The gross features of the bandstructure are derived from contributions due to the CuO_2 planes and CuO chains. The Fermi surface for Y123 as calculated by Krakauer *et al.* [10] is shown in Fig.1.3. The figure illustrates the origin of the different bands with the central two sections being due to the CuO_2 planes and the top and bottom sections being due to the CuO chains. The left and right panels reflect the amount of dispersion along the *c*-axis of the structure.

1.3 The Cuprate Families

There exist a great many cuprate superconductors. The simplest family structure, the first to be discovered by Bendorz and Müller [2], is of the form $La_{2-x}M_xCuO_{4-y}$ (M=Ba, Sr, or Ca). The structure consists of stacked alternate layers of the $LaCuO_3$

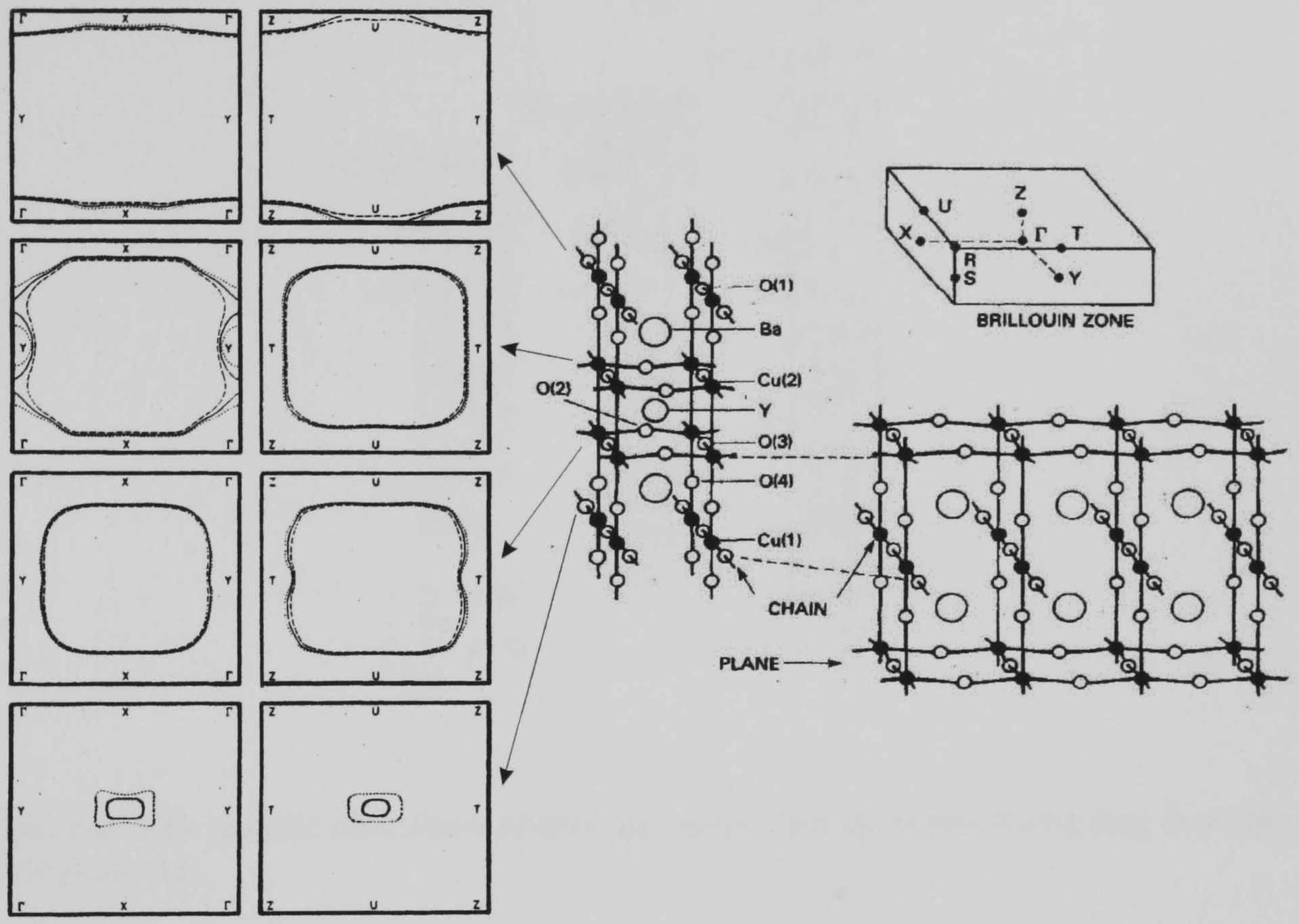

Figure 1.3: The bandstructure of Y123 as calculated by Krakauer *et al.* [10] The arrows relate the portion of the Y123 structure (plane or chain) with the bandstructure. The left column is calculated at the centre of the Brillouin zone and the right column is calculated at the top/bottom of the Brillouin zone. Adapted from Ref.[9]

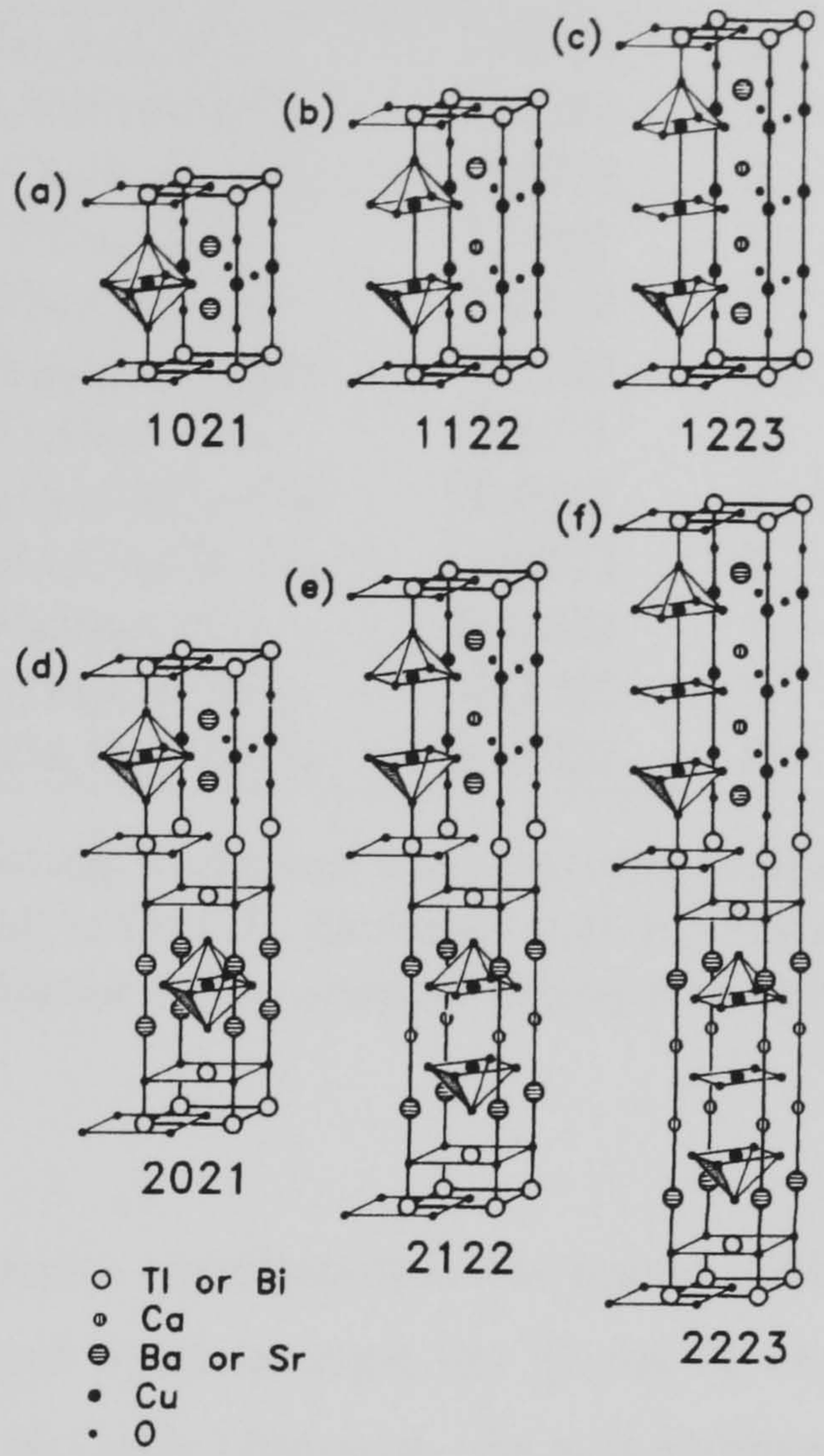

Figure 1.4: The generic structures shared by many cuprate superconducting families. Taken from [11].

perovskite and LaO along the c-axis such that the Cu sites in one perovskite layer are aligned with the La sites in the next perovskite layer [11]. Typical superconducting transition temperatures for this material are 37 K, 32 K and 17 K for Sr, Ba and Ca substituted for M respectively at concentrations of $x \sim 0.15$ [12].

Apart from cation substitution, cuprate families can also vary in the size of their repeat units. Examples of these are $Bi_2Sr_2Ca_{n-1}Cu_nO_{2n+4}$ (n=1, 2 or 3), $Tl_mBa_2Ca_{n-1}Cu_nO_{2(n+1)+m}$ (m=1 or 2, n=1, 2 or 3), $HgBa_2Ca_{n-1}Cu_nO_{4n}$ (n=1, 2 or 3) and $YBa_2Cu_{n+2}O_{n+6}$ (n=1 or 2) with a further addition to this family being

Compound	Abbreviation	n	T_c(K)
$Bi_2Sr_2CuO_6$	Bi2021	1	7
$Bi_2CaSr_2Cu_2O_8$	Bi2122	2	94
$Bi_2Ca_2Sr_2Cu_3O_{10}$	Bi2223	3	110
$TlBa_2CuO_5$	Tl1021	1	50
$TlBa_2CaCu_2O_7$	Tl1122	2	80
$TlBa_2Ca_2Cu_3O_9$	Tl1223	3	110
$Tl_2Ba_2CuO_6$	Tl2021	1	90
$Tl_2Ba_2CaCu_2O_8$	Tl2212	2	107
$Tl_2Ba_2Ca_2Cu_3O_{10}$	Tl2223	3	125
$HgBa_2CuO_4$	Hg1201	1	95
$HgBa_2CaCuO_7$	Hg1212	2	92
$HgBa_2Ca_2Cu_3O_8$	Hg1223	3	133

Table 1.1: Superconducting transition temperatures compared to numbers of CuO_2 layers. The general trend is that T_c increases with n. The abbreviations can be used to relate the superconductor to the corresponding structure in Fig.1.4. Values from [11]

$YBa_4Cu_7O_{15}$. The value of n corresponds to the number of CuO_2 layers present in the compound. It is a general trend amongst the Tl and Bi cuprates that T_c is strongly related to the number of CuO_2 planes, n. As n is increased the transition temperature increases (see Table1.1). It has been suggested [13, 14] that as the number of CuO_2 planes is increased, the electronic density of states is increased which in turn increases T_c. The Tl, Bi and Hg based cuprates largely share the same structure. The Tl based cuprate has 6 basic structures, three of which it shares with the Bi cuprate. The Tl combinations are termed Tl(1021), Tl(1122), Tl(1223), Tl(2021), Tl(2122) and Tl(2223) where the numbers correspond to the subscripts in the chemical formulae. The first three of these combinations are shared by the Bi-cuprate with the Hg-cuprate displaying only the (1021), (1212) and (1223) structures. The Hg-cuprate system also has some 'intergrowth' phases [15] but are not discussed here. These structures are shown in Fig.1.4.

1.4 Normal State and Pseudogap Properties of High Temperature Superconductors

The normal state properties of the High T_c cuprates set them apart from conventional metals. In plane resistivity measurements on optimally doped cuprates have been seen to follow a linear temperature dependence over a wide temperature range extrapolating to $\rho_{ab}(0) \sim 0$. In $La_{1.85}Sr_{0.15}CuO_4$ [16, 17] this linear behaviour has been seen to continue up to 1000 K. For the optimally doped cuprates, doping Zn impurities into the CuO_2 planes results in an increase in the residual resistivity. This increase takes the form of Matthiessen's rule where a constant resistivity term is added into the temperature dependence of the resistivity. Taken on its own this appears to be a familiar result consistent with standard metallic transport. Consider the Drude formula

$$\rho = \frac{m^*}{ne^2\tau} \tag{1.1}$$

where m^* is the mass of the carrier responsible for transport, n is the carrier density, e is the charge of the carrier and τ is the carrier scattering lifetime. For a metal n should be independent of temperature and so a linear temperature dependence of $\rho(T)$ implies $\rho(T) \propto 1/\tau$. The measured Hall coefficient ($R_H = 1/ne$) for optimally doped cuprates varies as $\sim 1/T$ implying that the carrier concentration varies as $\sim T$ and hence the scattering rate is proportional to T^2 rather than T thus producing seemingly contradictory results.

Overdoping of the cuprates generally leads to a fall in resistivity. The in plane resistivity develops positive curvature eventually reaching $\rho_{ab}(T) \sim A + BT^2$ for extreme overdoping. The resistivity along the c-axis is much greater than in the plane due to a lack of coherent transport. Underdoped Y123 shows non-metallic $\rho_c(T)$ at low temperature. Extreme underdoping leads to a $\rho_c(T)$ which increases at low temperatures appearing semiconductor like. The non metallic behaviour may be due to the presence of oxygen vacancies and substituted cations acting as blocking layers, between the CuO_2 planes, thus reducing the electron mean free path [18].

This behaviour gradually disappears with increased doping [19] becoming metallic. Metallic c-axis resistivity has been observed in the double chain, naturally underdoped stoichiometric cuprate $YBa_2Cu_4O_8$. In this material the presence of an extra CuO chain, and the lack of disorder between the CuO_2 planes, allows coherent charge transport to take place along the c-axis. This is in stark contrast to the localized charge models which model c-axis charge transport as due to single electrons tunneling between CuO_2 planes [20].

The normal state thermal conductivity of optimally doped Y123 was measured by Yu *et al.* [21]. The thermal conductivity contribution due to phonons and charge carriers are of the same order of magnitude [17]. Using the Wiedemann-Franz law, the electronic contribution to the thermal conductivity was identified and subtracted from the measured value leaving the phonon contribution. The electronic thermal conductivity, calculated using the Wiedemann-Franz relation using the measured resistivity, is greater along the b-axis reflecting the higher carrier concentration due to the presence of the CuO chains assuming an isotropic phonon contribution. Yu *et al.* found that both κ_a^{el} and κ_b^{el} are essentially temperature independent. The measured thermal conductivity increases sharply at T_c reflecting the reduction in electron-phonon scattering due to the formation of Cooper pairs.

The topic of the pseudogap has been extensively studied and has been the topic of a number of recent reviews [22, 23]. Due to the huge volume of published work on this topic, any discussion of the cuprate superconductors should necessarily include at least a brief discussion of the pseudogap.

The presence of a normal state pseudogap has been identified in the underdoped region of all of the cuprate families. The pseudogap appears to be related to the superconducting gap in that it evolves smoothly into the superconducting gap [24] with doping. The magnitude of the pseudogap remains constant through T_c, the superconducting transition temperature [25]. The pseudogap also appears to have the same symmetry as the superconducting gap. ARPES [26], Raman [27] and NMR [28, 29] provide evidence that the pseudogap has $d_{x^2-y^2}$ symmetry. Resistivity measurements

show cross over behaviour where the slope of the resistivity develops a kink at the temperature (T^*) corresponding to the opening of the pseudogap. The naturally underdoped $YBa_2Cu_4O_8$ shows linear temperature dependence to the in plane resistivity from high temperature ($\sim$ 1000 K) down to $\sim$ 180 K [30]. At this point the gradient of the resistivity increases noticeably. The temperature at which the kink occurs has been identified by NMR measurements to be the temperature at which the pseudogap opens [31]. The reduced resistance at the opening of the pseudogap is ascribed to the reduction of electron scattering from spin excitations. This leads to the pseudogap often being referred to as a spin gap. The fact that the pseudogap can be observed in ARPES measurements, which is sensitive to charge, means that the pseudogap is not just a spin gap but a true normal state gap in both spin and charge channels. Heat capacity measurements have also identified the presence of the pseudogap. Plots of $\gamma = C_{el}/T$ vs T [17] show that this contribution is approximately constant above T_c for optimally and overdoped cuprates until the heat capacity anomaly is reached after which it decreases rapidly. As the doping level is reduced to below optimal, γ begins to fall above T_c and the heat capacity anomaly is much smaller and more rounded. Below T_c, the decrease in γ approximately follows the same temperature dependence for all dopings.

Just as for the superconducting gap, the inclusion of impurities into the CuO_2 plane can have a profound effect on the pseudogap. Zheng *et al.* [32] found that the inclusion of small amounts of Zn impurities ($\sim$ 1%) in $YBa_2Cu_4O_8$ is enough to completely suppress the pseudogap i.e., the temperature at which the pseudogap opens up is pushed below T_c. In optimally doped $YBa_2Cu_3O_{7-\delta}$, Zn impurities suppress T_c three times more than Ni [33]. A similar effect occurs for the suppression of the pseudogap. Zn is found to suppress T^* four times as much as the same concentration of Ni. As for the suppression of T_c, Zn impurities are thought to induce local moments which disrupt local antiferromagnetic correlations, which implies that the pseudogap and the superconducting arise from the same origin (see below).

1.5 Pairing Symmetry of High Temperature Superconductors

The BCS "Theory of Superconductivity" [34] was extremely successful in describing the superconducting properties of the superconductors that were known prior to the discovery of the cuprates. For this reason the BCS theory was a natural starting point for theories concerning these new materials. The pairing mechanism responsible for superconductivity in the BCS framework is due to phonons providing a weak attractive mechanism between electrons of equal and opposite momenta, leading to the formation of Cooper pairs. The BCS theory makes the approximation that the attractive potential between two electron-like excitations $|\xi_{\mathbf{k}}|$ and $|\xi_{\mathbf{l}}|$ is $V_{\mathbf{kl}} = -V$ below an energy defined by a cutoff frequency, $\hbar\omega_c$, and $V_{\mathbf{kl}} = 0$ above this energy. The cutoff frequency is typically of order the Debye frequency. This approximation removes the momentum dependence from the pairing potential making it isotropic. An isotropic pairing potential naturally leads to an isotropic superconducting gap. A fully gapped Fermi surface precludes low energy quasiparticle excitations. This manifests itself in the thermodynamic behaviour of the superconductor as exponentially activated temperature dependence in all properties which come from the quasiparticle density of states. In early measurements performed on the cuprate materials, a combination of poor sample quality and experimental resolution meant that deducing the temperature dependence of a thermodynamic property, such as penetration depth, was non trivial [35]. As higher grade samples became available, and with the arrival of more sensitive measurement techniques, it became apparent that a fully gapped order parameter could not describe the behaviour of the cuprate superconductors. Experimental evidence pointed to the presence of low energy quasiparticle excitations inconsistent with conventional superconductors of the BCS form.

With the isotropic BCS theory found to be inadequate, theoretical attention turned to pairing mechanisms which could better describe the behaviour of the cuprates. A natural theoretical model to pursue was the Hubbard model [36] since it

was already being considered at the time to describe the physics of organic and heavy-fermion materials. A three band Hubbard model can be applied to the CuO_2 planes considering the one electron $d_{x^2-y^2}$ Cu orbitals and the p_σ orbitals of the O. This 3 band model can be further simplified by considering a square lattice consisting only of Cu atoms connected by an effective one electron transfer, t, and an onsite repulsion, U, which acts if two electrons occupy the same site. The Hubbard hamiltonian is given by

$$H = -\sum_{\langle ij\rangle s} t(c_{is}^\dagger c_{js} + c_{js}^\dagger c_{is}) + \sum_i U n_{i\uparrow} n_{i\downarrow} \tag{1.2}$$

where $c_{is}^\dagger$ creates an electron of spin s on site i and n_{is} is the number operator $c_{is}^\dagger c_{is}$. This describes the band in which superconducting pairs can form due to onsight Coulomb and short range spin-spin interactions. For half filling ($\langle n_{i\uparrow} + n_{i\downarrow}\rangle = 1$) and large U, each site typically has one electron. If electrons on neighboring sites have opposite spin they can hop over and back, lowering the energy of the system by a term proportional to $-t^2/U$ which sets the energy scale for the exchange interaction $J = 4t^2/U$. Monte Carlo simulations at half filling show [37] that the Hubbard hamiltonian displays long range antiferromagnetic order ie., the spins on adjacent sites align antiferromagnetically. Away from half filling at $\langle n\rangle = 0.87$ the long range antiferromagnetic order disappears but short ranged antiferromagnetic correlations persist and become peaked about the $q = (\pi, \pi)$ direction. Berk and Schrieffer [38] considered the effect that these collective excitations have on the effective electron-electron interactions. They found that the short ranged antiferromagnetic excitations lead to an anisotropic electron-electron interaction, V_{eff}, which would have the symmetry of the spin excitations. V_{eff} is attractive for adjacent sites along the longitudinal and transverse directions and repulsive along the diagonal.

Taking this model one step further Millis, Monien and Pines (MMP) [39] developed a phenomenological spin-spin correlation function $\chi_{MMP}(q, \omega)$,

$$\chi_{MMP}(q, \omega) = \frac{\chi_Q}{1 + \xi^2(q - Q)^2 - i\omega/\omega_{SF}} \tag{1.3}$$

χ_Q is the static spin susceptibility at $Q = (\pi, \pi)$, ξ is a temperature dependent

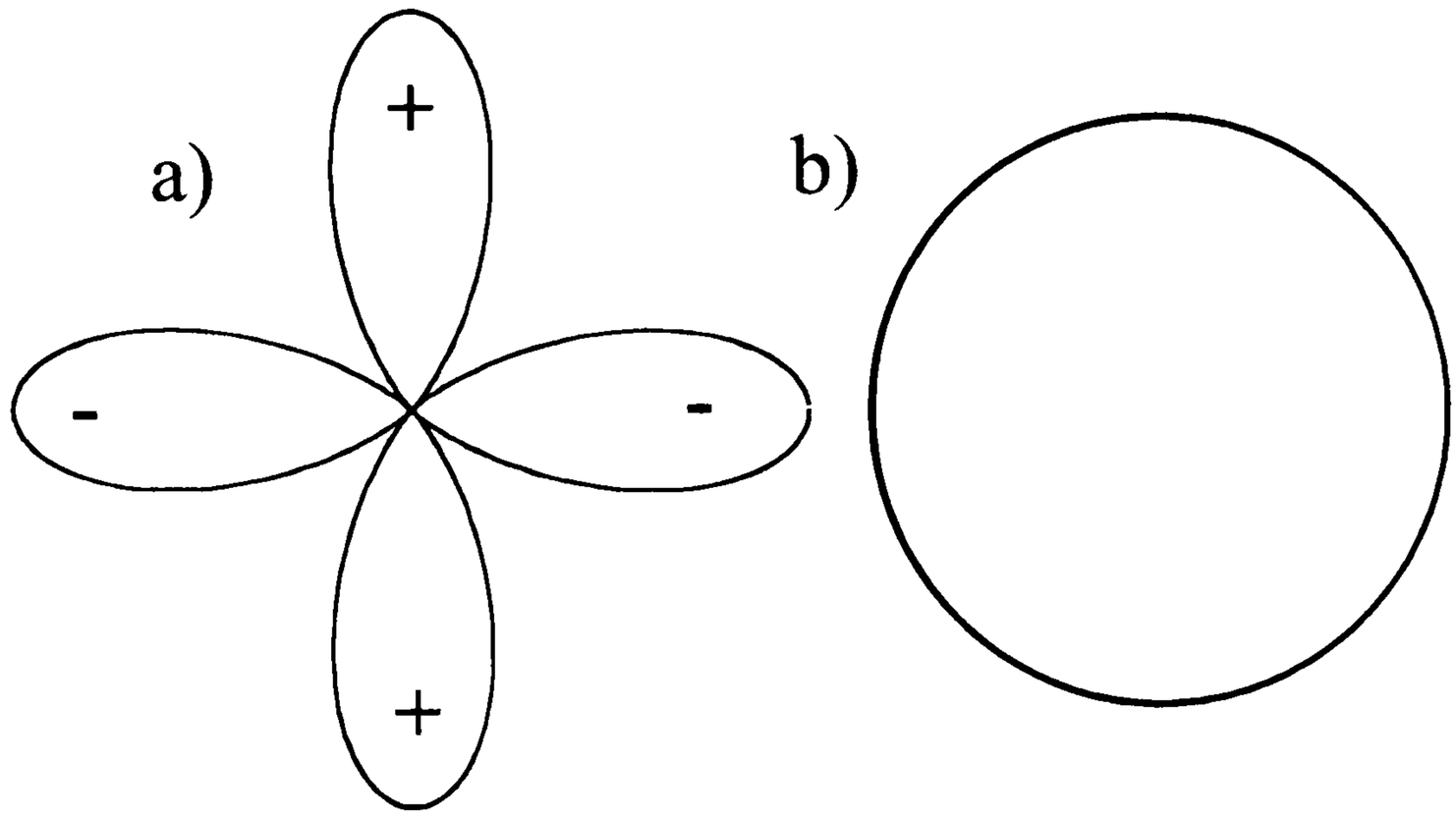

Figure 1.5: Schematic of a)the $d_{x^2-y^2}$ and b) the isotropic s-wave order parameters. The (+) and (-) reflects the phase of the order parameter.

antiferromagnetic correlation length and ω_{SF} is the frequency of the spin fluctuations. Values for χ_Q, ξ and ω_{SF} are taken from fits to NMR data [40, 41]. The effective potential is given by

$$V_{\text{eff}}(q,\omega) = \bar{g}2\chi_{MMP}(q,\omega) \tag{1.4}$$

where $\bar{g}$ is the coupling constant. Again the effective potential has the same symmetry as the magnetic excitation spectrum χ_{MMP}. The effective potential given in Eq.(1.4) become repulsive along the $q = (\pi, \pi)$ direction. These potentials therefore lead to an order parameter which drops to zero along certain directions of the Brillouin zone forming nodes on the Fermi surface. The symmetry of this gap is of the form $\Delta_0(\cos p_x - \cos p_y)$ which is the $d_{x^2-y^2}$ symmetry. Using the MMP formalism, and including the experimentally derived parameters, yields a predicted transition temperature to the $d_{x^2-y^2}$ pairing state of ~ 90 K [42] which is in excellent agreement with Y123. Fig.1.5 shows the form of the $d_{x^2-y^2}$ order parameter and compares it

to the isotropic s-wave case. The order parameter has four nodes at the Fermi energy. The presence of des in the order parameter means that quasiparticles can be excited at arbitrarily low energies.

At the time of formulation of this theory, experimental evidence for the $d_{x^2-y^2}$ order parameter was somewhat slight and relied almost entirely on the NMR measurements. For a $d_{x^2-y^2}$ order parameter the spin-lattice relaxation rate for ^{63}Cu should follow a T^3 dependence at low temperature which was indeed observed [43]. Today, the general consensus within the physics community is that the high temperature superconductors do indeed pair with $d_{x^2-y^2}$ symmetry. A number of key experiments were performed pointing to low lying quasiparticle excitations inconsistent with a fully gapped Fermi surface. Further experiments, sensitive to the phase of the order parameter, pointed to a π-phase change existing between adjacent lobes of the order parameter. The general features of all of these experiments point to an unconventional order parameter with $d_{x^2-y^2}$ symmetry. For a recent review of experiments investigating the pairing symmetry in the HTS see Tsuei and Kirtley [44].

Angle resolved photoemission spectroscopy (ARPES) measurements performed by Ding *et al.* mapped out the Fermi surface of $Bi_2CaSr_2Cu_2O_8$ [45]. By collecting energy dispersion curves (EDCs) around the Fermi surface an energy gap at the Fermi energy was resolved along certain spectroscopic directions.

The original experiment collected 15 EDCs around the Fermi surface and used these to map out the angular dependence of the gap. The gross features are that the gap is a maximum along the Γ-S direction (parallel to the a or b crystal directions) and a minimum along the Γ-Y direction (at 45° to the a or b directions). Quantitative measurements of gap properties were not possible due to the relatively poor energy sensitivity compared to the magnitude of the gap, however, a node in the gap was still clearly resolved. See Fig. 1.6.

Superconductors with $d_{x^2-y^2}$ order parameter symmetry are predicted to display a temperature dependence of the penetration depth which is linear. Early μSR [46]

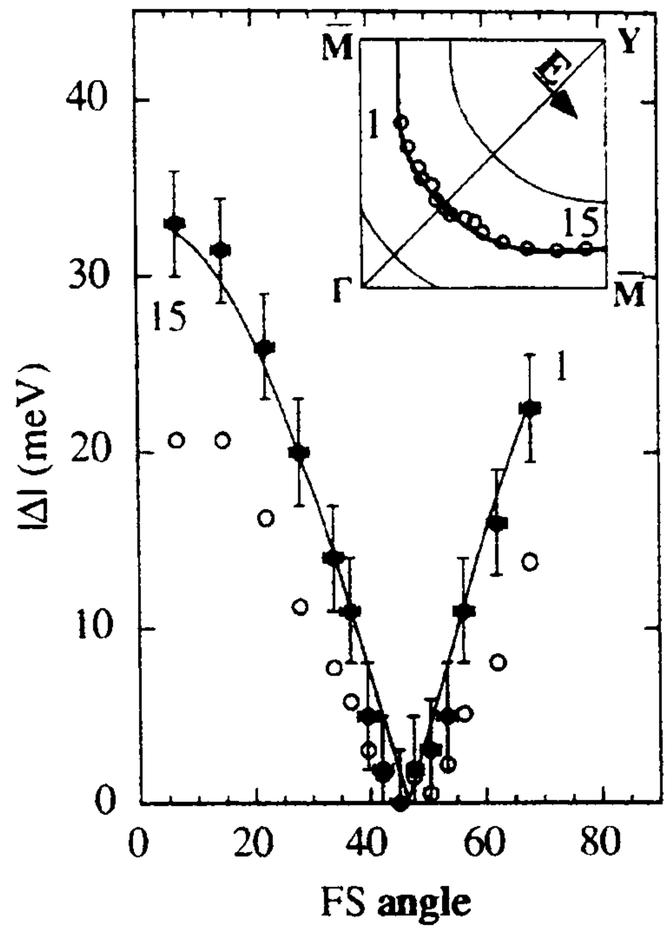

Figure 1.6: ARPES measurements clearly resolve a node in the order parameter after Ding *et al.*[45]

and magnetization measurements [47] appeared to show that this was not the case for the cuprates. The penetration depth data was interpreted as being approximately exponential; a result certainly not compatible with d-wave theory. As higher quality samples became available, further results appeared to disagree with the earliest measurements. Penetration depth measurements by Hardy *et al.* [48] on $YBa_2Cu_3O_{6.95}$ single crystals revealed a strong linear component in the magnetic penetration depth between 3 K and 25 K as measured using a microwave cavity technique.

Fig.1.7 shows the penetration depth measured by Hardy *et al.* Two samples are shown which both show approximately linear temperature dependence. As a comparative test the fully gapped s-wave superconductor $Pb_{0.95}Sn_{0.05}$ was measured using the same technique. This material showed an exponential decrease in $\lambda(T)$ below T_c with very weak temperature dependence below $T/T_c < 0.4$, consistent with a BCS s-wave superconductor (see Section 1.9).

The existence of a superconducting gap with nodes at the Fermi surface along certain crystal directions would result in quasiparticle excitations at arbitrarily low energies. Any impurity scattering would produce a residual quasiparticle density

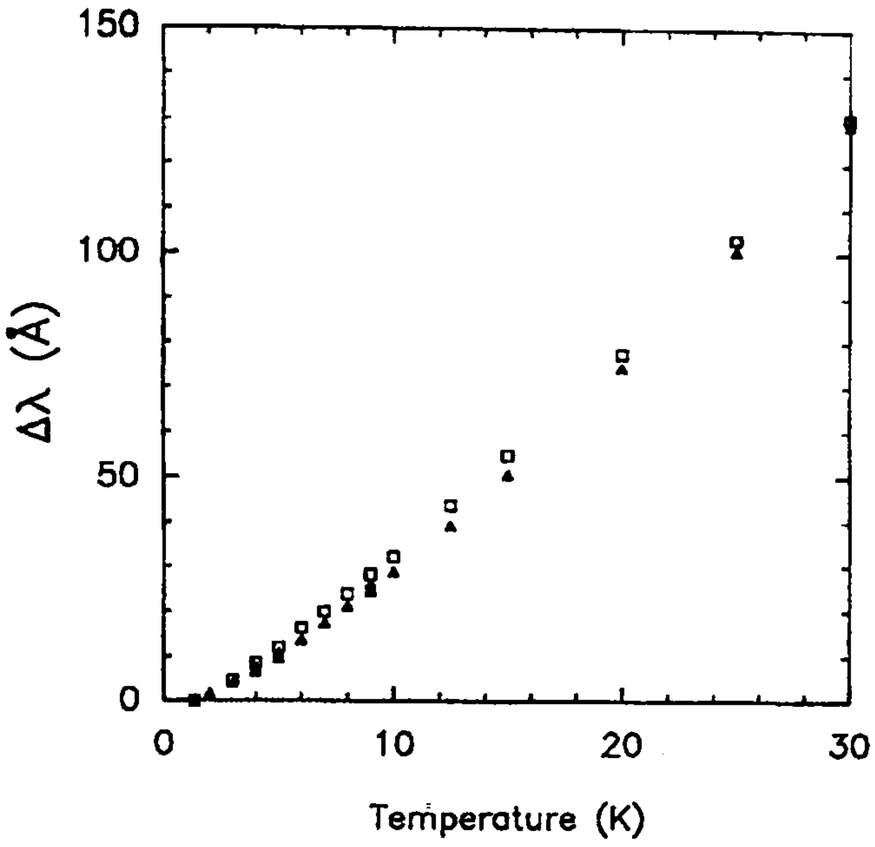

Figure 1.7: Penetration depth measurements of two $YBa_2Cu_3O_{6.95}$ single crystals by Hardy *et al.* [48]. This highly linear behaviour is strong evidence for $d_{x^2-y^2}$ superconductivity.

of states which should dominate thermal conductivity for $T \ll T_c$. Lee proposed [49] that for a superconducting gap with *d*-wave symmetry, quasiparticle transport should be independent of scattering rate and hence impurity concentration, as $T \rightarrow 0$. The impurity dependence of the thermal conductivity was investigated by Taillefer *et al.* [50] and the existence of the residual normal fluid in Y123 was established. The inclusion of Zn impurities which strongly suppress T_c did not have any effect on the thermal conductivity at low temperatures and all doping levels extrapolated to a common value of κ_0/T at zero temperature. The value of κ_0/T is proportional to the ratio of the quasiparticle velocities normal and tangential to the Fermi surface. The existence of a residual density of states at low temperature is a particular feature of a superconducting gap with nodes at the Fermi surface. Thermal conductivity for a fully gapped superconductor would be exponentially activated and not of the power law form observed by Taillefer *et al.*

Again using thermal conductivity measurements, the spatial dependence of the order parameter was investigated in Y123 by Aubin [51] *et al.* A DC magnetic field

of 3T was applied within the sample plane and the thermal conductivity measured. The sample was rotated at $\sim 1°$ intervals and the thermal conductivity measured at each point. Scattering processes are strongly dependent on the direction of the superfluid which is determined by the direction of the static magnetic field. A 4-fold 6% modulation was observed in $\kappa/\kappa_{(H=0)}$ which was qualitatively in agreement with a d-wave order parameter. The data was fit to a $d_{x^2-y^2}$ order parameter with a small s-wave component. The result showed essentially $d_{x^2-y^2}$ character with a 10% upper limit of an s-wave component to the gap.

Like thermal conductivity, heat capacity is also a bulk thermodynamic measurement. Unfortunately, heat capacity measurements are difficult to interpret in HTS since the electronic contribution at low temperatures is small. Furthermore, the expected electronic heat capacity for an order parameter with a line of nodes is expected to vary as T^2, which is difficult to separate from the T^3 phonon contribution. More compelling evidence for the $d_{x^2-y^2}$ order parameter comes from field dependent heat capacity measurements. Volovik [52] calculated the field dependent contribution to the specific heat for a superconductor with a line of nodes in the order parameter. In the low temperature limit ($T/T_c \ll \sqrt{(H/H_{c2})}$) the electronic T^2 term is replaced by a linear in T term which goes as $\sim T\sqrt{H/H_{c2}}$. Heat capacity measurements at constant temperature should follow a $\sqrt{H}$ dependence. This behaviour was observed by Moler *et al.* [53] in Y123 single crystals. Further evidence for this effect was observed by Revaz *et al.* [54]. Measurements of the anisotropic component of the field dependent specific heat $C(T, B\|c) - C(T, B \perp c)$ on Y123 single crystals showed scaling behaviour as predicted for a superconductor with a line of nodes [55, 56].

Whilst the experiments above provide evidence for a d-wave order parameter and information regarding the steepness of the gap at the nodes, they give no indication as to the phase of the order parameter. An anisotropic s-wave order parameter can have lines of nodes but does not change phase around the Fermi surface. A π-phase change between subsequent lobes of the order parameter is a particular feature of the d-wave order parameter. Observation of a phase change in the order parameter has

been observed in SQUID experiments. A review of these experiments is provided in Refs. [57] and [44]. Experiments by Wollman *et al.* [58] were performed using Y123 single crystals and Pb, a conventional superconductor, to form a Y123-Pb DC SQUID. The Pb is in contact with the a and b surfaces of the Y123 crystal forming a ring. The order parameter sampled at these surfaces should be π out of phase for a $d_{x^2-y^2}$ order parameter. In order to maintain phase coherence, a spontaneous supercurrent must flow. This was indeed observed and the relationship between critical current and applied magnetic field also confirmed the existence of a π-phase change between the two lobes of the order parameter. Control experiments were performed in a similar fashion. DC SQUIDs were made with the Pb ring in contact with the same surface of the Y123 crystal. In this case no current was observed as expected for a SQUID of this orientation.

1.6 Penetration depth response in High T_c cuprates

1.6.1 London Penetration Depth

In 1935 the London brothers derived phenomenological equations for the magnetic response of superconductors within electromagnetic fields [59]. This work introduced the concept of a length scale (λ_L), intimately related to the superconductivity. which described the attenuation of the magnetic field, known as the London penetration depth. The length scale was shown to be related to the number density of the charge carriers responsible for the superconductivity. This result implied that the stronger the superconductivity of the material was, the better it would exclude magnetic flux. The current density was shown to respond to an applied dc magnetic field as

$$\mathbf{J} = -\frac{\mathbf{A}}{\mu_0 \lambda_L^2} \tag{1.5}$$

where λ_L is the London parameter which is the length scale over which magnetic fields are screened from the bulk of the superconductor, and $\mathbf{A}$ is the vector potential defined as $\mathbf{B} = (\nabla \times \mathbf{A})$. The London parameter is given by

$$\lambda_L^2 = \frac{m}{\mu_0 n_s e^2} \tag{1.6}$$

where m is the mass of an electron, n_s is the number density of superconducting electrons and e is the charge of the superconducting electron. The London parameter remains the same if rather than considering single electrons we use the mass of a Cooper pair, $2m$, the charge of a Cooper pair, $2e$ and the number density of Cooper pairs $(n_s/2)$.

By taking the curl of Eq.(1.5) and recalling $(\nabla \times \mathbf{B}) = \mu_0 \mathbf{J}_s$ yields

$$\nabla^2 B = \frac{B}{\lambda_L^2} \tag{1.7}$$

which in 1-dimension has the solution

$$B(x) = B_0 \exp\left(\frac{-x}{\lambda_L}\right) \tag{1.8}$$

The London penetration depth can be derived from the BCS theory in the local limit. The local limit implies that the magnetic field is slowly varying over the length scale of a Cooper pair. The cuprate superconductors typically have $\xi_0 \ll \lambda_0$ which means that they are well within the local limit and are well described by the London penetration depth.

1.6.2 Penetration Depth from the BCS theory

Whereas the zero temperature value of the penetration depth ($\lambda(0)$) is described by the superfluid response to an applied magnetic field, its temperature dependence is dominated by thermally excited quasiparticles. In order to gain a simple physical insight into the penetration depth response we can consider Eq.(1.6). If given sufficient energy, a quasiparticle can be excited above the superconducting gap. If sufficient quasiparticles are excited this will have the effect of reducing the condensate (n_s) and therefore increasing the penetration depth. More precisely, the response actually depends on the probability of a quasiparticle being thermally excited above the gap over a energy range of $\sim k_B T$. This in turn depends on the structure of the quasiparticle density of states. If the density of states at low temperature is small then the change in penetration depth will also be small. For the case of an s-wave superconducting gap, the density of states is zero below the gap resulting in a very flat temperature dependence to the penetration depth at low temperature. Eq.(1.9) is the BCS equation for the change in the penetration depth due to thermally excited quasiparticles

$$\frac{\Delta\lambda(T)}{\lambda(0)} = -\int_{-\infty}^{\infty} \frac{N(E)}{N(0)} \frac{\partial f}{\partial E} dE \tag{1.9}$$

The energy of a thermally excited quasiparticle is $E_k = \sqrt{\Delta^2 + \epsilon_k^2}$ where Δ is the magnitude of the superconducting gap and ϵ_k is the kinetic energy of the normal state excitation. The quasiparticle density of states for an s-wave superconductor is given by

$$\frac{N_s(E)}{N(0)} = \frac{d\epsilon}{dE} = \begin{cases} \frac{E}{(E^2-\Delta^2)^{\frac{1}{2}}} & E > \Delta \\ 0 & E < \Delta \end{cases} \tag{1.10}$$

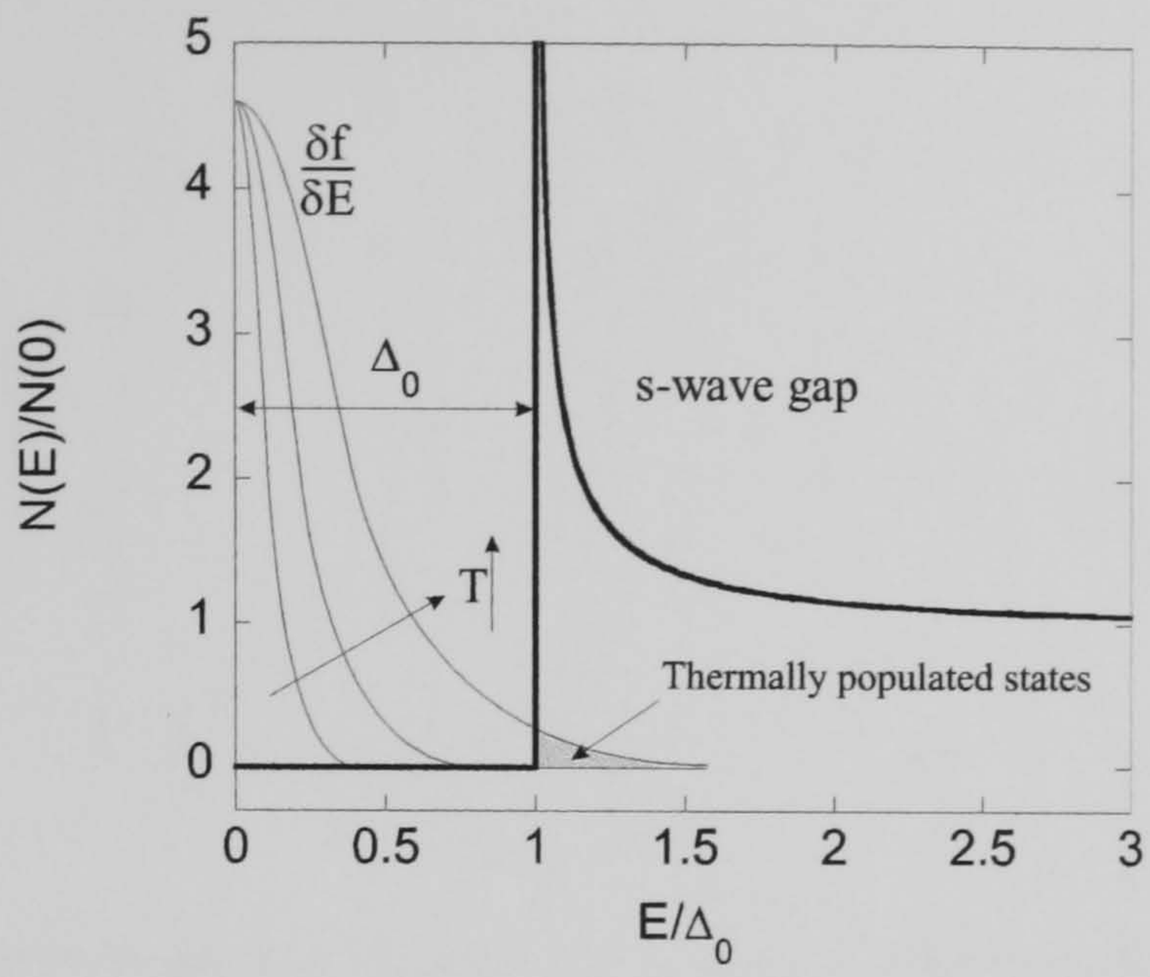

Figure 1.8: Plot of the density of states for an s-wave superconductor. A schematic of the Fermi function differentiated with respect to energy at fixed temperature. At higher temperatures the states can be thermally populated.

The density of states for an s-wave gap is plotted in Fig.1.8. A schematic of $\delta f/\delta E$ is also shown. As temperature increases this differential widens in energy. At high enough temperatures thermally excited quasiparticles can populate states beyond the gap energy. Solving Eq.(1.9) for an s-wave superconductor with $T \ll \Delta$ gives

$$\frac{\Delta\lambda(T)}{\lambda(0)} = \sqrt{\frac{\pi\Delta_0}{2k_BT}} \exp\left(-\frac{\Delta_0}{k_BT}\right) \tag{1.11}$$

The exponentially activated $\lambda(T)$ behaviour occurs in fully gapped superconductors and is observed in all thermodynamic properties for s-wave superconductors at low temperature.

For non s-wave superconductors the penetration depth change due to thermally excited quasiparticles can be considered in much the same way. As discussed in Section 1.5, the most likely candidate for the pairing symmetry of the HTS is the $d_{x^2-y^2}$ order parameter. This order parameter varies around the Fermi surface in both amplitude and phase. Penetration depth measurements are sensitive to the change in magnitude of the gap around the Fermi surface since this modifies the quasiparticle

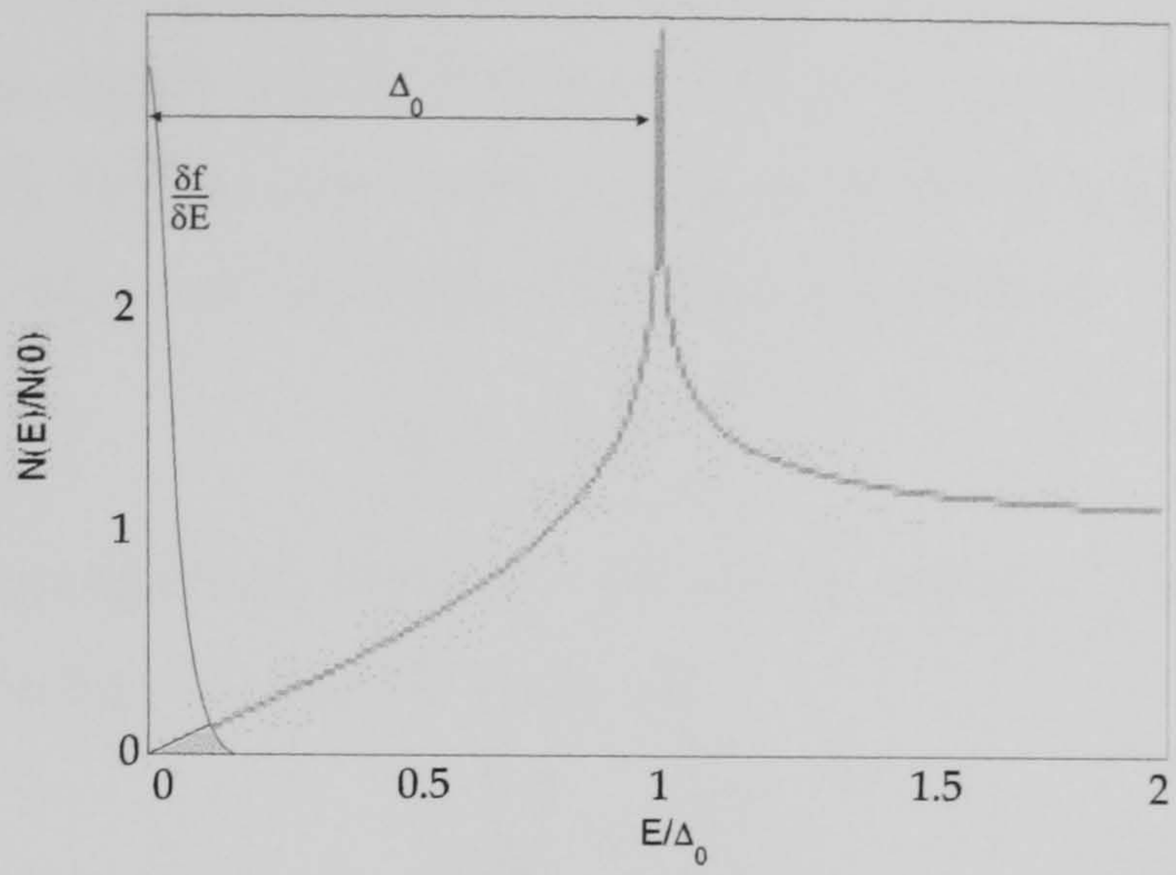

Figure 1.9: Plot of the density of states for a $d_{x^2-y^2}$ order parameter. A schematic of the Fermi function differentiated with respect to energy at fixed temperature. Quasiparticles can be thermally populate states at arbitrarily low temperatures.

density of states. For a $d_{x^2-y^2}$ order parameter the angle averaged density of states is given by

$$\frac{N(E)}{N(0)} = \frac{1}{\pi}\int_0^{\pi/4} \frac{E}{(E^2 - (\Delta_0 \cos 2\theta)^2)} d\theta \tag{1.12}$$

since

$$\Delta = \Delta_0 \cos 2\theta \tag{1.13}$$

The integral is performed over an eighth of the Fermi surface since the $d_{x^2-y^2}$ gap function is symmetrical over this period. Solving this gives the quasiparticle density of states. At $T \ll \Delta$ this is

$$\frac{N(E)}{N(0)} = \frac{E}{\Delta_0} + \frac{1}{4}\left(\frac{E}{\Delta_0}\right)^3 + \frac{9}{64}\left(\frac{E}{\Delta_0}\right)^5 + ... \tag{1.14}$$

To a first approximation, the density of states is linear in energy at low temperature. Quasiparticles can thermally populate states at arbitrarily low temperatures due to the nodes on the Fermi surface. At low temperatures the penetration depth will be dominated by these excitations. For simple $d_{x^2-y^2}$ symmetry, the order parameter will have the form of Eq.(1.13). In general the gap can take any form compatible with $d_{x^2-y^2}$ symmetry eg.$\Delta = \Delta_0(\cos 2\theta + \cos^3\theta)$. In order to simplify calculations, Xu *et*

al.[60] modelled the order parameter as being linear from the node up to the gap edge rather than following some periodic function. The order parameter was considered to be dependent on only two factors i) the maximum value of the gap (Δ_0) and ii) the angular slope of the gap near the node evaluated at the node

$$\mu \equiv \frac{1}{\Delta_0}\frac{d|\Delta(\theta)|}{d\theta} \tag{1.15}$$

In their model the quasiparticle density of states for the $d_{x^2-y^2}$ at $|E| \ll \Delta_0$ still has the same linear in energy density of states [60]

$$\frac{N_s(E)}{N(0)} \simeq \frac{2|E|}{\mu\Delta_0} \tag{1.16}$$

If Eq.(1.9) is solved using the quasiparticle density of states from Eq.(1.16), the low temperature dependence of penetration depth is given by

$$\frac{\Delta\lambda(T)}{\lambda(0)} = \frac{4k_BT\ln 2}{\mu\Delta_0} \tag{1.17}$$

μ therefore determines the coefficient of linear temperature dependence for the penetration depth in the clean limit. Since $\Delta(\theta) = \Delta_0\cos(2\theta)$, $\mu = 2$ for the $d_{x^2-y^2}$ order parameter.

1.6.3 Interpretation of Penetration Depth Anisotropy

The cuprate superconductors show large anisotropy in the penetration depth. The anisotropy is typically defined as $\nu = \lambda_c/\lambda_{ab}$. For Y123 the anisotropy is relatively small with $\nu^2 = (m_c/m_{ab})$=6 [61] where m_c and m_{ab} are the electron masses associated with the each penetration depth component. The penetration depth anisotropy in other cuprates such as $Bi_2Sr_2CaCu_2O_8$ can be as high as ν^2=50 000 [61]. Chandrasekhar and Einzel [62] discuss the consequences of this anisotropy on the London penetration depth. By relating the penetration depth anisotropy directly to the London penetration depth Eq.(1.6) it is possible to ascribe an anisotropic effective mass due to some anisotropic dispersion relation

$$\xi_k = \frac{\hbar^2}{2}\left(\frac{k_{ab}^2}{m_{ab}} + \frac{k_c^2}{m_c}\right) \tag{1.18}$$

where m_c and m_{ab} are the anisotropic effective band masses, k_{ab} and k_c are the components of $\mathbf{k}$ along the ab-plane and c-axis respectively. This dispersion relation implies an ellipsoidal Fermi surface. Fig.1.3 shows bandstructure calculations for Y123. These calculations show that the total Fermi surface is comprised of contributions from several sheets which does not lead to the assumed ellipsoidal dispersion. It is therefore intrinsically flawed to interpret penetration depth results in this way. Chandrasekhar and Einzel argue that a more physical interpretation of penetration depth results should be structured around known electronic dispersion relations.

In order to interpret penetration depth in terms of the London equation means introducing an effective (m/n) which has no connection to the true band mass or carrier density. The superfluid tensor integral (T) is defined such that $\mu_0 \mathbf{j}_q = -\mathsf{T}\,\mathbf{A}_q$. The superfluid tensor is comprised of two terms which represent the diamagnetic (T_D) and paramagnetic (T_P) response of the superfluid.

$$\mathsf{T} = \mathsf{T}_D - \mathsf{T}_P \tag{1.19}$$

with

$$\mathsf{T}_D = \frac{\mu_0 e^2}{4\pi^3} \int d^3k \left(-\frac{\partial n_k}{\partial \varepsilon_k} \right) (\mathbf{v}_k \mathbf{v}_k) \tag{1.20}$$

and

$$\mathsf{T}_P = \frac{\mu_0 e^2}{4\pi^3} \int d^3k \left(-\frac{\partial f(E_k)}{\partial E_k} \right) (\mathbf{v}_k \mathbf{v}_k) \tag{1.21}$$

The $(\mathbf{v}_k \mathbf{v}_k)$ tensor can be approximated to its value at $\epsilon_k = \mu$ since the derivative in each integrand is approximately zero except for $|\varepsilon_k - \mu|$ less than a few times Δ_k and $\Delta_k \ll \mu$.

These equations simply to

$$\mathsf{T}_D \cong \frac{\mu_0 e^2}{4\pi^3} \oint dS_F \frac{\mathbf{v}_F \mathbf{v}_F}{v_F} \tag{1.22}$$

and

$$\mathsf{T}_P \cong \frac{\mu_0 e^2}{4\pi^3} \oint dS_F \frac{\mathbf{v}_F \mathbf{v}_F}{v_F} \int_{\Delta_k}^{\infty} \left(-\frac{\partial f(E_k)}{\partial E_k} \right) \frac{E_k}{\sqrt{(E_k^2 - \Delta_k^2)}} \tag{1.23}$$

Several conclusions are drawn from Eqs.(1.22)and (1.23). T_D is independent of temperature but does reflect the anisotropy of ε_k. The paramagnetic contribution (T_P)

is zero at $T = 0$ and rises monotonically to equal τ_D at T_c. If the gap is anisotropic, τ_P reflects the anisotropies of both ε_k and Δ_k and is temperature dependent. For an isotropic gap τ_P is temperature independent and will have the same anisotropy of τ_D.

At zero temperature the supercurrent response is purely diamagnetic. The response is due to the integral over the Fermi surface of the tensor product of the Fermi velocity and the vector surface element. The significance of this is that any flat portions of the Fermi surface parallel to the supercurrent make no contribution to it and therefore act to increase the penetration depth. Small values of the Fermi velocity would also serve to increase the penetration depth. Chandrasekhar and Einzel suggest that a combination of these effects are likely to be the source of the comparatively large values of the penetration depth in the cuprates.

This interpretation serves to highlight the usefulness of interpreting the penetration depth in the cuprates in terms of their bandstructures, Fermi surfaces, Fermi velocities and energy gaps rather than assuming non-physical effective masses and superfluid concentrations. The penetration depth components λ_a and λ_b were calculated by Szotek *et al.* [63] for Y123 as a function of temperature from bandstructure with no adjustable parameters. The penetration depth calculations were compared with the results of Carrington *et al.* [8] and found to be in reasonable agreement adding weight to this interpretation.

1.6.4 Effect of Impurities on $\lambda_L(T)$

Conventional superconductors

The discussion of the penetration depth so far has concentrated on clean superconductors ($l \gg \xi_0$). Eq.(1.5) is the London relation which relates the supercurrent response to the presence of a magnetic field. The London, or local, limit states that the change in field is small over the size of a Cooper pair. Although this is the situation for HTS, this need not be the case for conventional superconductors. For non type II superconductors the relation between the supercurrent response and applied field will have

some spatial dependence which corresponds to a q dependence of the response kernel in Fourier space [64]. The real space response kernel $J(R,T)$, as proposed by BCS. was approximated by Pippard [65] in what is now termed the Pippard exponential. The relation between the BCS $J(R,T)$ and the Pippard exponential is

$$\int_0^\infty J(R,T)dR = \xi_0 = \int_0^\infty \exp(-r/\xi_0)dR \tag{1.24}$$

The two expressions are normalized at $T = 0$ and are both equal to 1. The BCS $J(0,T)$ function has a small temperature dependence which changes it smoothly from $J(0,0) = 1$ to $J(0,T_c) = 1.33$. The Pippard exponential has no temperature dependence and remains equal to unity at all temperatures for $R = 0$. The effects of impurity scattering is to make the electrodynamic response more local. The penetration depth is therefore modified from $\lambda_L(T)$ to some effective value $\lambda_{\text{eff}}(l,T) > \lambda_L(T)$ where l is the mean free path. $\lambda_{\text{eff}}(l,T)$ is calculated from

$$\frac{\lambda_L^2(T)}{\lambda_{\text{eff}}^2(l,T)} = \frac{\int_0^\infty J(R,T)\exp(-R/l)dR}{\xi_0} \tag{1.25}$$

which must be evaluated numerically.

In the "extreme dirty limit" ($l \ll \xi_0$) the integral reduces to $J(0,T)l$ giving

$$\lambda_{\text{eff}}(l,T) = \lambda_L(T)\left(\frac{\xi_0}{l}\right)^{1/2}[J(0,T)]^{-1/2} \tag{1.26}$$

As stated above, $J(0,T)$ varies from 1 to 1.33 between $T = 0$ and $T = T_c$ and therefore represents only a small correction.

Another approximation is to use the Pippard exponential ($\exp(R/\xi_0)$) rather than $J(R,T)$ in Eq.1.25. The integral in Eq.(1.25) therefore becomes equal to the Pippard coherence length given by

$$\xi^{-1} = \xi_0^{-1} + l^{-1} \tag{1.27}$$

and so

$$\lambda_{\text{eff}}(l,T) = \lambda_L(T)\left(\frac{\xi_0}{\xi}\right)^{1/2} = \lambda_L(T)\left(1+\frac{\xi_0}{l}\right)^{1/2} \tag{1.28}$$

This approximation reduces to $\lambda_L(T)$ in the pure limit. This approximation is inexact in that it does not contain the factor $[J(0,T)]^{-1/2}$ of the "extreme dirty limit". A

better approximation is rather than to approximate $J(R,T)$ with the straight Pippard exponential, it is replaced by $J(0,T)$ multiplied by a modified form of the Pippard exponential i.e $J(0,T)\exp-[J(0,T)R/\xi_0]$. This approximation is used since it agrees with the value of $J(R,T)$ at $R=0$. This gives

$$\lambda_{\text{eff}}(l,T)=\lambda_L(T)\left(\frac{\xi_0'}{\xi'}\right)^{1/2}=\lambda_L(T)\left(1+\frac{\xi_0'}{l}\right)^{1/2} \tag{1.29}$$

where the modified Pippard coherence lengths are given by

$$\frac{1}{\xi'}\equiv\frac{1}{\xi_0'}+\frac{1}{l}\equiv\frac{J(0,T)}{\xi_0}+\frac{1}{l} \tag{1.30}$$

Eq.(1.29) is the better approximation since it reduces to the "extreme dirty limit" for small l and can also approximate the $q\approx 0$ (local limit) due to the presence of $J(0,T)$ in the approximation.

$d_{x^2-y^2}$ order parameter

The presence of line nodes at the Fermi surface causes impurities to have a very different effect on the penetration depth at low temperature in d-wave superconductors than in fully gapped superconductors. Gor'kov *et al.*[66] and Ueda and Rice [67] showed that an infinitesimal amount of disorder leads to a non-zero density of states at zero energy for an order parameter with line nodes. At low enough temperature the superconducting properties should reflect the behavior of their corresponding normal state Fermi-liquid properties. The penetration depth of the superconducting state, however, has no normal state analog and so cannot simply be described by a normal state property. Hirschfeld and Goldenfeld [68] considered the effect of strong scattering impurities on the low temperature penetration depth. The low temperature penetration depth should vary as $\lambda\sim\lambda_0+c_2T^2$ where c_2 varies as Γ^{-1}. Γ is a constant dependent of impurity concentration and scattering strength. At higher temperature the penetration depth recovers the usual d-wave temperature dependence of $\lambda\sim\lambda_0+c_1T$. The coefficient c_1 is of order λ_0/T_c. The two temperature regimes are interpolated by the expression $\lambda(T)=aT^2/(T^*+T)$. Fitting this expression to

experimental data yields a value for $T^* \simeq c_1/c_2$. This leads to T^* increasing as the impurity coefficient (Γ) increases. Experiments by Bonn *et al.* [33] studied the effect of introducing impurities into a clean $YBa_2(Cu_{1-x}X_x)_3O_{6.95}$ system where X=Zn or Ni. Zn and Ni preferentially substitute for Cu(2) atoms which lie within the CuO_2 planes. The Ni and Zn impurities have a different effect on the the penetration depth and, more fundamentally, on T_c. Above T_c Ni and Zn increase the dc resistivity of the materials by similar amounts for the same impurity concentration implying similar normal state scattering rates. A striking observation is that the inclusion of Zn impurities suppresses $T_c \sim 3$ times more than Ni does. This would suggest that the Zn impurities, which are non magnetic, fundamentally disrupt the superconducting pairing mechanism in such a way that Ni does not. Bonn *et al.* also saw that the low temperature penetration depth is indeed modified as predicted by Hirschfeld and Goldenfeld. Fig.1.10a shows the calculated superfluid density by Hirschfeld and Goldenfeld. As the impurity content is increased the superfluid density moves away from low temperature linear behaviour over to T^2. Fig.1.10b shows the penetration depth is indeed modified by the presence of Zn impurities in the way predicted by Hirschfeld and Goldenfeld. The solid line is a fit to the dirty d-wave formula of Hirschfeld and Goldenfeld.

1.6.5 Further contributions to the Penetration Depth

The penetration depth for the cuprate high temperature superconductors (HTS) are well described by the BCS penetration depth in the clean London limit. The measured penetration depth, however, may contain contributions other than $\Delta\lambda_L$.

Unlike the penetration depth, the superconducting coherence length ξ_0 cannot be measured directly and must be calculated from the upper critical field. $\xi_0^2 = \mu_0 H_{c2}/2\pi\phi_0$. The coherence length for Y123 is typically calculated to be $\xi_0 \sim 14$Å. Kosztin and Leggett [69] argue that in the case of $d_{x^2-y^2}$ superconductors it is appropriate to introduce an anisotropic coherence length $\xi(k) = v_f/\pi|\Delta(k)|$. The low temperature penetration depth response is dominated by the small region of the Fermi

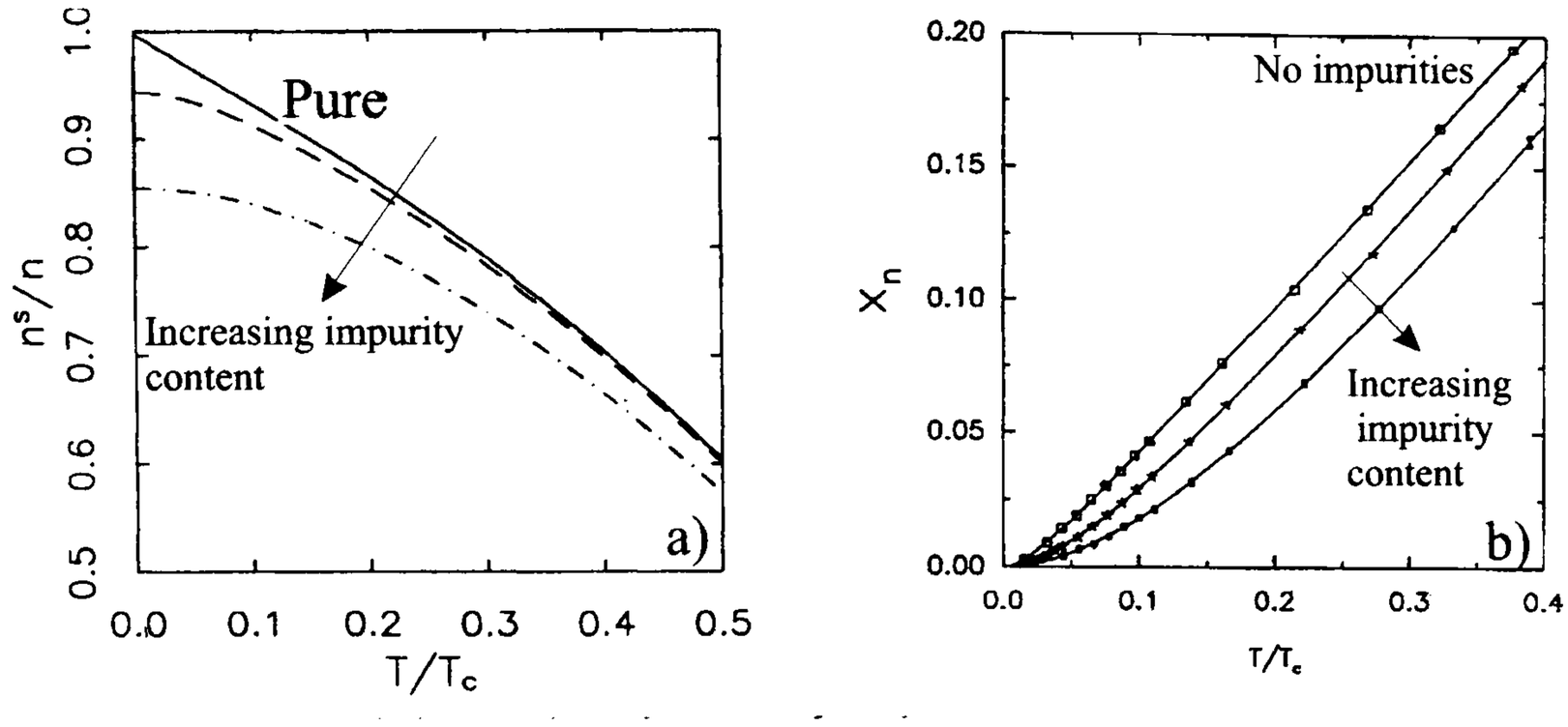

Figure 1.10: a) The calculated superfluid density with increasing impurity content by Hirschfeld and Goldenfeld [68]. b) The measured normalized superfluid density. $x_n = 1 - \lambda^2(0)/\lambda^2(T)$ with increasing impurity content after Bonn *et al.*1.10. The solid line is a fit to the dirty *d*-wave formula of Hirschfeld and Goldenfeld.

surface around the nodes of the order parameter. At these points the order parameter $\Delta \rightarrow 0$ causing the coherence length to diverge. The large nodal coherence length results in the local limit ($\xi_0 \ll \lambda_0$) being violated. The effect of this on the penetration depth is that the linear temperature dependence will cross over to T^2 below some temperature. The cross over temperature is $T^*=\alpha_0\Delta_0$ where $\alpha_0 \equiv \xi_0/\lambda_0$. Typical values for Y123 single crystals are $\xi_0 = 14$Å, λ_0=1400Å and $\Delta_0 \approx$250K [69], leading to an expected cross over temperature $T^*\approx$2.5K. This puts the cross over region into the temperature range whereby unitary scatterers can also change the temperature dependence from $T \rightarrow T^2$. An important prediction of the non-local theory to the measured magnetic penetration depth is that it should only be observed for measurements with the measurement field applied perpendicular to the *ab*-plane of the sample. This differs from the effect due to impurities since impurity effects would change $T \rightarrow T^2$ independent of sample orientation.

The presence of paramagnetic impurities can introduce an extra term into the temperature dependence of the penetration depth. The analysis by Cooper [70] to explain the temperature dependence of the electron doped superconductor $Nd_{1.85}Ce_{0.15}CuO_{4-y}$.

describes the effect of paramagnetic sites on the penetration depth. It was shown that the presence of Nd^{3+} ions complicated the interpretation of the measured $\Delta\lambda(T)$ since the Nd^{3+} ions have a Curie-Weiss like susceptibility $\chi(T) = \chi_0 + C/(T + \Theta)$ where C is the Curie constant for the material and Θ is the antiferromagnetic interaction strength. The penetration depth measured is $\lambda(T) = \lambda_L(T)/\sqrt{\mu}$ where μ is the magnetic permeability ($\mu = 1 + \chi$). The $Nd_{1.85}Ce_{0.15}CuO_{4-y}$ data was subsequently re-analyzed and the intrinsic response of the superfluid was shown to be best explained by the $d_{x^2-y^2}$ order parameter rather than s-wave which was the initial interpretation. Again, as for the case of impurities, this Curie term should be isotropic ie.. the effects should be observed in all measurement orientations, unlike non-local effects.

Chapter 2

Experimental Techniques

2.1 Introduction

This chapter is a discussion of the techniques, both experimental and analytical, used in the measurement of the magnetic penetration depth in HTS single crystals. Following a discussion of the experimental apparatus, a significant portion of the chapter is dedicated to the preliminary measurements needed to accurately quantify the extrinsic, non-sample, contributions to the measured signal. Following a discussion of the definition of the three different penetration depth components λ_a, λ_b and λ_c, the remainder of the chapter is dedicated to the process of relating the experimentally measured quantity Δf, a frequency shift, to $\Delta\lambda$, a change in penetration depth, with the measurement field applied within or perpendicular to the sample plane.

2.2 The Tunnel Diode Oscillator

2.2.1 Circuit Design

The tunnel diode oscillator is based on a high stability technique originally developed by Van Degrift [71] to accurately measure the dielectric constant of liquid helium. The circuit used for the measurement of penetration depth is sensitive to the change

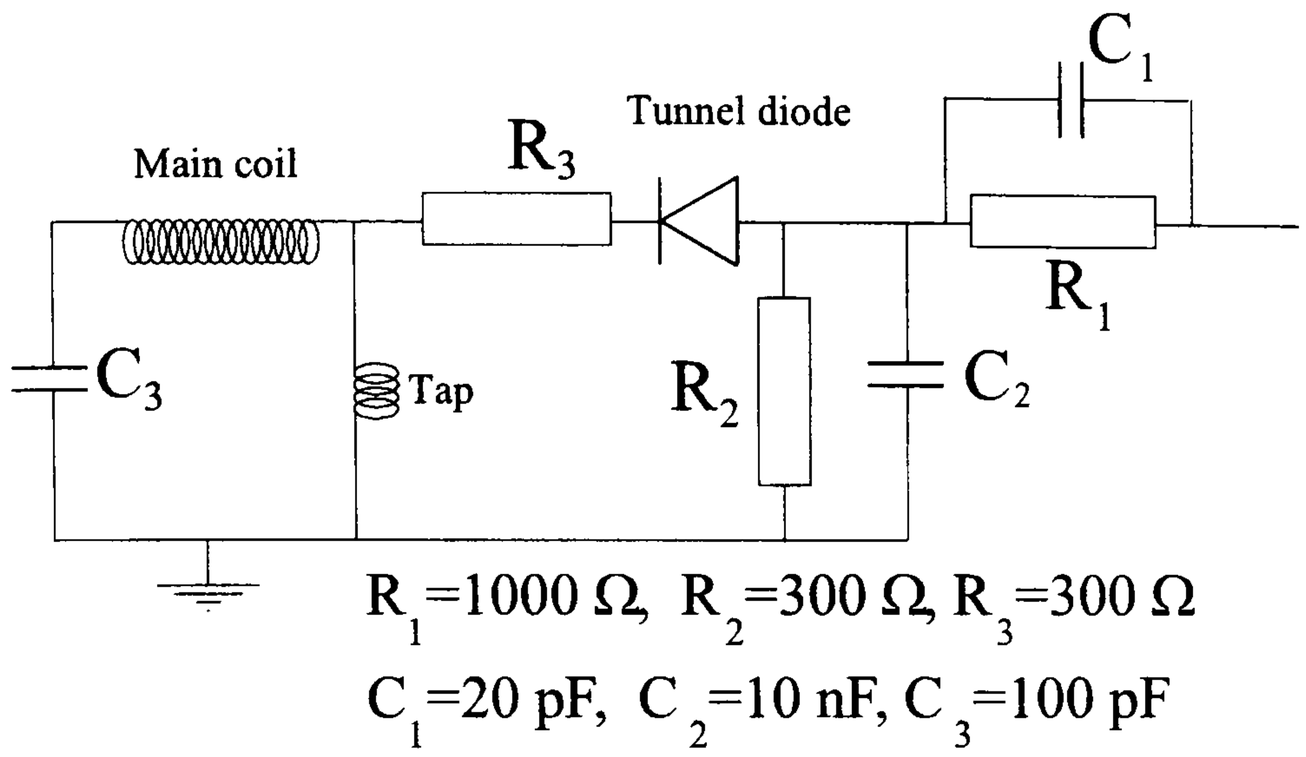

Figure 2.1: The oscillator circuit

in inductance of the sense coil. As the penetration depth of the material being measured changes, the effective sample volume also changes, resulting in a change in the resonant frequency of the LC circuit. A schematic of the resonant circuit is shown in Fig. 2.1. dc power is supplied by a current source at room temperature. For optimal rf-shielding the power is delivered down the same solid co-axial cable that carries the oscillator signal to the room temperature electronics. Resistor R_1 aids rf isolation whilst passing the dc current. R_2 provides the correct dc bias for the tunnel diode to operate. C_1 is a small valued capacitor which allows only a small portion of the signal back to the room temperature electronics. C_2 is the by-pass capacitor which is set to a large value in order to appear as a short circuit for the ac signal at the operating frequency of ~12 MHz. The fundamental frequency occurs at $\omega = 1/\sqrt{LC}$. The inductance of the measurement coil is approximately 1.2 μH and C_3=100 pF. The tunnel diode has a small amount of intrinsic capacitance across it. When adding capacitors in series, the effective capacitance will always be less than the value of the smallest capacitor. Since $C_p \ll C_3$, the effective capacitance which determines the fundamental frequency will be small, driving the fundamental to high frequency. The inclusion of resistor R_2 is to suppress the effect of the parasitic capacitance, meaning that the frequency of oscillation is set by C_3. The frequency changes measured when

running the experiment are attributed to changes in the inductance of the measurement coil. This requires good stability in the components used. If the frequency is related to some unpredictable parasitic capacitance the required stability may not be achieved and so it is important that this effect is suppressed.

Van Degrift outlines some empirical expressions that can be used to calculate approximate values for each of the components [71]. The values depend upon two factors; the maximum allowable power (P) and the oscillating frequency. The actual values used for each of the components largely agree with those obtained by the following expressions. The tunnel diode is assigned a value R_n which is negative. R_n corresponds to the effective negative resistance of the tunnel diode which compensates for the losses in the circuit. $R_n \approx v_d^2/P$, where v_d is the voltage amplitude of the oscillation ($\sim$10mV) and P is the power of the tunnel diode. The value of R_3 must be large enough to stop any parasitic oscillation but not so large as to disturb the fundamental oscillation. A value $R_3 \approx |R_n|/4$ is advised [71]. R_2 is calculated using the criteria that it should be large enough to properly bias the circuit whilst again not wasting dc power. The recommended value is given by $R_2 \approx |R_n + R_3|/4$. R_1 is chosen such that $R_1 \geq |R_n|$ if $C_2 \approx 1000/(\omega_0 |R_n|)$. C_1 is chosen such that $C_1 \approx 10^{-5} C_2 |R_n|/50\Omega$, where 50Ω is the input impedance of the first amplifier at room temperature. Once these values were set, the final parameter to be determined was the size of the tapping coil. This was done on a trial and error basis. The circuit was cooled down to 77 K with different size tap coils until a strong fundamental frequency was observed using a spectrum analyzer.

Before winding the measurement and tap coils, the effect of coil geometry was considered. Hoult and Richards [72] considered the effects of coil windings on the signal to noise ratio achieved in NMR experiments. The signal to noise ratio goes as $\sim \sqrt{Q}$ where Q is the quality factor of the circuit. The Q factor is related to the width of the resonance in frequency. The sharper the resonance, the higher the Q factor is. It was shown that the way coils are wound, in particular the spacing between consecutive turns, affects the Q factor of the circuit. The Q factor is optimal for

coils with a winding turn separation of r, the radius of the wire. Winding coils with this turn separation presents some practical difficulty. Coils with a turn separation of $2r$ are much easier to wind and still produce an increase in Q compared to coils with no turn separation. The separation of $2r$ is achieved by winding the coil in a normal manner but using a pair of wires rather than a single wire. Once the required number of turns is wound, both wires are secured to the coil former using General Electric (GE) varnish diluted with acetone. When the varnish is dry. one wire can be carefully unwound leaving an intact coil with adjacent turns separated by the diameter of the wire. Both the measurement and tap coils were wound by this method. The measurement coil was wound on Mylar wrapped around a 1 mm drill blank. The wire was glued in place with a small amount of Stycast 1266 resin and allowed to dry. When dry, the coil was placed inside a coil former turned from a Stycast resin rod. The coil was accurately centred within the Stycast former using brass alignment fittings made specifically for this task. The small space between the coil windings and the wall of the former is filled with Stycast and left to dry. If the process is successful, it is possible to remove the drill blank from the centre of the coil. By winding the coil in this way, the so-called fill factor η (the ratio of usable volume of the coil to the actual volume of the coil) is maximized. The signal to noise ratio goes as $\sim \eta$ meaning that the extra effort involved in winding the coil on the *inside* of the coil former is well rewarded. The sense coil currently used has 55 turns. The tap coil is wound directly onto a 1 mm diameter sapphire rod and glued using GE varnish. The turns are separated by the diameter of the wire as described above. The tap coil contains 22 turns and is housed within a gold plated copper box to maximize rf shielding. The whole oscillator circuit is further rf-shielded by a gold plated copper can.

2.2.2 Room Temperature Electronics

The room temperature electronics are shown schematically in Fig. 2.2. The capacitor isolates the amplifiers and mixer from the dc current source. The ac signal is amplified using two ZFL500LN minicircuits rf amps connected in series with a working frequency range of 0.1 to 500 MHz. The two amps provide a factor ~ 250 gain. The signal then enters a ZLW2 minicircuits mixer. The signal is mixed with an externally provided high frequency ac source which is set to differ from the experimental signal by ~3kHz. The local oscillator is always set ~3kHz *lower* than the oscillating circuit. The choice of setting the local oscillator higher or lower is arbitrary but in order to relate the change in frequency of the oscillating circuit to an increase or decrease in penetration depth, it is necessary to know 'which side' of the oscillation the local oscillator is on. Setting the local oscillator below the oscillating circuit means that an increase in the measured frequency corresponds to a decrease in the measured penetration depth. The external frequency can be changed during an experimental run if needed. This may be necessary, for example, when measuring the superconducting transition of a large sample where the total frequency shift may be >3kHz. The mixer provides a further factor 4 in gain. Following the mixer, the signal is amplified once more using a EG& G 5210 with a further gain of 500 and narrow banded between 1 and 3kHz. At this stage it is passed to the counter which is read via a PC interface. The counter and local oscillator are locked together using a high stability 10 MHz frequency source.

2.2.3 Experimental Configuration

The tunnel diode oscillator circuit as discussed above is mounted at the end of the cryogenic system shown in Fig. 2.3a. The cryogenic apparatus is built around a main pumping tube down which are passed the thermometer and heater wires. a smaller pumping tube to the 1 K pot and the solid coaxial cable which carries the oscillator signal. The 1 K pot is pumped at room temperature and fills continuously through a capillary impedance. Outside the main tube are two brass sheets which carry current

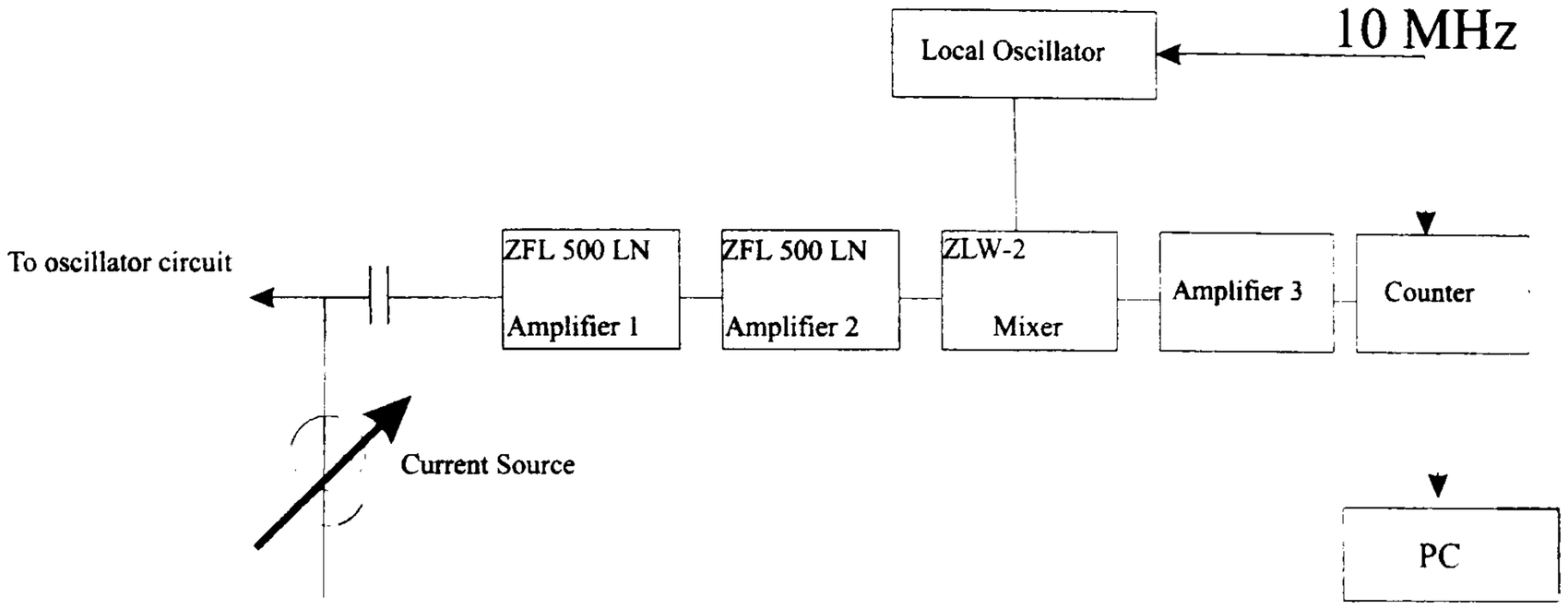

Figure 2.2: Schematic of the room temperature electronics which drive the oscillator and amplify the signal.

to the magnet. Sheets are used to provide a maximum surface area over which they can be cooled by gas boil off from the helium bath. The magnet leads pass through into the evacuated portion of the system where the experiment is housed.

Fig. 2.3b shows the portion of the experiment which is under vacuum. In order to achieve the lowest base temperature possible, attention has been paid to heatsinking various parts of the experiment at different temperatures to minimize the heatload from room temperature. The thermometer and heater wires are wrapped around a copper stud which is at 4.2 K. The G10 rod, used for sample extraction, comes down the pumping tube from room temperature. To attach it directly to the sample stage would present a large heat load. The G10 rod is therefore broken and a copper block inserted which is heatsunk via a copper braid to a copper arm which is at 4.2 K. The G10 rod is secured to the sample stage via a grub screw.

Fig. 2.4 shows a schematic of the sample holder. The sample is mounted upon a sapphire rod with dimensions such that it is centred in the measurement coil. The sample holder is heatsunk using copper braid at the pot temperature. A quartz tube is glued to the copper stage using Stycast 1266 epoxy. At the end of the quartz tube is another copper stage upon which a Lakeshore Cernox 1050 thermometer is mounted. The quartz tube is used since it acts as a weak thermal link between between the two copper stages of the sample holder. The weak thermal link allows

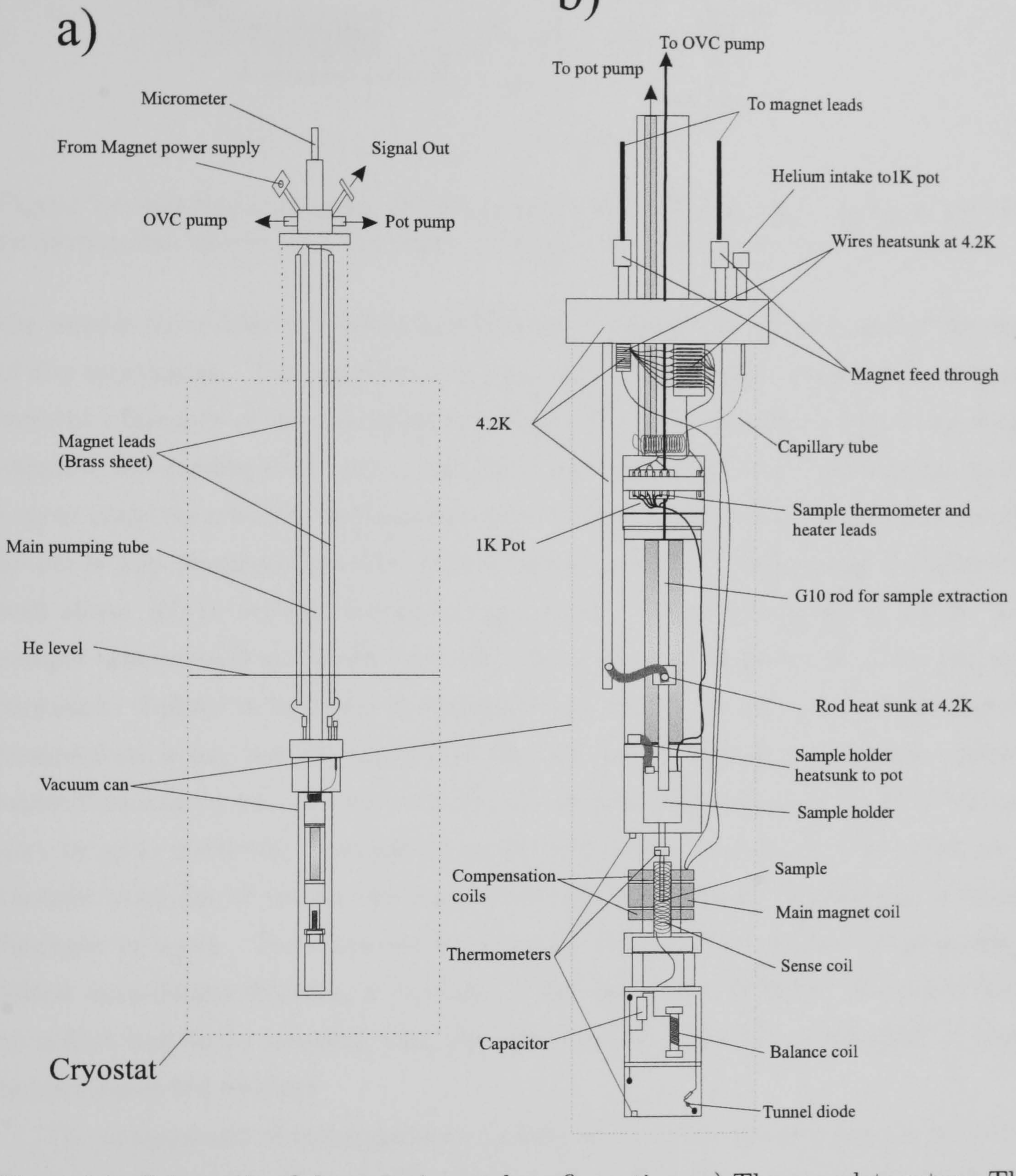

Figure 2.3: Schematic of the experimental configuration. a) The complete setup. The portion contained within the cryostat is outlined. b) The portion of the experimental setup maintained under vacuum.

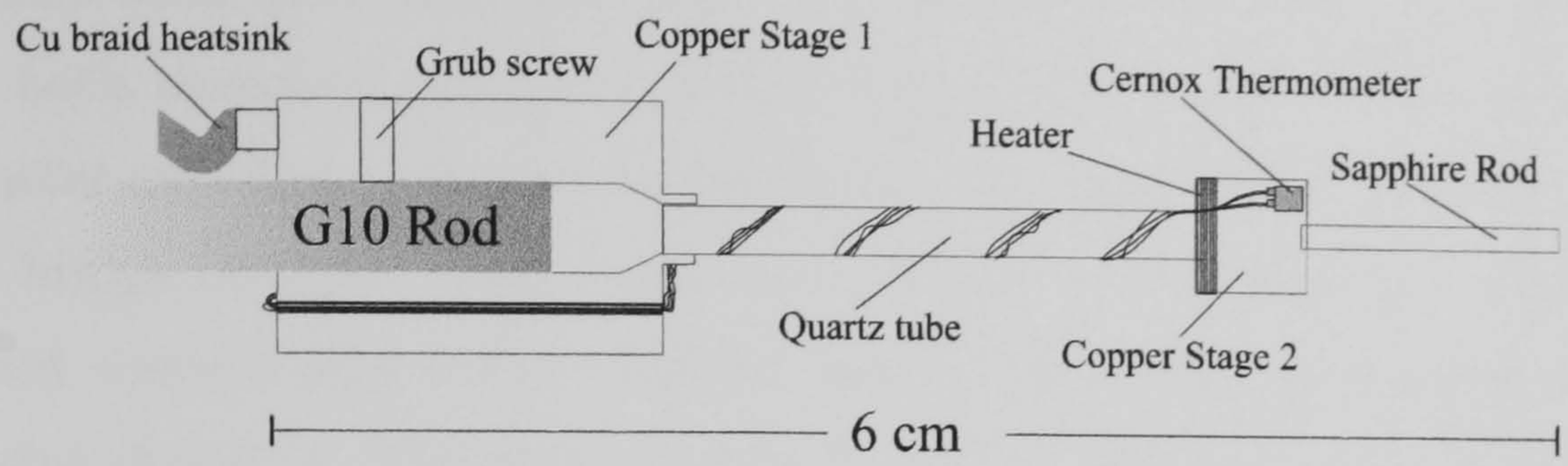

Figure 2.4: Schematic diagram of the sample holder. This sample holder is used for measuring the sample with the probe field applied along the c-axis of the crystal.

the sample to be heated without significantly changing the temperature of the rest of the experiment. The sapphire rod, upon which the sample is mounted, is glued into the other side of the second copper stage. The good thermal conductivity of the sapphire rod ensures that both it and the sample are at the same temperature as the copper stage upon which the Lakeshore Cernox thermometer is mounted. The sample heater is also mounted upon the second copper stage. The sample can be heated to well above 100 K without the main experimental stage heating above 1.5 K. The sample temperature is usually $\sim$50 mK above the pot temperature when properly heatsunk. Failure to heatsink the sample stage effectively can result in the sample temperature being over 100 mK hotter than the pot. The base temperature achieved varies from run to run. A usual running temperature for the pot is $\sim$1.38 K but can vary by up to $\pm$100 mK. The most likely source of variation in pot base temperature is thought to be due to partial blockages of the capillary tube feeding the pot by frozen Nitrogen or water. The strongest evidence for this is that the base temperature is lowest immediately following a blockage. If the impedance is higher, the pot is likely to collect less liquid meaning that the heat load from 4.2 K is lower and so lower temperatures are reached.

The temperature of the apparatus is measured at three points using Cernox thermometers as shown in Fig. 2.3. The thermometers attached to the sample holder and electronics are Cernox 1050's. The thermometer attached to the pot stage is a Cernox 1030 which have a lower operating range than the 1050's. These three points can be

temperature controlled independently. The sample temperature and pot temperature are both measured using a Lakeshore model 340 temperature controller. The thermometer attached to the oscillator electronics stage is read and controlled using a 3-lead bridge method. The control temperature is set using a variable resistor. The circuit controls at a temperature at which the thermometer resistance is equal to the value dialed in. The value used is 2800 Ω corresponding to a temperature of 4.6 K. The temperature is typically controlled to $\sim$ 0.1 mK. The stability of the electronic stage temperature is recorded in the data file in case it is needed for diagnostic purposes.

2.3 Oscillator Characteristics

The high stability of the LC-oscillator allows for data to be acquired over many hours and the results averaged in order to reduce noise. This is particularly important when measuring small samples with small overall frequency shifts. For samples such as these, the background contribution must be accurately determined to allow the intrinsic frequency shifts, due solely to the sample, to be accurately converted to a change in penetration depth. The oscillator will typically drift $\sim$ 0.01 Hz over 12 hours with a peak to peak frequency noise of 0.05 Hz.

2.3.1 Extrinsic Effects

A number of preliminary measurements must be performed before the frequency shift measured from the oscillator can be converted into a change in penetration depth of a superconducting sample. Any material placed within the sense coil, such as the sample holder, will contribute to the frequency shift of the oscillator as a function of temperature or field. All responses not arising from the crystal alone must be subtracted from the raw data.

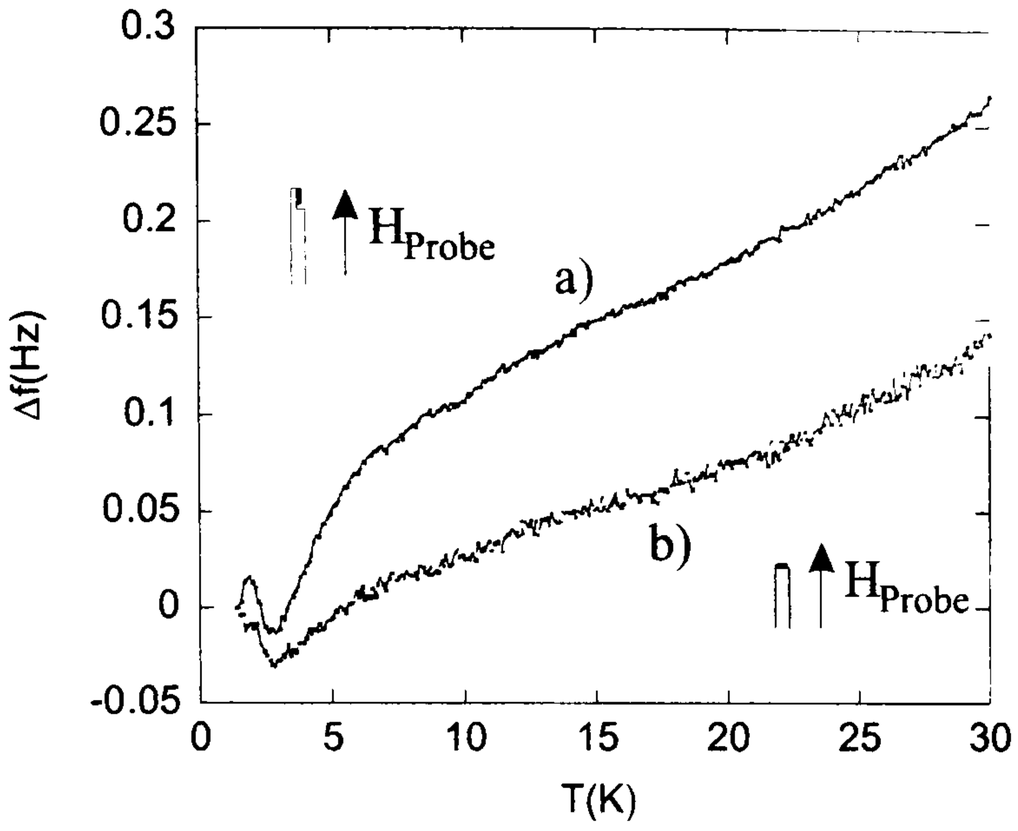

Figure 2.5: Frequency response of the sapphire rod used to apply measurement field a) within the sample plane and, b) perpendicular to the sample plane.

Frequency shift due to Sapphire Sample Holder

In order to measure the penetration depth response with the excitation field applied within or perpendicular to the sample plane, two different sample holders are used. The frequency response has been measured for each of these. Figure 2.5 shows the effect of temperature upon the frequency response due to the sapphire rods which position the sample plane a) parallel to the measurement field and b) perpendicular to the measurement field. The frequency response above ~ 6 K is due almost entirely to the effect of the changing pot temperature (See below). The appropriate background response must be subtracted from each data set in order to isolate the sample response. This must be done before converting the frequency shift into $\Delta\lambda$ since the calibration factor is sample dependent (see Section 2.3.3).

It is desirable to measure samples at fixed field whilst sweeping the temperature. In order to do this an adequate background response must be taken at the appropriate field value and over the correct temperature range. Figure 2.6 shows the frequency response of both sapphire sample holders. The temperature dependence of the sapphire rods can be seen to have some field dependence. Both sample holders qualitatively

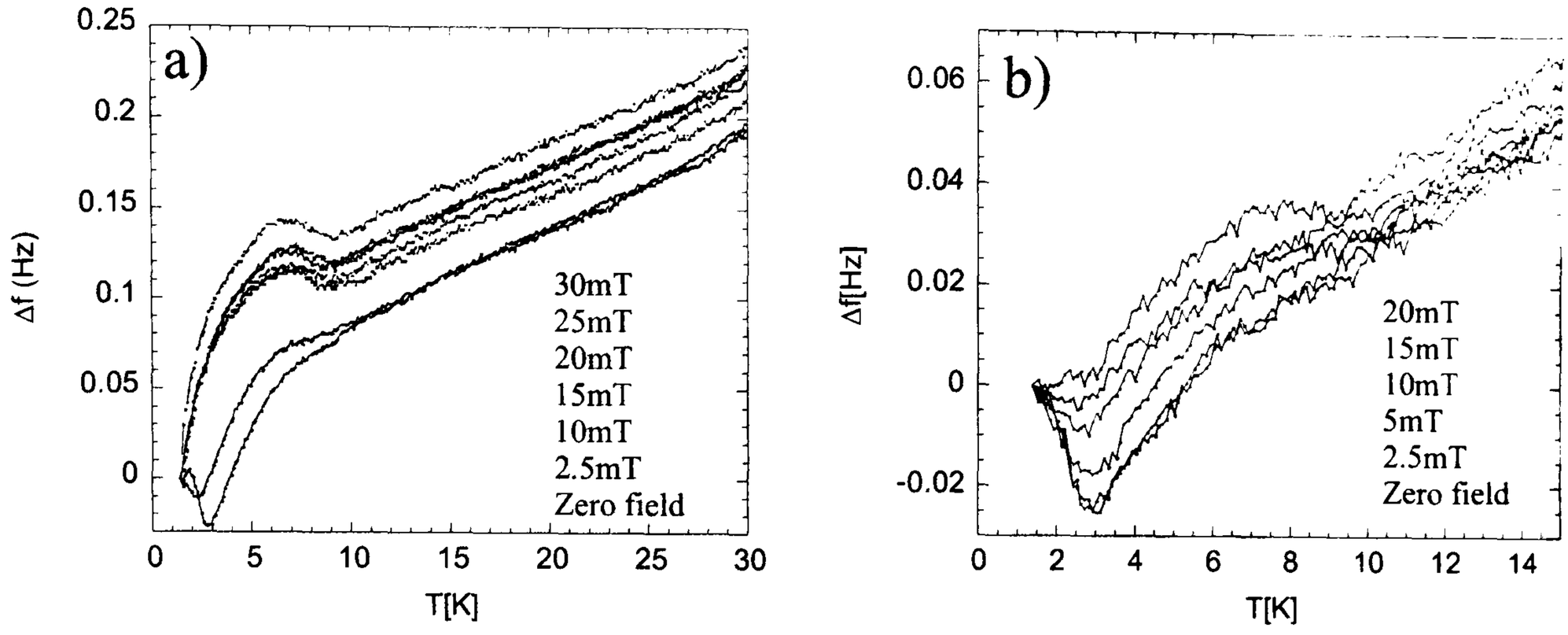

Figure 2.6: Frequency response of the sapphire rods as a function of dc magnetic field a) measurement field applied within the sample plane and, b) measurement field applied perpendicular to the sample plane.

show very similar behaviour. In zero field the frequency shift initially falls and reaches a minimum at $\sim$ 3 K. Above this temperature the frequency shift again rises. Applying a dc magnetic field causes this behaviour to be suppressed above $\sim$2.5 mT for the in-plane sample holder in Figure 2.6a. The sample holder in Figure 2.6b shows similar behaviour although the downturn is never completely suppressed. This behaviour perhaps suggest that the sapphire contains some paramagnetic component which is saturated above a certain field value and no longer contributes to the field dependence of the sapphire rod.

Effect of Pot Temperature upon Measured Frequency

The oscillator frequency can be strongly affected by any change in the pot temperature with time. The effect of temperature change can be directly measured by sweeping the pot temperature and measuring the frequency change of the oscillator as shown in Fig 2.7. It is then possible to subtract this constant frequency change from the data. As the temperature of the sample stage is swept, a heat load is placed on the the pot causing the temperature to change. Since this loading also occurs whether a

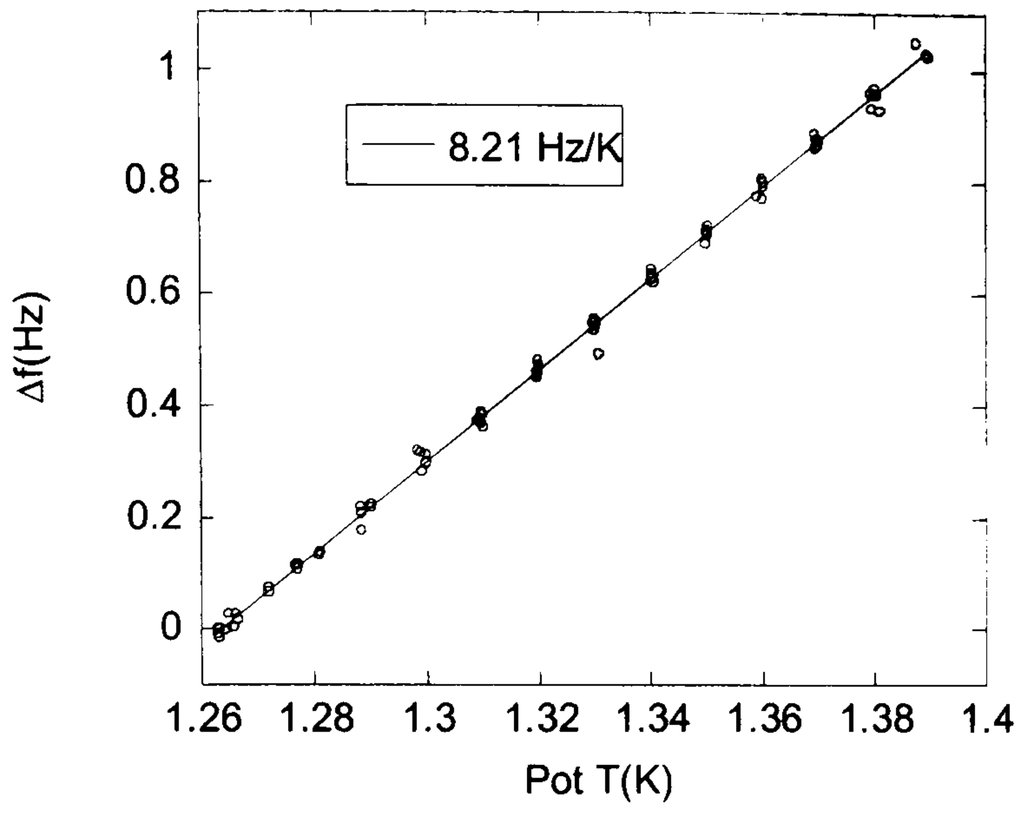

Figure 2.7: Frequency response of oscillator as a function of pot temperature.

sample is present or not the effect of the pot temperature changing will be accounted for in the background measurements for the sapphire rods since the small mass of the samples mean they have negligible effect. The effect of pot heating is naturally present in Fig.2.5 and Fig.2.6. If the effect of the pot is subtracted from the raw data, the frequency response is flat above ~ 10 K. The pot temperature is recorded in the raw data so the validity of this assumption can be checked from run to run.

Effect of Magnetic Field on Measurement Coil

Another measurement that can be performed is sweeping the dc magnetic field at fixed sample temperature. Since the sample temperature is constant, the heat load upon the pot will be constant and hence there is no contribution. The magnet contains a set of compensation coils on either side to minimize the stray magnetic field on the measurement electronics. The precise origin of this field dependence is not known. Since the coil is sensitive to changes in volume on the sub-Angström level, any slight movement of the measurement coil, even on the sub-Angström level, will cause a frequency shift. This may be the origin of the field dependence of the coil. If coil movement is the source of this background, the movement must occur in a very

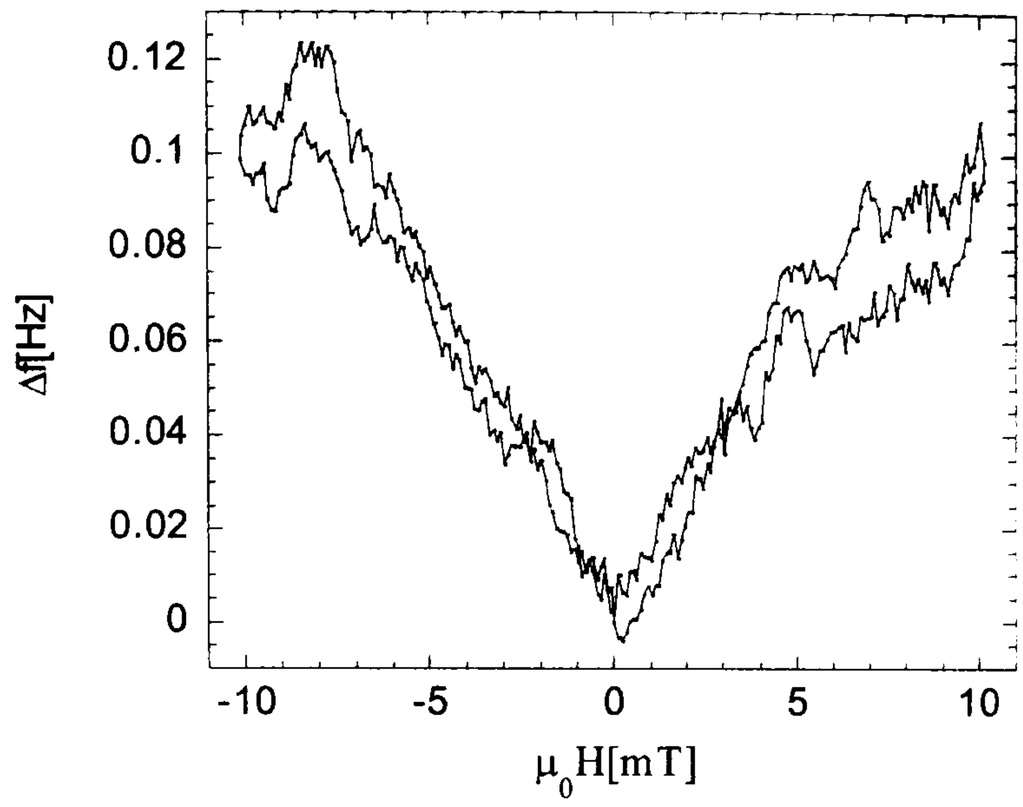

Figure 2.8: Frequency response of oscillator as a function of applied magnetic field. This background can be used with the sample mounted in either orientation since the holder is not present.

reproducible manner since the field dependent background itself is very reproducible. This background is easily determined by extracting the sample from the measurement coil and sweeping the dc magnetic field at the same rate as in the experiment. The background for a field sweep up to 10mT can be seen in Fig. 2.8.

2.3.2 Definition of λ_a, λ_b and λ_c

The component of the penetration depth which is probed during a measurement is entirely dependent upon the sample orientation within the probe field. A sample mounted at an arbitrary angle to the probe field will give a response that contains components of the penetration depth from all crystal directions i.e λ_a, λ_b and λ_c. The component measured is defined by the direction of the diamagnetic supercurrent response and so the direction of the probe field along the crystal axes. Fig.2.9 shows the measurement configuration with the probe field applied within the sample plane. along the b-axis of the crystal. In this orientation the supercurrents will circulate along two of the crystal directions: a and c. The measured penetration depth is

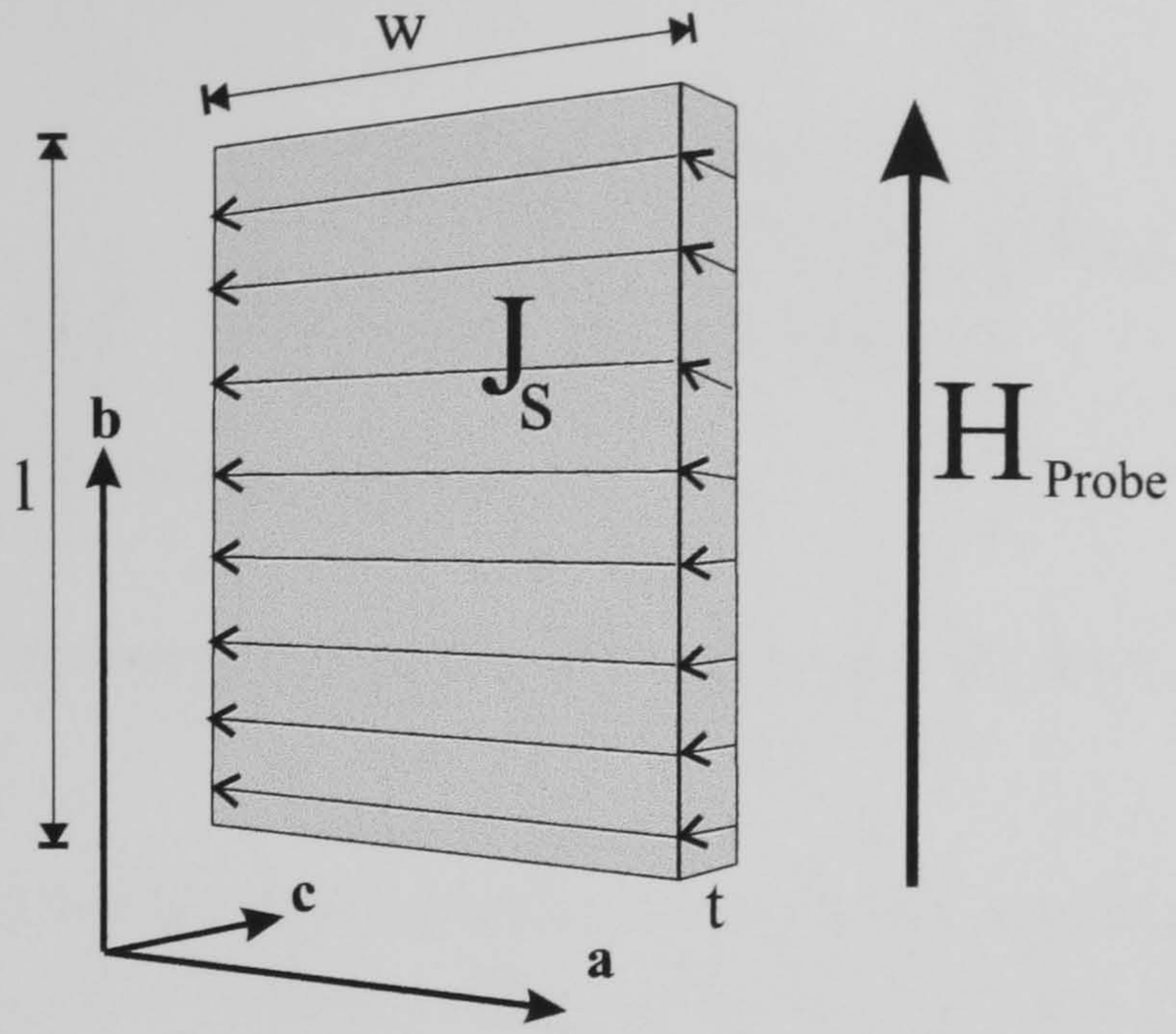

Figure 2.9: The measured component will contain $\Delta\lambda_a$ and $\Delta\lambda_c$ since the screening currents circulate along the a and c axes.

therefore defined to be comprised of λ_a and λ_c. Similarly, if the measurement field is applied along the a-axis, the supercurrents will circulate along the b and c-axes, hence the measured contribution is λ_b and λ_c. The relative contribution of each component depends on the sample geometry. λ_{eff} contains contributions due to λ_a and λ_c of the form [33]

$$\lambda_{eff} = \lambda_a + \frac{t}{w}\lambda_c \tag{2.1}$$

For a typical sized Y123 crystal of width 800μm and thickness 10μm, the effective penetration depth would be

$$\lambda_{eff} = \lambda_a + 1.25\%\lambda_c \tag{2.2}$$

Since Y123 has a penetration depth anisotropy $\lambda_c \sim 6\lambda_a$ [61], measuring $\lambda(T)$ in this configuration would result in only a small correction due to λ_c. The geometrical arguments presented above mean that the majority contribution measured for this material is still λ_a for the measurement field applied along the b-axis.

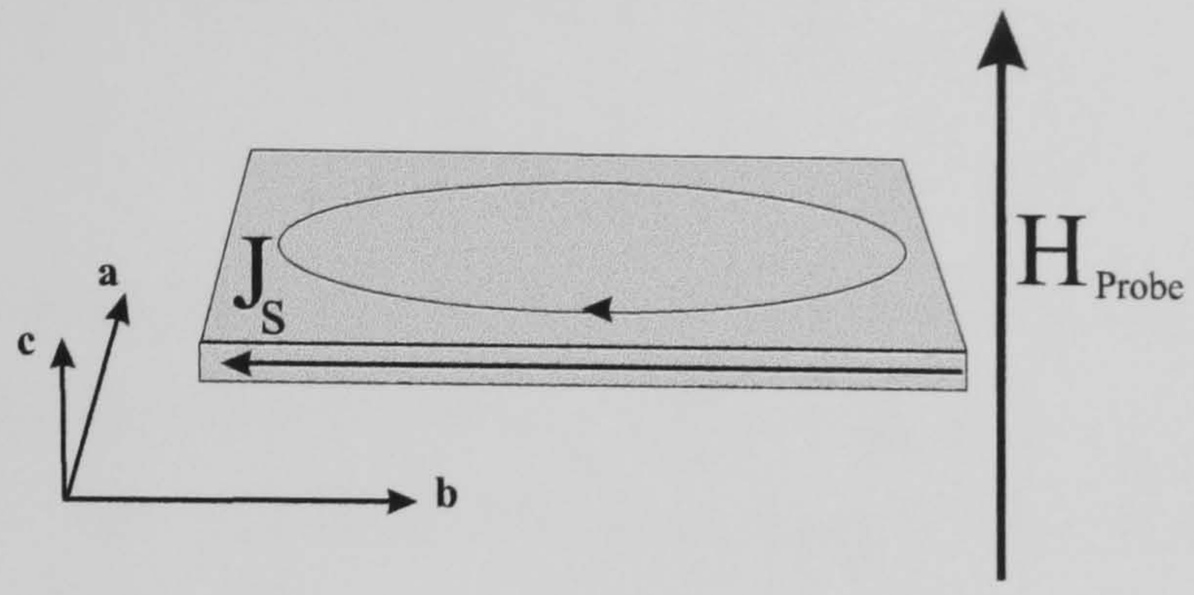

Figure 2.10: The screening currents are confined to the *ab*-plane and so the measured component is $\Delta\lambda_{ab}$.

For measurement fields applied perpendicular to the sample plane as in Fig 2.10, the screening currents will circulate solely in the *ab*-plane thus giving λ_{ab} with no λ_c contribution.

Once the extrinsic contributions to the measurement have been quantified, it is possible to measure the frequency shift in the oscillator and convert it to a corresponding change in penetration depth. For thin platelet samples with the measurement field applied within the sample plane, the frequency shift can be related to the change in penetration depth simply if the sample geometry is known (see Section 2.3.3). For measurements of the magnetic penetration depth with the measurement field applied perpendicular to the sample plane, the extraction of $\Delta\lambda$ is somewhat more difficult and will be the subject of Section 2.3.4.

2.3.3 Determination of $\Delta\lambda$ for in-plane measurement configuration

The calibration is performed by measuring the total frequency shift due to a crystal of known thickness with the measurement field applied in the ab-plane. For a Y123 single crystal the component of the penetration depth is λ_a or λ_b as defined in Section 2.3.2. If the coil calibration constant is known the frequency response of the coil can

be related directly to a change in penetration depth using

$$\delta f = \alpha 2\Delta\lambda wl \tag{2.3}$$

The calibration constant relating the volume change within the coil to the change in the resonant frequency was accurately determined to be $\alpha = 217.265$ kHz/mm^3. The total frequency shift due to the sample being extracted from the coil at low temperature is given by

$$\Delta f_0 = \alpha wlt \tag{2.4}$$

It is therefore possible to calculate the expected value for the sample extraction from the coil. This is a good test to see if the sample dimensions were accurately measured using an optical microscope. The sample holder can be extracted from the measurement coil at low temperature via the G10 rod which is attached to the holder. A stepper motor, attached to a micrometer, pulls the sample holder from the measurement coil. The results of such an extraction are included in Fig. 2.11. To calibrate the coil Δf_0, the frequency shift due to the sample being extracted from the measurement coil, must be measured. Fig. 2.11 shows three curves. The top curve is the frequency response due to the extraction of the sapphire rod. This must be subtracted from the total response (middle curve) which contains both the sample and sapphire contributions. The resulting curve is the isolated frequency change for the sample alone, which in this orientation is $\Delta f_0 = \alpha wlt$ where w is the sample width, l the length and t is the sample thickness. It is noted that the total frequency shift due to the sample extraction shown in Fig. 2.11 is not typical of the majority of samples measured in this study and is shown solely to emphasize reproducibility. Typical values for the sample extraction are $\Delta f_0 \sim 2000$ Hz for the YBCO single crystals measured in Chapter2. The sapphire response is therefore a ~10% contribution to the raw extraction frequency shift. From now on, all reference to frequency shift due to sample extraction (Δf_0) assumes that the appropriate sapphire contribution has been subtracted. Combining Eqs. 2.3 and 2.4 means that the coil calibration constant

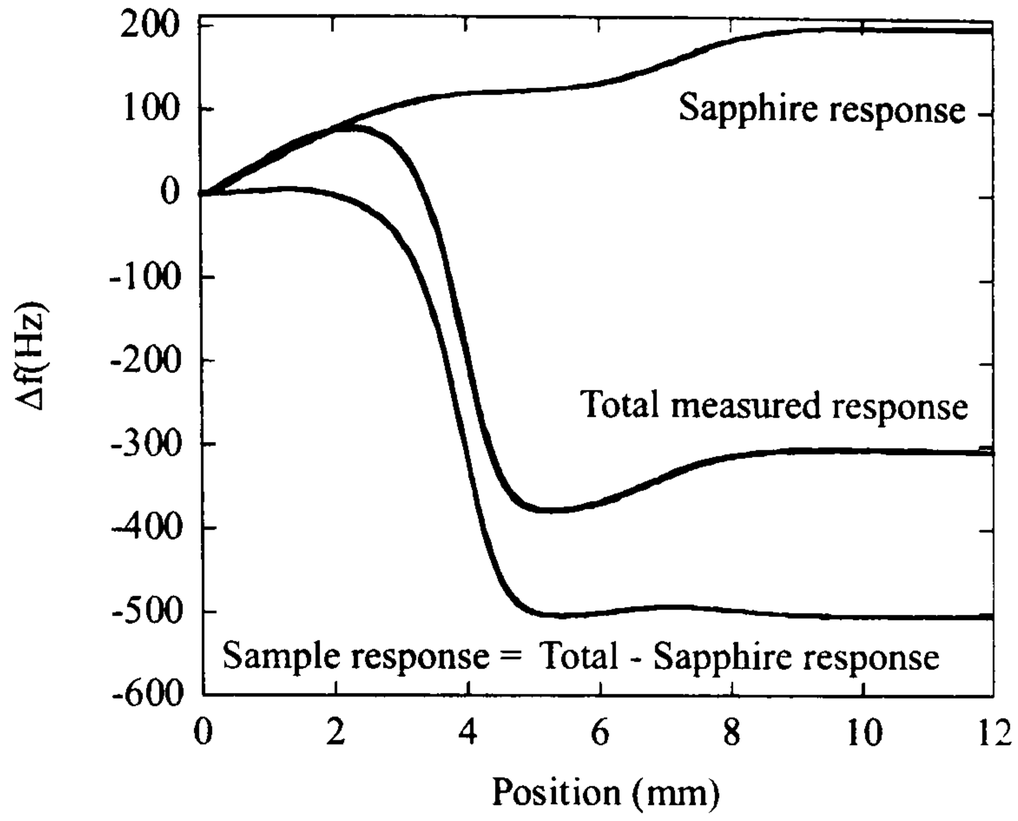

Figure 2.11: The raw sample response is isolated by subtracting the bare sapphire response from the measured total response.

does not appear in the final expression

$$\frac{\delta f}{\Delta f_0} = \frac{2\Delta\lambda}{t} \tag{2.5}$$

Rearranging this expression gives

$$\Delta\lambda = \frac{\delta f}{\Delta f_0}\frac{t}{2} \tag{2.6}$$

For thin platelet samples with the measurement field applied within the *ab*-plane of the sample the above expression is correct. For thicker samples, there is some field enhancement due to demagnetizing effects meaning that the measured penetration depth will be enhanced by the demagnetizing factor $D = 1/(1-N)$. The consequences of demagnetizing factors are discussed in terms of their effect on ac-susceptibility measurements by Goldfarb *et al.*[73].

A magnetized body will produce within itself a demagnetizing field which is superimposed on the applied field. The resulting internal field will be the applied field minus the demagnetizing field. For the special case of ellipsoidal bodies, **H** the internal field and **M** the magnetization, are uniform and parallel to the applied field.

The internal field for this case is $\mathbf{H}_a - D\mathbf{M}$. For bodies of general shape. the situation is more complicated since the internal field will vary in strength and direction throughout the body.

For an ellipsoid of revolution, N, the scalar demagnetizing factor. can be estimated as a function of the aspect ratio (α) of the sample where α =width/thickness.

For $\alpha > 1$ (ie., field applied within the ab-plane)

$$N = (\alpha^2 - 1)^{-1}[\alpha(\alpha^2 - 1)^{-1/2}\cosh^{-1}\alpha - 1] \tag{2.7}$$

For a sample of dimensions of $a \times b \times c$=0.35mm×0.22mm×0.1mm a value of N can be estimated using Eq.(2.7) using an average of a and b yielding $\alpha = (0.35 + 0.22)/(2 \times 0.1)$=2.85 and N=0.12. Using these results $D = 1/(1 - N)$=1.1, meaning the measured penetration depth would be a factor 1.1 greater than the true penetration depth.

2.3.4 $\Delta\lambda$ out of plane measurement configuration

In order to better separate the components λ_a, λ_b and λ_c it is desirable to use a measurement orientation where one of these components is not present. By applying the measurement field perpendicular to the ab-plane, screening currents will circulate solely in the ab-plane, thus giving a penetration depth contribution λ_{ab} which is a geometrical average of λ_a and λ_b. In this orientation it is more difficult to relate the measured frequency shift to a change in penetration depth because of demagnetizing effects. Analytical solutions to the London equations exist for certain geometries such as spheres, infinite bars or cylinders in a longitudinal field or a cylinder in a perpendicular field [74]. Since the high T_c cuprates are typically thin platelet samples these solutions do not apply.

Recently, a method was developed by Prozorov *et al.* [75] that allows the measured frequency of a rf LC oscillator to be accurately related to the change in penetration depth in this orientation. The London equations were solved numerically in 2 dimensions and then extended to 3 dimensions.

The effect of the penetration depth is to change the effective volume of the sample. The ratio of the change in the effective sample volume (ΔV^{λ}) to the effective volume (ΔV^{0}) is equal to the penetration depth divided by an effective dimension ie., $\Delta V^{\lambda}/\Delta V^{0} = \lambda/R$. The effective volume of the sample is equal to the actual sample volume multiplied by the demagnetization factor of the sample. The change in volume is estimated for the top and sides of the sample independently. For a disc of width $2w$ and thickness $2d$ we can assume that the field at the top and bottom surfaces are given as in [76] and the field at the sides is constant. In this analysis. the demagnetization factor cancels out of the expression when the volume ratio is taken. For the disc model, $R = 0.28w$. The approach of Prozorov *et al.* is to again consider a sample of width $2w$ and thickness $2d$. The demagnetisation factor was calculated to be $D = 1/(1-N) \approx 1 + w/2d$ and compared with the susceptibility of Nb cylinders of different aspect ratios. The measured magnetic susceptibility for the Nb cylinders was found to agree well with a demagnetizing factor of $1 + w/2d$ up to values of $w/d = 10$. This demagnetizing factor was used when considering both the effective volume ($\Delta V^{0} = \pi w^2 2d(1 + w/2d)$) and the change in volume due to the sides of the sample ($\Delta V_s^{\lambda} = 4\pi wd(1 + w/2d)$). The change in volume due to the top and bottom was calculated analytically to be

$$\Delta V_{t+b}^{\lambda} = 2\pi m^2 \lambda (1+m^2)\left[\sin^{-1}\left(\frac{1}{\sqrt{1+m^2}}\right) - \frac{m}{1+m^2}\right] \tag{2.8}$$

where $m = 2d/w$. Adding this to ΔV_s^{λ} and dividing by ΔV^{0} can be equated to λ/R where R is the effective dimension of the sample. The λ contribution cancels and leaves an expression which relates w and t to R.

$$R = \frac{w}{2\{1 + [1 + (\frac{2d}{w})^2]\arctan(\frac{w}{2d}) - \frac{2d}{w}\}} \tag{2.9}$$

This expression accounts for the demagnetization and can be used in Eq.(2.10) below.

In the thin limit ($d \ll w$)$R \approx 0.2w$. The validity of this solution was checked by measuring the penetration depth of BSCCO, Y123 and Nd thin films and comparing the expected value given by this method with an independent measurement. The

expected frequency shift was calculated for samples in the limit $\lambda \ll$R was found to be

$$\frac{\Delta f}{f_0} = \frac{V_s}{2V_0(1-N)}\left(1-\frac{\lambda}{R}\right) \tag{2.10}$$

where V_s is the sample volume and V_0 is the effective coil volume. The quantity $\Delta f_0 \equiv V_s f_0/[2V_0(1\text{-}N)]$ is directly measured by the frequency shift due to removing the sample from the coil (see Section 2.3.3). The change is λ is therefore given by

$$\Delta\lambda = -\delta f \frac{R}{\Delta f_0} \tag{2.11}$$

Using Eq.(2.11) Prozorov *et al.* found good agreement between their measured values of λ(T) in Y123 and BSCCO single crystals and Nd thin film samples.

The calculation outlined above calculates the penetration depth contribution due to the top/bottom of the crystal and the sides. By assuming a demagnetising factor $(1/1-N) = (1+w/2d)$ in the thin limit i.e. $w \gg d$

$$\frac{\lambda_{sides}}{\lambda_{top}} = \frac{5}{2\pi} \tag{2.12}$$

This result shows that the field penetration from the top of the crystal remains significant in this orientation.

The results for single crystals presented in later chapters were analysed using this method for sample calibration when measuring single crystals with the probe field perpendicular to the sample plane. Care has been taken to ensure that the calibration value obtained by this method is accurate. As discussed in the previous Section, for Y123 crystals the measured quantity in both orientations should be λ_{ab} since the correction due to λ_c is small. This was found to be the case with a typical accuracy of $\sim$5%.

Chapter 3

Observation of Andreev Boundstates in $YBa_2Cu_3O_7$

3.1 Introduction

Penetration depth measurements have proved a powerful tool in identifying the superconducting gap symmetry at low temperature. The temperature dependence of the penetration depth has several clearly identifiable characteristics depending on the order parameter symmetry. Fully gapped superconductors will show exponential temperature dependence. A gap with nodes at the Fermi level will show linear temperature dependence possibly crossing over to T^2 below some temperature in the presence of impurities or due to non-local effects. The $d_{x^2-y^2}$ order parameter cannot be characterized by the presence of nodes solely. A strongly anisotropic s-wave superconductor could have nodes but the phase of this order parameter remains constant around the Fermi surface. The $d_{x^2-y^2}$ order parameter has both nodes and a π-phase change around adjacent lobes of the order parameter. Although the $d_{x^2-y^2}$ order parameter has both nodes and a π-phase change around adjacent lobes, it is the position of these lobes that identifies it. The lobes of the $d_{x^2-y^2}$ order parameter lie along the (100) and (010) crystal orientations whereas the d_{xy} order parameter lies at 45° to this. A measurement which could identify the presence of nodes, their cystallographic

orientation *and* the presence of a phase change around the Fermi surface would provide strong evidence, not just for unconventional superconductivity but, for the type of symmetry present. The observation of surface Andreev boundstates in $YBa_2Cu_3O_7$ provides strong evidence for an order parameter with nodes on the Fermi surface. a phase change between adjacent lobes of the order parameter; the direction of these lobes being the (100) and (010) crystal directions i.e the $d_{x^2-y^2}$ order parameter.

3.2 Andreev Reflection and Surface States for *s*-wave Order Parameters

The mechanism by which a normal current is converted to a supercurrent at a metal-superconductor interface was first studied by Andreev in 1964 [77]. This process initially presented a problem to the understanding of superconductivity. Although it was well established some years before by the BCS theory [34] that superconductivity occurs as a result of electron-like quasiparticles forming Cooper pairs resulting in an energy gap in the density of states, this same energy gap did not appear to prevent normal electrons with sub gap energies from entering the superconductor and becoming part of the supercurrent. Andreev proposed that any mechanism by which normal electrons entered the superconductor must involve them becoming Cooper pairs by a process of electron-hole conversion since there exist no states in the superconductor with energy $\mid E \mid < \Delta$.

The mechanism proposed by Andreev can be understood by considering an ideal interface consisting of a normal metal and a superconductor [17],[78]. It is assumed that the interface between the two materials is such that there is perfect transmission of electrons between the electrodes when both materials are in the normal state i.e. no scattering processes occur at the interface. Electrons in the normal metal with energy $\mid E \mid < \Delta$, below the energy of the superconducting gap. cannot enter the superconducting electrode. There also exists no normal scattering process which can

scatter the electron away from the normal-superconductor interface. Andreev proposed that the electron could be converted into a hole with the opposite momentum. An electron approaching the superconductor interface encounters a rising dispersion curve. The excitation energy of the electron must be conserved resulting in its **k** value decreasing. The group velocity of the electron is $(dE/dk)/\hbar$ which falls to zero at the metal-superconductor interface. The group velocity becomes reversed resulting in a hole retracing the electron path away from the interface back into the normal electrode. The energy of the reflected hole is $E^h = E_F - p^2/2m$. The process results in 2 electron-like quasiparticles entering the superconductor as a Cooper pair. This total process is termed Andreev reflection and is a direct consequence of all quasiparticle states being comprised of electron and hole wavefunctions.

The process of Andreev reflection is accompanied by a phase shift $-\gamma(E) \mp \chi$, where γ =arccos$(E/\mid \Delta \mid)$ and χ is the phase of the superconducting order parameter. $(-)$ corresponds to electron to hole conversion and $(+)$ to hole to electron conversion [78]. The wavefunctions of the electron and hole states penetrate into the superconductor over a length scale of the coherence length $\xi_0 = \hbar v_F/\Delta$. Although the exact profile of Δ near the surface can be calculated, the essential physics of the situation can be understood by modeling $\Delta(x)$ as a step function $\Delta(x) = \Delta\Theta(x)$ [78].

A vacuum-metal specular interface next to a superconducting region represents a quantum well in which boundstates can form due to the phase-shift process which is part of Andreev reflection. The process is illustrated by considering a two dimensional system of an s-wave superconductor with an anisotropic order parameter as in Fig 3.1. The boundstate energy is given by the Bohr-Sommerfeld condition which states that the total phase accumulated during one cycle must be quantized into units of 2π. Fig. 3.1 shows a single electron in the normal metal undergoing a specular reflection at the metal-vacuum interface and then entering the superconductor via the Andreev reflection of a hole. The hole then undergoes the same process in reverse as it retraces the electron's path and enters the superconductor by the Andreev reflection of an electron. The boundstate corresponds to the closed quasiparticle trajectory

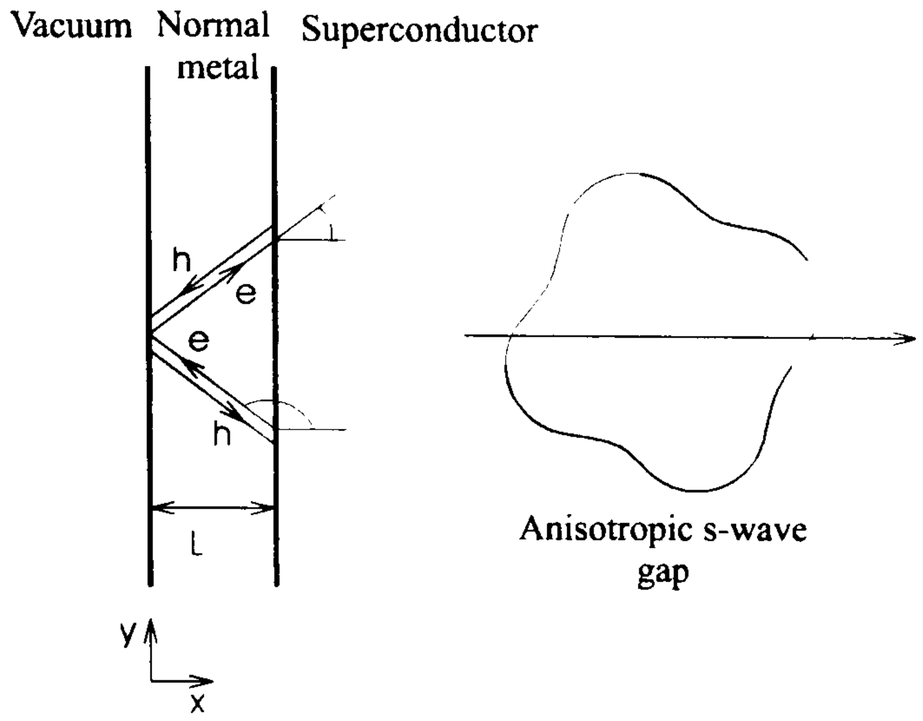

Figure 3.1: Schematic diagram of electron and hole like quasiparticles undergoing specular reflection at a normal-vacuum interface. The electron like quasiparticle undergoes Andreev reflection at the normal-superconductor interface and a hole is back reflected. After Löfwander *et al.*[78]

(comprised of electron and hole states) within the normal metal.

The total phase accumulated during the process can be considered in two parts: i) During the Andreev reflection process phase will be accumulated as the electron is retro-reflected as a hole and again when the hole is retro-reflected as an electron. As mentioned above this phase shift is $-\gamma^e - \chi^e$ for the electron trajectory and $-\gamma^h + \chi^h$ for the retro-reflected hole trajectory. ii) The second contribution to the total phase change is due to the phase accumulated during propagation through the normal metal region, $\beta = 2L(k^e - k^h) + \beta_0$. The first term of the expression is due to the ballistic motion of the particles and β_0 is the phase accumulated upon specular reflection at the vacuum-metal interface. The wavevectors for the particles are given by $\hbar k^{e,h} = [2m(E_F cos^2\theta \pm E)]^{1/2}$. Writing the Bohr-Sommerfeld quantization condition gives

$$(-\gamma^e - \chi^e) + (-\gamma^h + \chi^h) + \beta(E) = 2n\pi \tag{3.1}$$

For an isotropic s-wave gap (amplitude and phase constant) $\gamma^e = \gamma^h = \gamma$ and $\chi^e = \chi^h$, therefore Eq. (3.1) becomes

$$-2\gamma + \beta(E) = 2n\pi \tag{3.2}$$

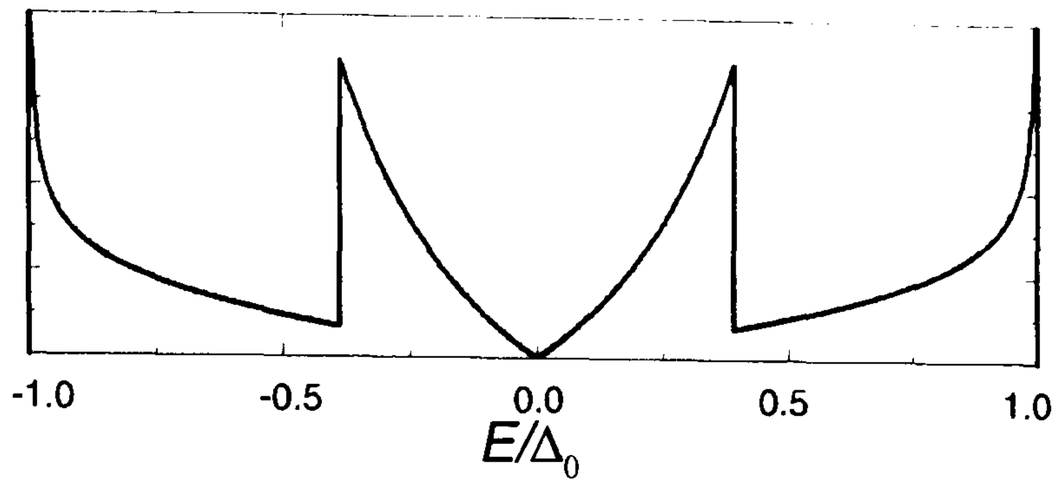

Figure 3.2: Density of boundstates for an isotropic *s*-wave superconductor. After Löfwander *et al.*[78]

Recalling $\gamma = \arccos(E/|\Delta|)$ and rearranging, the position of an excitation of energy E within the gap is given by

$$\frac{E}{\Delta} = \pm \cos\left(\frac{\beta(E)}{2}\right) \tag{3.3}$$

where again, + (-) corresponds to electron (hole) like states. Eq.(3.3) relates an excitation of energy E with trajectory θ, to the position it occupies within the superconducting gap. In the presence of a normal metal region the ballistic contribution to the phase shift in the bulk, $\beta_{ballistic} = 2L(k^e - k^h) \approx 4LE/\hbar v_F \cos\theta$, will dominate over the surface scattering phase shift β_0 [78]. Including this dominant contribution and solving as for Eq. (3.3) yields

$$\frac{E}{\Delta} = \pm \cos\left(\frac{2LE}{\Delta\xi_0 \cos\theta}\right) \tag{3.4}$$

Integrating over all particle trajectories and summing over energy gives the excitation density of states as in Fig. 3.2 which is a plot of the density of boundstates for $L = 1.5\xi_0$. Eq.(3.4) therefore pushes allowed low-lying excitation energies out towards E/$\Delta \approx$1 at the gap edge.

For an anisotropic s-wave superconductor the above argument must be modified slightly due to the fact that the magnitude of the superconducting gap from which the electron is Andreev reflected need not be of the same magnitude as that encountered by the hole, therefore $\gamma^e \neq \gamma^h$. Since the phase of the order parameter is still constant. low lying boundstate energies still occur at the gap edge and not at $E/\Delta = 0$. For this

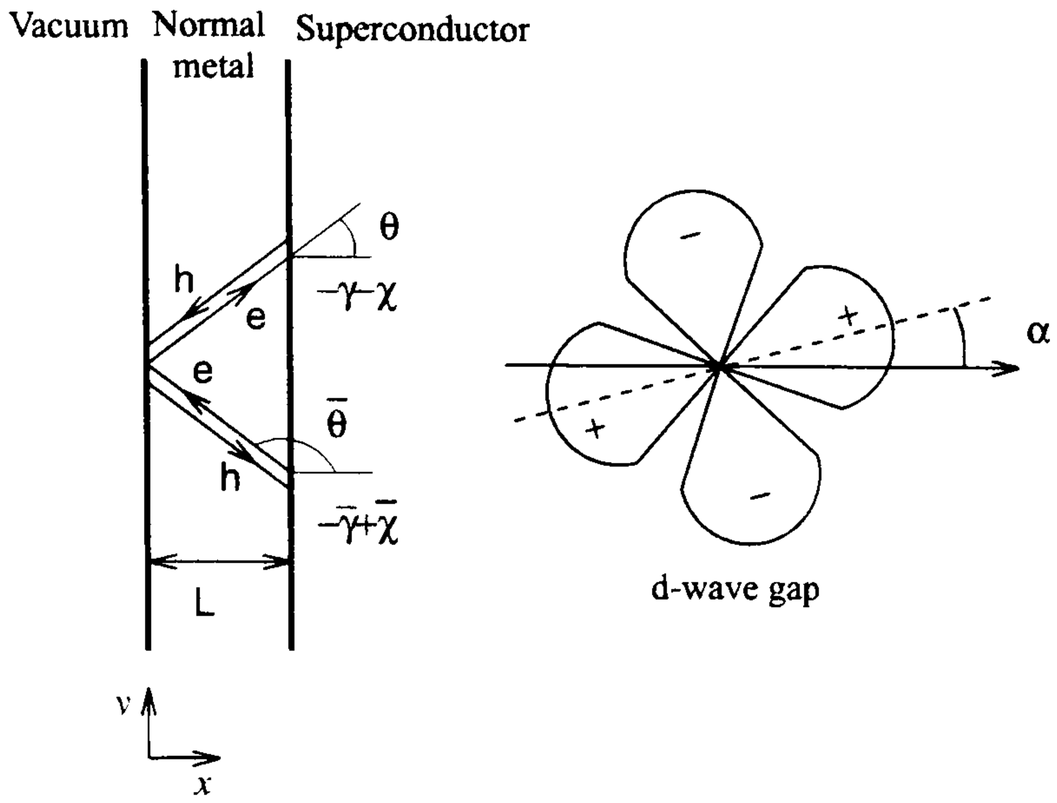

Figure 3.3: Schematic diagram of a vacuum, normal metal, superconductor (INS) configuration. The superconductor has $d_{x^2-y^2}$ symmetry meaning that electron and hole quasiparticles may be incident on portions of the order parameter with different phase and amplitude. After Löfwander *et al.*[78]

situation the density of boundstates at the surface will be sensitive to the orientation of the order parameter with respect to the surface direction.

3.3 Zero Energy Boundstates as a Consequence of the $d_{x^2-y^2}$ Order Parameter

The above analysis discussed the consequences of Andreev reflection from an s-wave superconductor, both isotropic and anisotropic. Although the presence of an anisotropic order parameter modifies the density of boundstates formed, it still precludes the formation of zero energy boundstates away from the gap edge. The consequences of a vacuum-metal-superconductor configuration will be considered again but now with the superconductor having an order parameter of $d_{x^2-y^2}$ symmetry. Such a configuration is shown in Fig. 3.3. As for the anisotropic s-wave case, the magnitude

of the superconducting gap is not constant and so boundstate formation will be sensitive to the orientation of the order parameter relative to the specular surface. The $d_{x^2-y^2}$ case also has an added orientation dependence due to the change in phase of the order parameter. The effect of a π-phase change between adjacent lobes leads to dramatic consequences which differentiate this order parameter markedly from the anisotropic s-wave case. For an electron incident to the surface at an arbitrary angle, the Bohr-Sommerfeld condition of Eq.(3.1) must still be true. Now however, the assumption that the amplitude and phase of the order parameter are the same for both Andreev scattering processes need not be true. The amplitude of the $d_{x^2-y^2}$ order parameter varies as

$$\Delta(\theta) = \Delta_0 \cos[2(\theta - \alpha)] \tag{3.5}$$

where α is the angle of the order parameter relative to the surface normal. For a surface at an angle $\alpha = \pi/4$ to the order parameter particles of all trajectories will go through a π-phase change in the order parameter. In this orientation $\chi^h = \chi^e + \pi$ and the order parameter is of the same amplitude upon Andreev reflection for both the electron and hole giving $\gamma^e = \gamma^h$. The Bohr-Sommerfeld condition again is

$$(-\gamma^e - \chi^e) + (-\gamma^h + \chi^e) + \beta(E) = 2n\pi \tag{3.6}$$

becoming

$$-2\gamma + \pi + \beta(E) = 2n\pi \tag{3.7}$$

Again we can solve as for Eq.(3.3), again assuming the dominant ballistic condition ($\beta_{ballistic} \approx 4LE/\hbar v_F \cos\theta$) now yielding for the $d_{x^2-y^2}$ case

$$\frac{E}{\Delta} = \pm \cos\left(\frac{\pi}{2} - \frac{2LE}{\xi_0 \Delta \cos\theta}\right) \tag{3.8}$$

or alternatively

$$\frac{E}{\Delta} = \pm \sin\left(\frac{2LE}{\xi_0 \Delta \cos\theta}\right) \tag{3.9}$$

The consequence the π-phase shift of the $d_{x^2-y^2}$ order parameter is that Eq.(3.9) has solutions for zero energy excitations at position E/Δ=0 for all trajectories in the

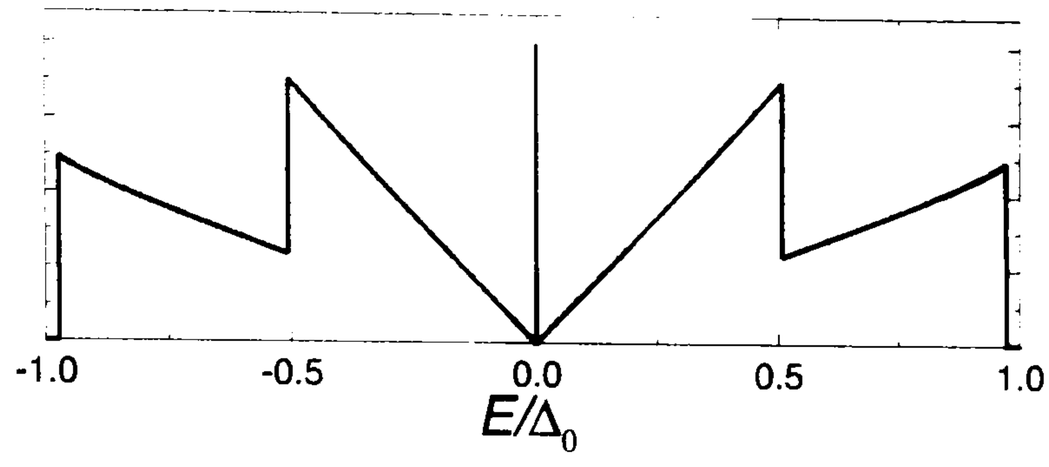

Figure 3.4: Density of boundstates for a vacuum, normal metal, $d_{x^2-y^2}$-symmetry superconductor. Boundstates can form at zero energy in this system. After Löfwander *et al.*[78]

$\alpha = \pm\pi/4$ orientation. The density of boundstates is plotted in Fig. 3.4 again for a normal layer $L = 1.5\xi_0$. For a single crystal this orientation would correspond to specular scattering from a (110) oriented surface with the Andreev boundstates being confined to within a few coherence lengths of the surface.

By similar considerations it is possible to orient the vacuum-normal interface with respect to the order parameter at such angles where no zero energy boundstates can exist. For a surface oriented at angles $\alpha = \pm n\pi/2$ the phase over all quasiparticle trajectories remains constant i.e. $\chi^h = \chi^e$ and results in a boundstate density of states qualitatively the same as in the anisotropic s-wave scenario.

3.4 Splitting of the Andreev Boundstates

Having a large density of states at the Fermi energy from the zero energy boundstates is energetically unfavourable. If the delta function in the density of states could be split this would lower the total free energy of the system. A split could be realized by the presence of a sub-dominant order parameter. An order parameter less sensitive to surface pair breaking than the $d_{x^2-y^2}$ could pair the broken Cooper pairs which occur at the surface. A combination such as $d_{x^2-y^2} \pm is$ is energetically favourable. The appearance of a subdominat order parameter would introduce a further phase shift at the surface by an amount $\chi_{rel} = \arctan(\Delta_s/\Delta_d)$. For the $\alpha = \pi/4$ orientation

Eq.(3.7) becomes

$$-2\gamma + \pi + \mp 2\chi_{rel} = 2n\pi \tag{3.10}$$

This extra contribution shifts the peak seen in the DOS as in Fig.3.4 away from $E/\Delta = 0$, thus lowering the energy of the system.

$$\frac{E}{\Delta_d} = \sin\left(\mp \arctan\frac{\Delta_s}{\Delta_d}\right) \tag{3.11}$$

which is

$$E_{MGS} = \mp\Delta_s \tag{3.12}$$

Therefore the midgap state is shifted away from zero energy to the edge of the sub dominant order parameter. Electron like quasiparticles are shifted below the Fermi energy, thus becoming populated, and hole like above thus removing the degeneracy between electron-like and hole-like states. Since only the electron-like states are populated a net surface current results, the direction of the current is determined by whether $d_{x^2-y^2}+is$ or $d_{x^2-y^2}-is$ occurs. The spontaneous surface current is indicative of broken time reversal symmetry. A signature of the presence of such a sub dominant order parameter would be the appearance of a spontaneous current below a secondary critical temperature corresponding to the critical temperature of the sudominant order parameter.

Andreev surface boundstates, whether spontaneously splitting or not, can be further split by the application of a dc magnetic field. The magnetic field couples to the surface boundstates via the same mechanism that also shifts the continuum states. The shift in energy is given by $\delta E = e\mathbf{v}_f \cdot \mathbf{A}$. In this process, quasiparticles that are co-moving with superfluid density are shifted up in energy by an amount δE and counter moving particles are shifted down in energy by δE. This will be discussed further in the context of penetration depth measurements

3.5 Effect of Surface Andreev Boundstates on Penetration Depth

In Section 1.6 the change in penetration depth due to thermally excited quasiparticles was discussed. It was shown that the change in penetration depth with temperature is intimately related to the quasiparticle density of states. Penetration depth is a strong probe of these states and at low temperature allows a great deal of information to be gathered regarding the symmetry of the order parameter for a particular material. Details regarding order parameter symmetry (and impurity level in unconventional superconductors) are obtained since this dominates the density of states at low temperatures. In the discussion above (Section 3.3). it was established that the presence of ABS causes a delta-peak in the quasiparticle density of states to occur. Since penetration depth measurements are very sensitive to low energy excitations, this peak will have a strong effect on the penetration depth.

ABS only occur at zero energy when electron and hole-like quasiparticles are specularly scattered through a π-phase shift in the order parameter. Such a phase change in the order parameter only occurs for specular reflection at non-(100), (010) or (001) surfaces. The formation of ABS at zero energy is therefore strongly dependent on the direction of the supercurrent flow ($\mathbf{J}_S$). Chapter 2 describes the LC-oscillator used to measure the penetration depth in the work presented here. This technique allows the measurement field to be applied in two orientations; either within the sample plane or perpendicular to it. Fig.3.5 illustrates the difference between the two measurement orientations. The surfaces at which quasiparticles are incident are very t in these two measurement configurations. Zero energy ABS would not be expected to contribute to the penetration depth for the orientation shown in Fig.3.5a. In this orientation quasiparticles are incident upon large non-pair breaking surfaces. The edges of the sample have a negligible contribution to the penetration depth since the samples are thin. Fig.3.5b shows the orientation where ABS would form and contribute to the penetration depth. All quasi-particle trajectories incident

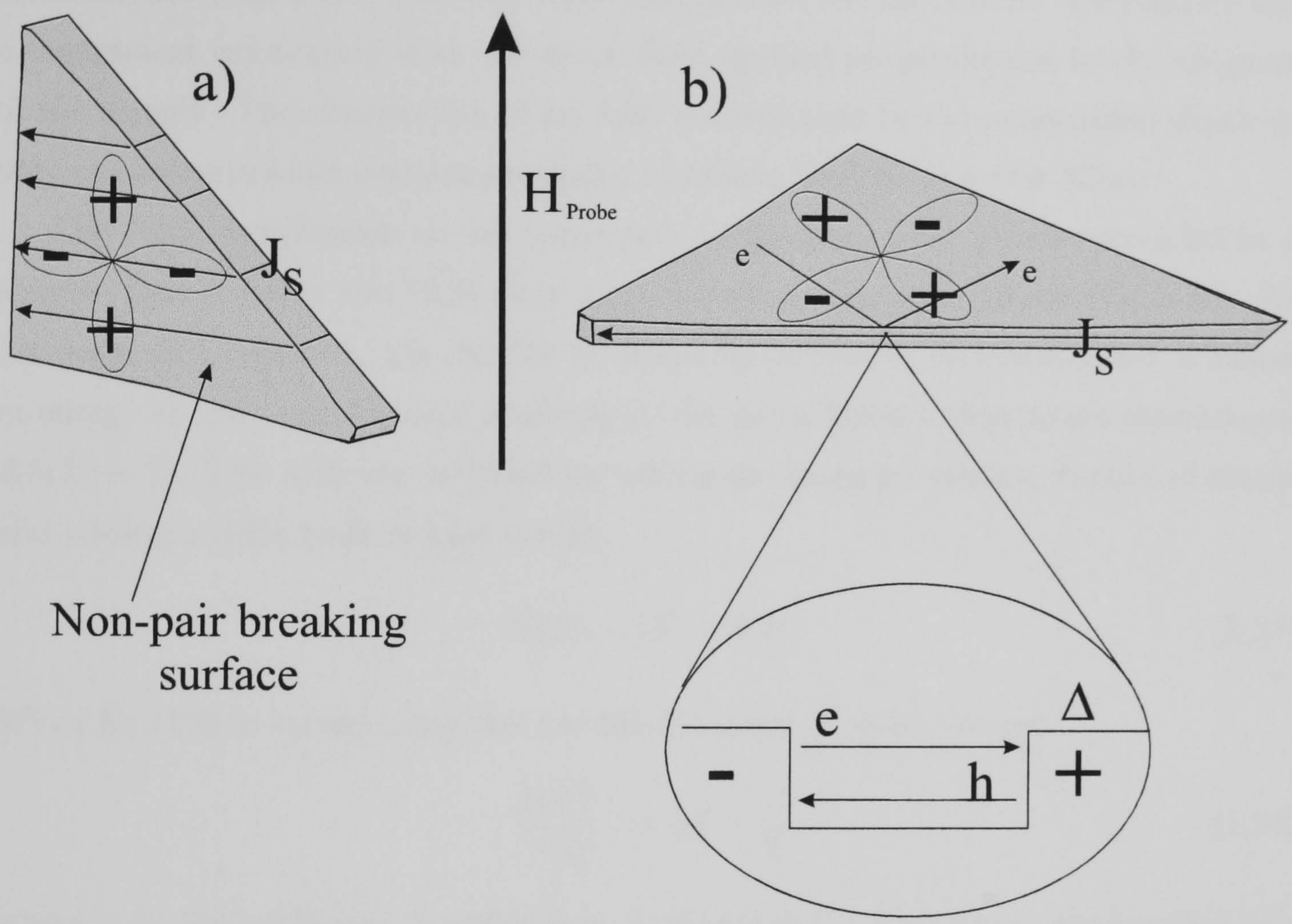

Figure 3.5: (a) The penetration depth response comes from large non-pair breaking surfaces (b) At certain surfaces quasi-particles experience a π-phase shift in the order parameter causing the formation of ABS. In this orientation the penetration depth response is dominated by these surfaces.

on the (110) surface will be subject to a π-phase change in the order parameter resulting in ABS formation. The step function shows the order parameter either side of the surface having different phase. In the orientation of Fig.3.5b. ABS would also be expected to form to some extent on the other surfaces, for certain quasiparticle trajectories, since these surfaces are not perfectly orthogonal to the (100) and (010) orientations. This shows that any ABS contribution should only be observed for the measurement orientation with the probe field applied perpendicular to the *ab*-plane of the sample. The observation of an ABS contribution to the penetration depth in only one measurement orientation would be strong evidence for this effect.

The ABS contribution to the measured penetration depth can be modeled in a simple manner using the BCS expression for the penetration depth (Eq.(1.9). As discussed in Chapter 1, the density of states for a *d*-wave superconductor is linear in energy at low temperatures resulting in the usual linear temperature dependence $\Delta\lambda(T) \sim T$. The ABS are included by taking the standard *d*-wave density of states and adding a delta peak at zero energy.

$$N(E) \sim |E| + \delta(E) \tag{3.13}$$

When Eq.(1.9) is solved using this modified density of states we get

$$\frac{\Delta\lambda(T)}{\lambda(0)} = \alpha T + \frac{\beta}{T} \tag{3.14}$$

where α is the coefficient as defined in Section(1.6.2). This result implies that the penetration depth should diverge at low temperature in the presence of zero energy ABS.

Although this simple model predicts qualitative behaviour for the modification of the penetration depth due to ABS, a more complete model is required in order to calculate the magnitude of the coefficient β. A model for the temperature and field response of the penetration depth in the presence of ABS was given by Barash *et al.* [79]. When describing the effect of ABS on the penetration depth, two competing effects were considered: the conventional shielding current contribution due to the

Meissner effect monotonically reducing the penetration depth and, a paramagnetic contribution from zero energy boundstates which serves to increase the penetration depth. By considering these two competing effects two temperature scales are identified, $T_{m0} \sim \sqrt{\xi_0/\lambda_0}T_c$, the temperature at which a minimum in penetration depth is reached and, $T_s \sim (\xi_0/\lambda_0)T_c$, the temperature at which a spontaneous supercurrent could occur as a consequence of boundstate population.

This model accounts for Fermi surface effects and also the effect of impurities on the penetration depth. The temperature dependence of the penetration depth within the temperature range $(\xi_0/\lambda_0)T_c \ll T \ll T_c$ is given by

$$\lambda(T) = \lambda_0 + a\frac{T}{T_c}\lambda_0 + \frac{\mu_0\pi e^2 N_f \lambda_0^2}{4T}\langle v_{f,y}^2(\mathbf{p}_f)|v_{f,x}(\mathbf{p}_f)|\Theta(\mathbf{p}_f)\rangle_{S_f} \qquad (3.15)$$

where λ_0 is the zero temperature value of the penetration depth, v_f is the Fermi velocity, N_f is the density of states at the Fermi level and $\Theta(\mathbf{p}_f)$ is a function equal to unity over portions of the Fermi surface where zero energy boundstates can occur, and zero elsewhere. For a $d_{x^2-y^2}$ superconductor with a cylindrical Fermi surface

$$\lambda(T) = \lambda_0 + a\frac{T}{T_c}\lambda_0 + \frac{\hbar v_f}{6k_B T}\|\sin^3\theta| - |\cos^3\theta\| \qquad (3.16)$$

where θ is the angle that a surface makes with the (110) crystal direction. This function equals zero for samples with pure (100) and (010) surfaces and unity for a pure (110) sample. This model makes an explicit link between sample shape and the magnitude of the ABS contribution. The measured ABS contribution to the penetration depth in single crystals should be strongly correlated with their shape. From this expression, the β coefficient given in the simple model in Eq.(3.14) is shown to be $\beta = (\hbar v_f/6k_B T)$ multiplied by the shape correlation factor $g(\theta) = \|\sin^3\theta| - |\cos^3\theta\|$. Assuming v_f=2×10^5 ms^{-1} [9], the ABS contribution should be $\beta = 2.5 \times 10^3 g(\theta)$ Å. The magnitude of β could be reduced from this value if the sample surfaces are non ideal ie., if the scattered quasiparticles do not pass through a π-phase change in the order parameter at (110) surfaces due to surface roughness or faceting.

The presence of impurities serves to broaden the boundstates in energy [79]. In the Barash theory, this is accounted for by performing the same analysis which leads to Eq.(3.16) but with impurities included by broadening the Matsubara energies from $(\varepsilon_n \rightarrow \varepsilon_n + \gamma(\mathbf{p}_f))$ which leads to the modified expression for the penetration depth

$$\lambda(T) = \lambda_0 + a\frac{T}{T_c}\lambda_0 + \frac{\mu_0 e^2 N_f \lambda_0^2}{2\pi T}\left\langle v_{f,y}^2(\mathbf{p}_f)|v_{f,x}(\mathbf{p}_f)|\Theta(\mathbf{p}_f)\psi'\left(\frac{1}{2}+\frac{\gamma(\mathbf{p}_f)}{2\pi T}\right)\right\rangle_{S_f} \quad (3.17)$$

where again λ_0 is the zero temperature value of the penetration depth, N_f is the density of states at the Fermi level and ψ' is the derivative of the digamma function. The broadening of the boundstates shifts the minimum in $\lambda(T)$ to lower temperature whilst at the same time causing a reduction in the magnitude of the upturn in penetration depth. To a good approximation the second term in Eq.(3.14) can be fitted to $\beta/(T+T^*)$ where T^* is related to the broadening of the boundstates due to impurities.

The field dependence of the ABS can also be modelled simply using the same physical arguments presented for the temperature dependence. As mentioned in Section(3.4), the application of a dc magnetic field serves to split the ABS. The field splits the boundstates in energy by an amount given by the Doppler shift of the quasiparticle energy levels $e\mathbf{v}_f \cdot \mathbf{A}$. The boundstate contribution to the density of states is therefore changed from from $\delta(E)$ to $\delta(E + e\mathbf{v}_f \cdot \mathbf{A})$. This quasiparticle density of states can be included in Eq.(1.9) and solved to obtain the field dependence of the ABS giving

$$\frac{\Delta\lambda(T,H)}{\lambda(0)} = \frac{\beta}{4T}\cosh^{-2}\left[\frac{\mu_0 e\lambda\mathbf{H}\cdot\mathbf{v}_f}{2k_BT}\right] \quad (3.18)$$

Eq.(3.18) shows that the $\sim 1/T$ divergence will be suppressed when the applied field exceeds the temperature dependent field scale $\tilde{H} = k_BT/(\mu_0 e v_f \lambda) = H_0 T/T_c$, where H_0 is of order the thermodynamic critical field $\mu_0 H_c = \Phi_0/\lambda_0\xi_0$.

As for the case of the temperature dependence of the ABS, the model of Barash *et al.* [79] provides a more accurate physical description of the field dependence of the ABS. Again, the model considers the effects of the diamagnetic screening current along with the paramagnetic contribution due to the ABS. The full expression for the

temperature and field dependence of the penetration depth is

$$\lambda(T,H) = \frac{\lambda^{scr}(T,H_{scr})}{1+4\pi\lambda^{scr}(T,H_{scr})\int_0^\infty Q^{ABS}(x,T)dx} \tag{3.19}$$

where $\lambda(T,H_{scr})$ is the contribution due to screening currents taken at an effective field H_{scr} which is greater than the applied magnetic field due to the paramagnetic contribution of the zero energy boundstates. The integral of the boundstate kernel Q^{ABS} describes the paramagnetic contribution to the penetration depth due to the ABS given by

$$Q^{ABS}(x,T)dx = \frac{i\mu_0 e N_f}{4\pi A(0)}\left\langle v_{f,y}(\mathbf{p}_f)|v_{f,y}(\mathbf{p}_f)|\Theta(\mathbf{p}_f)\times\psi\left(\frac{1}{2}+\frac{\gamma(\mathbf{p}_f)+(i/4\pi)\mu_0 e v_{f,y}(\mathbf{p}_f)A(0)}{2\pi T}\right)\right\rangle_{S_f}$$

where $A(0)$ is the vector potential at the surface ($x=0$), ψ is the digamma function and $\gamma(\mathbf{p}_f)$ is the broadening of the boundstates due to impurities. Combining these two expressions and solving at constant temperature gives the isolated field response of the boundstates.

$$\frac{\delta\lambda(H)}{\lambda(0)} = \delta\lambda^{ABS} i\frac{\tilde{H}_0}{H}\left\langle v_x v_y\ \psi\left(\frac{1}{2}+\gamma+\frac{iev_f\lambda\mu_0 H}{2\pi k_B T}\right)\right\rangle_{FS} \tag{3.20}$$

where v_x and v_y are the velocities parallel and perpendicular to the Fermi surface, ψ is the digamma function and γ is the broadening of the boundstates due to impurities which is a constant for a given sample.

3.6 Review of Evidence for Surface Andreev Boundstate Formation

As described in Section 3.3, zero energy boundstates occur as a natural consequence of the π-phase shift between lobes of the $d_{x^2-y^2}$ order parameter. Observation of such states provides strong evidence for the existence of an order parameter of this symmetry. Since the zero energy Andreev boundstates occur within a few coherence lengths

of the surface, experiments sensitive to the density of states at the surface of the superconductor can be used to identify this zero energy boundstate enhancement. A number of tunnelling measurements have been performed investigating different aspects of Andreev boundstates. Measurements of the zero bias conductance peak (ZBCP) have been performed as a function of surface orientation [80], [81] and as a function of applied magnetic field [82]. Penetration depth measurements of oriented Y123 thin films also provide evidence of a correlation between order parameter orientation and surface boundaries [83]. These experiments, and their accompanying conclusions, will be discussed below.

3.6.1 Surface Tunnelling Experiments

Measurements by Geerk *et al.* [84] observed an unusual feature in the tunnelling spectrum of *ab*-oriented thin films. The tunnelling spectrum revealed a large peak in the conductance at zero bias. This feature was thought to be due to spin-flip scattering of the tunnelling electrons due to magnetic impurities at the insulating barrier. It was not until some six years later that Hu [85] postulated that the zero bias peak in tunnelling conductance could be due to Andreev boundstates forming at the sample surface. Tunnelling measurements by Covington *et al.* [82] in Y123 thin film junctions also observed a zero bias conductance peak (ZBCP). The ZBCP in this measurement however, was seen to spontaneously split in zero field. This splitting can arise as discussed above in Section 3.4 due to the presence of a sub-dominant order parameter. The application of higher magnetic fields further splits the ZBCP as can be described by a Doppler shift in the boundstate energy with respect to the superfluid. The evolution of the ZBCP position with magnetic field was modelled by Fogelström *et al.* [86]. The tunnelling measurements were performed in the *ab*-plane of the Y123 junctions oriented in the (110) and (100) orientations.

The splitting of the ZBCP with increasing magnetic field is shown in Fig.3.6. Fig.3.7 shows a plot of the peak position as it varies with increasing magnetic field. The solid line is a theoretical calculation for the evolution of the ZBCP splitting

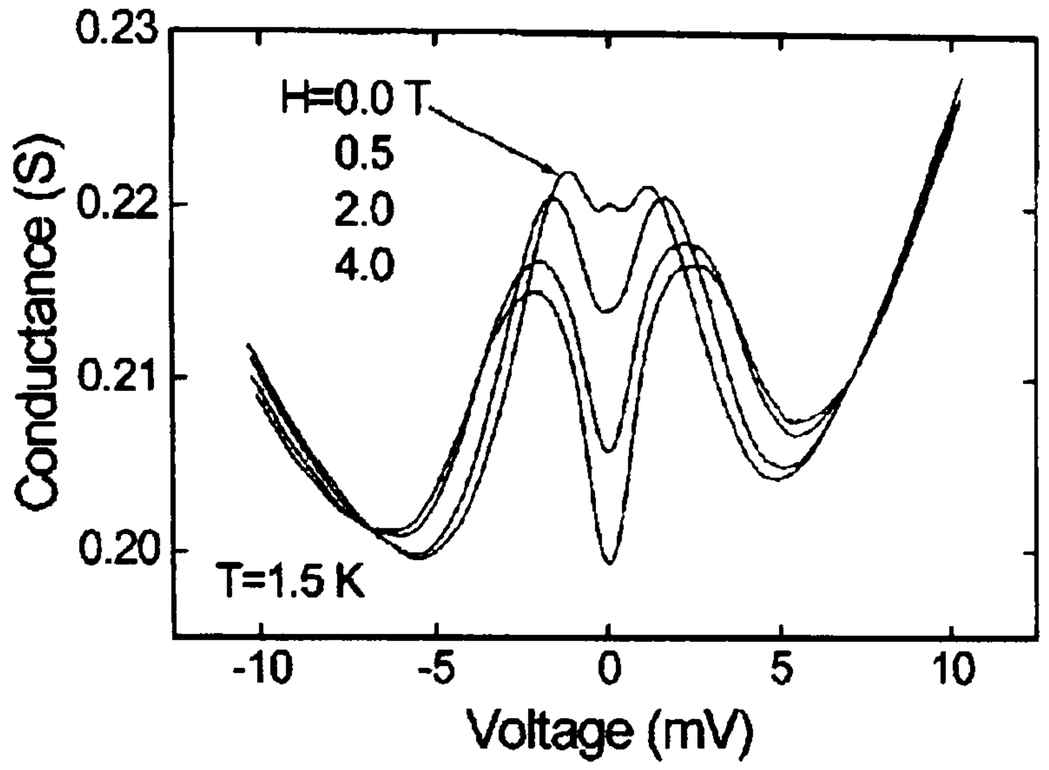

Figure 3.6: The zero bias conductance peak (ZBCP) is seen to split in zero field indicative of a sub dominant order parameter that breaks time reversal symmetry. The ZBCP is further split by the application of a dc magnetic field. After Covington *et al.* [82]

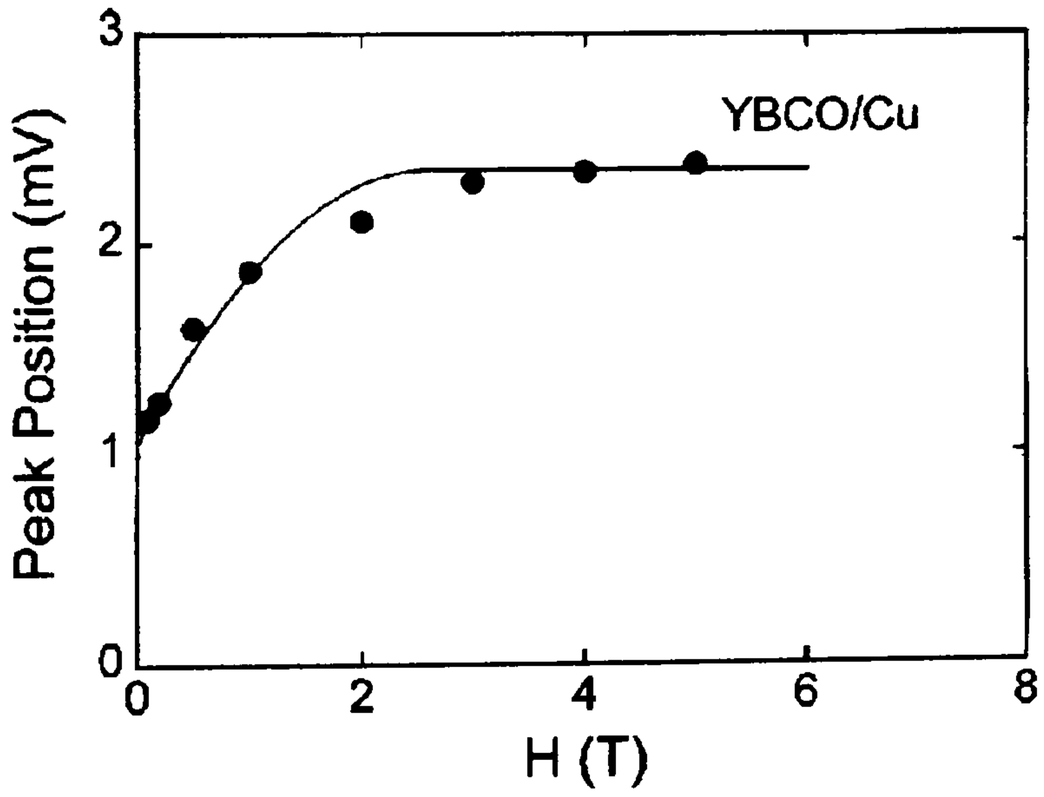

Figure 3.7: Plot of the variation of the peak position with applied magnetic field. Solid line is the calculated evolution of the splitting with magnetic field. After Covington *et al.* [82]

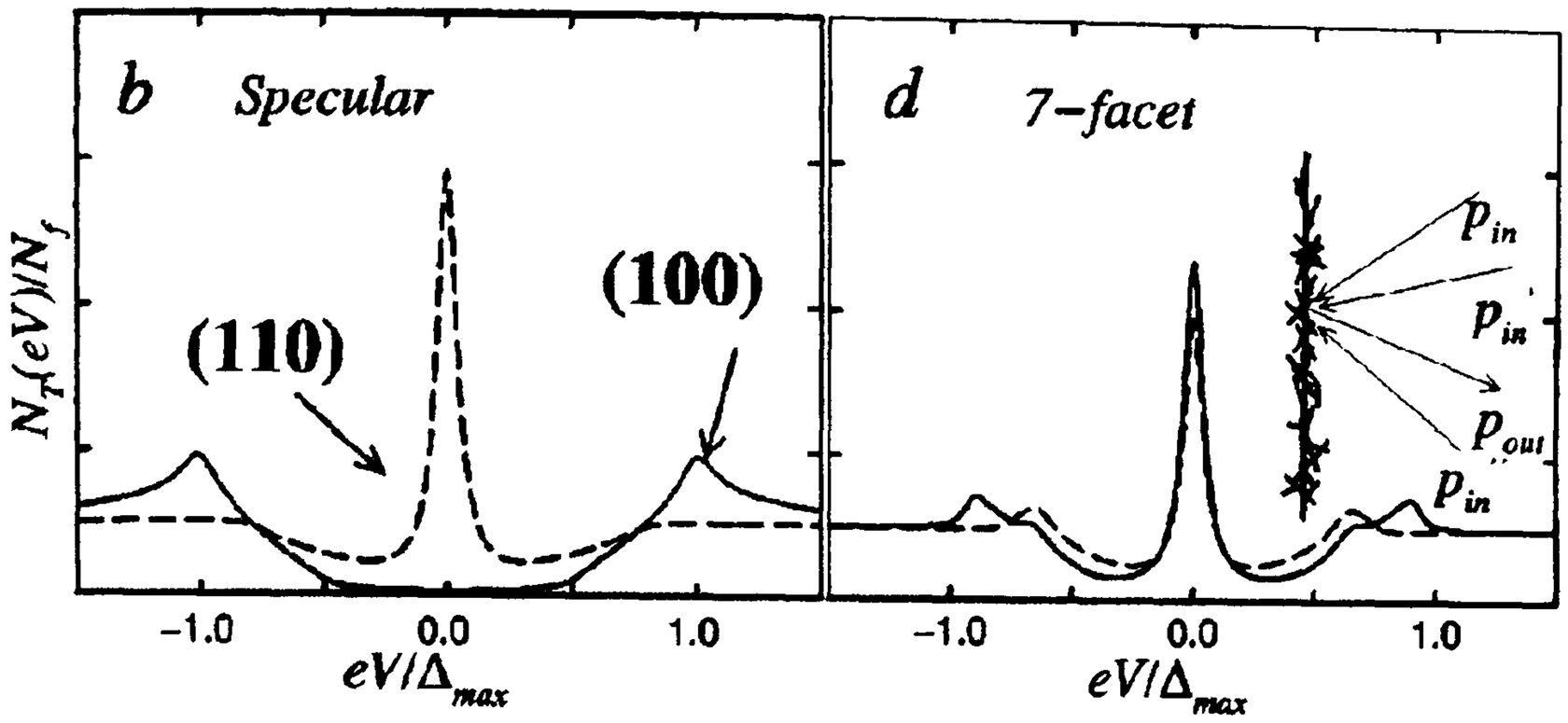

Figure 3.8: Calculated response for tunneling in the (100) and (110) orientations. Surface faceting creates a ZBCP in the forbidden (100) direction. After Fogelström *et al.* [86]

for a sub-dominant order parameter with s-wave symmetry. The surface transition temperature was measured to be T_s=7K since this is the temperature at which the peak spontaneously splits. The surface and bulk transition temperatures are given relative weights such that $T_{c1} = xT_{c2}$. The effect of surface roughness is to reduce $T_s < T_{c2}$. The measured T_s=7K corresponds to $T_{c1} = 0.15T_{c2}$ when roughness is included. The relative weights of the two order parameters allows the calculation of δ_s, the magnitude of the spontaneous splitting in zero field. The measured value T_s=7K gives a value $\delta_s = 0.15\Delta_0 = 1.05$meV. The value directly taken from experiment is $\delta_s = 1.16$meV showing good agreement between theory and experiment. The further evolution with field is given by $\delta(H) = \delta_s + \Delta(H/H_0)[1 - \frac{1}{2}(H/H_c^*)]$ for H$\leq H_c^*$ where H_c^* is the pair breaking critical field determined by quasiparticle excitations at the nodes of the $d_{x^2-y^2}$ order parameter [87]. The solid line in Fig.3.7 shows calculated values for $\delta(H)$ using only the relative weights of the two order parameters as determined by experiment.

The theory of ABS formation predicts that boundstates will only form along certain crystalographic orientations. Measurements by Covington *et al.* showed the spontaneous splitting of the ZBCP for junctions made with (110) oriented films.

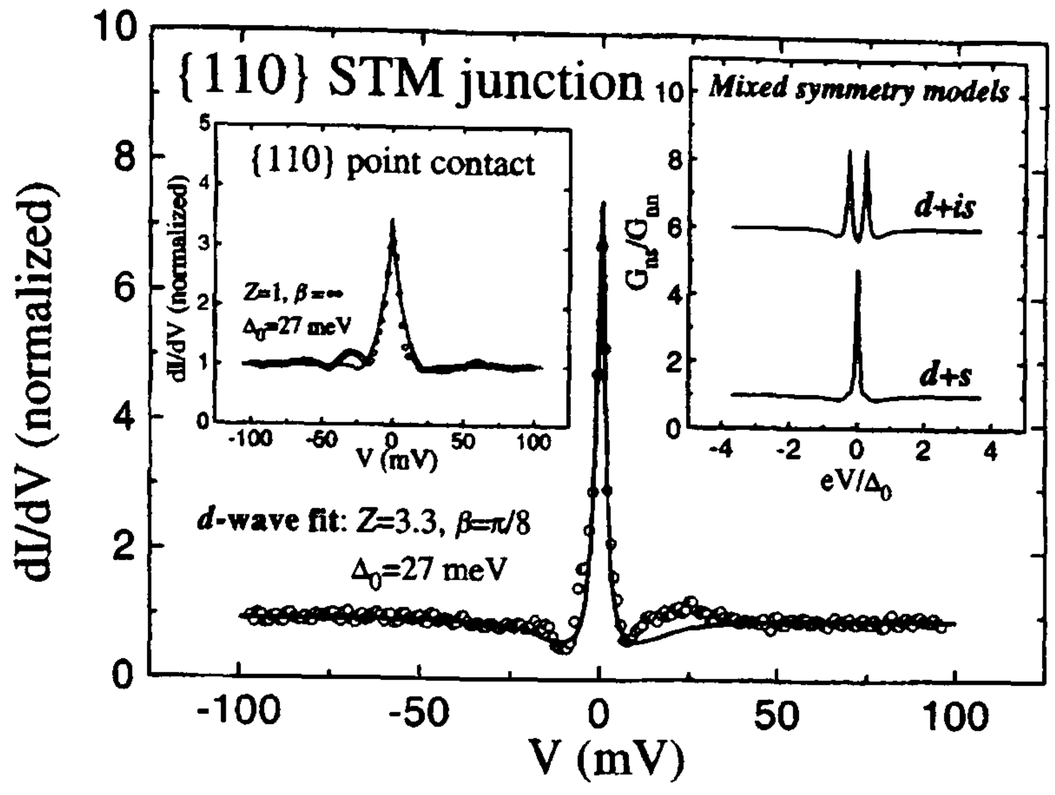

Figure 3.9: Measured ZBCP for (110) direction. Right inset shows calculated effect of sub dominant order parameter contribution. After Wei *et al.* [80]

Measurements were performed on (100), (110) and (103) oriented Y123 films. No significant anisotropy was reported between any of the orientations. This observation could be taken as strong evidence against ABS being responsible for the effects described above. This issue was also addressed by Fogelström *et al.* Since a specular (100) surface is non pair breaking, ABS effects should not be seen for films of this orientation. The effect of roughness at a classically non pair breaking surface is to introduce multi-faceted surfaces at angles away from the (100) direction. These surfaces can form ABS for certain quasiparticle trajectories. Fig. 3.8 shows the calculated effect of faceting on the ZBCP. The inclusion of 7 facets at the (100) surface makes the tunnelling spectrum taken at this surface to be virtually indistinguishable from that of a (110) surface.

Tunnelling measurements by Wei *et al.* [80] on Y123 single crystals are in qualitative agreement with the findings of Covington [82] and Fogelström [86] for aligned thin films. The tunnelling measurements were performed in low transmission mode by scanning tunnelling microscopy (STM) with a Pt-Ir tip. Point contact measurements were performed by driving the tip into the crystal surface giving high transmission tunnelling. Fig. 3.9 shows the ZBCP measured by both STM and point contact

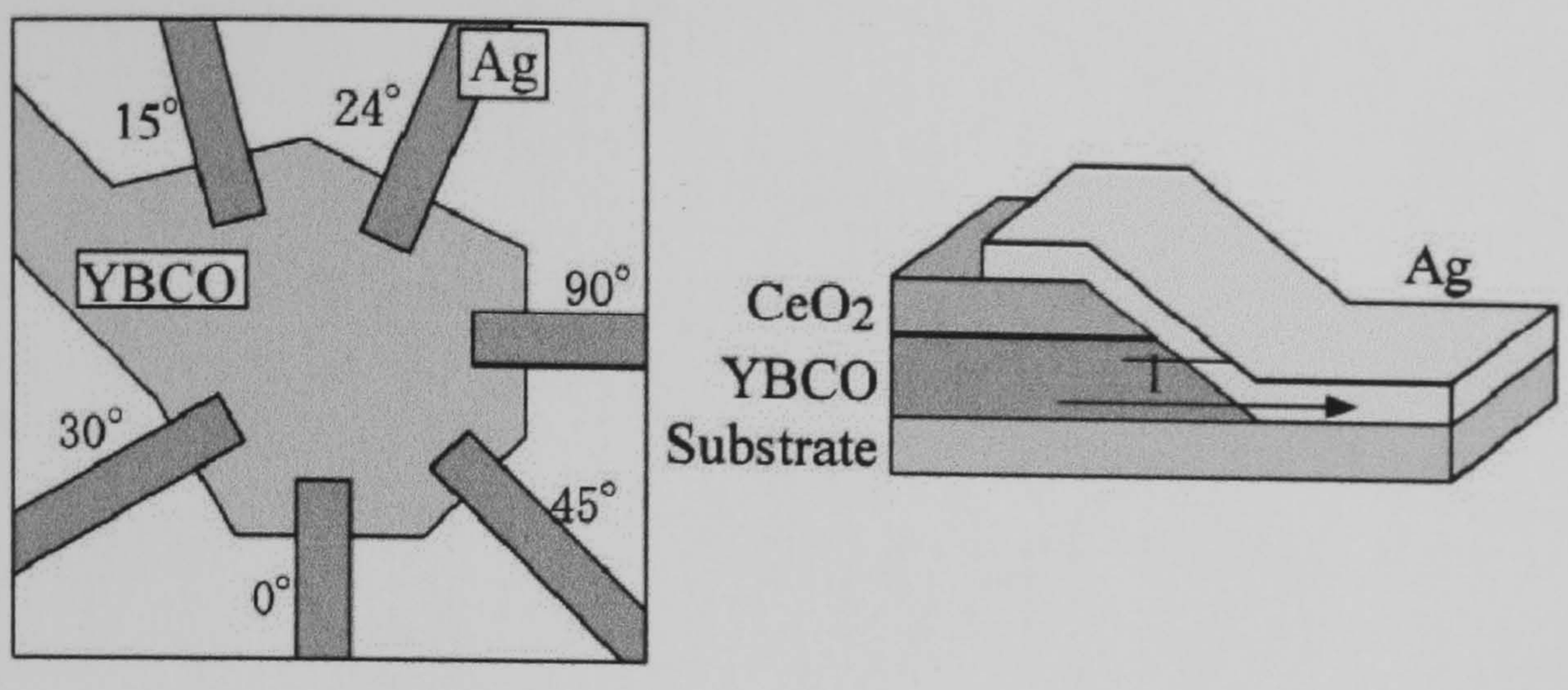

Figure 3.10: Schematic of ramp-edge junction geometry. Sample consists of 6 ramp-edge junctions on a single Y123 chip. After Iguchi*et al.* [81]

methods at T=4.2K. The point contact measurement (inset) is somewhat broader than than the STM spectrum but both scans are in qualitative agreement. Neither spectra show any evidence of spontaneous ZBCP splitting. Fig. 3.9 also shows a fit to the data using a method formulated by Hu [85]. The parameters are Z, the barrier strength, β, the tunnelling cone and Δ_0 magnitude of the gap. The results of mixed symmetry models show that there should be no $d+is$ contribution since there is no splitting however, a $d+s$ combination, which does not break time reversal symmetry, could be present. High impedance junctions usually lack a gap like feature and is the reason why the spectrum is largely flat away from the ZBCP. Along the (100) face a ZBCP is again seen as a result of surface faceting for the STM junction. For the point contact an inverse gap function was observed which is consistent with high transmission junctions. A gap like feature is observed for STM tunnelling into the (001) surface. This surface is expected to be very uniform for Y123 single crystals and hence no ZBCP is observed since no faceting occurs. Again simulations were performed for $d+s$ and $d+is$ order parameters. It was concluded that any sub dominant surface order parameter contribution would have to be $< 5\%$.

So far, details of tunnelling experiments have focused on the (100) and (110) directions. The conventional ABS theory states that no ZBCP should be observed

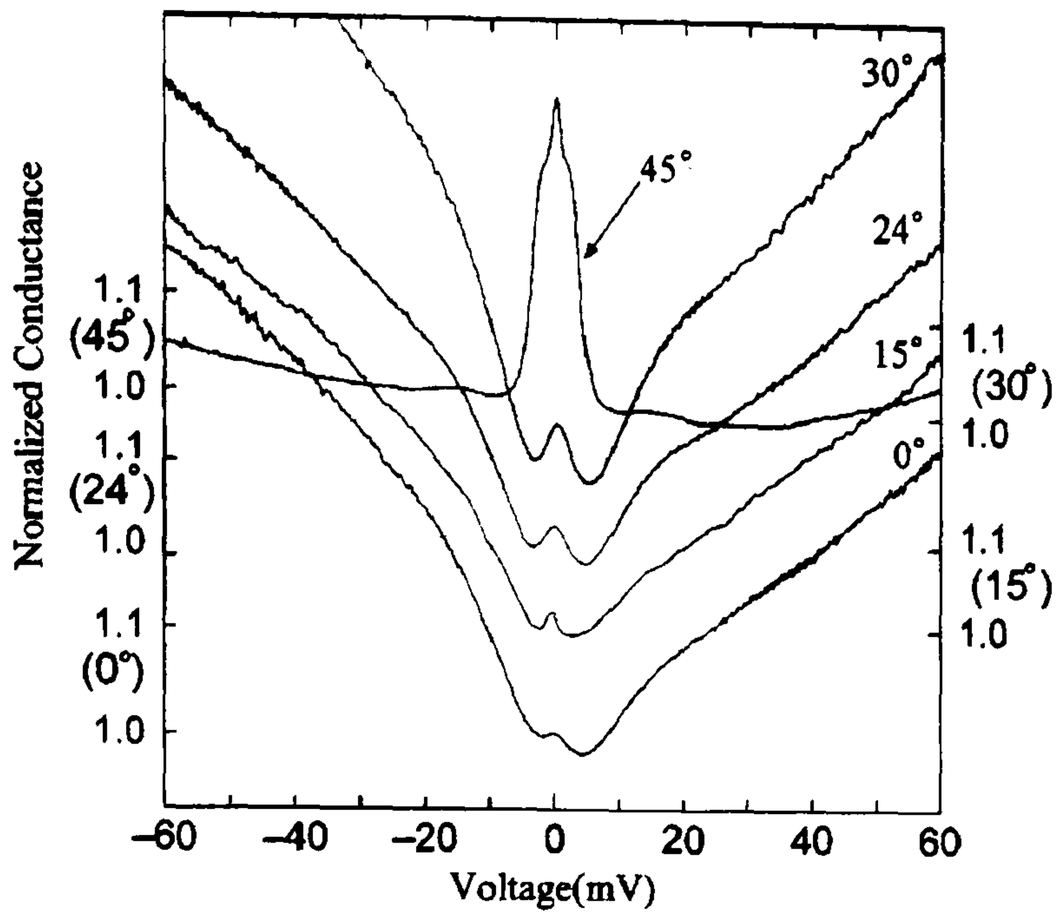

Figure 3.11: Measured tunneling conductance as a function of the angle the interface makes with the (100) direction. After Iguchi*et al.* [81]

along the (100) direction and the maximum ZBCP should be observed for the (110) direction where all quasiparticle trajectories are boundstate forming. Iguchi *et al.* [81] measured tunnelling spectra on a single Y123 chip with 6 ramp-edge junctions fabricated at different orientations to the crystal axes. Fig. 3.10 shows a schematic of the ramp-edge junction chip and the corresponding tunnelling data. In this data (as for the data presented in [82] and [80]) a ZBCP is observed for the $\alpha = 0°$ (100) orientation. The ZBCP is somewhat smaller though, indicating higher quality surfaces. The magnitude of the ZBCP shows strong dependence on the orientation of the junction as in Fig. 3.11. This orientation dependence would be expected from the simple analysis of Section 3.3. As the quasiparticle trajectory is increased from $\alpha = 0°$, an increasing number of quasiparticle trajectories are boundstate forming until $\alpha = 45°$ where all quasiparticle trajectories form boundstates in the absence of surface roughness.

3.6.2 Previous Penetration Depth Measurements

Andreev boundstates have been shown to form within a few coherence lengths of the surface by tunnelling experiments. Measurement techniques sensitive to the surfaces of superconducting samples should therefore also be sensitive to the formation of ABS. Surface impedance measurements probe the surface over the length scale of the penetration depth and so will also be sensitive to the presence of ABS. From Section(3.5), the magnitude of the paramagnetic contribution to the penetration depth due to ABS should vary as a function of the quasiparticle scattering directions with respect to the order parameter, reaching a maximum when all quasiparticle trajectories undergo a π-phase change in the order parameter at 45° to the lobes of the $d_{x^2-y^2}$ order parameter. Walter *et al.* [83] measured the penetration depth in irradiated Y123 thin films. Au^{18+} ions were used to create defect tracks in Y123 thin films at specific angles to the superconducting order parameter. The films were measured by a mutual inductance technique in coils employing a racetrack geometry rather than circular windings (Fig.3.12 right). The ion tracks are at $\alpha = 0°.22°$ and 45° where $\alpha = 0°$ is the (100) direction and $\alpha = 45°$ is the (110) direction which should correspond to maximal boundstate formation. The penetration depth can be seen to increase as the ion tracks are varied away from the $\alpha = 0°$ direction. The data also shows that there is some upturn contribution to the penetration depth even for the non-irradiated sample. This effect is not predicted by the ABS theory and arises from an extrinsic effect. Walter *et al.* cite pair breaking due to bulk defects and grain boundaries as a possible reason for the upturn. If the films are not well aligned, trajectories will always exist whereby the quasiparticles can pass through the π-phase change in the order parameter. Any bulk pair breaking mechanism which creates a large paramagnetic contribution to the penetration depth could be the origin of the upturn in the non-irradiated film. The presence of pair breaking paramagnetic impurities cannot be ruled out. The presence of impurities will not, however, explain the increase in magnitude of the upturn as a function of ion damage orientation. This is evidence for ABS being the origin of the upturn effect in these irradiated films.

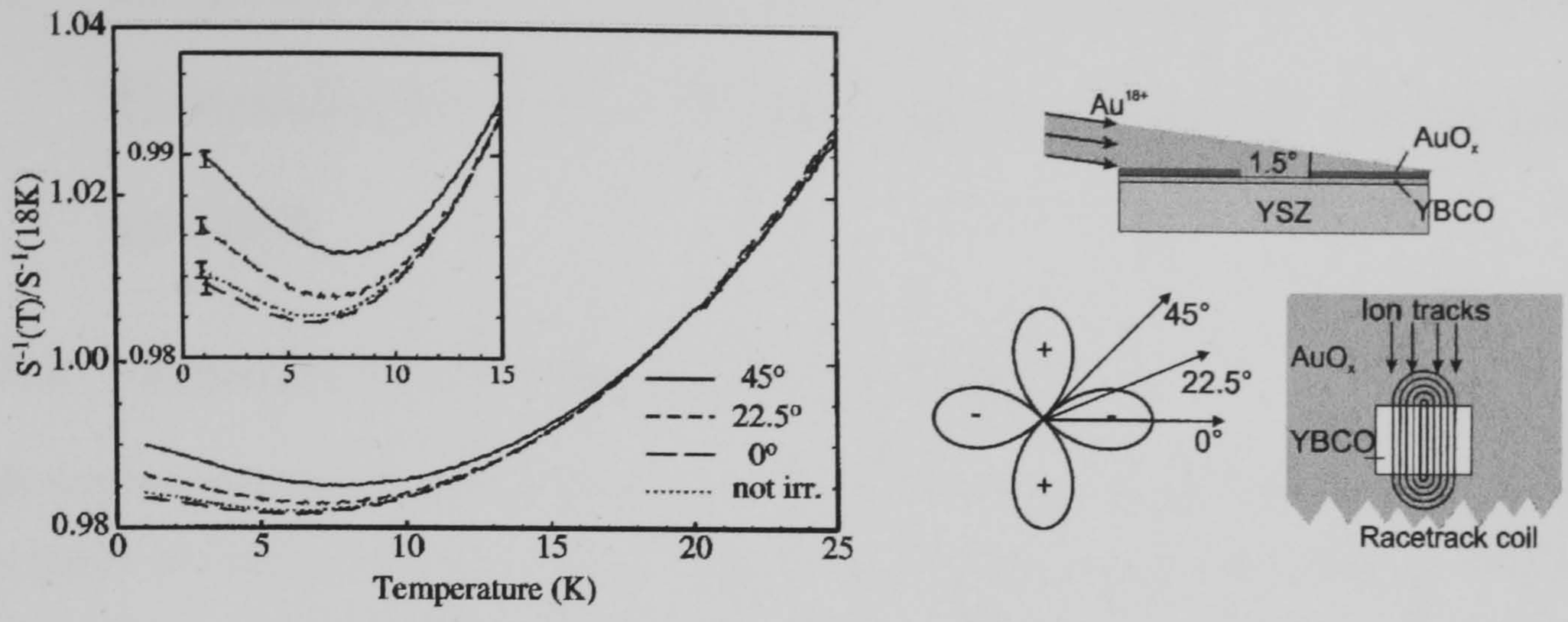

Figure 3.12: The paramagnetic current contribution due to Andreev boundstates increases with irradiation angle and so increases the penetration depth at low temperature. The irradiation geometry and measurement configuration is shown on the right. After Walter*et al.* [83]

The results as a whole strongly point to ABS being responsible for the upturn in these irradiated thin films.

3.7 Experimental Observation of Surface Andreev Boundstates via Penetration Depth Measurements

3.7.1 Temperature dependence of ABS

This section discusses experimental data acquired using the LC-oscillator technique described in earlier chapters. A number of key pieces of evidence will reveal ABS as the origin of the penetration depth anomaly observed in these crystals. Such evidence includes temperature dependence, field dependence, measurement orientation and crystal shape dependence of the penetration depth. These effects are described qualitatively by the simple model presented above and quantitatively by the more complete ABS theory of Barash *et al.* as described in Section(3.5).

The magnetic penetration depth was studied in four optimally doped $YBa_2Cu_3O_{7-\delta}$ (Y123) single crystals. Crystals A, C and D were grown by A. Carrington. Sample B was grown by J. Giapintzakis [8] and the a and b axes identified via x-ray diffraction by A. Carrington. All samples were grown in yttria stabilized zirconia crucibles [88] and annealed for 3 weeks in flowing oxygen at 500 °C to reach optimal doping. Crystals A, B and D showed T_c ~94 K with a typical width of ~0.2 K. Sample C showed T_c ~93 K again with a transition width of ~0.2 K. Optical microscopy with polarized light showed the crystals to be >90% twin free.

Measurements were performed with the excitation field applied along the a, b and c axes of the crystals. As discussed in Chapter 2, the component of the penetration depth measured (in the thin limit) for Y123 single crystals is λ_a for the excitation field applied along the b-axis and λ_b for the excitation field applied along the a-axis. For the excitation field applied along the c-axis the penetration depth will be a geometrical average of λ_a and λ_b. These properties of Y123 mean that the measured component of the penetration depth with the probe field applied within the sample plane and perpendicular to the sample plane should essentially be the same. A notation will be

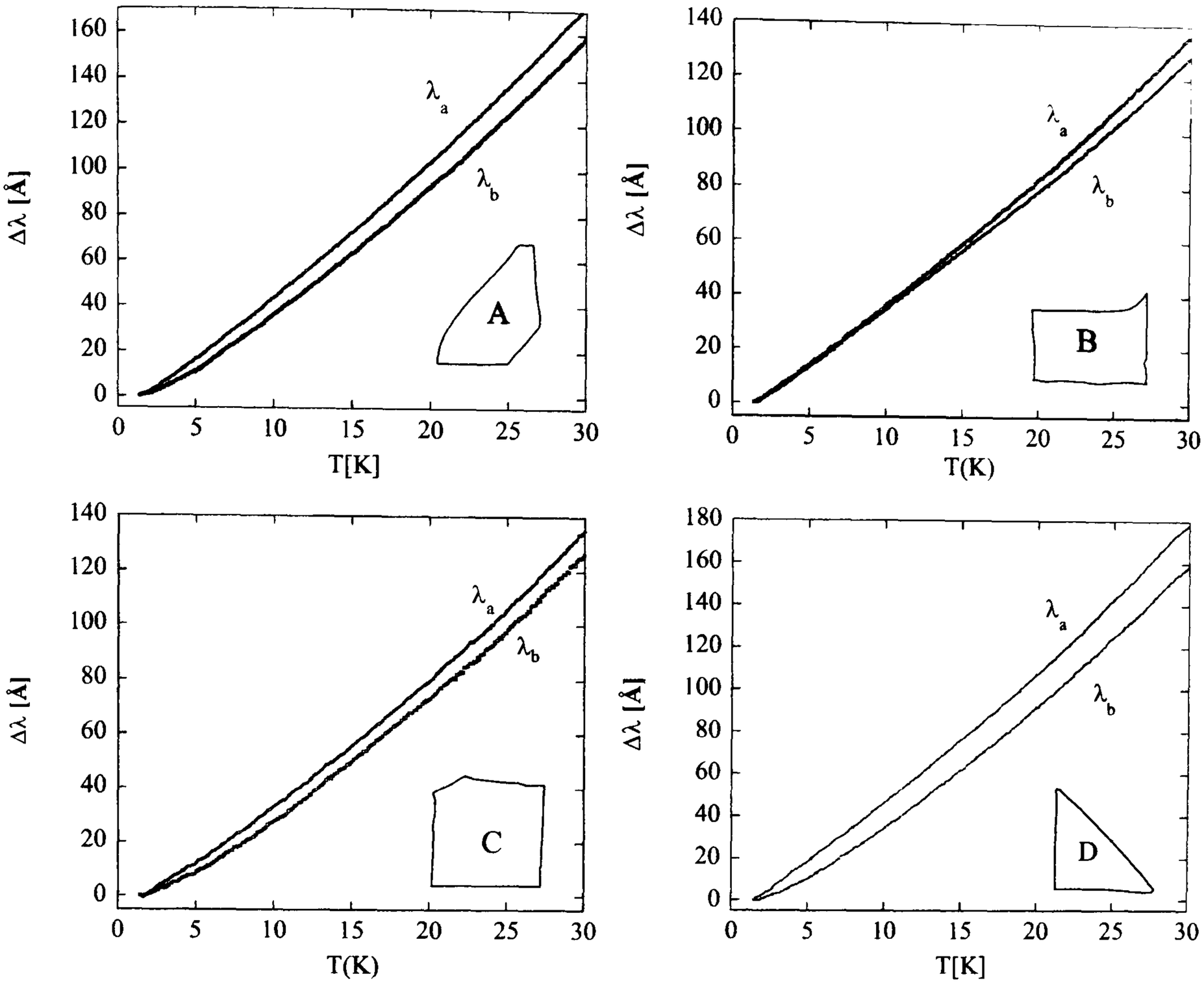

Figure 3.13: $\lambda_a(T)$ and $\lambda_b(T)$ for four optimally doped $YBa_2Cu_3O_{7-\delta}$ single crystal. $\lambda_a(T)$ generally shows greater linear character than $\lambda_b(T)$

introduced at this point to signify measurement orientation and measured component. For fields applied within the sample plane, the resulting component of the penetration depth probed will be termed λ_a or λ_b as defined previously. The geometrical average of these components ie., the average of λ_a and λ_b as weighted due to sample dimensions will be termed $\lambda_{ab}^{a,b}$. The penetration depth component as measured with the probe field along the c-axis (screening currents circulating solely in the ab-plane) will be termed λ_{ab}^{c}.

Fig.3.13 shows the temperature dependence of the four Y123 single crystals. Generally $\Delta\lambda_a(T)$ shows more linear character than $\Delta\lambda_b(T)$ and $d\lambda_a(T)/dT$ is slightly

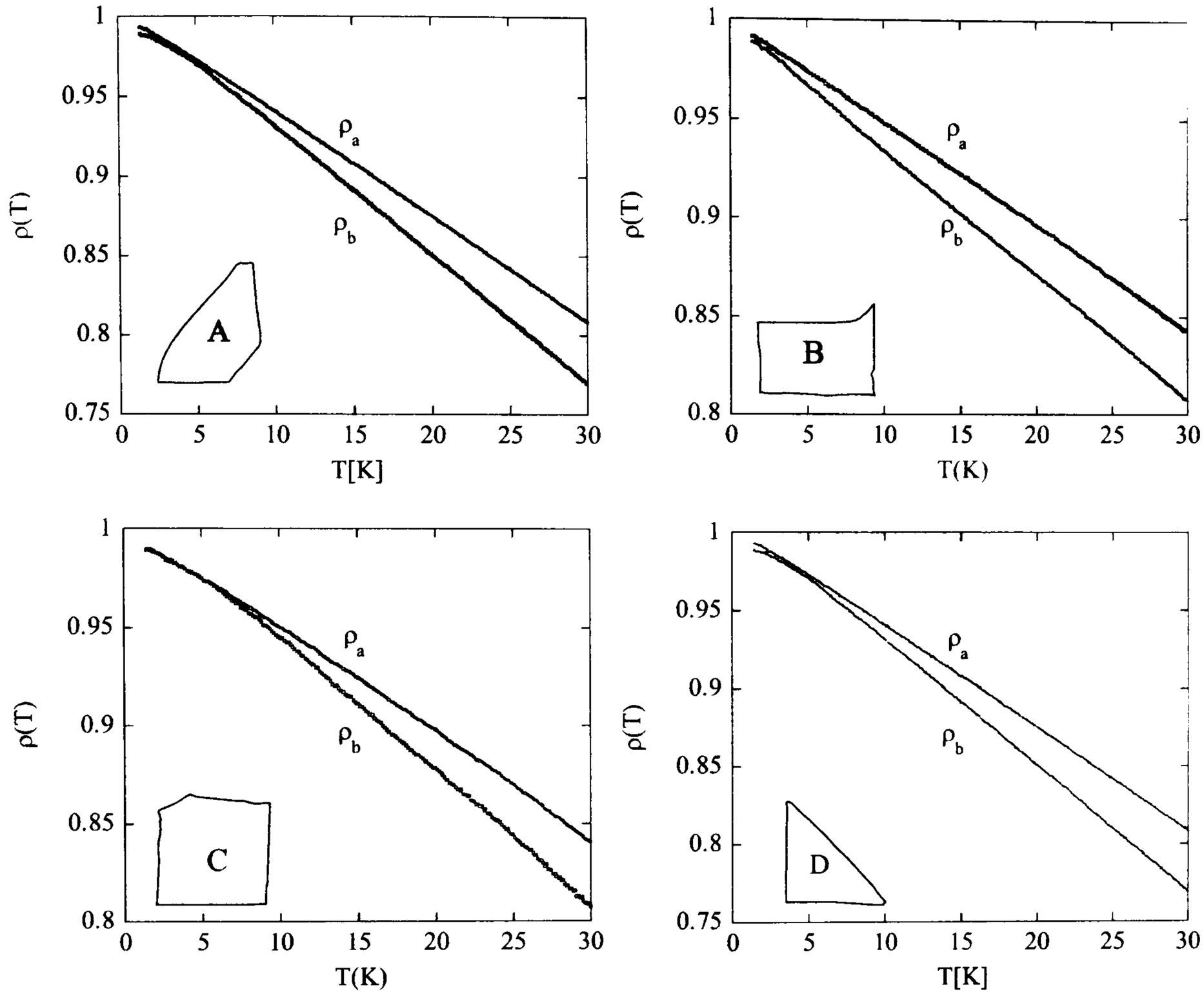

Figure 3.14: The superfluid densities for all four optimally doped $YBa_2Cu_3O_{7-\delta}$ single crystals ($\rho(T) = [\lambda(0)/\lambda(T)]^2$) with the measurement field applied in plane, calculated using the values $\lambda_a(0) = 1600$ Å and $\lambda_b(0) = 1200$ Å[89].

Sample	$d\lambda_a/dT$ (K)	$d\lambda_b/dT$ (K)	T_a^* (K)	T_b^* (K)
A	5.7	5.3	1.9	3.3
B	4.3	4.2	0.7	1.5
C	4.5	4.2	3.8	4.9
D	5.9	5.3	1.6	4.3

Table 3.1: Summary of $d\lambda(T)/dT$ for the four samples. T^* values for each sample are from fits to $\rho(T) = 1 - (aT^2/(T^* + T))$ [68].

larger than $d\lambda_b(T)/dT$. The normalized superfluid densities ($\rho(T) = [\lambda(0)/\lambda(T)]^2$) are shown in Fig.3.14 using values of $\lambda_a(0)$=1600 Å and $\lambda_b(0)$=1200 Å as measured by Basov *et al.* [89]. Fitting the data to the Hirschfeld and Goldenfeld [68] dirty d-wave expression $\rho(T) = 1 - (aT^2/(T^* + T))$ yields values for T^*. Values for T^* and $d\lambda/dT$ are shown in Table(3.1). The values presented in Table(3.1) are largely consistent with previously published results for optimally doped Y123 [48, 75, 89]. The values for T^* are greater for ρ_b than ρ_a in all samples. The difference between these two measurements is likely to arise from the presence of the CuO chains running along the b-axis of the Y123 structure. The superfluid density for this direction is comprised of contributions due to the CuO chains and CuO_2 planes given by $\rho_b = \rho_{chain} + \rho_{plane}$ [90] whereas the superfluid density along the a-axis, ρ_a, is solely due to the CuO_2 planes. This implies that the CuO chains have a greater impurity content or, more likely, oxygen vacancies which cause some increased pair breaking at low temperature resulting in the finite density of states behaviour predicted by Hirschfeld and Goldenfeld.

Applying the measurement field perpendicular to the sample plane should yield a penetration depth response which is the average of the two components shown in Fig.3.13. Fig.3.15 shows the penetration depth behaviour with the measurement field applied perpendicular to the sample plane. In this orientation the sample calibrations can be performed using the method described in Chapter 2. By assuming an effective sample dimension, derived from the surface area of the sample, and measuring the frequency shift due to the extraction of the sample, the oscillator frequency shift can be related to a change in penetration depth. An alternative method of sample calibration utilizes the fact that the penetration depth response in thin Y123 samples should be the same in both measurement orientations. For example, for a square Y123 sample the measured penetration depth with the measurement field applied perpendicular to the sample plane, should be the average of $\Delta\lambda_a(T)$ and $\Delta\lambda_b(T)$ ie., $(\Delta\lambda_a(T) + \Delta\lambda_a(T))/2$. If $\Delta\lambda_a(T)$ and $\Delta\lambda_b(T)$ are measured in the in-plane configuration, it is possible to average the data and obtain the expected penetration depth

response for the measurement field applied perpendicular to the sample plane. The frequency response for the sample measured with the probe field perpendicular to the sample plane can therefore be normalized to the averaged data to provide an accurate calibration. The normalization method and the analytically derived calibration constant method agree well. For sample A the difference between the two methods is ~8%. The other samples show better agreement with the two calibration methods agreeing to within 3 to 5%. The normalization method was used in the data analysis since it avoids the intrinsic uncertainty associated with assuming an effective sample dimension. Also, normalizing the curves at high temperature means that the trends in the data at low temperature are more transparent.

Fig. 3.15 shows a consistent pattern of behaviour between the four Y123 samples. All crystals show significant differences between the two measurement orientations even though the component of the penetration depth probed in both orientations is the same. The data for sample D from 1 K to 300 mK was taken by R. Prozorov and R.W. Giannetta at the University of Illinois at Urbana-Champaign using the same experimental technique in a ^{3}He refrigerator. This data shows that the increase in penetration at low temperature continues to rise. The increase in penetration depth at low temperature for the four Y123 crystals presented here is interpreted as due to surface Andreev boundstates (ABS) forming at zero energy within the superconducting gap. As discussed above, for zero energy boundstates to form at the crystal surfaces, quasiparticles must pass through a π-phase change in the order parameter. This can happen through specular reflection at non-(100), (010) or (001) surfaces. The measurement orientation whereby the quasiparticles are confined to the sample plane is the only orientation that zero energy ABS should form and have any effect on the measured penetration depth.

The fact that the low temperature upturn is seen only in one orientation rules out a number of sources of the upturn. Contaminants, such as paramagnetic impurities. should provide no orientation dependence to the presence of an upturn. The presence of paramagnetic impurities can introduce an extra term into the temperature

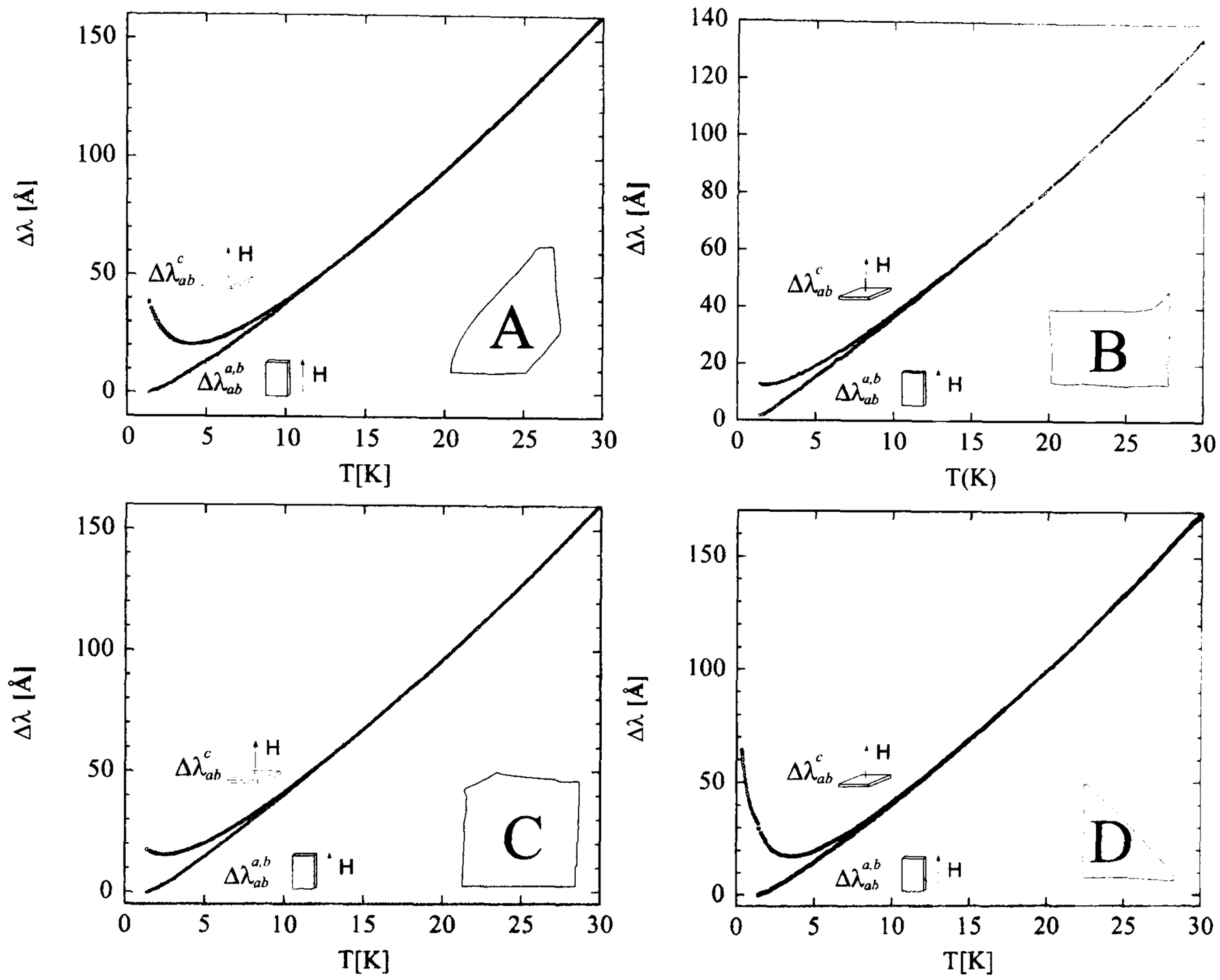

Figure 3.15: Penetration depth response with the probe field applied perpendicular to the *ab*-plane (upper curves) normalized to $\lambda^{a,b}_{ab}$. An outline of each crystal is shown (bottom right).

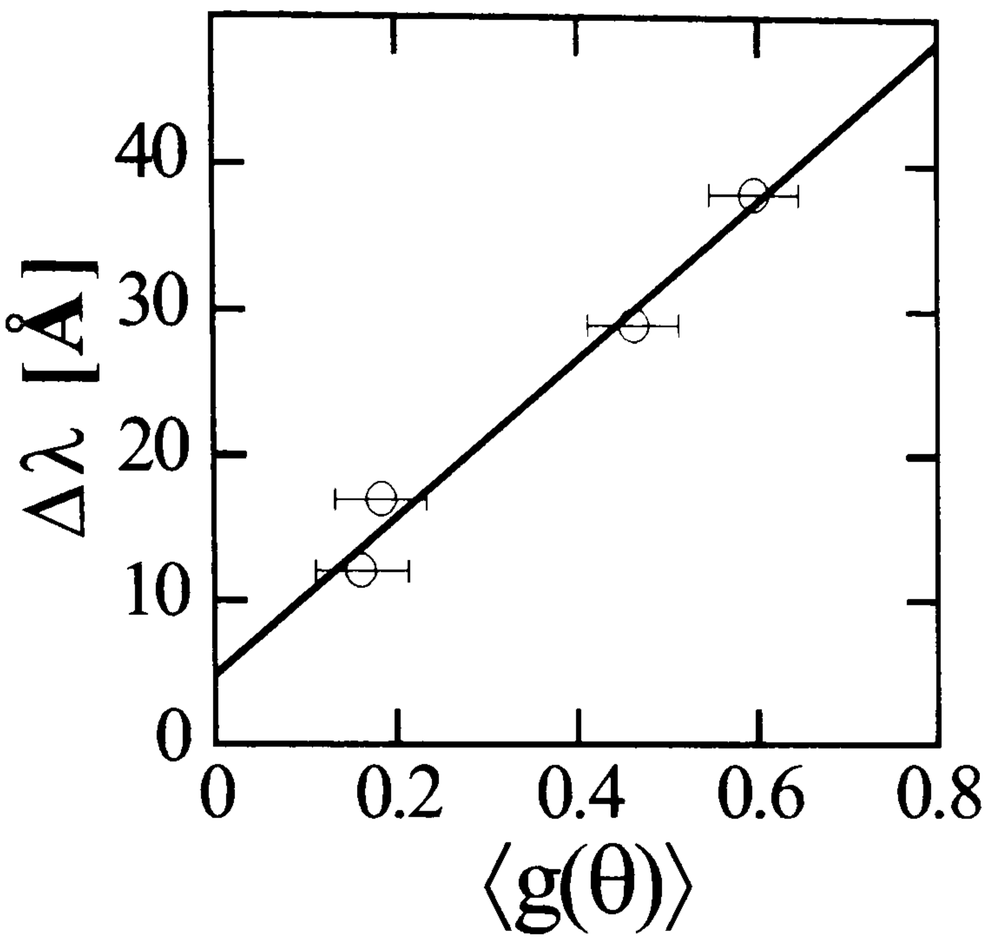

Figure 3.16: Plot of $\Delta\lambda$ against $\langle g(\theta) = | \, |\sin^3\theta| - |\cos^3\theta| \, | \rangle$ for all crystals.

dependence of the penetration depth. The analysis by Cooper [70] to explain the temperature dependence of the electron doped superconductor $Nd_{1.85}Ce_{0.15}CuO_{4-y}$. describes the effect of paramagnetic sites on the penetration depth. It was shown that the presence of Nd^{3+} ions complicated the interpretation of the measured $\Delta\lambda(T)$ since the Nd^{3+} ions have a Curie-Weiss like susceptibility $\chi(T) = \chi_0 + C/(T + \Theta)$ where C is the Curie constant for the material and Θ is the antiferromagnetic interaction strength. The penetration depth measured is $\lambda(T) = \lambda_L(T)/\sqrt{\mu}$ where μ is the magnetic permeability ($\mu = 1 + \chi$). Since the Nd^{3+} ions are throughout the structure their effect is observed for the probe field applied within and perpendicular to the sample plane. Measurements by Alff *et al.* [91] on $Nd_{1.85}Ce_{0.15}CuO_{4-y}$ show that the paramagnetic contribution to the penetration depth is present for the excitation field applied both perpendicular and parallel to the sample plane.

As discussed in Section(3.5) the magnitude of the ABS contribution should be related to the sample shape by $\Delta\lambda^{ABS} \sim g(\theta)$ where $g(\theta) = \| \sin^3\theta| - |\cos^3\theta \|$ and θ is the angle that a crystal surface makes with the (110) direction. The $g(\theta)$ function

was calculated using digital images of each crystal. This function was calculated individually for each side of the crystal and then all sides were summed as a ratio of the side length to the crystal perimeter. The magnitude of the upturn due to ABS is defined as the difference between the measured penetration depth in the two orientations at the base temperature ($\sim$ 1.4 K). Fig.3.16 shows the values of the upturn for each crystal plotted against the $g(\theta)$ function. The error bars for $g(\theta)$ are derived by calculating the $g(\theta)$ function independently several times. The magnitude of the upturn as a function of $g(\theta)$ can be seen to fit a straight line within the uncertainty. The small value of the y-intercept points to surface roughness below the optical resolution of the digital images not being a major factor in determining the $g(\theta)$ coefficient. This result is somewhat surprising since tunnelling measurements show that surface faceting has a significant effect on the formation of ABS. Tunnelling measurements by Wei *et al.* [80] showed ABS contributions at all surfaces. This effect was predicted by Fogelström *et al.* [86] where even small amounts of surface faceting were shown to promote ABS formation at all surfaces.

The temperature dependence of the penetration depth contribution due to ABS can be isolated by subtracting the two curves shown in Fig.3.15. Fig.3.17 shows the isolated ABS contribution for samples A and D. These curves can be fit to $\Delta\lambda^{ABS} = c/(T+T^*)$ which gives a quantitative value for the broadening of the bound-states due to impurities. The fits yield $c = (120 \pm 20)$ Å K and $T^* = (0.8 \pm 0.2)$ K for both samples. The low value of T^* implies that the boundstates are only slightly broadened by impurities. Assuming $v_f = 2 \times 10^5$ ms^{-1} from bandstructure calculations [9] the ABS coefficient is $\beta = 2.5 \times 10^3 g(\theta)$Å K. This value is significantly larger than the value given from the fit. There are a number of reasons that the experimentally derived value of β could differ from the theoretical value. The theory assumes 100% specular scattering and a cylindrical Fermi surface. A lesser amount of specular scattering would reduce boundstate formation. The cylindrical Fermi surface approximation given by $g(\theta) = \|\sin^3\theta| - |\cos^3\theta\|$ may not represent the true Fermi surface of Y123 accurately enough to provide a good quantitative agreement between

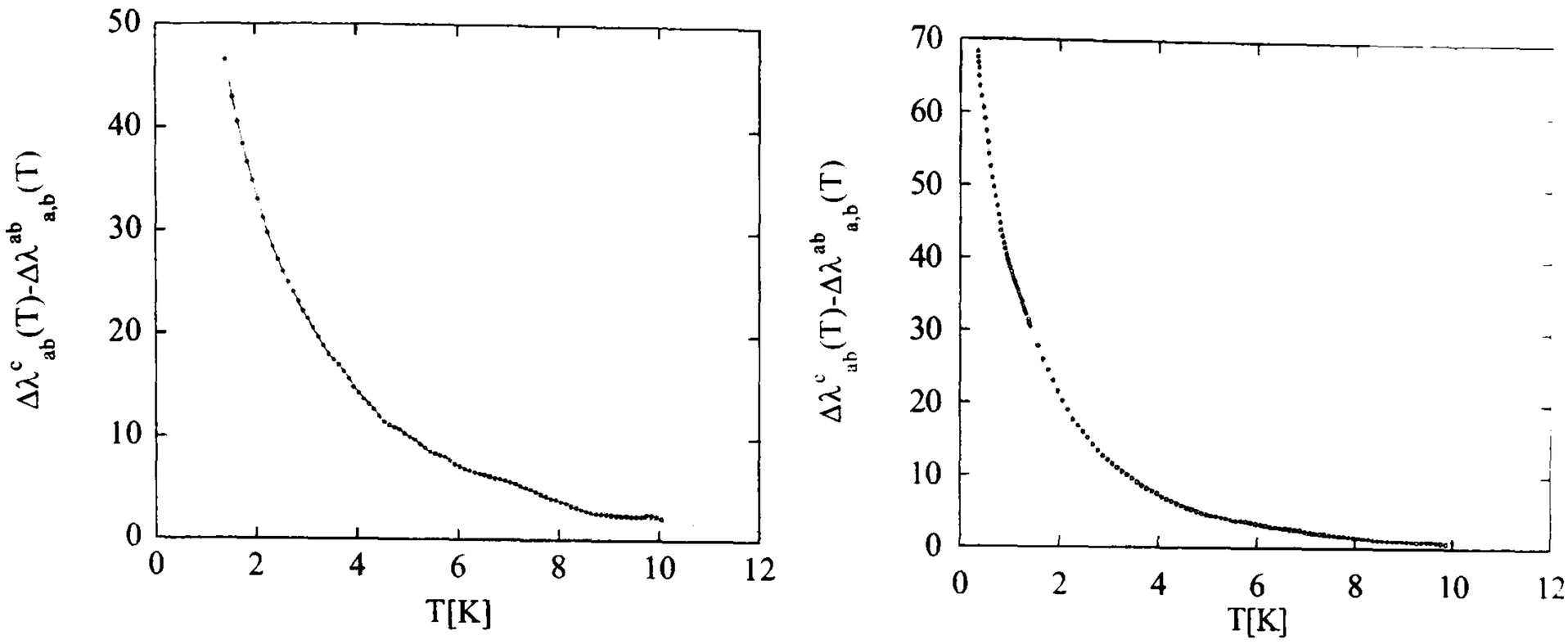

Figure 3.17: The isolated ABS contribution for Sample A (left) and Sample D (right). Data for sample D for $T < 1$ K was taken by R. Prozorov and R.W. Giannetta.

the theory discussed in Section(3.5) and experiment.

3.7.2 Field dependence of ABS

The application of small dc magnetic fields was found to have a profound effect on the boundstate contribution to the penetration depth. The field dependence of the ABS was investigated in two ways: either sweeping the temperature at fixed field, or sweeping the field at fixed temperature. In both cases it was seen that fields of order $\sim$ 10 mT were sufficient to completely suppress the ABS contribution. As discussed above, the effect of a dc magnetic field can be modelled simply by Doppler shifting the delta peak in the quasiparticle density of states from zero energy ie., $\delta(E) \rightarrow \delta(E + e\mathbf{v}_f\mathbf{A})$. The resulting field dependence is therefore

$$\frac{\Delta\lambda(T,H)}{\lambda(0)} = \frac{\beta}{4T}\cosh^{-2}\left[\frac{\mu_0 e\lambda\mathbf{H}\cdot\mathbf{v}_f}{2k_BT}\right] \tag{3.21}$$

Fig.3.18 shows the effect of a small dc magnetic field on the temperature dependence of the penetration depth for sample D. The boundstate contribution is reduced as the magnetic field is increased. The data in Fig.3.18 shows the effect of applying the magnetic field at base temperature ($T \sim 1.4$ K). The effect of applying the magnetic

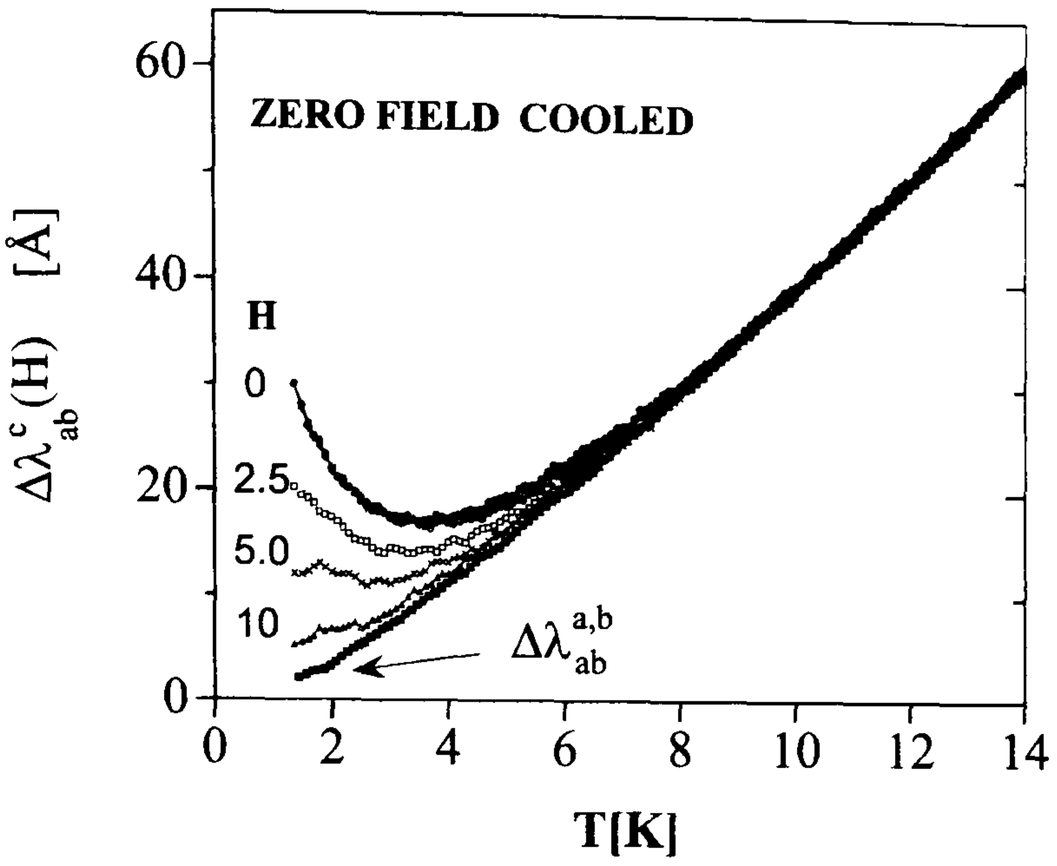

Figure 3.18: Small DC magnetic fields dramatically suppress the ABS contribution. The lowest curve shows data for the $\lambda_{ab}^{a,b}$ orientation in zero field

field above T_c was also investigated and is shown in Fig.3.19. When field cooling the sample the ABS contribution is suppressed less than when the sample is zero field cooled and the field applied at the base temperature. A simple reason for the difference between zero field cooling and field cooling is the effective demagnetizing factor. Applying the magnetic field above T_c will result in a uniform distribution of flux throughout the sample. The field value at the centre of the sample is likely to be approximately the same as at the sample edge. The zero field cooled case will be very different. Due to the large aspect ratios of the samples, the field will be much enhanced at the crystal edges due to the demagnetizing factor. An average demagnetizing factor $\eta_{av} = 1/(1-N_{av})$ is estimated by comparing the frequency shifts for each sample when extracted from the measurement coil in both measurement orientations. For sample A, $\eta_{av} = 13.1$ and $\eta_{av} = 11.7$ for sample D. The field at the crystal edges will therefore be an order of magnitude larger in the zero field cooled case than for the field cooled measurements explaining the smaller suppression of the ABS.

Fig.3.20 shows the field response of the ABS at constant temperature for sample

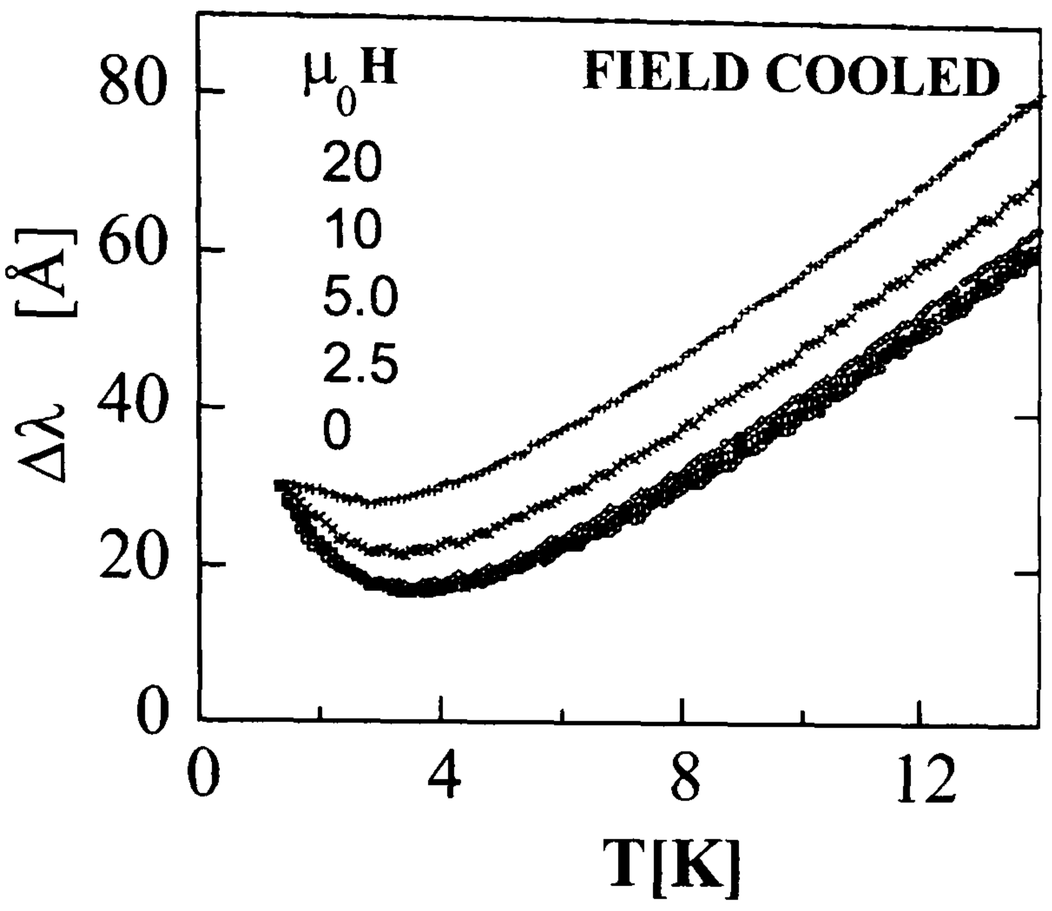

Figure 3.19: The ABS contribution to the penetration depth is suppressed less when field cooled compared to applying the same magnetic field at the base temperature.

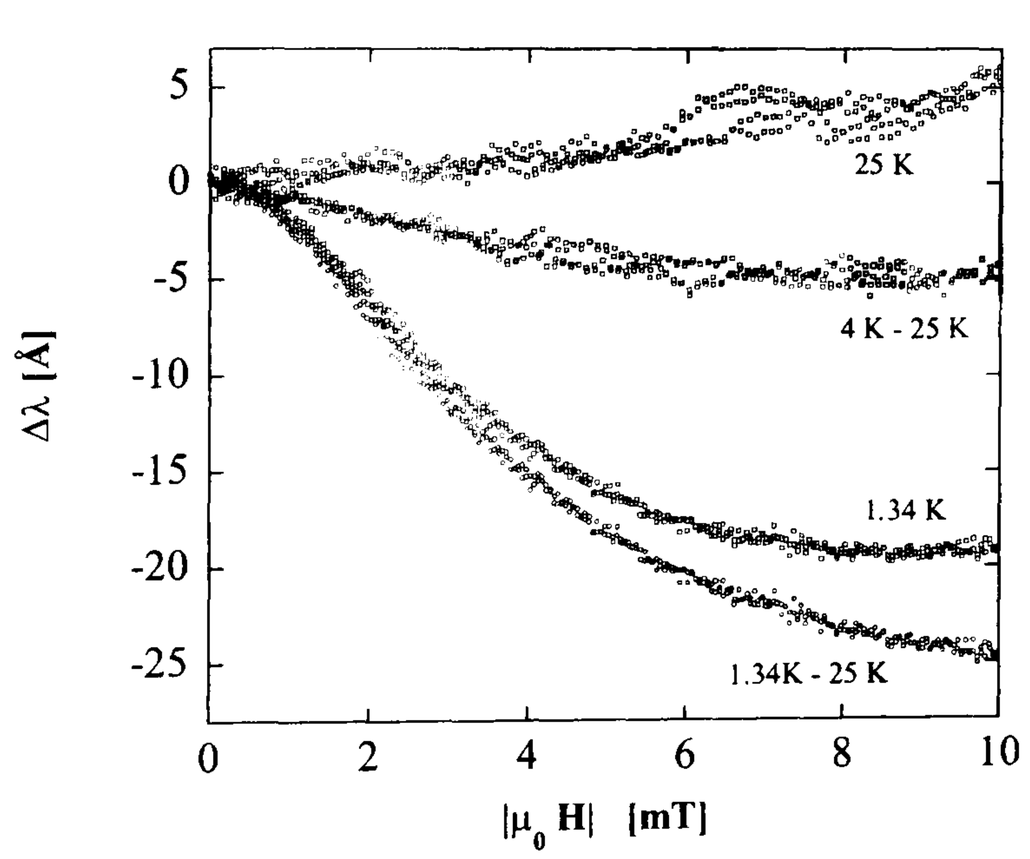

Figure 3.20: Field response of sample D at fixed temperature. The top curve is the essentially temperature independent response of the continuum. The bottom curve is the isolated ABS response.

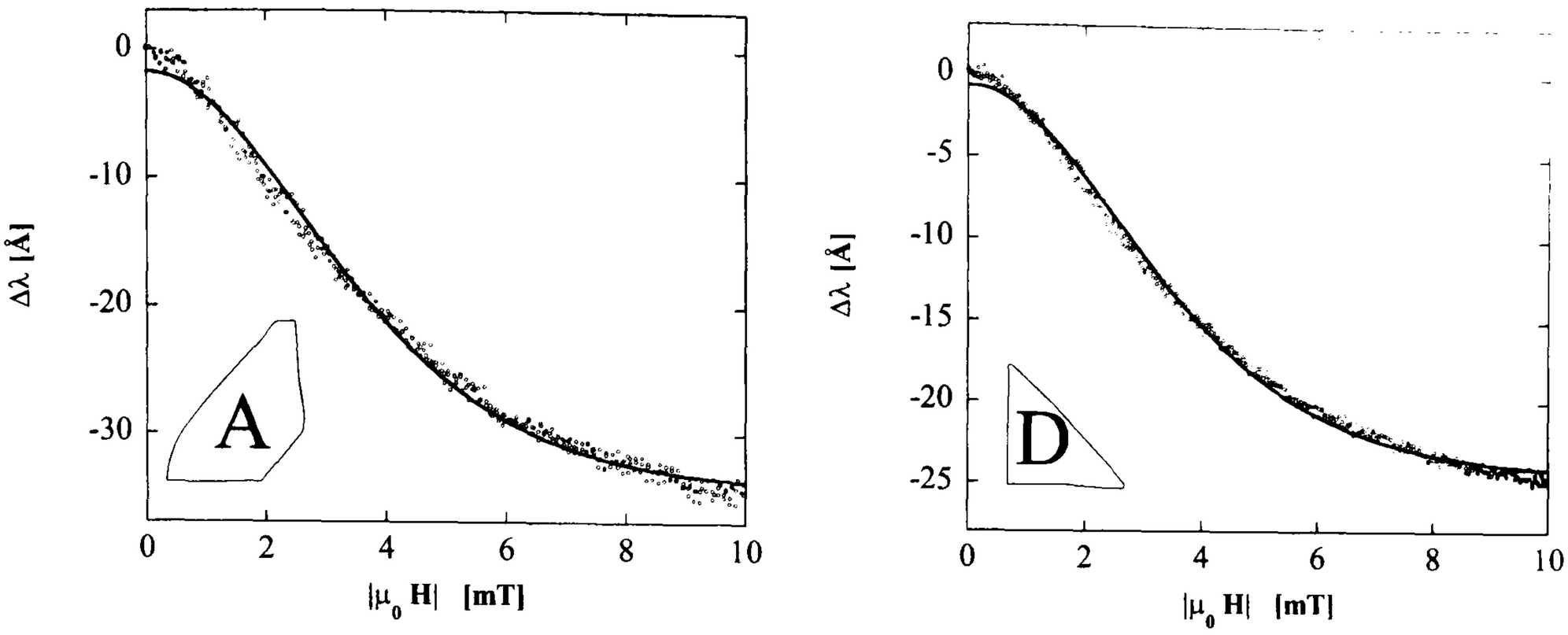

Figure 3.21: Fits to Eq.(3.18) for samples A and D.

D. Above $T \sim 10$ K the sample response becomes approximately temperature independent. The top curve represents the temperature independent response to the magnetic field. This curve is subtracted from the data taken at the base temperature (T=1.34 K) to give the bottom curve. The (4 K - 25 K) curve illustrates how the ABS contribution is diminished as temperature is raised. Samples B and C do not show a large upturn in the temperature dependence of the penetration depth. The field dependence of the penetration depth at fixed temperature in these samples is due almost entirely to the bulk supercurrents rather than ABS.

Fig.3.21 shows data for samples A and D with the temperature independent response subtracted. Both sets of data are fit to Eq.(3.21). As can be seen the very simple model for the magnetic response of the ABS fits the experimental data very well. The results of the fits in Fig.3.21, including the effect of the field enhancement, are summarized in Table(3.2).

Although the simple model for the field dependence of the ABS fits the data reasonably well, such a model does not account for realistic Fermi surface effects or the effect of impurities. For a square Fermi surface, quasiparticle trajectories at the same angle of incidence are equivalent over the whole side. For a more realistic Fermi

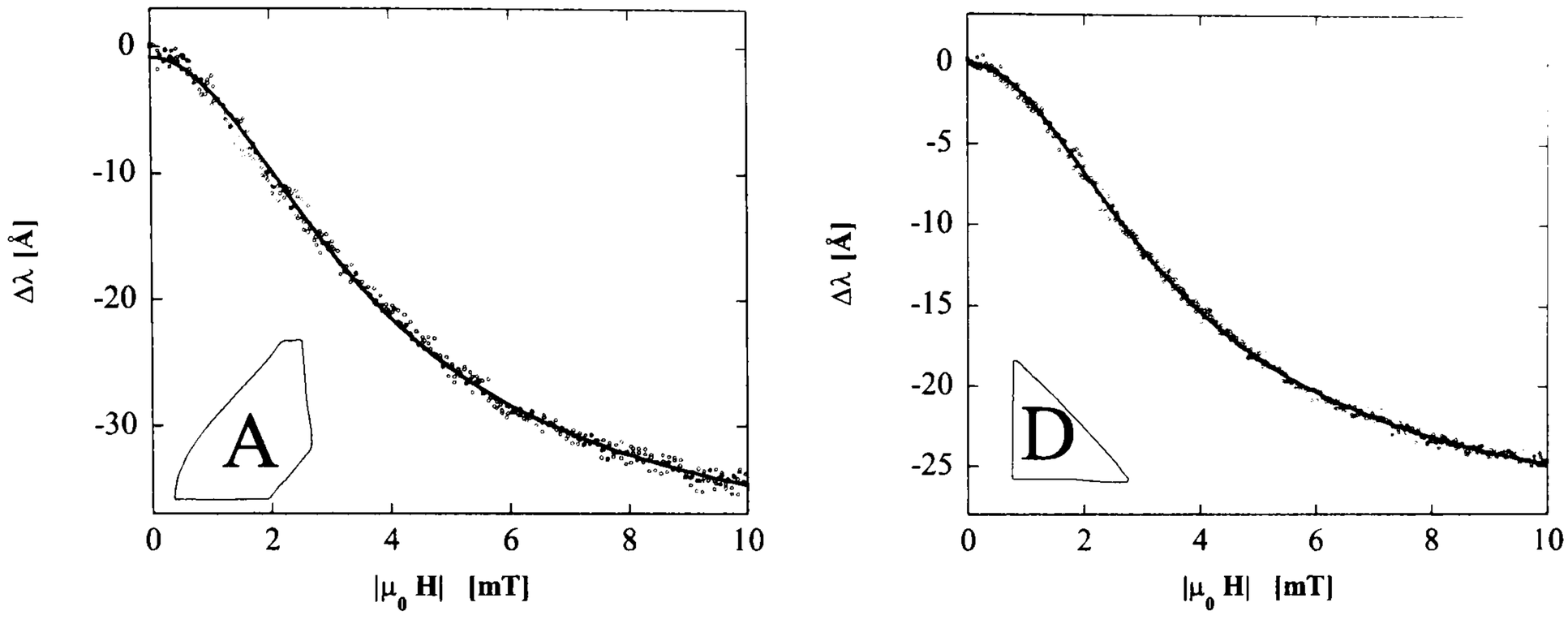

Figure 3.22: Fits for samples A and D to Eq.(3.22) which accounts for impurities and averages over the Fermi surface.

Sample	η_{av}	$\mu_0\tilde{H}$ (mT)	$\mu_0\tilde{H}_{\text{eff}}$ (mT)	v_f ($\times 10^5$ ms^{-1})
A	13.1	1.9	24.9	0.3
D	11.7	1.9	22.2	0.4

Table 3.2: Summary of results of fits to Eq.(3.18) to samples A and D.

surface, such as a cylinder, quasiparticle trajectories are not equivalent and so some averaging over the Fermi surface must be done to account for this. The description of the effect of ABS on the penetration depth by Barash *et al.* [79] accounts for both impurities and Fermi surface effects.

In Fig.3.17, the isolated ABS contribution to the penetration depth was shown. These curves were fit to $\Delta\lambda^{ABS}(T) = c/(T + T^*)$ to identify an experimentally determined parameter related to the broadening of the boundstates due to impurities. In Eq.(3.20), the parameter relating to the broadening of the ABS is γ. In order to account for the measured broadening of the ABS due to impurities, it is necessary to relate the measured T^* to the corresponding value of γ. This can be done by plotting out Eq.(3.17) using different values of γ and fitting to $\Delta\lambda^{ABS}(T) = c/(T + T^*)$ thus relating γ to T^*. The gradient of the linear term can be set equal to that derived from experiment and the magnitude of the ABS term is set by the value of c yielded from a fit to the data. The value of the γ term can be included in Eq.(3.20) and this can be evaluated numerically. To acquire an expression to fit to the field dependent data it was noted that $Im(\psi(1/2 + ix)) = \pi/2\tanh(\pi/x)$. The numerically evaluated field dependent penetration depth from Eq.(3.20), which includes the impurity contribution, is fit using $\Delta\lambda/\lambda = (\alpha + 1/(\beta x)\tanh(\beta x))$. This gives the value which modifies the field scale over which the boundstate contribution is suppressed. The expression used to fit to the data in Fig.3.22 is

$$\Delta\lambda(H) = a + \frac{b}{H}\tanh\left(\frac{0.79H}{c}\right) \tag{3.22}$$

where $c{=}\tilde{H}/\pi$ and $\tilde{H} = k_B T/(\mu_0 e v_f \lambda)$. The results of fits to Sample A and D in Fig.3.22 are shown in Table(3.3).

The Fermi velocities derived from these fits agree well with that derived from heat capacity measurements by Wang *et al.* [92] on slightly overdoped Y123. Wang *et al.* deduced a value of $v_f = 1.4 \times 10^5$ ms^{-1}. The agreement of these results also adds weight to the interpretation of Barash *et al.* for the effect of the ABS on the penetration depth. The fact that two independent thermodynamic techniques yield

Sample	η_{av}	$\mu_0\tilde{H}$ (mT)	$\mu_0\tilde{H}_{\text{eff}}$ (mT)	v_f ($\times 10^5$ ms^{-1})
A	13.1	0.55	7.2	1.1±0.2
D	11.7	0.55	6.4	1.2±0.2

Table 3.3: Summary of results of fits to samples A and D including effects of impurities and averaging over quasiparticle trajectories.

such similar values for v_f suggest that this value may be more accurate than the value of $v_f = 2.5 \times 10^6$ ms^{-1} yielded by ARPES studies [93].

3.8 Andreev Boundstates in other Cuprates

All of the data presented so far has focused on $YBa_2Cu_3O_7$. This section will present evidence for ABS formation in a different cuprate. ABS formation occurs as a direct consequence of the $d_{x^2-y^2}$ order parameter. At present, the body of evidence shows that all HTS have $d_{x^2-y^2}$ symmetry. That said, it would be reasonable to expect ABS to be observed in all HTS. Measurements on slightly underdoped $Bi_2Sr_2CaCu_2O_8$ (BSCCO) have shown evidence for ABS formation. The measurements were performed by Prozorov *et al.* using the same LC-oscillator technique as described in Chapter2 attached to a ^{3}He cryostat. The sample in this setup can be cooled to $\sim$ 300 mK. Fig.3.23 shows temperature sweeps performed on this sample as a function of field. The small field pinning in BSCCO means that the sample cannot have fields applied following a zero field cool but must be cooled through T_c with the field applied. The general trend is that the zero field measurement shows the largest upturn. This upturn decreases at higher fields. The small pinning also means that field sweeps at constant temperature cannot be performed. The field scale for the suppresion of the ABS is larger in BSCCO than in Y123. One of the reasons for this may be that field cooling serves to reduce the demagnetizing factor of the sample. This effect was observed in the Y123 samples also. With this in mind the field scales between the two materials may be more similar than it at first appears. The conclusion to

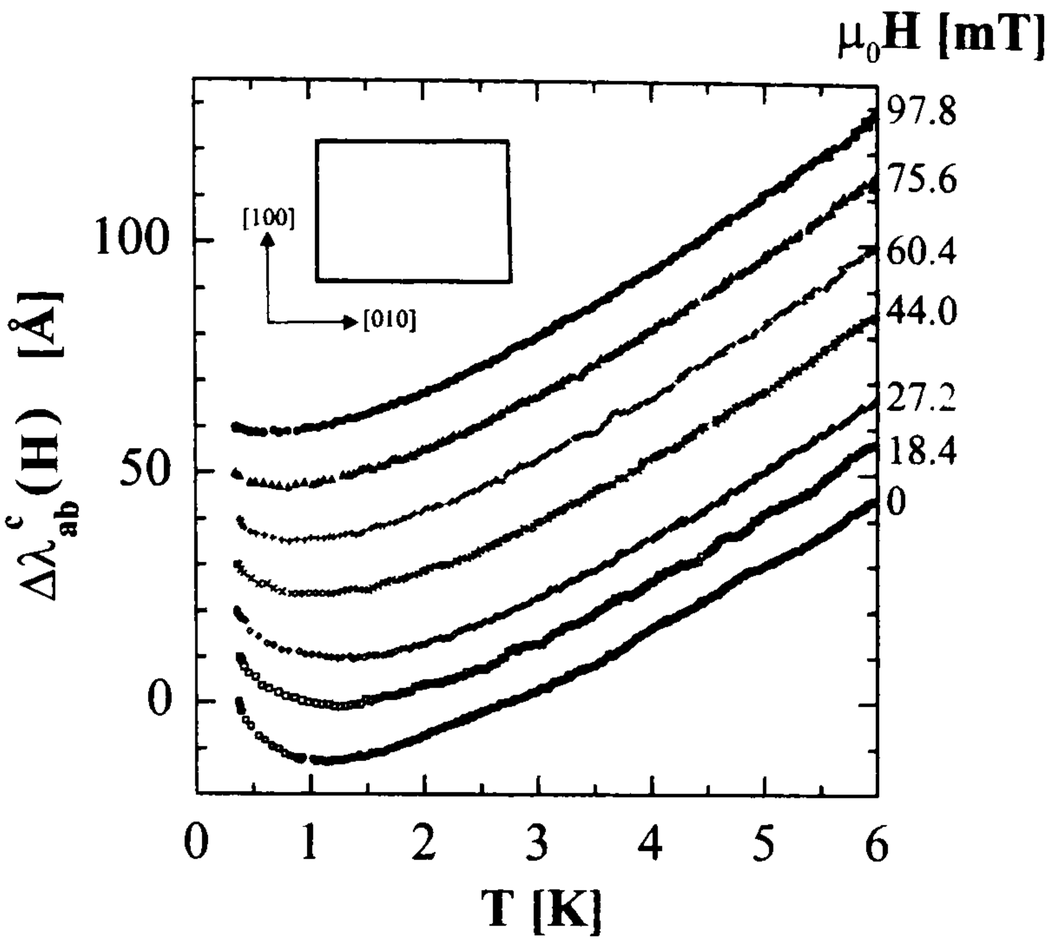

Figure 3.23: A low temperature upturn in the penetration depth is observed in $Bi_2Sr_2CaCu_2O_8$ as measured by R. Prozorov and R.W. Giannetta [94]

draw from the BSCCO result is that the field scale is still small in keeping with the ABS theory. Fig.3.24 shows the same sample, measured by the author in Bristol, with the probe field applied within the sample plane. Unlike $YBa_2Cu_3O_7$, the penetration depth measured in this orientation is dominated by $\Delta\lambda_c(T)$. The inset shows that the ABS contribution appears to have moved to higher temperature. This sample is rectangular in shape with the crystal edges running along the (100) and (010) directions. For samples with small non (100) and (010) surfaces, surface degradation could lead to an increased ABS contribution to the measured penetration depth as long as specular scattering persists. For samples with large (110) surfaces, degradation of the surfaces would reduce the ABS contribution to the penetration depth.

Preliminary evidence has revealed no ABS penetration depth contribution in underdoped $Tl_2Ba_2CuO_6$ or $YBa_2Cu_4O_8$ down to the base temperature of the experiment ($\sim$ 1.4 K). Although the presence of ABS is strong evidence for an order parameter with $d_{x^2-y^2}$ symmetry, the lack of ABS is not strong counter evidence. As discussed earlier, a number of factors can decrease the ABS contribution. A lack of

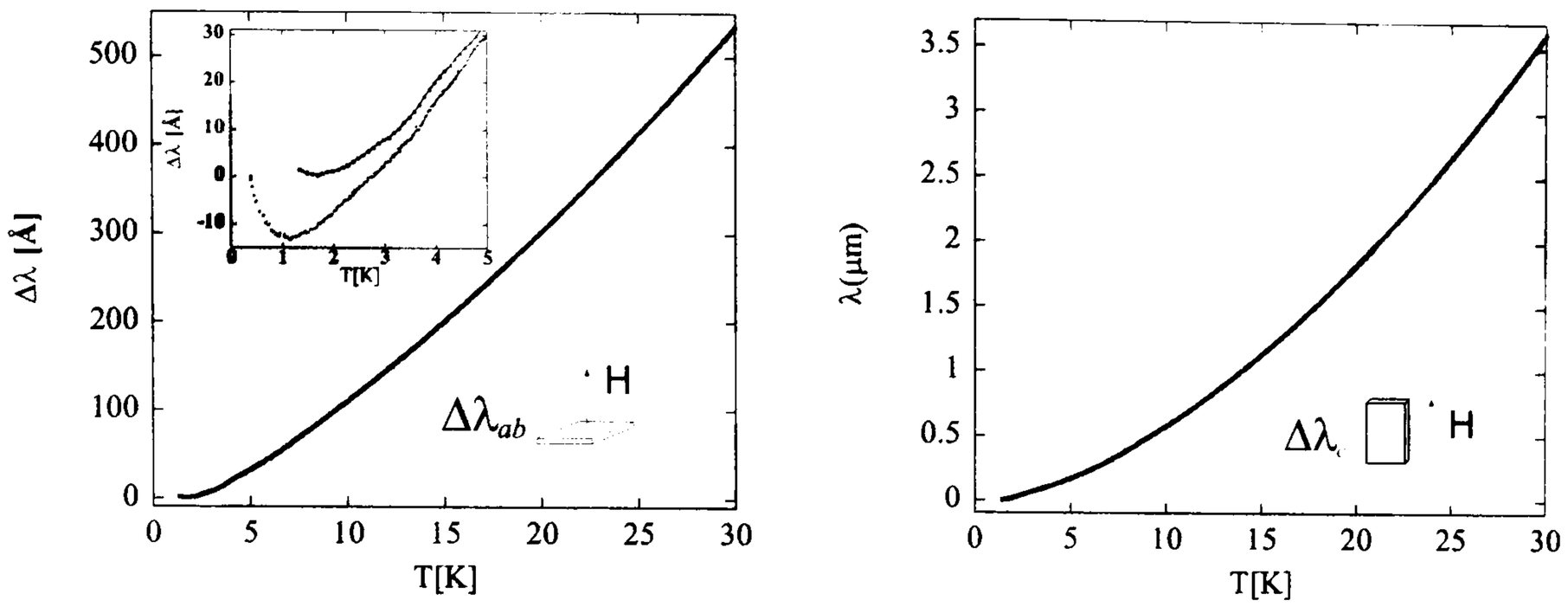

Figure 3.24: Data for the same $Bi_2Sr_2CaCu_2O_8$ sample as shown in Fig.3.23 measured with the probe field applied perpendicular to the sample plane (left) and within the sample plane (right). The inset shows the low temperature data compared to that measured by R. Prozorov and R.W Giannetta on the same sample down to 300 mK. The measurement with the probe field applied within the sample plane shows no boundstate contribution as expected.

clean specular surfaces could prevent the formation of ABS at zero energy. In other materials the temperature scale for the observation of the $1/T$ term in the penetration depth may be much smaller resulting in the effect becoming observable at some temperature < 1.4 K, ie. below the base temperature of this experiment.

3.9 Non ABS Penetration Depth Anomalies

The previous section discussed the observation of anomalous penetration depth behaviour due to ABS. The case for ABS relies on three pieces of evidence: i) Measurement orientation dependence ii) Surface orientation (shape) dependence and, iii) Small field scale associated with the suppression of the effect. Anomalous features associated with the penetration depth not fitting the above criteria, particularly i) and iii), can be said to arise from sources other than ABS.

Measurements were performed on a $HgBa_2Ca_2Cu_3O_{(8+\delta)}$ single crystal which was previously used in a heat capacity study [95]. Penetration depth data for the crystal

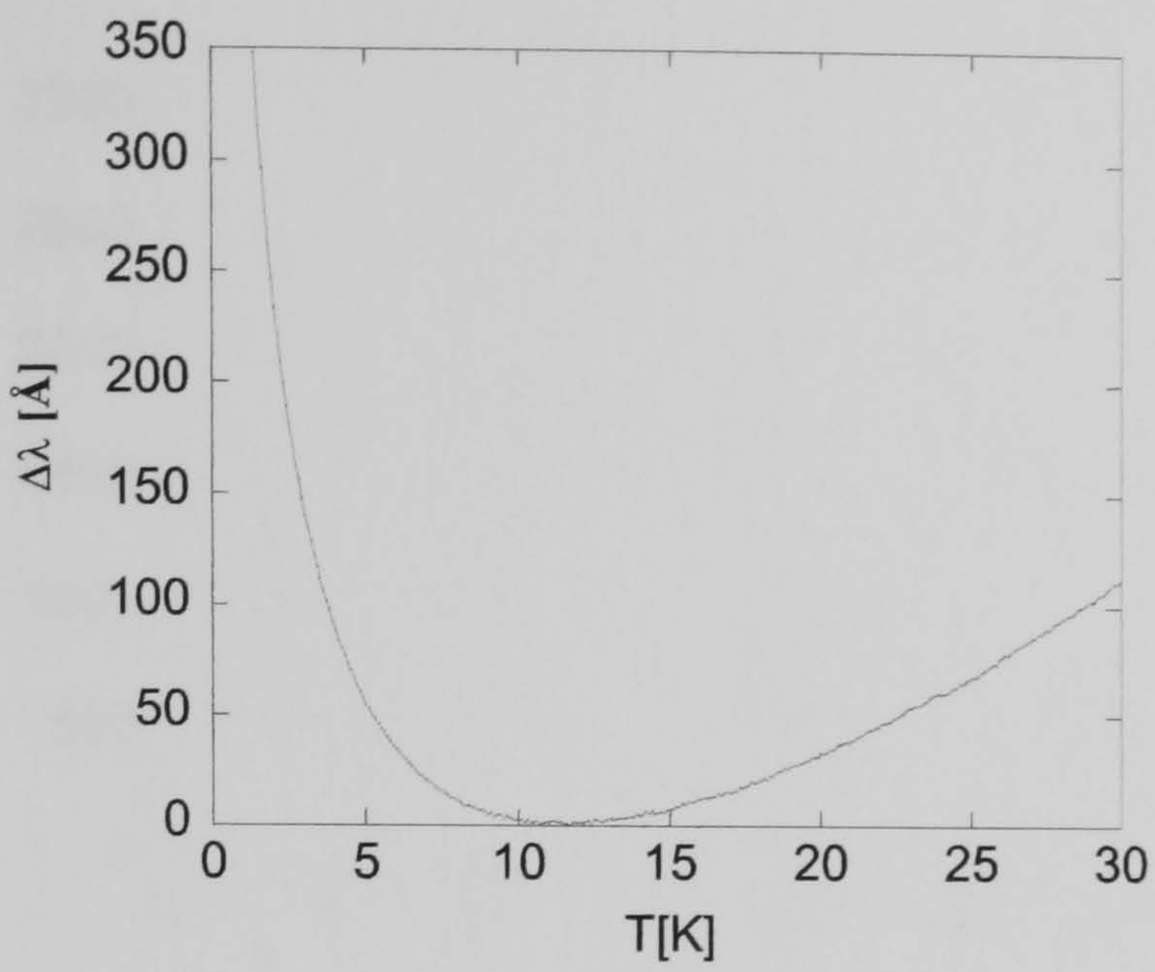

Figure 3.25: Data for a $HgBa_2Ca_2Cu_3O_{(8+\delta)}$ single crystal mounted in the $\Delta\lambda^c_{ab}$ orientation.

mounted in the $H\|c$ orientation (associated with ABS) is shown in Fig.3.25.

The sample appears to have a large ABS component. As before, this sole measurement is not sufficient to conclude that ABS are responsible for the upturn in the penetration depth. Fig.3.26 shows data for the same crystal with the measurement field applied within the ab-plane. Unlike Y123, the component of the penetration depth probed for this crystal in the $H\|ab$ orientation is not λ_{ab} since the sample width:thickness ratio is 3:1 meaning this orientation will be dominated by λ_c (See Section(2.3.3)). The two orientations probe different components of the penetration depth but any ABS contribution should only be present in the $H\|c$-axis orientation. Fig.3.26 clearly shows an increase in penetration depth at low temperature larger in magnitude than in the $H\|c$ orientation. The larger increase in the $H\|ab$ orientation is due to $\Delta\lambda_c$ which is larger than $\Delta\lambda_{ab}$ dominating.

Assuming that the paramagnetic contribution to the penetration depth is due to either a contaminant or oxygen loss which is isotropic around the crystal surface it should be possible to fit the data accounting for the paramagnetism and extract the intrinsic penetration depth response. Following the analysis of Cooper [70], the

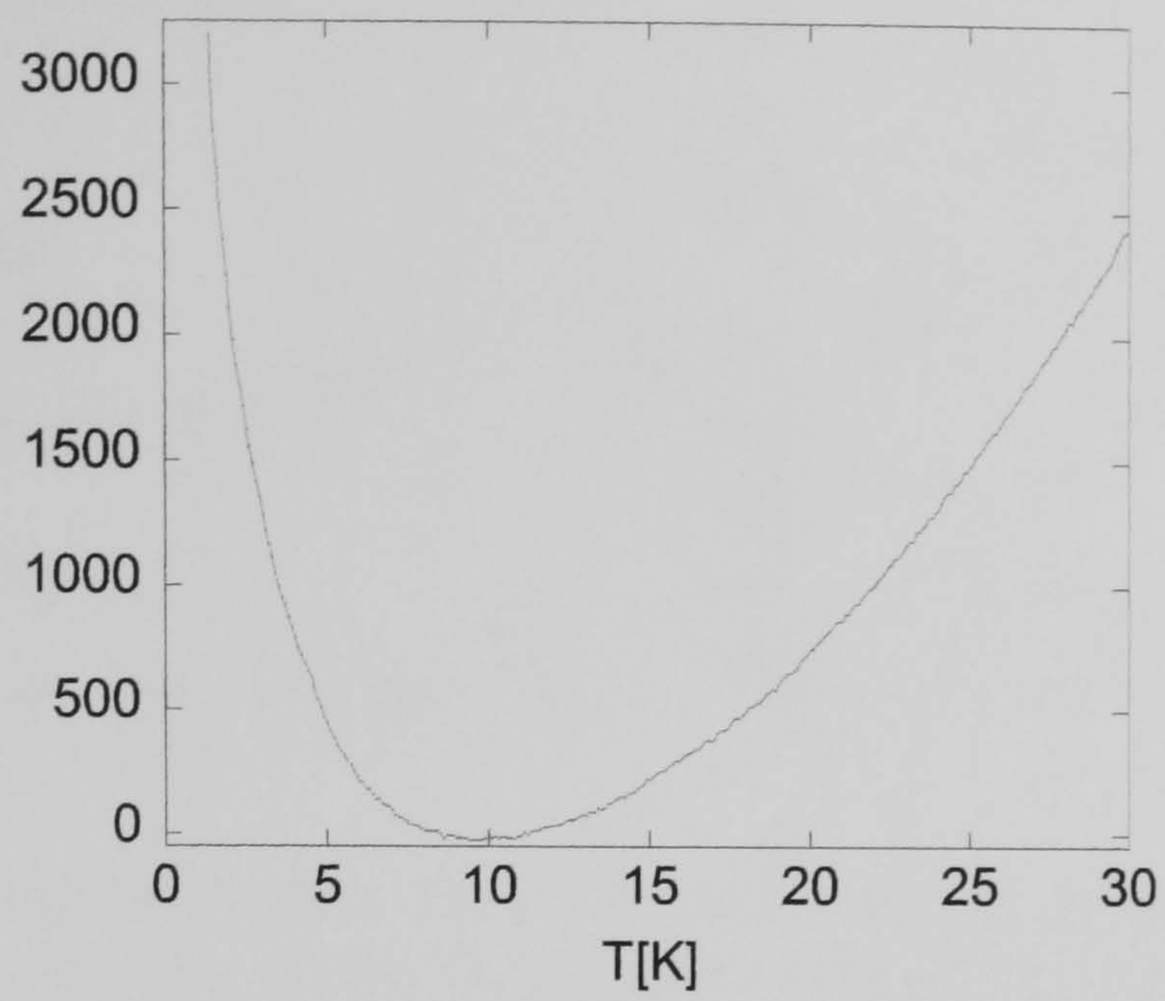

Figure 3.26: A large increase in penetration depth is also seen in this orientation meaning that ABS are not the cause of this effect.

measured penetration depth ($\lambda(T)$) will be the London penetration depth ($\lambda_L(T)$) modified by some contribution due to the paramagnetic sites

$$\lambda(T) = \lambda_L(T)\sqrt{\mu(T)} \tag{3.23}$$

where μ is the magnetic permeability given by $\mu(T) = 1+C/(T+\Theta)$ and C is the Curie constant. Fitting the data in Fig.3.25, which only contains contributions from λ_{ab}, to Eq.(3.23) allows $\Delta\lambda_{ab}(T)$ to be separated from the total response. Fig.3.27a shows the fit to Eq.(3.23) along with the corresponding $\lambda_{ab}(T)$ derived from it. $\lambda_{ab}(T)$ yielded by the fit is $\lambda_{ab}(T) = 13.4T^{1.0}$ Å. The linear temperature dependence was not imposed but was yielded by the fit. Other values yielded by the fit are $C = 101$ and $\Theta = 1.1$ K. Assuming that the source of the low temperature upturn is isotropic, the values of C and Θ can be used to fit the data for the measurement field applied within the sample plane. In this orientation the measured penetration depth will be $\Delta\lambda_{eff} = \Delta\lambda_{ab}(T)+(t/w)\Delta\lambda_c(T)$, where t is the thickness of the sample and w is the width. Since the sample dimensions are known, the temperature dependence of $\Delta\lambda_c(T)$ can be extracted. Eq.(3.23) can be fit to the data imposing the values of C and Θ yielded by

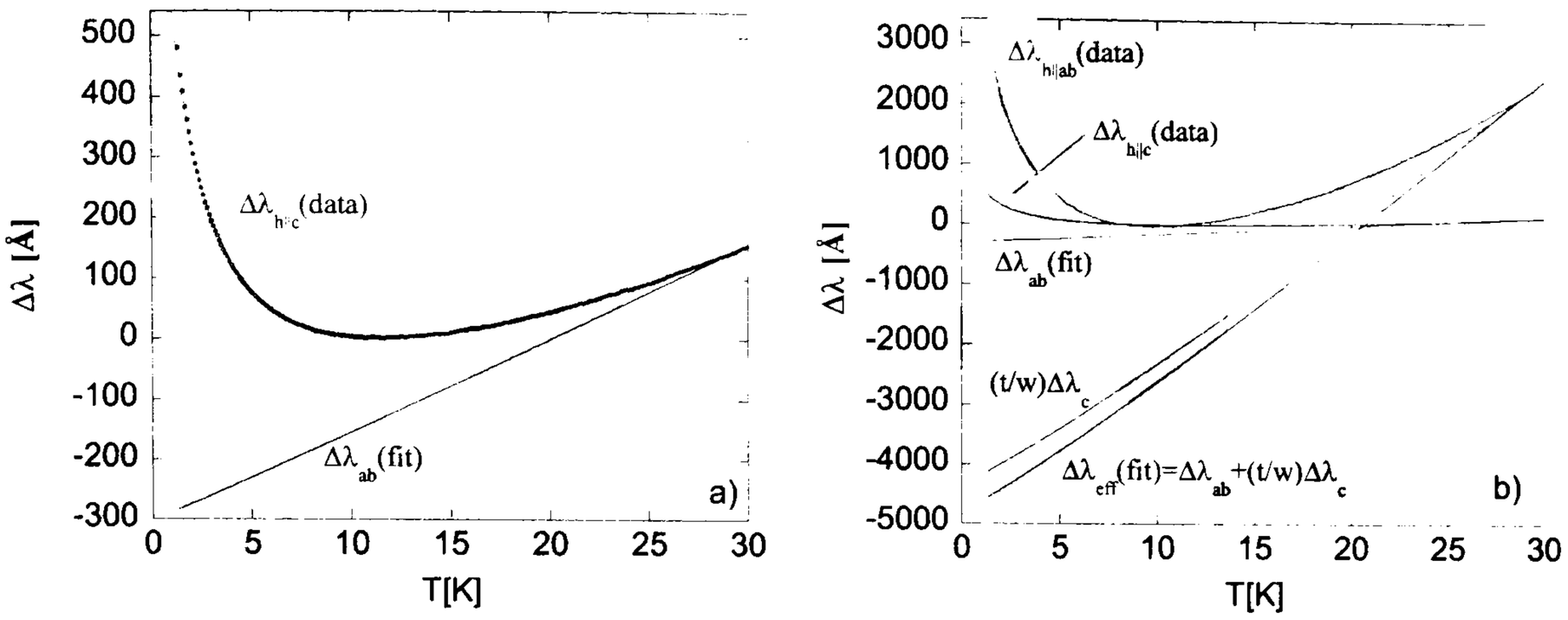

Figure 3.27: a)Measurement with the probe field applied perpendicular to the *ab*-planr of the sample. Fitting to Eq.(3.23) allows $\Delta\lambda_{ab}(T)$ to be extracted. b) This process is repeated imposing the behaviour of $\mu(T)$ given in the fit in a).

the fit in Fig.3.27a. Fig.3.27b shows this process. The data is fit fixing the values of C and Θ but leaving the gradient of the penetration depth, and the power law it follows, as fitting parameters. The fitted penetration depth is $\Delta\lambda_{eff} = 172T^{1.1}$ Å. Subtracting $\lambda_{ab}(T)$ from $\Delta\lambda_{eff}(T)$ gives $(t/w)\Delta\lambda_c(T)$. Multiplying this curve by (w/t) gives $\Delta\lambda_c(T)$ (not shown). The $\Delta\lambda_c(T)$ behaviour yielded by this process is essentially linear in temperature with $d\lambda_c(T)/dT = 750$ Å/K. The values of $d\lambda_{ab}(T)/dT$ and $d\lambda_c(T)/dT$ yielded by this analysis are much larger than previously published values [96] for this material which show $d\lambda_{ab}(T)/dT$=4 Å/K and $d\lambda_c(T)/dT = 10$ Å/K. The $\lambda_c(T)$ behaviour in Ref.[96] has a temperature dependence which follows T^2 rather than the approximately linear in temperature given by the fit. The transition temperature for this sample is $T_c = 120$ K and not 133 K which represents the optimally doped case. The results presented here are therefore representative of the an underdoped Hg1223 crystal. This may account for the differences in $d\lambda/dT$ found here compared with previously published values [96]. It is thought that the cause of the anomalous penetration depth behaviour is most likely due to deoxygenation at the surfaces.

The field dependence of the ABS is perhaps the most compelling piece of evidence

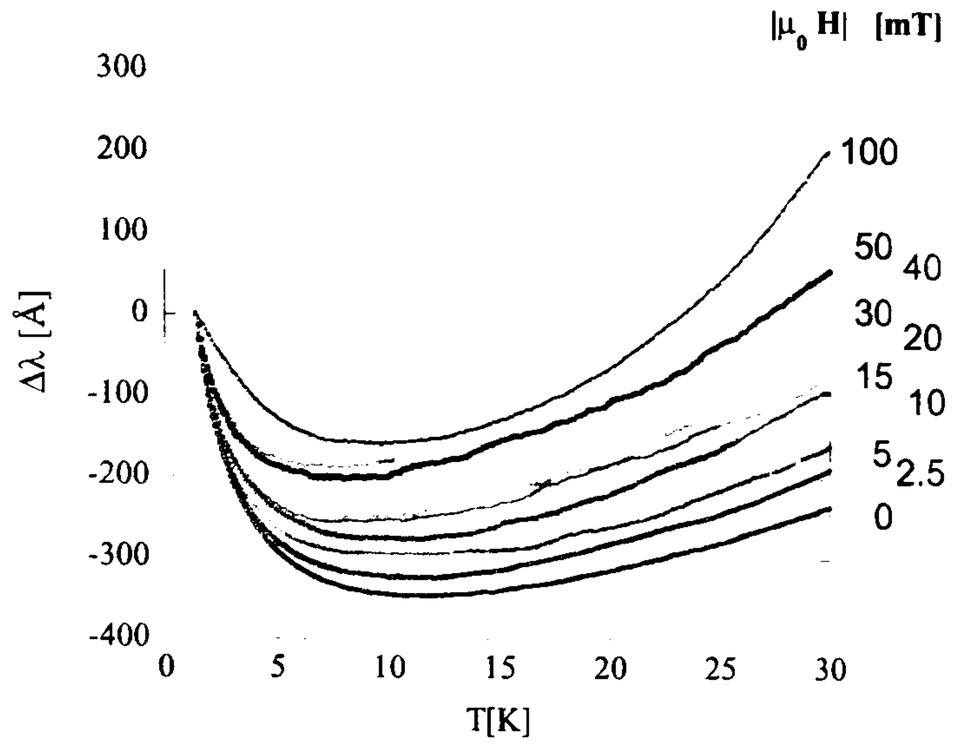

Figure 3.28: Comparatively large magnetic fields have little effect on the upturn in the penetration depth signaling that ABS are not responsible for the effect.

for their observation in penetration depth measurements. The very small field scale ($\sim 0.01H_0$) associated with the disappearance of the upturn is very much smaller than that associated with paramagnetic ions at the surface. A typical field scale for an effect associated with paramagnetic ions such as in the $Nd_{1.85}Ce_{0.85}CuO_{1-y}$ would be of order $k_BT/g\mu_B \simeq 1$ T, with $g = 2$ and $T = 1.4$ K. Fig.3.28 shows the effect of magnetic field on the penetration depth with the measurement field applied in the $\Delta\lambda^c_{ab}$ orientation. Fields up to 0.1 T have no effect on the upturn and merely serve to increase the continuum contribution to the penetration depth.

Taken as a whole, the evidence clearly shows that the low temperature upturn in the $HgBa_2Ca_2Cu_3O_{(8+\delta)}$ single crystal is not due to Andreev boundstates. The lack of measurement orientation dependence and the fact that large magnetic fields have no effect on the magnitude of the upturn, demonstrate that some other mechanism is responsible for the effect.

3.10 Summary

Evidence is presented which identifies a low temperature modification to the BCS penetration depth in $YBa_2Cu_3O_7$ (Y123) due to the formation of surface Andreev boundstates (ABS) at zero energy. Four optimally doped Y123 crystals were measured with the probe field applied along the a, b and c crystal axes. For each crystal $\Delta\lambda_b(T)$, $\Delta\lambda_a(T)$ and $\Delta\lambda_{ab}(T)$ were measured respectively. The superfluid densities were calculated for $\Delta\lambda_a(T)$ and $\Delta\lambda_b(T)$ and fit to the dirty d-wave expression of Hirschfeld and Goldenfeld [68]. The values of T^* yielded for the crystals ranged between 0.7 K to 3.8 K for ρ_a and 1.5 K to 4.9 K for ρ_b indicative of high sample purity. Applying the measurement field along the c-axis of the samples should yield a penetration depth which is the average of $\Delta\lambda_a(T)$ and $\Delta\lambda_b(T)$. Instead of this behaviour, a low temperature increase in the penetration depth was observed in all crystals. This low temperature increase in penetration depth is attributed to surface Andreev boundstates. The ABS contribution was only observed for the measurement orientation whereby quasiparticles were confined to the ab-plane. In this orientation quasiparticles are specularly reflected through adjacent lobes of the $d_{x^2-y^2}$ order parameter causing a delta peak in the quasiparticle density of states which introduces a $\sim 1/T$ dependence to the penetration depth. The magnitude of the ABS contribution to the penetration depth was seen to depend strongly on the shape of the crystal in a systematic way. The ABS contribution can be modified by the presence of impurities which broaden the delta peak in the quasiparticle density of states. A fit to $c/(T+T^*)$ yielded T^*=0.8 K indicating only slight broadening of the boundstates.

The application of small dc magnetic fields were found to have a profound effect on the temperature dependence of the ABS contribution to the penetration depth. An applied field of $\sim$ 10 mT was found to be sufficient to almost completely suppress the boundstate contribution to the penetration depth. This small field scale can be qualitatively understood in terms of the boundstates being Doppler shifted away from zero energy by an amount $\delta E = e\mathbf{v}_f \cdot \mathbf{A}$. The field dependence of the ABS was investigated at constant temperature. The ABS theory of Barash *et al.* [79] was

used to fit the field sweep at constant temperature data. The fits gave values for the temperature dependent field scale for the suppression of ABS. Values for the Fermi velocity, v_f, given by this field scale in samples A and D are $v_f = (1.1 \pm 0.2) \times 10^5$ ms^{-1} and $v_f = (1.2 \pm 0.2) \times 10^5$ ms^{-1} respectively, agreeing with previously published values for this material [92] as derived from heat capacity.

Evidence for ABS formation in a slightly underdoped $Bi_2Sr_2CaCu_2O_8$ single crystal has also been found. The low temperature increase in penetration depth was seen to be present only in the $H \| c$ measurement orientation where quasiparticles are confined to the *ab*-plane, as for Y123. The ABS contribution is again suppressed by the application of small magnetic fields.

A $HgBa_2Ca_2Cu_3O_{(8+\delta)}$ single crystal also displayed a low temperature increase in penetration depth. This behaviour was not attributed to ABS since it was present in both measurement orientations and the application of large magnetic fields had minimal effect on the magnitude of the upturn. The most likely cause of the low temperature increase in penetration depth in this sample is an isotropic paramagnetic contribution due to sample degradation.

Chapter 4

Superconducting Gap of Magnesium Diboride

4.1 Introduction

The discovery of superconductivity in MgB_2 in January 2001 [1] at the remarkably high temperature of $\sim$ 38 K has inspired a large body of work. In the clamour to reproduce this result a huge amount of often contradictory data has been presented on the Los Alamos pre-print server on a daily basis which still continues at the time of writing (August 2001). As higher quality samples become available, an emerging consensus is being established. The majority of measurements point to the existence of a fully gapped order parameter. Prior to this study, penetration depth measurements have pointed to a largely T^2 temperature dependence rather than the expected exponential temperature dependence associated with a fully gapped order parameter. This chapter contains data which clearly show an exponential temperature dependence to the penetration depth and fitted values for the gap are consisted with measurements from other techniques.

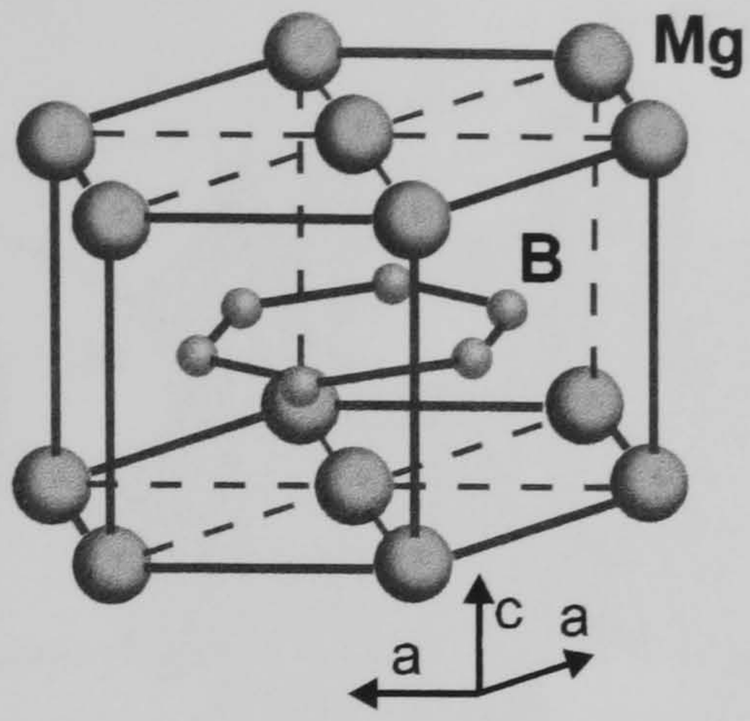

Figure 4.1: The layered structure of MgB_2 from ref. [97]

4.2 Review of MgB_2

MgB_2 has a simple layered structure with B layers ordered in a graphite like fashion separated by hexagonal close packed Mg layers. MgB_2 exhibits strong anisotropy along the B-B lengths with the interplane distance being a factor $\sim$2 longer than the intraplane separation. The B-B vibration modes are thought to play a crucial role in the high transition temperature of this compound [98, 99]. Bandstructure calculations indicate that the density of states at the Fermi level is predominantly of B like character. The Mg is substantially ionized due to its *s* electrons being fully donated to the B derived metallic conduction band. The strongly covalent B-B bond, coupled with an ionic component and large metallic density of states leads to strong electron-phonon coupling. Fig.4.2 shows the calculated Fermi surface of MgB_2 by Kortus *et al.*[99] The density of states at the Fermi level is almost entirely due to the B p orbital. The bands due to the p_z orbital, both bonding and antibonding, are isotropic in nature. The $p_{x,y}$ bands are much more 2-dimensional.

The obvious question facing the scientific community is which type of pairing mechanism could lead to such a high transition temperature in MgB_2. MgB_2 is comprised of light elements and the BCS [34] theory predicts that low mass elements result in higher frequency phonon modes which could lead to higher transition temperatures. The highest transition temperature is predicted hypothetically for superconducting

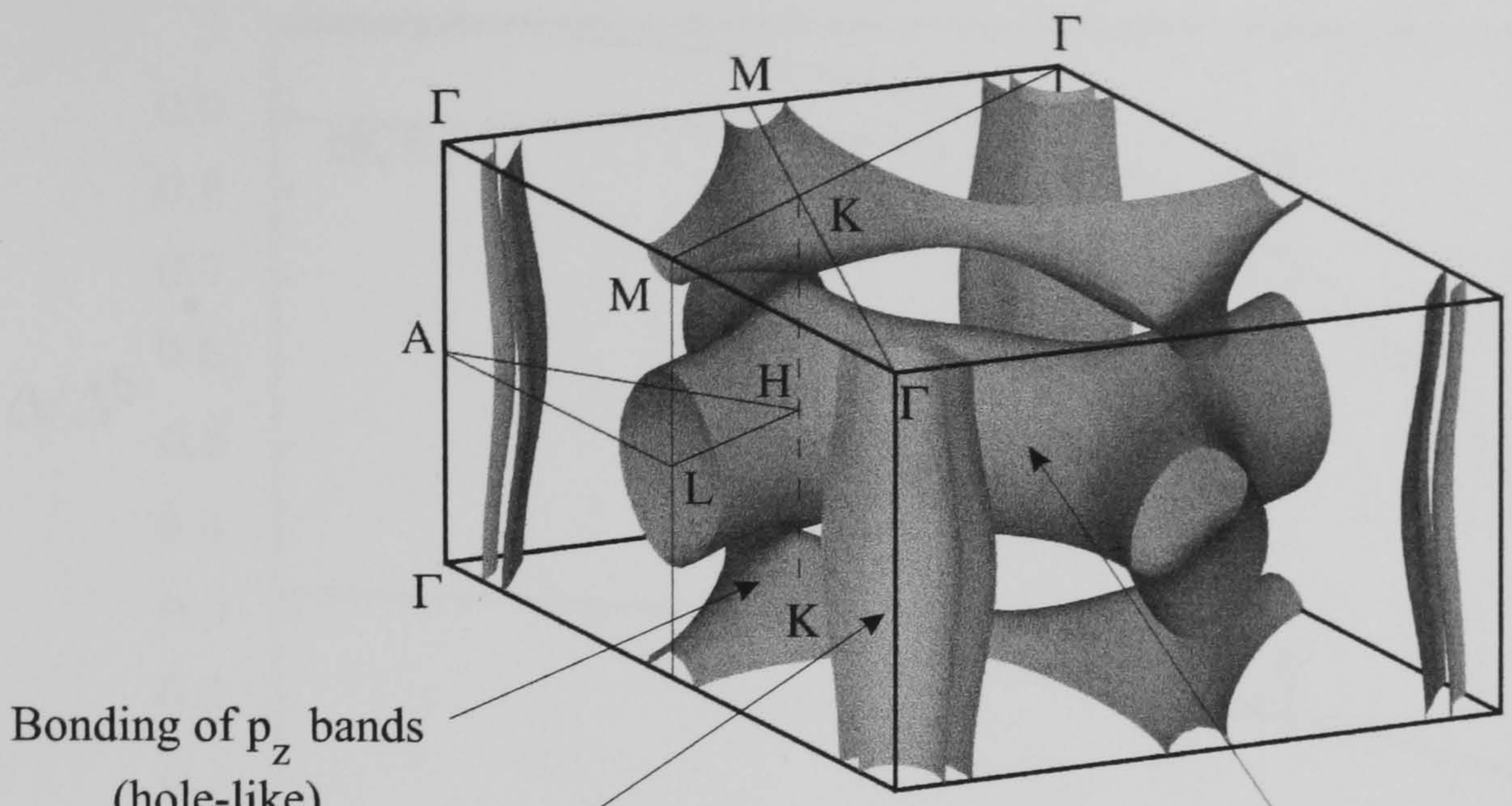

Figure 4.2: The Fermi surface of MgB_2 from ref. [99]. The density of states at the Fermi surface is almost entirely due to the B p orbital.

metallic hydrogen which consists solely of hydrogen, the lightest element, under extreme pressure. An important feature of phonon mediated BCS theory was the ability to explain the isotope effect in conventional s-wave superconductors. In order to establish the importance of phonon modes in the superconductivity of MgB_2, Bud'ko *et al.* [100] investigated the existence of the isotope effect for this material. The measurements were performed on high quality MgB_2 powders (99.5% pure Mg and >99.5% isotopically pure B). MgB_2 samples were made with different boron isotopes: ^{10}B and ^{11}B. Transition temperatures were measured using a SQUID magnetometer to obtain M/H vs. T for $Mg^{10}B_2$ and $Mg^{11}B_2$ samples. The transition temperatures were measured to be T_c=39.1 K for the $Mg^{11}B_2$ sample and T_c=40.1 K for $Mg^{10}B_2$. The shift in transition temperature was also verified with specific heat data. If enhancement scaled as the square root of the formula mass, an enhancement of $\Delta T_c = 0.87$ K would be expected. If the enhancement was due entirely to the change in B mass an enhancement of $\Delta T_c = 1.9$ K is predicted. The fact that the change is

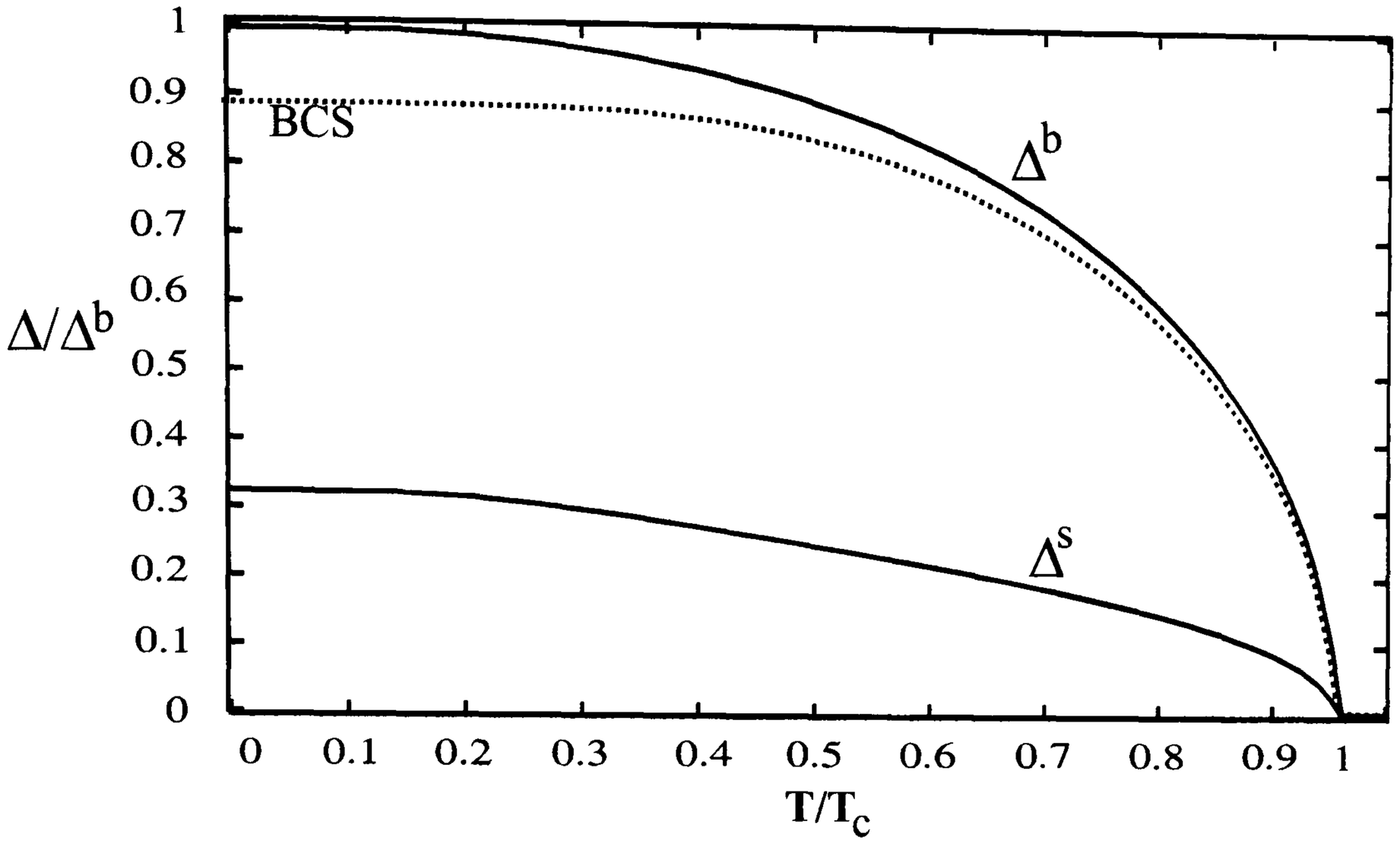

Figure 4.3: The calculated temperature dependence of the 2 order parameters originating at different electronic bands. The dashed line shows the BCS gap corresponding to the same T_c as the multigap model. Adapted from [101]

larger than the formula mass value implies that the phonon modes mediating superconductivity are boron-like in character in agreement with the findings of Kortus *et al.*

Further bandstructure calculations by Liu *et al.* [101] build on the work of [99] and identify the possibility of 2 distinct superconducting gaps originating from different bands crossing the Fermi surface. They calculate that in the clean limit the two gaps should differ in magnitude significantly. The gap due to the quasi 2-dimensional cylindrical hole sheets about the Γ-A line is calculated to be ~3 times greater than the gap on the 3-dimensional tubular networks arising from B p_z band. The temperature dependence of the gap as calculated in [101] is shown in Fig.4.3. The two gaps close at the same temperature. Thermodynamic measurements taken close to T_c will be more sensitive to the larger gap (Δ^b) since it is the more rapidly changing. Similarly thermodynamic measurements at low temperature will be most sensitive to

the smaller gap (Δ^s) as the larger gap is more temperature independent at low T.

The structural anisotropy of MgB_2 would suggest some anisotropy in the superconducting properties of the material would be likely. There is some disagreement about the magnitude of the anisotropy. de Lima *et al.* [102] have studied the coherence length anisotropy (ξ_{ab}/ξ_c) via the upper critical field anisotropy (H_{c2}^{ab}/H_{c2}^{c}) of aligned MgB_2 crystallites. The coherence length can be extracted from the upper critical field since $H_{c2}^{ab} = \phi_0/2\pi\xi_{ab}\xi_c$ and $H_{c2}^{c} = \phi_0/2\pi\xi_{ab}^2$, with the component of the coherence length probed being defined by the direction of the superfluid in a similar manner to the penetration depth components (see Section 2.3.2). The anisotropy in the coherence length was measured to be $\gamma = \xi_{ab}/\xi_c = 1.7 \pm 0.1$. Measurements by Lee *et al.* [103] on single crystal MgB_2, again using the anisotropy in H_{c2} yield a larger value for the anisotropy of $\gamma = 2.6 \pm 0.1$. Although the magnitudes of the anisotropy vary, the presence of some degree of anisotropy is established.

Bouquet *et al.* [104] and Wang *et al.* [105] have both performed heat capacity measurements on MgB_2. A contribution in excess of the BCS value for was observed by both groups at low temperature ($T < 0.4T_c$). The excess falls exponentially below $T \sim 0.1T_c$ implying that low lying excitations may be present which become gapped below $\sim 0.1T_c$.

Chen *et al.* [106] performed Raman spectroscopy measurements on polycrystalline MgB_2 samples. Two pair-breaking peaks were resolved below T_c suggesting that two superconducting energy gaps exist. The energies at which the pair-breaking peaks exist correspond to the binding energy of the superconducting Cooper pairs. The lack of polarization dependence to the Raman spectra suggest that the gaps must be largely isotropic although it was pointed out that a lack of polarization dependence can also result as a consequence of strong disorder in the material. The values of the gaps are quoted as $\Delta^s = 2.7$ meV and Δ^b =6.2 meV. These values are in good agreement with values measured or implied via other techniques as discussed later in this chapter (see Table 4.2).

Electronic Raman scattering measurements were performed on MgB_2 single crystals by Quilty *et al.*[107] on two samples. They conclude that the temperature dependence of the 2Δ pair breaking peak is consistent with a conventional *s*-wave BCS superconducting gap with $2\Delta/k_BT_c = 3.96 \pm 0.09$. Structure in the Raman spectra below the 2Δ peak was observed in one crystal but was attributed to poor sample quality rather than being due to the existence of a second smaller gap.

Point-contact tunneling measurements by Szabó *et al.* [108] also interpret their results in terms of two superconducting gaps both opening at T_c showing general BCS behaviour. Two superconducting gaps are clearly resolved at low temperature which gradually broaden as the temperature is increased. The data was fit with a thermally smeared two gap Blonder, Tinkham and Klapwijk (BTK) [109] model. The two gap model allows all the tunneling data taken as a function of temperature to be fit with the same values for each of the gaps maintaining the same relative weights of each gap. The field evolution of the tunneling features at different temperatures implies the suppression of the smaller superconducting gap by the field. Zero field data at higher temperatures ($T > 30$ K), where only one tunneling feature is resolved, can be fit using only one superconducting gap but this is inconsistent with the field dependent data.

The first penetration depth measurements on MgB_2 samples appear not to agree with the general consensus reached by other measurement techniques. Measurements of the penetration depth in polycrystalline MgB_2 samples by ac-susceptibility were performed by Chen *et al.* [110]. Their measurements conclude that the superfluid density $\rho(T) \sim T^{2.7}$ from T_c and a value of $\lambda(0) \approx 1800$ Å. Panagopoulos *et al.* [111] also used ac-susceptibility along with μSR to measure the penetration depth. The conclusions reached by these techniques was a temperature dependence of $\lambda(T) \sim T^2$ and $\lambda_{ab}(0) \sim 850$ Å. The data was interpreted as being evidence for low lying excitations arising as a consequence of nodes in the order parameter of the form given by Hirshfeld and Goldenfeld [68]. Pronin *et al.* [112] also interpret their penetration depth results, as taken from complex conductivity measurements on MgB_2 thin films.

as obeying a $\sim T^2$ temperature dependence. An anisotropic s-wave order parameter was suggested as the origin of the strong temperature dependence with a possible turn over to exponential temperature dependence at low temperature due to a finite gap.

The salient features of these experiments are that MgB_2 generally shows s-wave like behaviour. Tunneling measurements have resolved what appears to be two superconducting gaps [106], [108] although this behaviour has not been observed universally [107]. Penetration depth studies, however, do not point to s-wave behaviour as a power law temperature dependence has been observed by a number of groups [110],[111],[112].

4.3 Penetration Depth in MgB_2 Samples

The first batch of MgB_2 samples measured in this study were dense polycrystallites grown by P. Timms of the Department of Chemistry, University of Bristol. The growth process involved reacting Boron powder with Mg flakes at high temperature in an Argon atmosphere. The samples were generally dark grey in colour with some light grey flakes, thought to be Mg. The penetration depth response of one of these untreated polycrystallites is shown in Fig.4.4a. The sample was found to become superconducting with T_c=38 K in agreement with the transition temperatures found in other studies (see above). The temperature dependence of the magnetic susceptibility appears to display an anomalous downturn at low temperature. The response of this sample is thought to be dominated by the normal state skin depth of the Mg flakes. The downturn at low temperature could represent the Mg becoming superconducting due to the proximity effect. In an effort to remove the Mg flakes deposited in the growth process, the sample was etched in $\sim$ 0.5% HCl in ethanol. Upon placing the sample in the etching solution, a colourless gas (likely to be Hydrogen) was seen to form at the sample surface. Once the gas evolution stopped, the sample was removed from the etching solution and rinsed in ethanol. Following the etch, the temperature

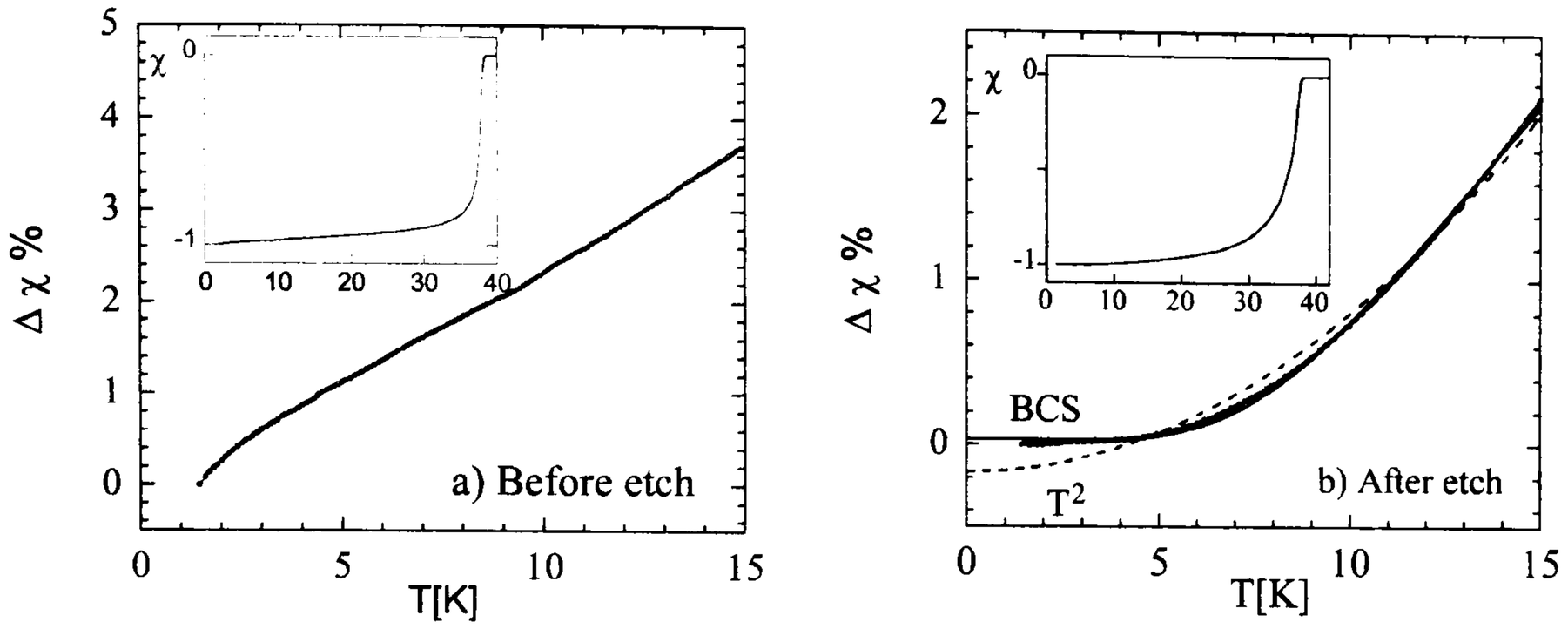

Figure 4.4: $\Delta\chi(T)\%$ for a dense polycrystalline MgB_2 sample. a) The susceptibility normalized to $\chi = -1$ for the as grown polycrystalline sample. b) The same sample after etching in $\sim 0.5\%$ HCl.

dependence of the susceptibility was found to have changed markedly as shown in Fig.4.4b.

In order to extract the penetration depth from magnetic susceptibility measurements of polycrystalline materials, certain conditions regarding the sample make-up must be met when preparing the sample (see below). For the dense polycrystalline sample, no attempt was made to obey these constrictions and so the penetration depth could not be determined. The magnetic susceptibility is still proportional to the penetration depth however, so the form of $\chi(T)$ still reflects $\lambda(T)$. The normalized susceptibility data was found to follow the BCS penetration depth behaviour for a fully gapped superconductor given in Eq.(4.1).

$$\Delta\lambda(T) \simeq \lambda(0)\sqrt{\frac{\pi\Delta_0}{2T}}\exp\left(\frac{-\Delta_0}{T}\right) \tag{4.1}$$

The susceptibility is normalized to $\chi = -1$ at the experimental base temperature (~ 1.4 K). This normalization condition does not change the value of Δ_0 yielded by the fit to Eq.(4.1). Fig.4.4b shows the BCS fit to the experimental data along with a T^2 fit. The T^2 fit was applied since this is the temperature dependence reported in other penetration depth measurements [111, 112]. It can be clearly seen that the BCS

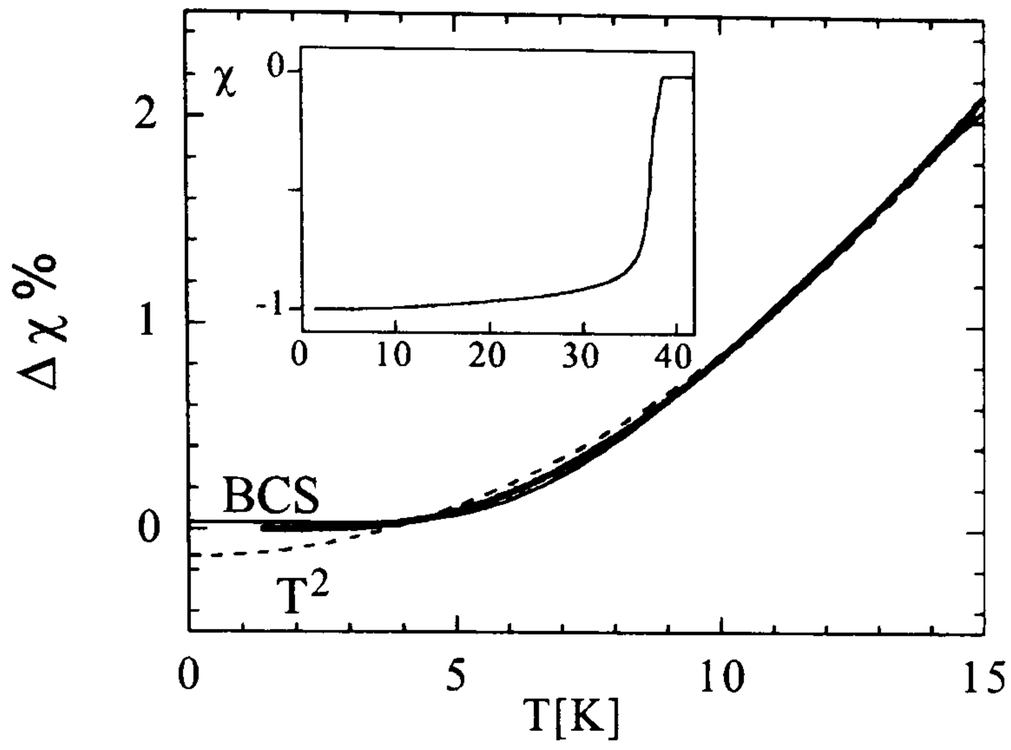

Figure 4.5: $\Delta\chi(T)\%$ for unsorted MgB_2 powder embedded in epoxy. The inset shows the transition temperature.

form fits the experimental data much better than the T^2 form. The BCS fit in Fig.4.4b yields a value of $\Delta_0 = (33 \pm 2)$ K. The uncertainty was derived from performing the fit from base temperature up to T=10 K, 12 K and 15 K and averaging the results.

Polycrystalline samples set in epoxy have been used to obtain absolute value for $\lambda(T)$ in the high T_c cuprates for many years with a large body of published work existing for the many cuprate systems (See for example Ref.[113]). The analysis involves accurately measuring the magnetic susceptibility for a sample of known grain size distribution in which the grain sizes are $\lesssim 5\lambda$ [113]. A polycrystalline test sample of unsorted commercially available (Alfa-Aesa) MgB_2 powder embedded in quick drying epoxy resin was prepared. This sample was used to investigate the superconducting properties of the commercial powder and ensure that the embedding process did not adversely affect the superconductivity of the MgB_2 powder. To prepare this sample, MgB_2 powder was cast directly into the epoxy with a mass ratio of MgB_2:Epoxy $\sim 1 : 6.5$. Fig.4.5 shows the temperature dependence of the susceptibility, again normalized to $\chi = -1$ at the base temperature. The data for the unsorted MgB_2 powder shows the same temperature dependence as the etched dense polycrystalline sample of Fig.4.4b. Fig.4.5 contains two fits to the experimental data. Again, the BCS form

fits the data much better than the T^2 fit. The BCS fit in Fig.4.5 yields a value of $\Delta_0 = (30 \pm 2)$ K. It was concluded that mixing MgB_2 powder with epoxy did not have any adverse effects on the superconductivity.

A second MgB_2 sample was prepared in order to extract $\lambda(0)$ and $\lambda(T)$. To prepare the second MgB_2 epoxy sample the raw powder was first ground in an agate mortar for ten minutes and the powder sizes sorted using a sedimentation process [114] to achieve particles of radii $\lesssim 5\lambda$. The distance that a particle of given radius will fall in a given time period can be calculated by equating the Stokes's drag force with the force on the particle due to gravity.

$$(m - m_f)g = 6\pi\eta v_t r \tag{4.2}$$

where m is the mass of the particle, m_f is the mass of displaced fluid, g is the acceleration due to gravity, η is the viscosity of the fluid and v_t is the terminal velocity of the particle in the fluid. Recalling $m = \rho V$ and $V = (4/3)\pi r^3$ and assuming that the particle reaches terminal velocity instantly such that $v_t = l/t$ gives

$$r^2 = \frac{9\eta l}{2g(\rho - \rho_f)t} \tag{4.3}$$

Values for the materials used are as follows: $\rho_{MgB_2} = 2.55\text{g cm}^{-3}$, $\rho_{acetone} = 0.78\text{g cm}^{-3}$, $\eta_{acetone} = 3.24 \times 10^{-3}\text{g cm}^{-1}\text{s}^{-1}$. The ground powder was transferred to a clean measuring cylinder, filled with acetone and shaken to ensure a uniform suspension. The suspension was left for ~1 hour and the top 5 to 10 cm decanted off and transferred to an evaporation stage. The process was repeated until enough sorted powder was collected to make a sample. Using this method, 15 mg of sorted MgB_2 was collected in 10 repetitions. The sorted powder sample contains MgB_2:Epoxy 1:5.2 by mass ($\sim$ 6% by volume). A sample of dimension $(0.76 \times 0.67 \times 0.1)$ mm^3 was cut from a larger MgB_2-epoxy composite.

To extract a quantitative value for the penetration depth from the sorted powder sample, the normalized magnetic susceptibility was calculated using [113]

$$\chi = \frac{\Delta f}{V_s\alpha - \Delta f(\frac{1}{3} - N)V_N} \tag{4.4}$$

Here $\Delta f = \Delta f_0 - \delta f$ is the sample pull out frequency shift minus the temperature dependent frequency shift due to the sample, V_s is the volume of superconductor. V_N is the volume of superconductor divided by the volume of the sample. N is the finite demagnetization factor of the composite and α is the coil calibration constant. The coil calibration constant was accurately determined to be α=217.265 kHz/mm^3 using a Pb sample of similar dimensions to the sorted epoxy sample. The sample was mounted with the measurement field applied along the long, thin axis and hence $N \approx 1$. The magnetic susceptibility is related to the magnetic penetration depth by

$$\chi = \frac{-\frac{3}{2}\sum_{i=1}^{\infty}\left(1 - \frac{3\lambda}{r_i}\coth(\frac{r_i}{\lambda}) + \frac{3\lambda^2}{r_i^2}\right) r_i^3 N_i}{\sum_{i=1}^{\infty} r_i^3 N_i} \tag{4.5}$$

Here r_i is the radius of the N_i grain. In order to relate χ to the penetration depth it is necessary to know the grain size distribution of the sample. This was measured using a JEOL JSM 6400 scanning electron microscope (SEM) at the University of Bristol. A number of images were taken of the sedimented powder. These images were digitized and a PC graphics package used to measure individual grain sizes. Each SEM image contains a calibration marker to enable the images to be used for accurate quantitative measurements. The size of the grains was measured along the longest dimension if one could be identified, although in general the grains had fairly random shapes with little elongation. No hexagonal MgB_2 crystallites were observed. As each grain was measured, a line was drawn through it on the electronic image to avoid double counting. Fig.4.6 shows the measured grain size distribution along with an SEM image of the sedimented MgB_2 powder. Inputting the grain size distribution into Eq.(4.5) and solving at each point gives $\lambda(T)$. Fig.4.7 shows the temperature dependence of the magnetic susceptibility along with the penetration depth. Fitting to Eq.(4.1), the BCS temperature dependence for a fully gapped superconductor gives $\Delta_0 = (30 \pm 2)$ K for the polycrystalline sample. The uncertainty is given by fitting the experimental data up to T=10 K, 12 K and 15 K then averaging the results.

The inset to the susceptibility data is not normalized but is derived using Eq.(4.4).

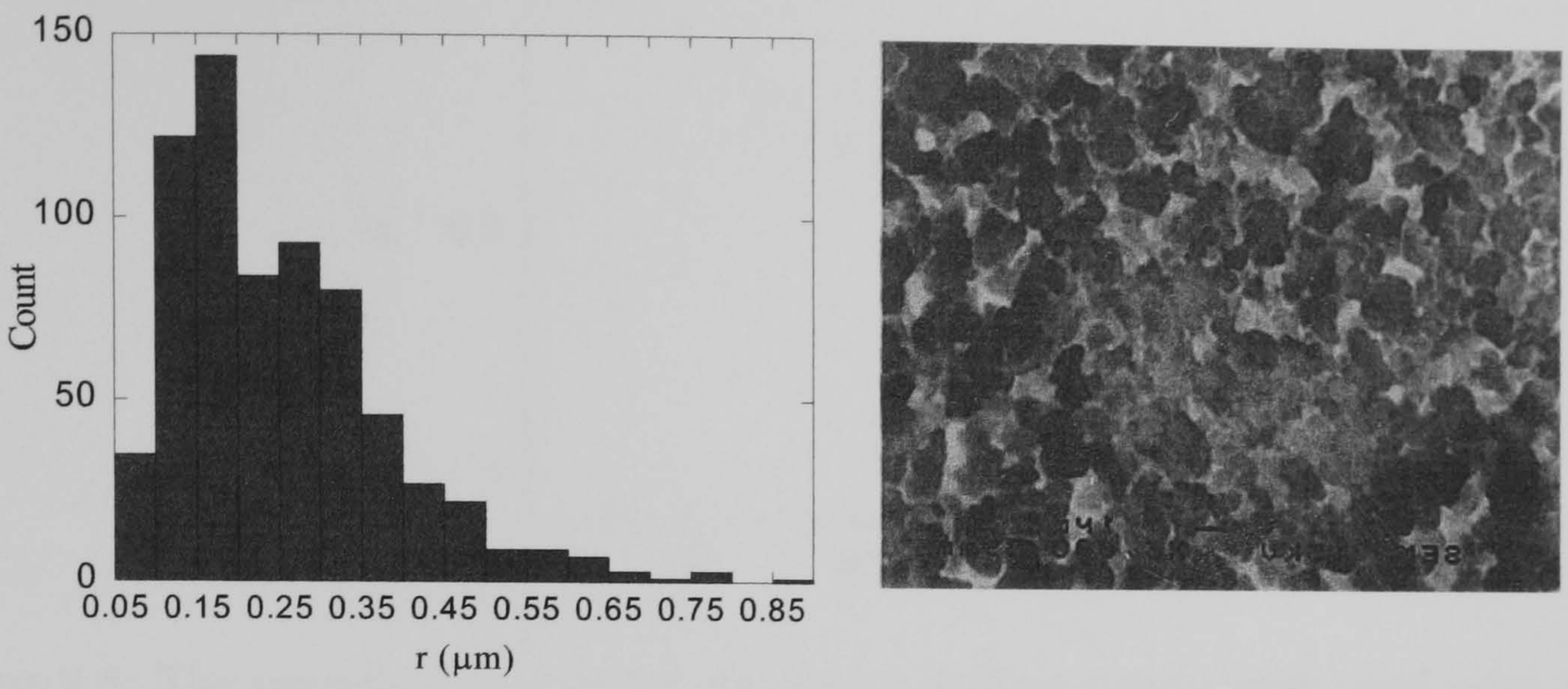

Figure 4.6: (Left image) Grain size distribution of the sedimented MgB_2 powder. (Right image) An SEM image of the powder from which some of the distribution data was taken.

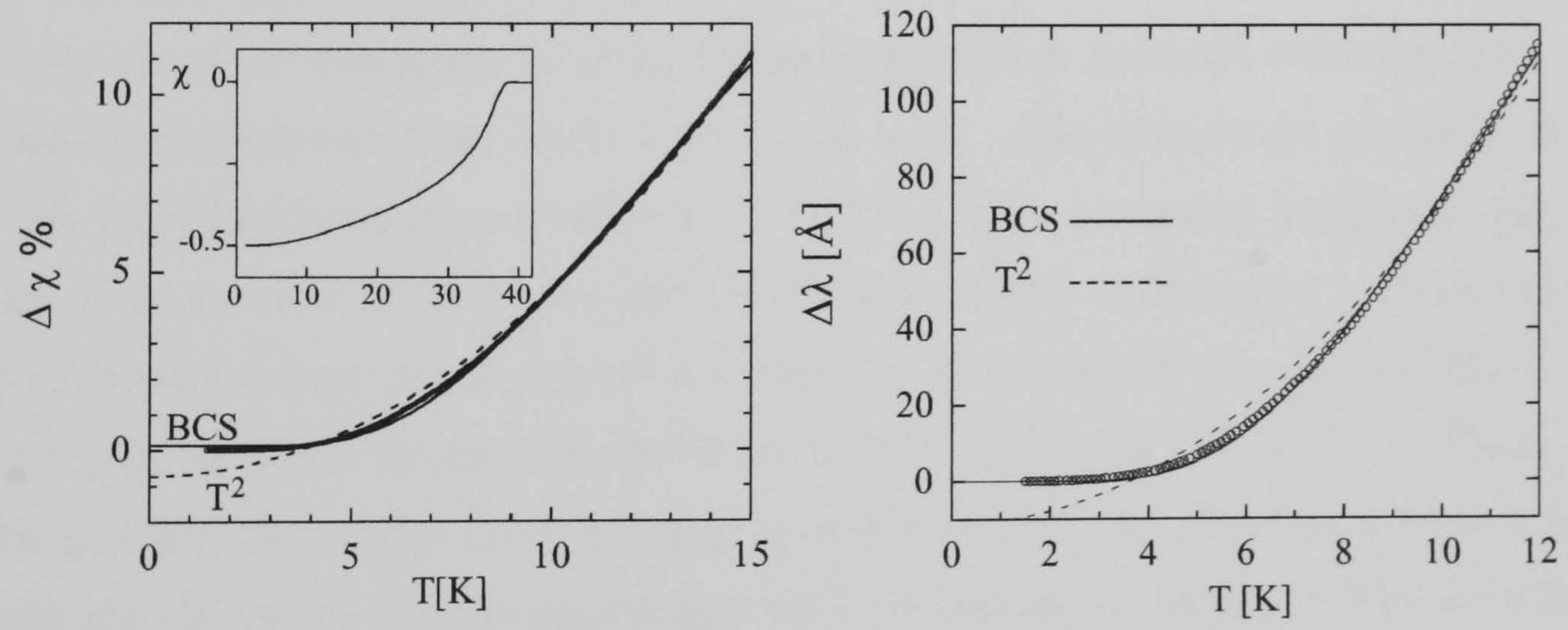

Figure 4.7: Left image: The measured magnetic susceptibility of the sorted polycrystalline MgB_2 sample as derived from Eq.(4.4). Right image: $\Delta\lambda(T)$ for the same sample calculated by solving Eq.(4.5).

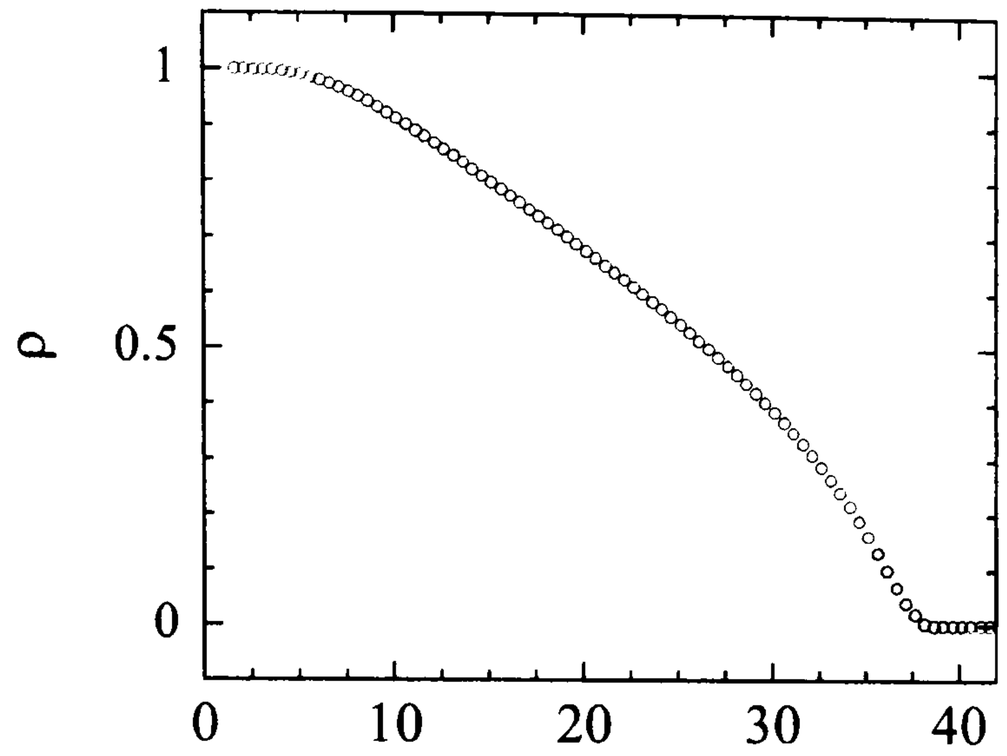

Figure 4.8: The superfluid density for the polycrystalline sample calculated using the value $\lambda(0) = 1600 \pm 200$ Å measured for this sample.

Using the absolute values for $\chi(T)$ for the polycrystalline sample yields absolute values for $\lambda(T)$. Extrapolating the data to zero temperature gives $\lambda(0) = 1600 \pm 200$ Å which is in good agreement with other studies [110, 115]. The uncertainty is derived from the uncertainty in χ_0. This value is used to calculate the superfluid density $\rho(T) = [\lambda(0)/\lambda(T)]^2$ as plotted in Fig.4.8.

Since no effort was made to align the polycrystalline samples, the measured $\lambda(0)$ contains contributions from both $\lambda_{ab}(0)$ and $\lambda_c(0)$. The anisotropy of MgB_2 single crystals [103] has been measured to be $\gamma = 2.6 \pm 0.1$. Assuming randomly oriented grains, it is possible to estimate the penetration depth component contribution to $\lambda(0)$. Although there is no general solution for the moment of a sphere when λ is anisotropic, solutions do exist in the limits $\lambda \gg r$ [116] and $\lambda \ll r$ [117]. These two limits give similar results for $\gamma \leq 3$ and to within $\pm 10\%$ the effective $\lambda(0) = 1.5\lambda_{ab}$. Combining this value for the anisotropy with the measured value of $\lambda(0) = (1600 \pm 200)$ Å, a value of $\lambda_{ab} = (1100 \pm 100)$ Å is given for the in plane penetration depth and $\lambda_c = (2800 \pm 100)$ Å. Measurements of the anisotropy performed on polycrystalline samples show $\gamma = 1.7 \pm 0.1$ [102]. Taking this value for the anisotropy gives values of $\lambda_{ab} = (1300 \pm 100)$ Å and $\lambda_c = (2100 \pm 100)$ Å.

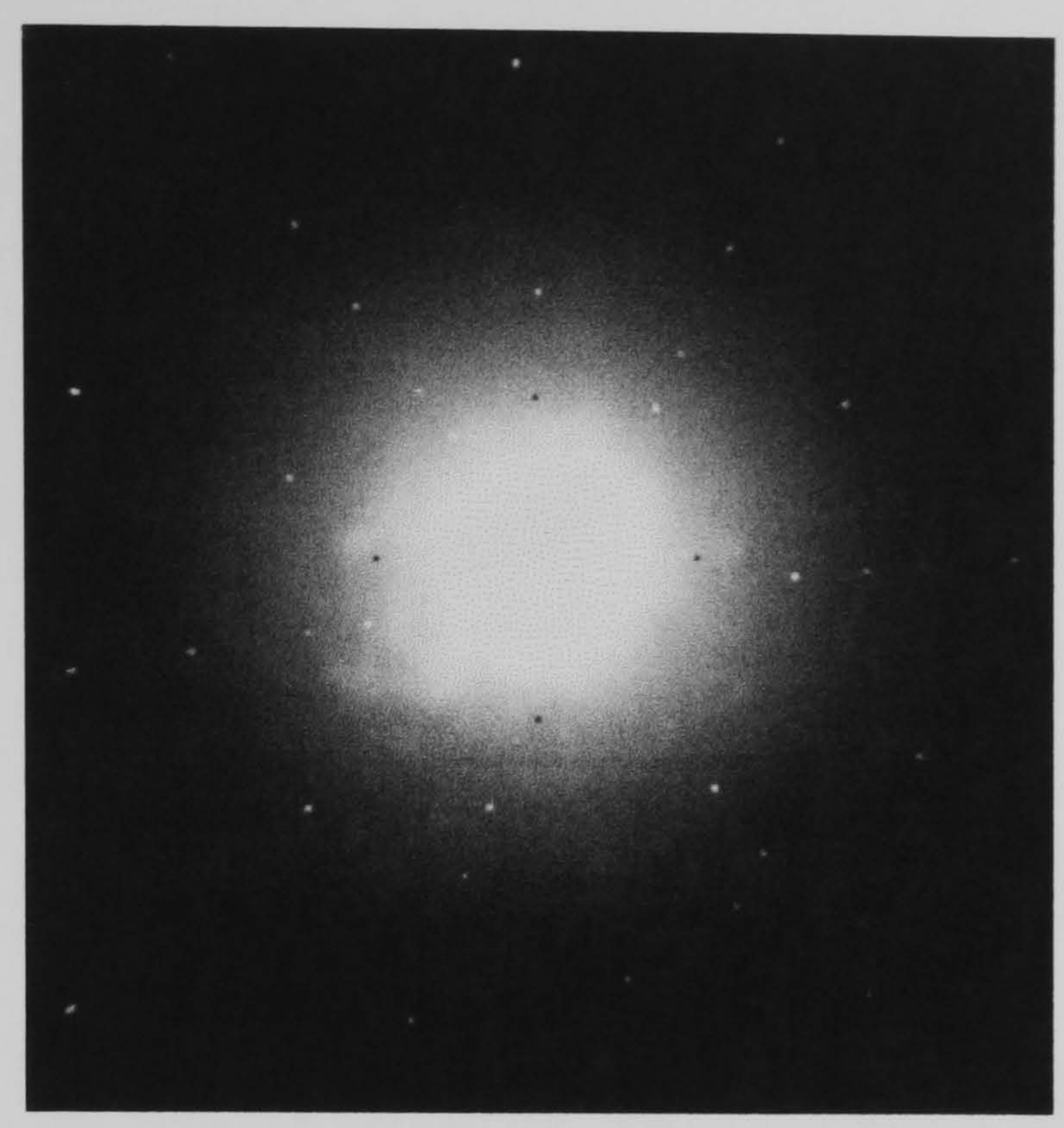

Figure 4.9: The image of an MgB_2 single crystal using an x-ray Laue camera taken by A. Carrington.

The fourth MgB_2 sample measured as part of this study was a single crystal grown by S. Lee at the University of Tokyo [103]. The single crystals were grown in a Mg-MgB_2-BN system at a pressure of 4-6 GPa at temperatures of 1400-1700°C for 5 to 60 minutes. The Mg and Mg-containing compounds catalyse the formation of MgB_2 and MgB_6 single crystals. The crystallographic orientation of the MgB_2 single crystal was established using an x-ray Laue camera by A. Carrington. Fig.4.9 shows the image contains strong regular spots indicative of well defined order in the sample.

The thin, plate-like crystal ($(0.35 \times 0.22 \times 0.1)$ mm^3) was found to have the c-axis along the smallest dimension. The method of extracting $\Delta\lambda(T)$ for single crystal MgB_2 is as described in Chapter 2. The single crystal sample was measured with the probe field applied perpendicular to the sample plane ($H \| c$) and with the probe field applied within the sample plane ($H \| a$). The $H \| c$ data was analyzed by the method discussed in Section 2.3.4 using Eq.(2.9). In the $H \| a$ orientation, the data must also be corrected for the demagnetizing factor using the inscribed ellipsoid

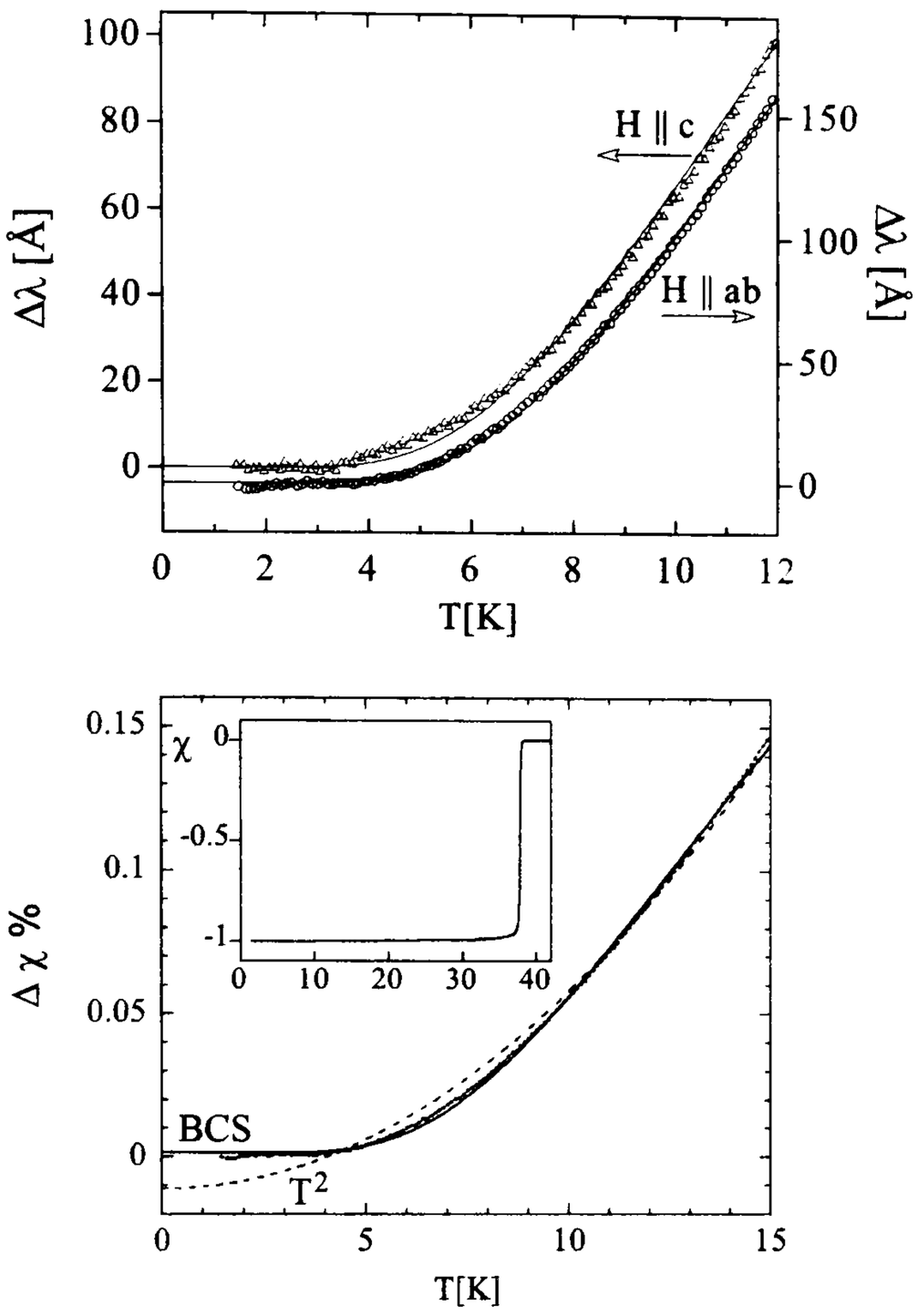

Figure 4.10: The normalized magnetic susceptibility and penetration depth for the MgB_2 single crystal. The inset to the $\chi(T)$ data shows a sharp superconducting transition. The bottom figure shows $\lambda(T)$ data with the measurement field applied perpendicular and within the sample plane.

approximation [73] as given by Eq.(2.7), since it is not in the thin limit. Fig.4.10 shows the normalized susceptibility and the penetration depth for the MgB_2 single crystal. The data taken with the measurement field applied perpendicular to sample plane only contains λ_a. The field applied within the sample plane will contain both λ_a and λ_c contributions (see Section2.3.2) with the the effective penetration depth being $\Delta\lambda_e = \Delta\lambda_a + (l_c/l_a)\Delta\lambda_c$ where l_a and l_c are the width and thickness of the sample. Fig.4.10 shows $\Delta\lambda_e \sim 1.4\Delta\lambda_a$. This difference is due to $\Delta\lambda_c$. The uncertainty in measuring the absolute values of l_a and l_c ($\sim 20\%$) means that no attempt to extract

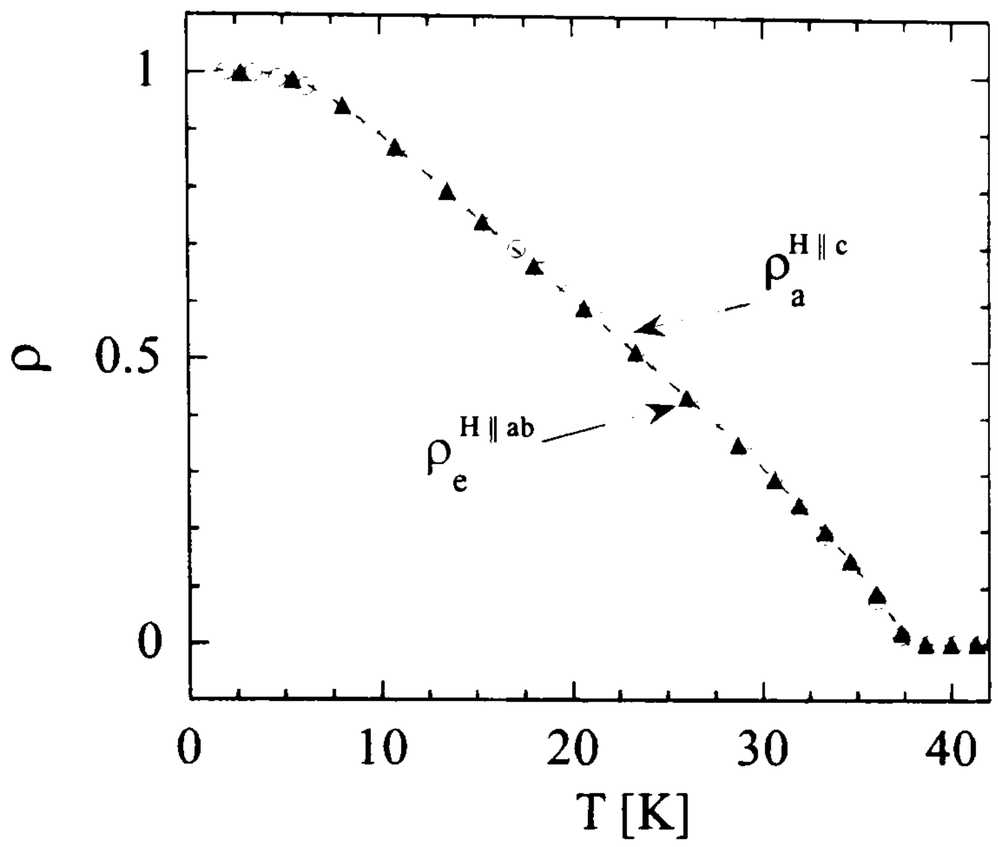

Figure 4.11: The superfluid density for the single crystal MgB_2 sample shown for both measurement orientations. (○) is the in plane superfluid density (λ_a), (▲) is the effective superfluid contribution (ρ_e) containing both ρ_a and ρ_c.

$\Delta\lambda_c$ has been made, however, the aspect ratio of (l_c/l_a)=2.2 for this crystal means $\Delta\lambda_c$ is between 1.5 and 2.5 times larger than $\Delta\lambda_a$ up to 12 K. Fitting to Eq.(4.1) gives $\Delta_0 = (29 \pm 2)$ K for λ_a $(H\|c)$ and $\Delta_0 = (32 \pm 2)$ K for the $H\|a$ orientation. Again, the uncertainties are given by fitting the experimental data up to T=10 K, 12 K and 15 K and averaging the results. Using the value of $\lambda_a(0)$=1100 Å derived from the polycrystalline sample, the superfluid density can be calculated for the $H\|c$ orientation which only contains $\lambda_a(T)$. Fig.4.11 shows the superfluid density for the single crystal in the $H\|ab$ orientation. The penetration depth in this orientation contains contributions due to both λ_a and λ_c and is referred to as λ_e. The effective superfluid density is therefore $\rho_e = [\lambda_e(0)/\lambda_e(T)]^2$. Choosing a value of λ_e=1750 Å means that ρ_e and ρ_a overlap almost exactly. This means that the two superfluid densities differ only by a scale factor, suggesting there is little anisotropy in the temperature dependence of the superfluid density.

Recent measurements using μSR by Niedermayer *et al.* [118] describe a temperature dependence to the penetration depth which agrees with the results presented

Sample	Δ_0 (K)
Dense polycrystallite	33 ± 2
Unsorted Powder in Epoxy	30 ± 2
Sorted Powder in Epoxy	30 ± 2
Single Crystal ($H \| c$)	29 ± 2
Single Crystal ($H \| a$)	32 ± 2

Table 4.1: Summary of gap values for all samples measured.

here. The penetration depth data of Niedermayer shows exponential behaviour typical of a BCS superconductor with a value of $\lambda_a(0) = 1000$ Å which agrees well with the value $\lambda_a(0) = (1100 \pm 100)$ Å presented here. Niedermayer *et al.* suggest that the $\lambda(T) \sim T^2$ observed by Panagopoulos *et al.* is not an accurate description of the penetration depth. In order to accurately interpret μSR data it is necessary to assume an ideal distribution of the flux line lattice. At low fields pinning can introduce disorder to the vortex lattice. Niedermayer observed a uniform flux line lattice only at fields $H_{ext} > 0.4$ T. They therefore conclude that the value of $H_{ext} = 45$ mT. as used by Panagopoulos, is too small to provide a uniform flux line lattice.

The results presented here consistently find an exponential temperature temperature dependence for all samples, both polycrystalline and single crystal. The results are summarized in Table(4.1)

4.3.1 Gap symmetry of MgB_2

The high transition temperature in MgB_2 has provoked much speculation as to the mechanism and the pairing symmetry of the order parameter. The main body of evidence at present points to the existence of a fully gapped superconductor however some experiments appear to have unusual features which are not entirely consistent a conventional *s*-wave superconducting gap.

Bouquet *et al.* [119] have developed a phenomenological two gap model to explain heat capacity data. The model, based on the α-model developed by Padamsee *et*

al. [120], takes two discrete superconducting gaps Δ_1 and Δ_2 which both close at a common T_c as fitting parameters, with the relative weight of the gaps as a third fitting parameter. Although the model is phenomenological in origin. the notion of different gaps being situated at different zones on the Fermi surface was suggested in bandstructure calculations [101]. The larger gap Δ^b is associated with the 2-dimensional sheets centred around the Γ point on the Fermi surface. The smaller gap Δ^s is associated with the 3-dimensional bands (see Fig.4.2). In order to relate the model to the penetration depth data presented here the superfluid densities due to each gap are calculated and summed giving the total superfluid response. The measured superfluid response can therefore be fit to give values for the gaps and their corresponding relative weights. Fits to the superfluid density, $\rho(T)$, where performed by A. Carrington. The superfluid density due to each superconducting gap is given by

$$\rho = 1 - \int_{-\infty}^{\infty} \frac{\partial f(E)}{\partial E} \frac{E}{\sqrt{E^2 - \Delta^2}} dE \tag{4.6}$$

where $f(E)$ is the Fermi function. At low temperature the superfluid density will be dominated by the smaller of the two gaps. The value for the gap yielded by fits to the penetration depth data at low temperature will therefore correspond to the smaller gap. The BCS temperature dependence of the gap is given by

$$\frac{1}{N_0 V} = \int_0^{\hbar\omega_c} \frac{\tanh\left(\frac{1}{2T}(E^2+\Delta^2)^{\frac{1}{2}}\right)}{(E^2+\Delta^2)^{\frac{1}{2}}} dE \tag{4.7}$$

Eq.(4.7) can be solved numerically to give the temperature dependence of the gap. Using the gap value yielded from fits to Eq.(4.1), the superfluid density contribution from the small gap can be calculated. The total superfluid density response is given by $\rho_{tot} = x\rho_b - (1-x)\rho_s$ where x is the relative weight of each gap. The experimentally yielded superfluid density, which contains contributions from both superconducting gaps, can be fit to yield the temperature dependence of the larger superfluid gap. The zero temperature value of the larger gap (Δ^b) is a fitting parameter along with the relative weight of each gap, x.

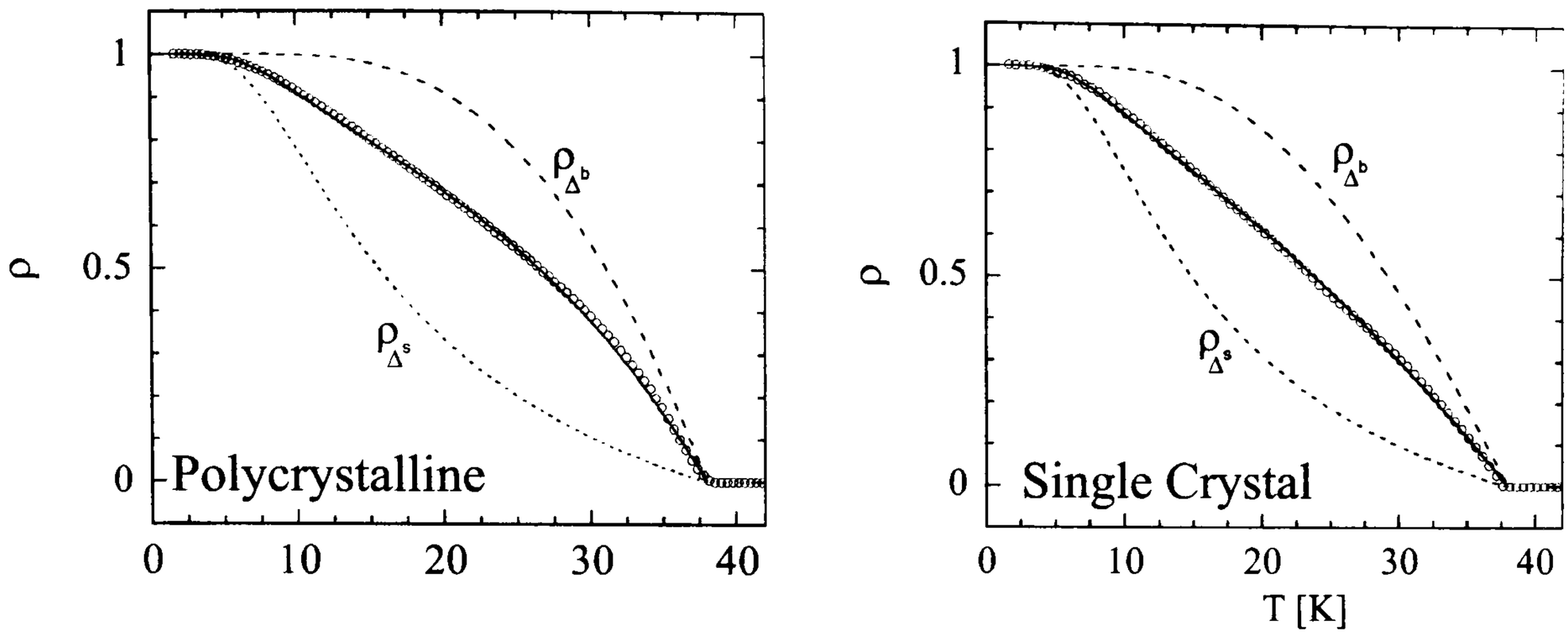

Figure 4.12: The superfluid density for the polycrystalline and single crystal MgB_2 samples can be fit using superfluid densities derived from two gaps. The solid line is the calculated superfluid response by summing the two separate superfluid densities.

Fig.4.12 shows the superfluid response due to the larger gap having become temperature independent below ~15 K. The value of Δ_0 from fits to Eq.(4.1) will therefore be equal to Δ^s. Fixing this value means only two fitting parameters are necessary, the value of the larger gap (Δ^b) and the ratio of their relative weights (x). The quality of the fits to the data is extremely good for both samples. For the polycrystalline sample Δ^s=30 K and Δ^b=89 K with a relative proportion of 40:60. The in-plane single crystal data gives values Δ^s=29 K and Δ^b=75 K with relative proportion 45:55. Bouquet *et al.* have applied this model to heat capacity data taken by several groups and also compare their results to findings of other experiments. Table 4.2 shows values calculated using the two gap model for specific heat data. Also included is a summary of values as derived via other methods. It can be seen that the values for the two gaps as derived from other experiments agree with the data presented here to within ±20% providing strong evidence for this phenomenological theory.

Haas and Maki [125] have proposed an alternative to the two gap model. In this

Technique	Δ^b (K)	Δ^s (K)	x:(1-x)	Ref.
Specific Heat	84	23	55:45	[104]
Specific Heat	72	25	50:50	[105]
Specific Heat	74	25	50:50	[121]
Raman	70	30	N/A	[106]
Photoemission	68	21	N/A	[122]
Tunneling	86	36	N/A	[123]
Point-contact spectroscopy	78	32	N/A	[108]
Point-contact spectroscopy	80	19	N/A	[124]
Bandstructure	76	25	53:47	[101]
μSR	68	30	~50:50	[118]

Table 4.2: Summary of gap values for the 2 gap model. Table adapted from [119].

model a single anisotropic s-wave gap is proposed. The gap has a k-dependence

$$\Delta(z) = \Delta \frac{(1 + az^2)}{(1 + a)} \tag{4.8}$$

where z is the cosine of the angle with respect to the c-direction and a is a fitting parameter which defines the anisotropy. The temperature dependence of the anisotropic gap is given by numerically solving

$$\frac{1}{N_0 V} \int_0^1 f(z)^2 dz = \int_0^1 \int_0^{\hbar\omega_c} f(z)^2 \frac{\tanh\left(\frac{1}{2T}\left(E^2 + \Delta(z)^2\right)^{\frac{1}{2}}\right)}{\left(E^2 + \Delta(z)^2\right)^{\frac{1}{2}}} dE dz \tag{4.9}$$

The superconducting gap is related to the superfluid density by

$$\Delta\rho_a = -6 \int_0^1 \int_{\Delta(z)}^{\infty} \frac{df(E)}{dE} \frac{E}{\left(E^2 - \Delta(z)^2\right)^{\frac{1}{2}}} z^2 dz dE$$

A fit to ρ_a for the single crystal data gives Δ/T_c=0.75. In order to fit this observed ratio a value of $a = 2.2 \pm 0.4$ is needed. The corresponding total gap anisotropy is $(1+a)$=3.2 ± 0.4. The calculated temperature dependence of ρ_a using this model is shown in Fig.4.13. The shape of $\rho_a(T)$ is dependent on the value of $\lambda_a(0)$ used. Choosing a value of $\lambda_a(0)$ ~650 Å will indeed cause the measured $\rho_a(T)$ to overlap the calculated $\rho_a(T)$ for the anisotropic gap model. This value for $\lambda_a(T)$ is almost

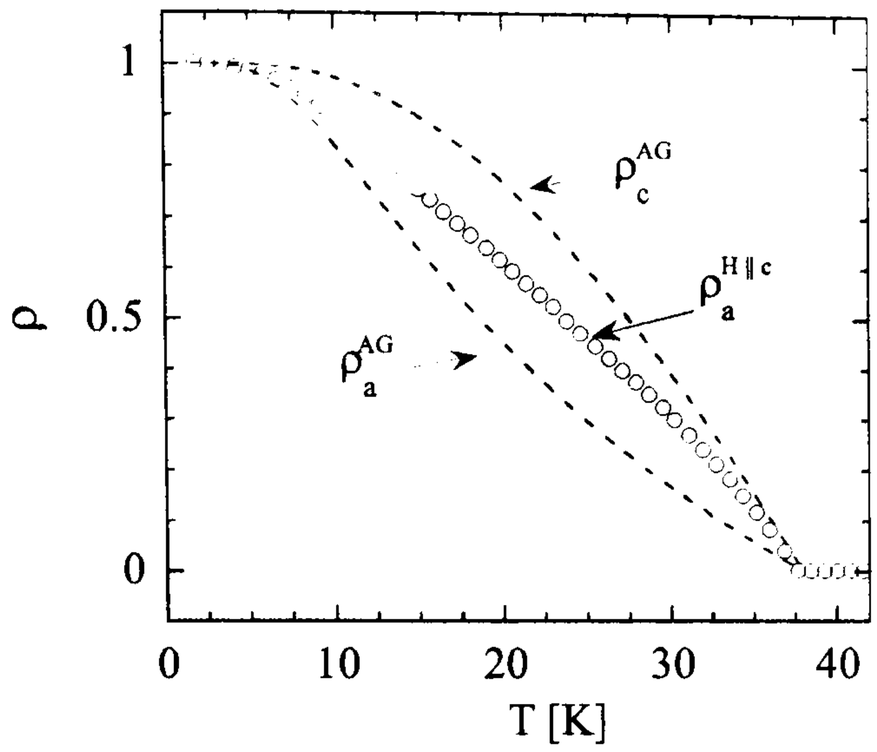

Figure 4.13: The superfluid density as calculated by the anisotropic gap model [125] compared to the experimental data.

a factor 2 below our estimate for $\lambda_a(0)$ and smaller than $\lambda_a(0)$ derived from other measurements [110, 111, 112, 118]. The penetration depth data presented here clearly do not agree with this theory.

4.4 Summary

The symmetry of the superconducting order parameter has been studied in MgB_2 samples of varying quality. The temperature dependence of the magnetic susceptibility has been seen to follow exponential behaviour of the BCS form. The first sample measured was a dense polycrystallite. Fits to the BCS expression, for the change in penetration depth due to thermally excited quasiparticles, for a fully gapped superconductor yield values for the gap $\Delta_0 = 33 \pm 2$ K for this sample. The second sample measured was made from commercially available MgB_2 powder cast into quick setting epoxy resin. This sample also displayed an exponential temperature dependence to the magnetic susceptibility which yielded a gap value of $\Delta_0 = 30 \pm 2$ K. A further epoxy sample was prepared again using commercially available powder. Prior to casting into epoxy, the powder was ground and then sorted using a sedimentation technique to achieve particles of grain size $\lesssim 5\lambda$ allowing absolute values for the penetration depth to be derived for this sample. Extrapolating the exponential temperature dependence of the sample to zero temperature lead to a value $\lambda(0) = 1600 \pm 200$ Å with a superconducting gap of $\Delta_0 = 30 \pm 2$ K, the same gap value as for the unsorted sample. The effective penetration depth of the randomly oriented grains was estimated to be $\lambda(0) = 1.5\lambda_a(0)$ giving a value of $\lambda_{ab}(0) = (1100 \pm 200)$ Å.

The temperature dependence of a MgB_2 single crystal was also measured. The sample was measured with the excitation field applied perpendicular to and within the sample plane. The data again fitted the BCS penetration depth behaviour very well giving values for the superconducting gap of $\Delta_0 = (29 \pm 2)$ K for λ_{ab} and $\Delta_0 = (32 \pm 2)$ K for the probe field applied within the sample plane which yields a penetration depth with some c-axis contribution. The data from all samples was found to follow an exponential temperature dependence which is strong evidence for a fully gapped order parameter. The measured zero temperature values of the penetration depth were used to calculate the superfluid density for the sorted powder epoxy sample and the single crystal. The superfluid density data was discussed in terms of a phenomenological two gap model. It was shown that the superfluid density data could be fit to the two

gap model yielding values for each superconducting gap which agreed well with data from other experiments fit either to the same phenomenological model or where two gaps were measured directly.

An anisotropic s-wave theory was also fit to the data. Although this theory could fit the superfluid density data by choosing a suitable value for $\lambda(0)$, this fitting value was much smaller than the measured value by a factor 2, well outside the experimental uncertainty.

Chapter 5

Significance of Chain Superconductivity in $YBa_2Cu_4O_8$

5.1 Introduction

The original motivation for performing penetration depth measurements on $YBa_2Cu_4O_8$ (Y124) single crystals was the possibility of observing Andreev boundstates (ABS). Zero energy ABS can form at the surfaces of *d*-wave superconductors due to the π-phase shift in the order parameter. Since the Y124 system is structurally very similar to that of $YBa_2Cu_3O_7$ (Y123) it was assumed that Y124 would be a natural candidate for ABS to occur. As will become apparent in Section5.4 evidence for ABS formation was not found but a further interesting feature was observed in the temperature dependence of the penetration depth. A rapid *decrease* in $\Delta\lambda(T)$ was observed consistently at low temperature in all samples measured. The change in emphasis of the experimental goal is apparent in that a large amount of time was originally dedicated to investigating any possible ABS presence in the system rather than the origin of the penetration depth down-turn. To this end measurements were initially performed on Y124 samples with shapes that would yield a strong ABS contribution in a Y123 system. The reason for the lack of ABS is not known but could be attributed to non-specular scattering occurring at rough sample surfaces or disorder at

the surface. The final measurements focused on samples with more uniform edges. The first of these samples was similar in shape to those used by Hussey *et al* [126] in thermal conductivity measurements. The second sample was rectangular but again with optically smooth surfaces. This chapter will focus mainly on these two samples and reveal the large differences that exist between the penetration depth behaviour in the Y124 and Y123 systems. The reader is asked to regard this chapter as a platform for further work which highlights the interesting physics of the Y124 system rather than a completed work with definite conclusions.

5.2 Review of $YBa_2Cu_4O_8$

Y124 was initially discovered as a planar defect in a Y123 single crystal [127, 128]. $YBa_2Cu_4O_8$ (Y124) is a naturally underdoped [129] stoichiometric cuprate similar in structure to $YBa_2Cu_3O_7$ (Y123) with $T_c \sim 80$ K some 10 K less than optimally doped Y123. Y124 contains 2 CuO chains running along the b-axis of the crystal in a similar fashion to the single CuO chains present in Y123. Since the Y124 compound is a clean naturally underdoped system, it has been used extensively to study the pseudogap properties of underdoped cuprates [22]. Y124, in contrast to underdoped Y123, displays 2 temperature scales during the opening of the pseudogap. At the upper cross over temperature T^0 the Knight shift changes from being temperature independent to decreasing linearly in T [31]. At the second cross over temperature T^* the Knight shift decreases faster than linear in temperature. Although the upper and lower cross over temperatures occur in compounds which demonstrate pseudogap behaviour, it is thought that the two temperatures arise from different, competing effects.

Thin, needle like, single crystals of Y124 were grown by Adachi *et al.* at the University of Tokyo using a self-flux method in a high pressure gas mixture as described in [130]. The a-axis component of resistivity $\rho_a(T)$ is due solely to the 2 dimensional CuO_2 planes. The b-axis component of resistivity $\rho_b(T)$ contains a contribution from

the 1 dimensional CuO chains as well as from the 2 dimensional CuO_2 planes. Hussey *et al.* [18] have measured the resistivity along each of the crystal axes up to 450 K. $\rho_a(T)$ varies essentially linearly from 450K with no obvious deviation in $d\rho_a(T)/dT$ at T=160-180 K which is the temperature range attributed to the opening of the pseudogap which removes the spin scattering channel in $\rho_a(T)$ [30]. The ratio of $\rho_a/\rho_b \approx 6$ with ρ_b being lower than ρ_a due to the presence of the chains. The resistivity along the *b*-axis was modelled as being due to the resistivity of the CuO_2 planes added in parallel to the resistivity of the CuO chains. By attributing all of the resistivity along the *a*-axis to the CuO_2 planes, the chain resistivity can be identified. The chain contribution to the resistivity was seen to follow $\rho_{chain}(T) = \rho_0 + AT^2$ indicative of itinerant electrons with Fermi liquid character. The chain contribution did not deviate from T^2 between 450 K and T_c indicating that no normal state gap is associated with the chains. Hussey *et al.* therefore conclude that the presence of a pseudogap is associated with the CuO_2 planes rather than the CuO chains. The extrapolated residual resistivity was determined to be $\rho_0 = 0.5\mu\Omega$cm. This very small value is indicative of negligible disorder/oxygen vacancies along the chains since 1 dimensional systems are very sensitive to disorder. $\rho_c(T)$ was identified to be significantly different to that observed in other underdoped cuprates. Underdoped Y123 shows non-metallic *c*-axis resistivity below T^*, the temperature at which the pseudogap opens. Y124 shows a cross over from incoherent *c*-axis resistivity to metallic behaviour, implying three dimensional conductivity, with decreasing T [18].

Further transport measurements by Hussey *et al.* [126] have identified unusual behaviour for the in-plane thermal conductivity in Y124. As discussed in Section 1.5. the prediction by Lee [49] of universal conductivity and its subsequent observation by Taillefer *et al.* [50] in Y123 was strong evidence for superconductivity with $d_{x^2-y^2}$ symmetry in this material. The observation of universal conductivity indicates the presence of nodal quasiparticles for negligibly small levels of disorder. Low temperature thermal conductivity [126] shows a T^3 dependence which extrapolates to zero at $T = 0$ attributed to phonon thermal conductivity. The linear $\kappa(T)$ term witnessed

in optimally doped Y123 and $Bi_2Sr_2CaCu_2O_8$ [131] was not seen in Y124. Hussey *et al.* suggest that quasi-particle localization removes the residual quasi-particle contribution from the low temperature thermal conductivity.

5.3 Chain Contribution to Superfluid Density

Penetration depth measurements on Y124 give values of $\lambda_a(0) = 2000$ Å [89], $\lambda_b\,(0) = 800$ Å (by Far Infra Red spectroscopy) [89] and $\lambda_c(0) = 6150$ Å (from AC susceptibility) [132]. Measurements on Y123 have identified power law behaviour for all components of the penetration depth, indicative of low energy quasi-particle excitations due to nodes in the gap. It has been shown theoretically that for weakly coupled CuO_2 planes, disorder can cause λ_c to follow T^2 without disrupting the linear temperature dependence of λ_a and λ_b [90, 96]. Panagopoulos *et al.* [132] measured the penetration depth of magnetically aligned polycrystalline Y124 samples using ac-susceptometry. The polycrystalline nature of the samples meant that it was not possible to distinguish the in-plane penetration depth components λ_a and λ_b and so an average value of the two were measured with $\lambda_{ab}(0) = 1300 \pm 200$ Å. Panagopoulos *et al.* observed a $\sqrt{T}$ temperature dependence to $\lambda_{ab}(T)$ and $\lambda_c(T)$ in agreement with data taken much earlier [133, 134] which also hinted at a distinctive rise in superfluid density at low temperature. The power law that the superfluid density follows usually reflects the energy dependence of the density of states at the node [60, 90]. A $\sqrt{T}$ dependence to the penetration depth represents a deviation from the linear in T behaviour associated with $d_{x^2-y^2}$ pairing symmetry.

NMR relaxation time T_1 [135] measurements on optimally doped Y123 identified a gap on the CuO chains below T_c implying that normal electrons are coupled into the superfluid density. With this in mind Xiang and Wheatley [90] investigated the superfluid anisotropy observed in Y124 ($\rho_b/\rho_a \simeq 6$) and optimally doped Y123 ($\rho_b/\rho_a \simeq 2$) [89] theoretically. Two models are proposed to explain the observed superconductivity on the CuO chains. A proximity model coupling the CuO chains

and CuO_2 planes through single electron tunneling was considered along with a pair tunneling mechanism whereby the chains and planes are coupled through Josephson like Cooper pair tunneling. For both models the superfluid response is dominated by quasi-particle excitations about the quasi 2 dimensional chain and plane Fermi sheets.

The proximity model uses a mean field Hamiltonian.

$$H = H_0 + H_1 \tag{5.1}$$

$$H_0 = \sum_k \left[\sum_n \varepsilon_{nk} c^\dagger_{nk\sigma} c_{nk\sigma} + \varepsilon_{\perp k} (c^\dagger_{1k\sigma} c_{2k\sigma} + \text{H.c}) \right] \tag{5.2}$$

$$H_1 = \sum_{nk} \Delta_n \gamma_{nk} (c^\dagger_{nk\uparrow} c^\dagger_{n-k\downarrow} + \text{H.c}) \tag{5.3}$$

The sum over n is over the plane ($n = 1$) and chain ($n = 2$) bands. ε_k is the energy of the single particle tunneling excitation given by $\varepsilon_{1k} = -2t(\cos k_a + \cos k_b) - \mu$. and $\varepsilon_{2k} = -2t_c(\cos k_b + \cos k_a) - \mu + \varepsilon_c$. μ is the chemical potential and ε_c is the relative energy between chains and planes. $\varepsilon_{\perp k} = -2t_\perp \cos(k_c/2)$ is the single electron hopping matrix element. The energy scale of ε_{1k}, ε_{2k} and $\varepsilon_{\perp k}$ are set by the values of the hopping constants t for the plane, t_c for the chain and $t_\perp$ the inter-layer hopping constant. $t_\perp$ is set much smaller than t and t_c to reflect the physical situation where interlayer hopping is less likely than intralayer of chain-layer hopping. Δ_n are the self consistent gap equations of the planes or chains and the pairing strength of these can be varied.$\Delta_2 = 0$ would correspond to a situation where the chain layer is intrinsically non-superconducting and the superconductivity in the chain is solely due to the proximity effect. γ_n represents the symmetry of the gap e.g. $\gamma_1 = (\cos k_b - \cos k_a)/2$ represents a $d_{x^2-y^2}$ symmetry gap on the plane band. Coupling between chains and planes is via single electron inter-layer hopping. The proximity model finds that the modification of the superfluid density in the a-direction due to chain hybridization is small and the temperature dependence is approximately the same as a pure 2 dimensional system with planes and chains decoupled. The temperature dependence of the superfluid density for the plane, $\rho_a(T)$, is linear at

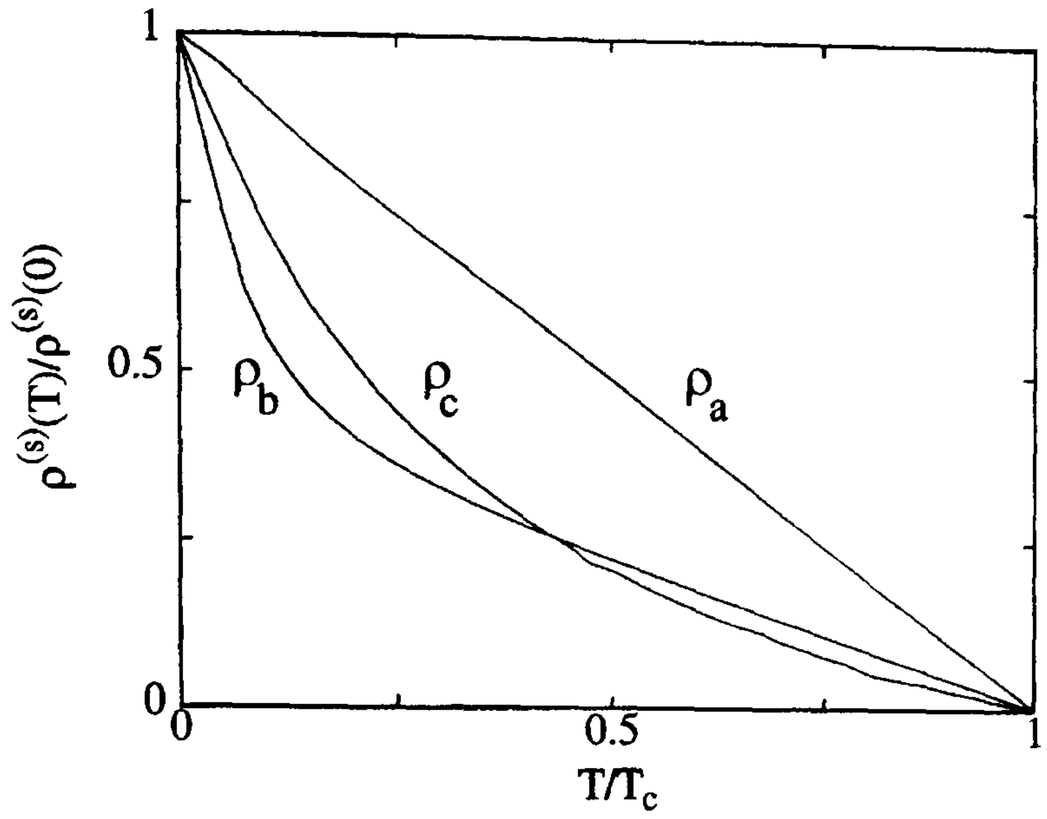

Figure 5.1: Calculated superfluid densities using the proximity model from [90].

low T for a planar gap with $d_{x^2-y^2}$ pairing symmetry. Along the b-direction the chain contribution becomes important. Close to T_c, $\rho_b(T)$ is dominated by the plane band and will follow the same power law dependence as $\rho_a(T)$. With no gap on the chains, the superfluid density along the b-direction $\rho_b(T)$ would behave as $\sqrt{T}$. This behaviour is inconsistent with the behaviour in optimally doped Y123, which also contains CuO chains, but may reflect the behaviour in Y124. For a situation with gaps on both the planes and chains the temperature dependence of the superfluid densities $\rho_a(T)$ and $\rho_b(T)$ may be linear in temperature when $T \ll (|\Delta_2|, |\Delta_1|)$ but for $|\Delta_2| \ll T \ll |\Delta_1|$ the upward curvature persists. For finite Δ_2 and $T \ll \Delta_2$ calculations show $\rho_c(T) \sim T^2$. The conclusion reached by Xiang and Wheatley was that although the single particle tunneling could describe the temperature evolution of ρ_a, it could not describe $\rho_b(T)$ and $\rho_c(T)$ for optimally doped Y123.

The second model considered by Xiang and Wheatley was developed using a formalism originally proposed by Wheatley, Hsu and Anderson [136]. This model uses the same kinetic energy term (H_0) in the Hamiltonian as the single electron tunneling model. The single electron tunneling potential term (H_1) is replaced with

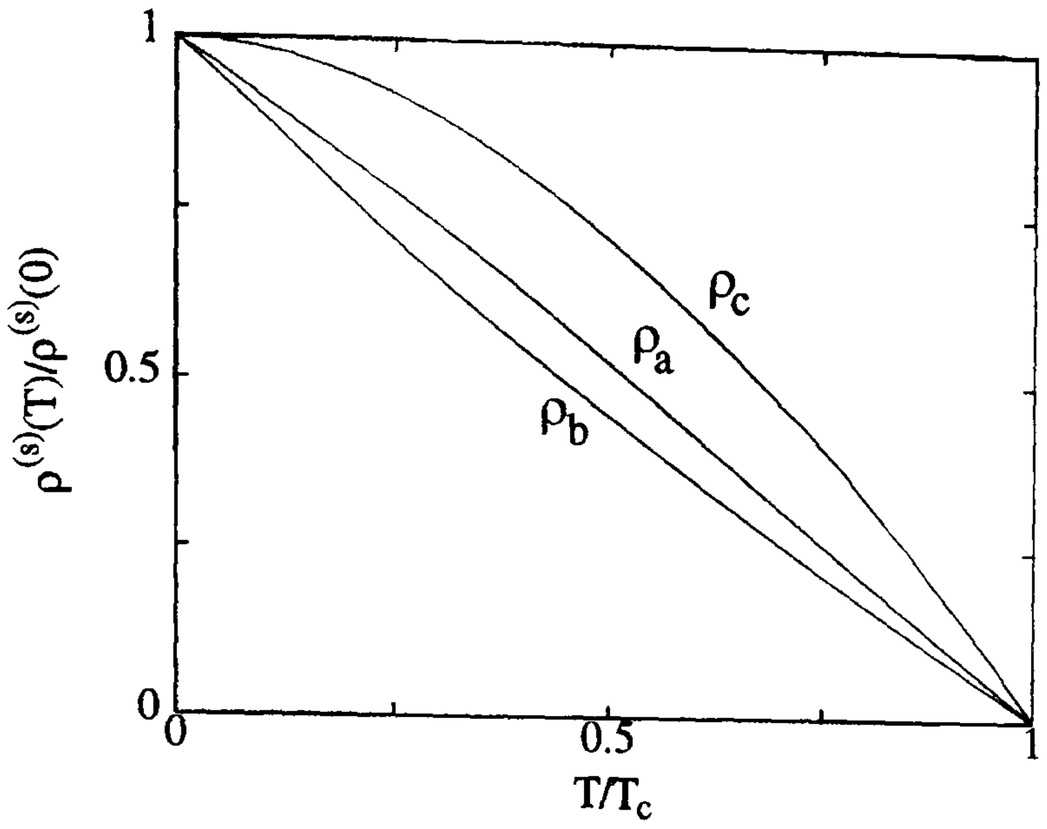

Figure 5.2: Calculated superfluid densities using the interlayer pair tunneling model from [90].

a singlet pair tunneling potential term

$$H_I = -\frac{\lambda}{4} \sum_{r,\delta=\hat{a},\hat{b}} (\hat{\Delta}^{\dagger}_{1,r,\delta} \hat{\Delta}_{2,r+\hat{c}/2,\delta} + \hat{\Delta}^{\dagger}_{1,r,\delta} \hat{\Delta}_{2,r-\hat{c}/2,\delta} + \text{H.c}) \tag{5.4}$$

where $\hat{\Delta}_{n,r,\delta}$ is the singlet pair operator. The pair tunneling model has the requirements that the plane and chains must have pairing functions of the same symmetry e.g. both s or d, if the admixture of s and d components is weak. If the two order parameters are set with different symmetries the only self consistent results to the mean field Hamiltonian is the trivial case of $\hat{\Delta}_n = 0$ i.e. no tunneling. The second constraint is that the superconductivity that exists on the chains and planes is not independent but that the gap parameters are linked. The ratios of the superfluid densities at zero temperature are determined by the ratios of the hopping constants. ρ_b/ρ_a is determined by t_c/t, and ρ_b/ρ_c is given by $t_\perp/t$. Fig.5.2 shows calculated values for $\rho_a(T)$, $\rho_b(T)$ and $\rho_c(T)$. The parameters were chosen such that the ratios of the superfluid densities correspond to experimental values for optimally doped Y123. The temperature dependencies of $\rho_a(T)$ and $\rho_b(T)$ in Fig.5.2 can be seen to be very similar. The low temperature behaviour of the superfluid density is approximately linear in temperature. The temperature dependence of $\rho_c(T)$ is varying as

approximately T^2.

The effective electron concentration on the chains can be changed by varying ε_c. By increasing ε_c the effective electron concentration on the chains is decreased in the model. As the electron concentration on the chains is reduced, the difference between $\rho_a(T)$ and $\rho_b(T)$ decreases but $\rho_c(T)$ remains different. This behaviour is in general agreement with previous doping dependence studies of the penetration depth [137].

5.4 Penetration Depth Measurements in $YBa_2Cu_4O_8$ Single Crystals

5.4.1 In Plane Penetration Depth in $YBa_2Cu_4O_8$

As stated in the introduction to this chapter, the initial motivation for measuring the magnetic penetration depth in high quality $YBa_2Cu_4O_8$ (Y124) single crystals was to observe Andreev boundstates forming at the surfaces. To this end five single crystals were measured with the measurement field applied perpendicular to the *ab*-plane of the samples. All samples displayed $T_c \sim 80$ K with a typical width of ~ 0.5 K. This is the measurement orientation in which ABS have been observed in $YBa_2Cu_3O_{7-\delta}$ (Y123) and $Bi_2Sr_2CaCu_2O_{8+\delta}$ single crystals (see Chapter 3). Fig.5.3 shows the measured magnetic penetration depth response of five Y124 single crystals. In this orientation the sample calibration is performed using the analytical method as described in Chapter 2. The calibration constant for each sample is given by Eq.(2.11). The sample dimension used in this equation is given by $R = w/5$ in the thin limit, where w is related to the surface area (A) of the crystal by $A = 4w^2$. Table 5.1 shows the dimensions of each sample and the surface area used in the sample calibration. The change in penetration depth for each sample is given in Table 5.1. Data by Panagopoulos *et al.* [132], shown in the inset of Fig.5.4, shows $d\lambda_{ab}(T)/dT = 10.5$ Å/K. A general decrease in the penetration depth can be seen which follows a power law T^x with $x \sim 1/2$. This temperature dependence continues

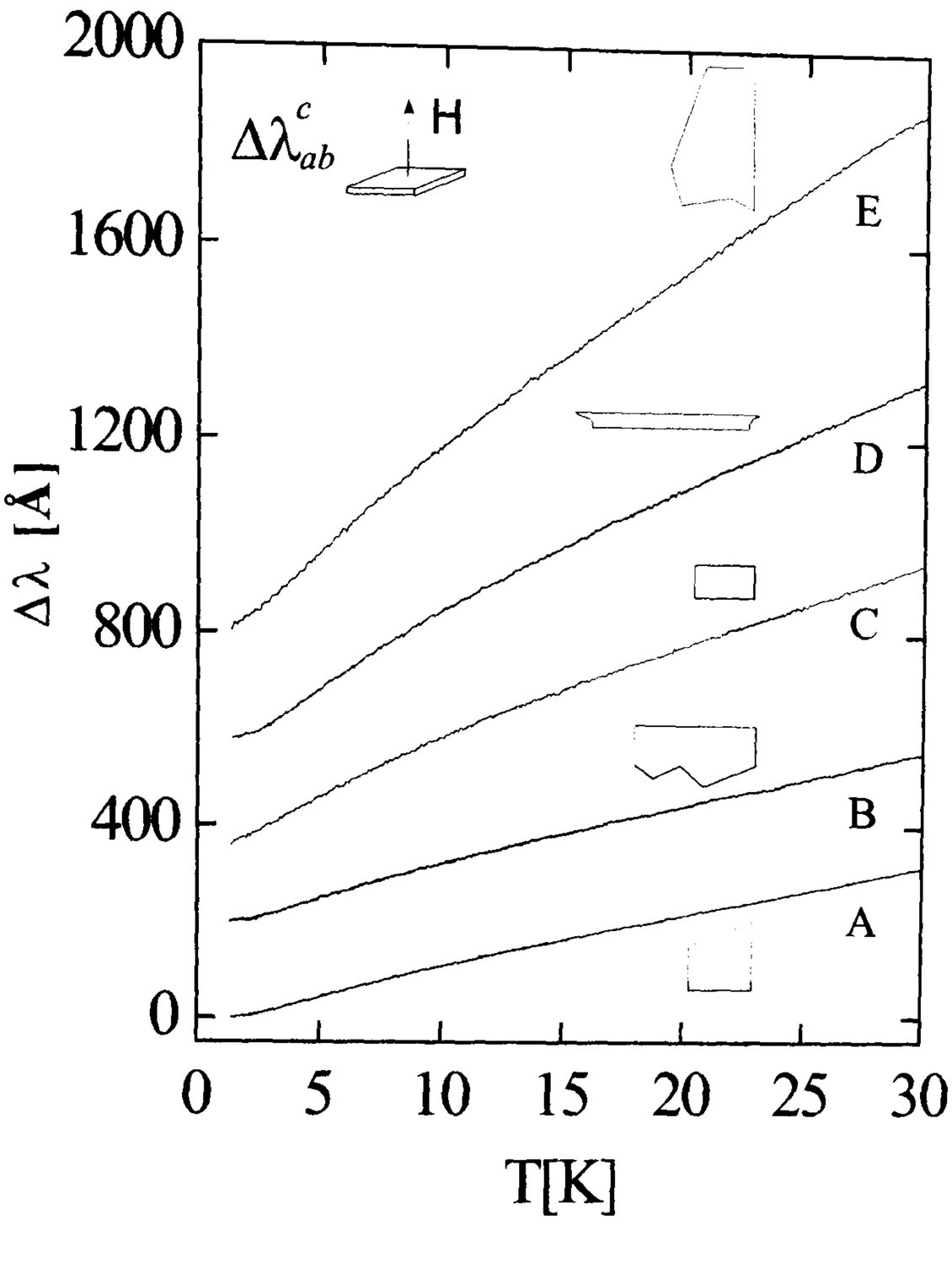

Figure 5.3: Penetration depth measurements on five $YBa_2Cu_4O_8$ single crystals offset from one another. A down-turn in the temperature dependence of the penetration depth is observed in all samples. The outline of each sample is displayed next to the corresponding curve.

Sample	Max length (μm)	Max width (μm)	Area ($\times 10^{-9}$ m^2)	$d\lambda_{ab}/dT$(Å/K)
A	279.3	176.4	44.0	(10.1±0.1)
B	205.8	191.2	36.1	(11.4±0.1)
C	235.2	139.7	32.9	(17.8±0.2)
D	95.6	469.3	44.0	(23.4±0.3)
E	323.4	198.5	54.2	(34.8±0.1)

Table 5.1: Summary of sample dimensions. Surface area is accurately determined and used in sample calibration.

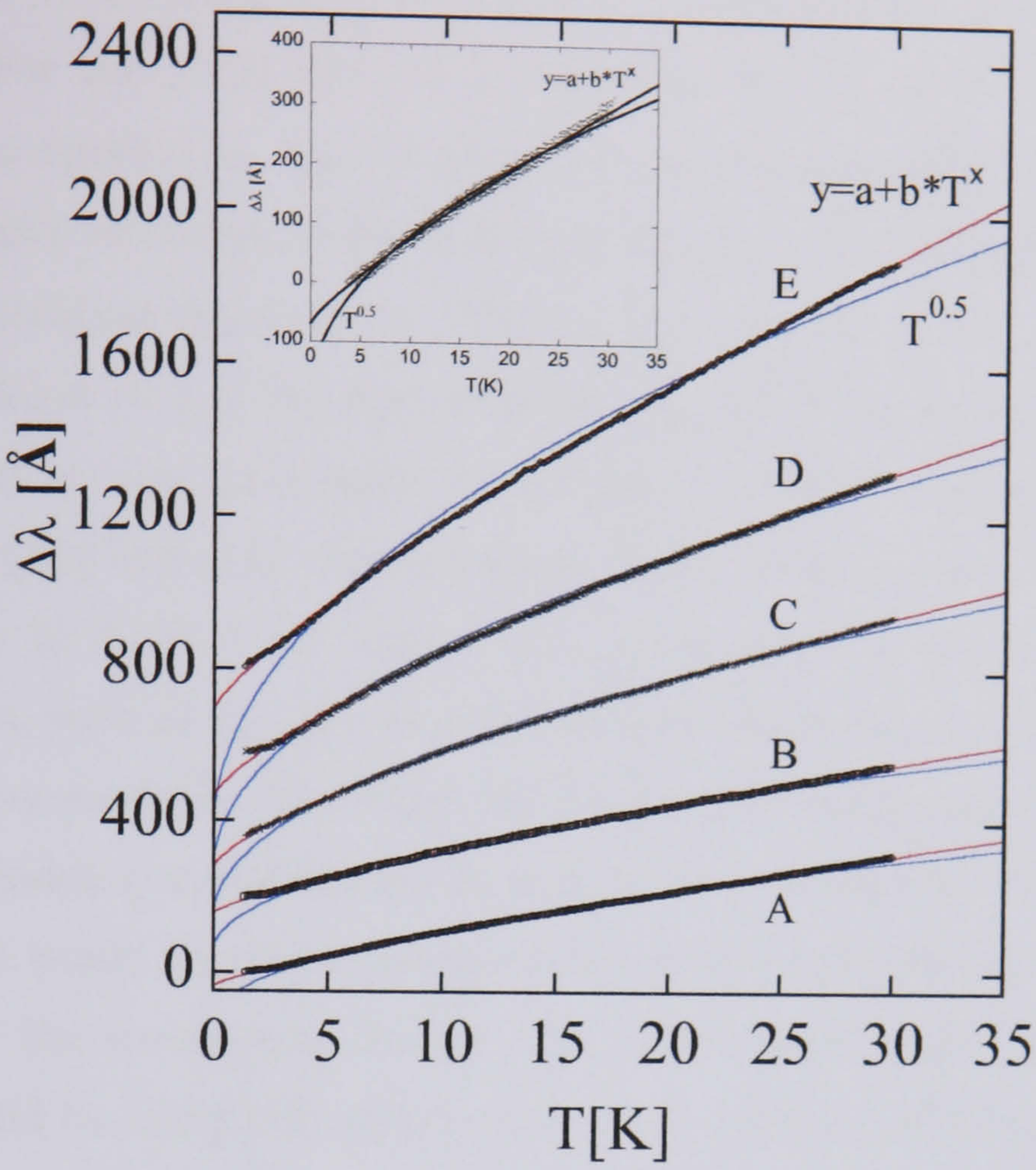

Figure 5.4: Fits to $a + bT^x$ and $a + b\sqrt{T}$ for the five Y124 samples measured with the probes field perpendicular to the ab-plane. Inset shows data from Ref.[132] with the same to fits applied.

down to low temperature where the penetration depth levels off. These observations are in contrast to the general linear behaviour observed in Y123. Fig.5.4 shows curve fits to the experimental data. The penetration depth can be seen to follow a $\sim T^x$ dependence with $x < 1$ over the temperature range shown which is up to $\sim 0.4T_c$. The data can be seen to fit $a + bT^x$ with $x = (0.70 \pm 0.05)$ much better than $\sqrt{T}$. This behaviour is in general agreement with the observations by Panagopoulos *et al.* in polycrystalline samples [132]. Panagopoulos *et al.* also observe a $\sim T^x$ dependence with $x < 1$. The inset to Fig.5.4 shows data from Ref.[132]. The data were interpreted as following a $\sqrt{T}$ power law although the inset to Fig.5.4 shows that the data also fits $a + bT^x$ with $x = 0.7$. Below ~ 2 K the penetration depth

deviates from the $\sim T^x$ with $x < 1$ to a $x > 1$ temperature dependence in some of the samples. For the Y123 system, a cross over from T to T^2 behaviour at low temperature is interpreted as due to impurity contributions [68] causing a residual quasiparticle density of states at the nodes of the $d_{x^2-y^2}$ order parameter. The low temperature penetration depth in the Y124 single crystals shows some evidence of this behaviour. Below ~ 2 K the curvature of $\Delta\lambda_{ab}(T)$ changes from $x < 1$ to $x > 1$ in all samples but is most noticeable in samples A,B and D suggesting that these samples have a higher impurity concentration. If the order parameter responsible for superconductivity in Y124 is not simply $d_{x^2-y^2}$ but contains some admixture of an s-wave component, such as $d_{x^2-y^2} + is$, the quasiparticle density of states will become fully gapped at low energies. The effect of this on the penetration depth is that the temperature dependence would change from power law to exponential. The measured penetration depth would therefore become temperature independent at temperatures much lower than the second gap energy. At temperatures only slightly below the gap energy it would be essentially impossible to tell exponential behaviour from some power law eg. T^2. This could be tested experimentally by measuring these samples to much lower temperature to see the effect. The fact that the degree to which the change in slope occurs appears to be strongly sample dependent perhaps points more to impurities being the source of the change in slope rather than the effect of a subdominant order parameter.

A $1/T$ contribution could also lead to an apparent leveling off of the penetration depth at low temperature. Such a contribution could arise from Andreev boundstates. Should ABS be contributing to the penetration depth a $1/T$ term would modify the intrinsic penetration depth response. The theory of ABS theory of Barash *et al.* [79] predicts the minimum in the penetration depth due to ABS to occur at $T_m = \varepsilon\sqrt{\xi_0/\lambda_0}T_c$. ε is related to the sample shape which for a $d_{x^2-y^2}$ superconductor $\varepsilon \sim ||\sin^3\beta| - |\cos^3\beta||^{1/2}$ where β is the angle between the sample surface and the (110) surface as defined in Section(3.7). Impurities will shift this minimum to lower temperature with strong impurity concentration suppressing the ABS contribution.

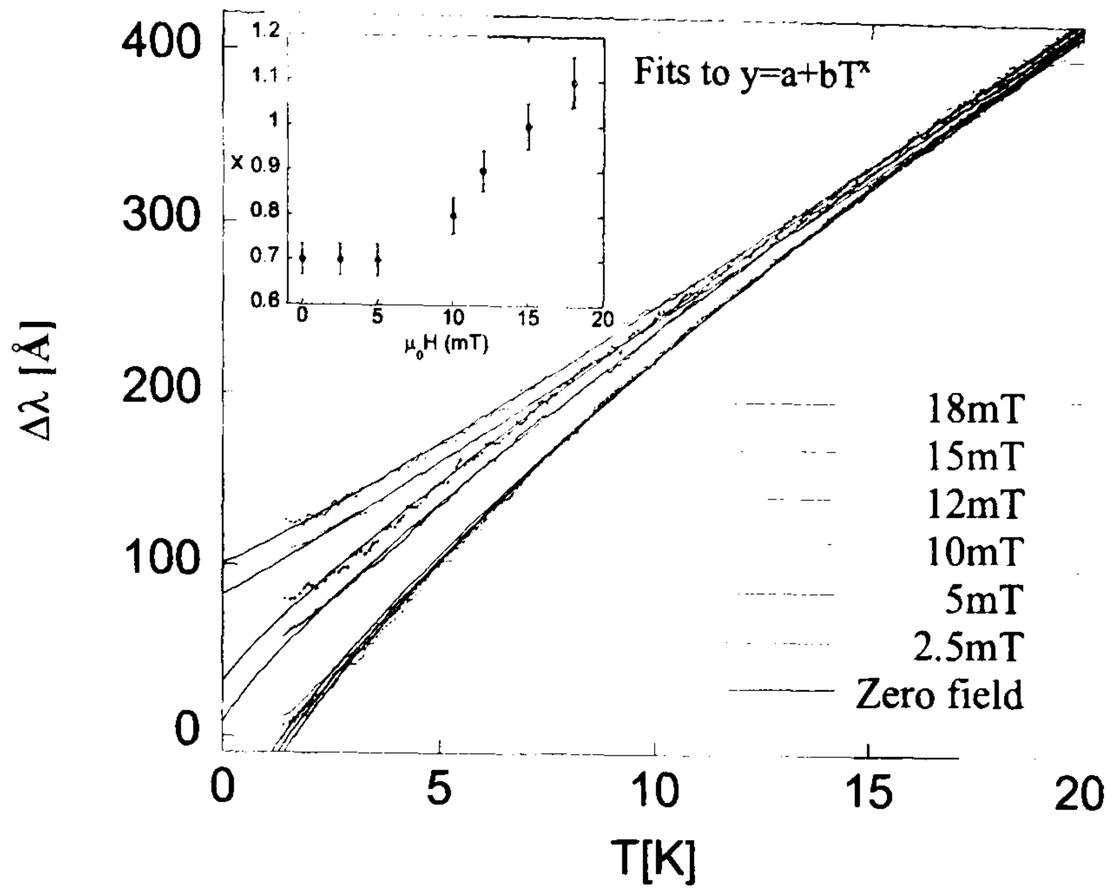

Figure 5.5: Effect of applied magnetic field on penetration depth in sample C. The application of a small magnetic field is seen to suppress the downturn in the penetration depth. The inset shows the values of x extracted from the fits to $y = a + bT^x$.

If the impurities shift the $1/T$ contribution to lower temperature a leveling off of the penetration depth may be observed. As in the case of the Y123 system the field dependence of the penetration depth should distinguish between ABS and other contributions. The application of a small magnetic field should suppress the ABS contribution to the penetration depth. This would result in the $\sim \sqrt{T}$ behaviour continuing to lower temperature.

Fig.5.5 shows the effect of an applied magnetic field on the penetration depth for Sample C. The temperature sweeps at all fields shown are completely reversible. The approximate onset of irreversibility occurs for applied fields in excess of 18mT. Temperature sweeps with fields above this value show irreversible behaviour for the first temperature sweep with subsequent sweeps retracing the same temperature dependence. The application of a magnetic field modifies the penetration depth behaviour in Y124 in an unusual way. For fields below 5 mT, the temperature dependence of the

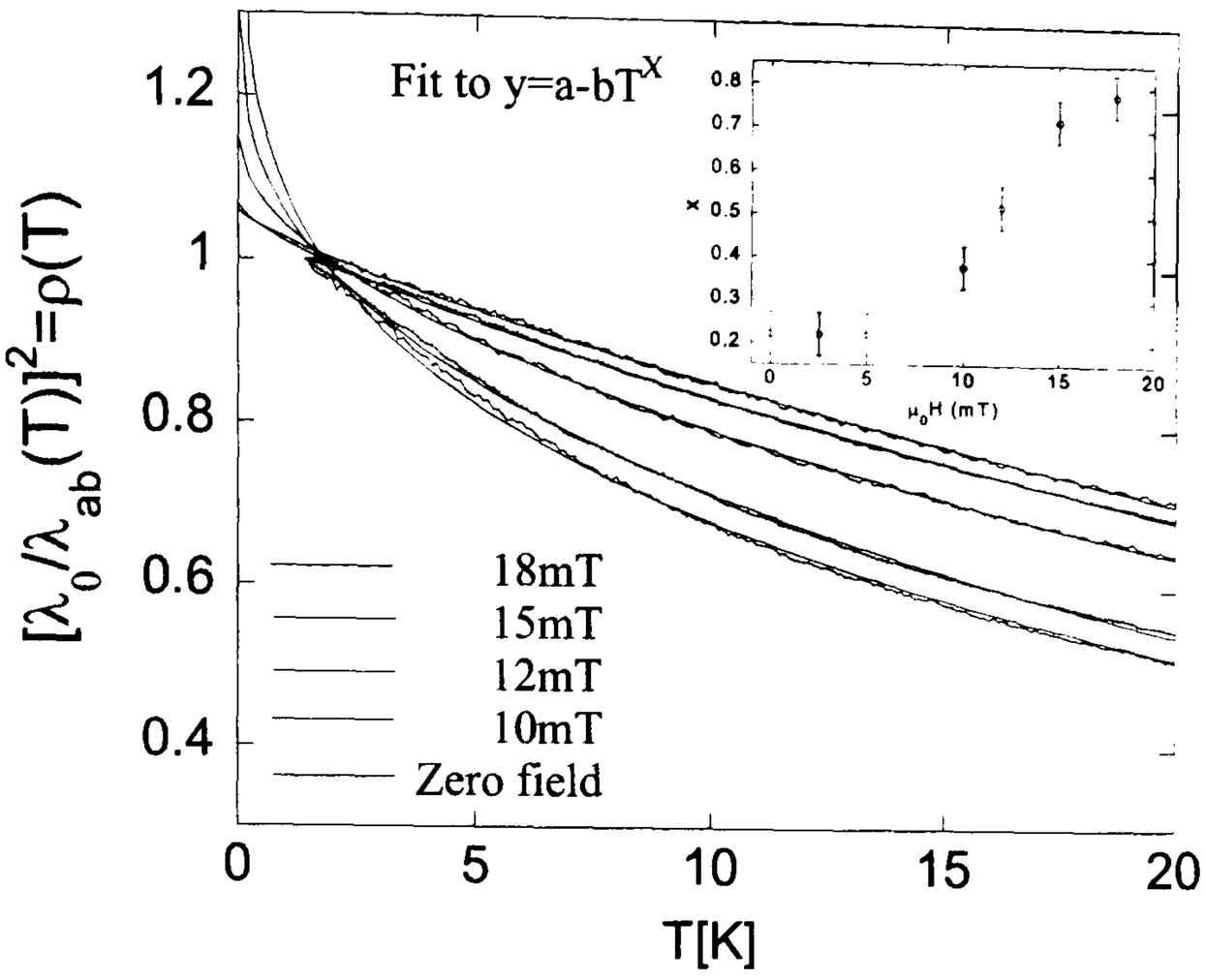

Figure 5.6: Effect of applied magnetic field on the superfluid density in Sample C. The application of a magnetic field changes the T dependence. The inset shows the values of x extracted from the fits to $y = a - bT^x$ to at all field values.

penetration depth does not vary from the zero field value. As the field is increased beyond this value the power-law temperature exponent increases. Above 15 mT the value of x becomes approximately linear in T. The detailed values of x in the T^x expression is perhaps not so important as the general trend ie., the behaviour of the penetration depth is modified from $T^{x<1}$ to approximately T^1. A better comparison with the results of Panagopoulos *et al.* should be done in terms of the superfluid density. The superfluid density is calculated using a value for $\lambda_0 = 1050$ Å given by $1/\lambda_{ab}^2 = (1/\lambda_a^2 + 1/\lambda_b^2)/2$, where $\lambda_a(0) = 2000$ Å and $\lambda_b(0) = 800$ Å[89]. Fig.5.6 shows the effect of an applied magnetic field on the superfluid density. The superfluid density results have a similar trend to the penetration depth. At low fields there is no change in the superfluid response. As the field is increased the exponent begins to change non-linearly. The low temperature increase in superfluid density begins to be suppressed by magnetic fields above ~ 5 mT. The superfluid densities at 2.5 mT and

5 mT are not plotted for clarity, since they do not differ from the zero field value. These results appear to suggest that the mechanism responsible for the low temperature increase in superfluid density is suppressed by the application of a magnetic field. If, as suggested by Panagopoulos *et al.*, the increase in superfluid density is due to superconductivity in the CuO chains, the application of a magnetic field may suppress this superconductivity thus reducing this effect. The field at the sample surface will be somewhat enhanced in this measurement orientation due to demagnetizing effects. By comparing the frequency shift due to extracting the sample from the measurement coil in both measurement orientations, it is possible to estimate this field enhancement. The frequency shift for the measurement field applied within the sample plane is Δf_0=52.4 Hz. With the measurement field applied perpendicular to the *ab*-plane Δf_0=506 Hz. This corresponds to a field enhancement of ~9.6. The change in superfluid density occurs for applied fields > 5 mT which corresponds to a surface field of $\sim$ 48 mT. Above this field the supercurrent may exceed $\mathbf{J}_c$ of the chains, reducing the superfluid density.

5.4.2 Isolation of Penetration Depth Components in $YBa_2Cu_4O_8$

As discussed in Section(5.3), the model of Xiang and Wheatley [90] describes the effect of chain superconductivity on the three components of the superfluid density ρ_a, ρ_b and ρ_c. In the proximity model, with no superconducting gap on the chains, whereby the CuO_2 planes and CuO chains are coupled via single electron tunneling only then $\rho_b(T) \sim \sqrt{(T)}$. This model assumes that chain-plane hybridization is small therefore $\rho_a(T)$ remains linear in T. The results presented in Fig.5.6 represent an average value of ρ_a and ρ_b. The results are broadly consistent with the proximity model of superconductivity on the CuO chains. Williams *et al.* [138] performed studies on Y124 to suppress superconductivity within the CuO_2 planes by Ni substitution. If the planes were intrinsically superconducting the substitution would be expected to decrease T_c with increasing Ni concentration. Once the superconductivity of the planes was destroyed the superconductivity of the chains would be exposed and T_c

would plateau with increasing Ni concentration. This was not observed and the decrease in T_c was found to be rapid and monotonic.

Since the data in Fig.5.6 represents an average value of $\rho_a(T)$ and $\rho_b(T)$ it is not possible to draw any conclusions as regards the behaviour of ρ_a and ρ_b separately without assuming some temperature dependence for one or other of the components. Panagopoulos *et al.* [132] also measured an average value for $\rho_a(T)$ and $\rho_b(T)$ in polycrystalline Y124. By assuming a linear $\rho_a(T)$ resulting from decoupled planes and chains, $\rho_b(T)$ is extracted from $\rho_{ab}(T)$. If $\rho_a(T)$ is entirely linear, all of the low temperature increase in superfluid density must be due to $\rho_b(T)$. Assuming the superfluid density along the a-axis is solely due to the planes and that the superfluid density along the b-axis is due to the chains *and* planes, subtracting the two contributions should give rise to the superfluid density of the chains. Whether this is a worthwhile exercise is entirely dependent on the validity of the assumption of the form of $\rho_a(T)$.

In single crystal samples it is possible, in principal, to isolate the components of the penetration depth and hence superfluid density, if the sample dimensions are determined accurately. The data presented above was measured with the measurement field applied perpendicular to the ab-plane thus yielding $\lambda_{ab}(T)$. As described in Section(2.3.3), measuring single crystal samples with the probe field applied within the sample plane will probe the penetration depth component in either the a or b direction with some component of λ_c as determined by

$$\Delta\lambda_{\|b}(T) = \Delta\lambda_a + \frac{t}{w}\Delta\lambda_c(T) \tag{5.5}$$

where the subscript ($\|b$) implies that the measurement field is applied along the b-axis. By measuring two crystals it should be possible to separate the λ_a and λ_c components. For two crystals labeled (1) and (2) the effective penetration depth measured will be

$$\Delta\lambda^{(1)}_{\|b}(T) = \Delta\lambda^{(1)}_a(T) + \frac{t^{(1)}}{w^{(1)}}\Delta\lambda^{(1)}_c(T) \tag{5.6}$$

$$\Delta\lambda^{(2)}_{\|b}(T) = \Delta\lambda^{(2)}_a(T) + \frac{t^{(2)}}{w^{(2)}}\Delta\lambda^{(2)}_c(T) \tag{5.7}$$

By solving the equations simultaneously $\Delta\lambda_c(T)$ can be determined and thus subtracted from the measured effective penetration depth to isolate $\Delta\lambda_a(T)$. Similarly by measuring the samples along the a-axis $\Delta\lambda_b(T)$ can also be isolated.

Samples C and D are used for this analysis. The dimensions ($a \times b \times c$) of Sample C are ($139.7 \times 235.2 \times 7.4$) μm^3 and ($95.6 \times 404.3 \times 20.9$) μm^3 for Sample D. Since the analysis relies on accurate determination of the sample dimensions it is worth commenting on the accuracy of the sample dimensions. The a,b and c dimensions were measured using optical microscopes with an accuracy of $\pm 3\mu$m for the a and b dimensions and $\pm 0.2\mu$m for the thickness (c-dimension). An independent check of the sample dimensions is provided using the sample extraction frequency shift Δf_0. For Sample C, $\Delta f_0 = -52.4$ Hz. The coil calibration factor has been accurately determined to be α=217.265 kHz/mm^3. Using the measured dimensions the calculated sample extraction value should be $\Delta f_0 = -53.0$ Hz. The two values agree to within $\sim 2\%$. For Sample D the measured extraction is $\Delta f_0 = -200.0$ Hz. The calculated value is $\Delta f_0 = -199.0$ Hz. The measured dimensions of both Sample C and D are therefore quoted with confidence. The major source of uncertainty in this analysis is the extremely small frequency shifts for Sample C in this measurement orientation. The uncertainty associated with the temperature dependence of the sapphire rod background is ~ 0.05 Hz. Typically, the uncertainty associated with $\Delta\lambda(T)$ is $<5\%$. Since the frequency shift up to 30K for Sample C is ~ 0.4 Hz this corresponds to an uncertainty of $\sim$13%. Combining this with the uncertainties in the sample dimensions, the subtraction of Eqs.(5.6) and (5.7) yields a total uncertainty of $\sim 26\%$ in the values of $\Delta\lambda_a(T)$, $\Delta\lambda_b(T)$ and $\Delta\lambda_c(T)$. For samples of arbitrary dimension, the simultaneous equations can be solved twice, once with values for $\Delta\lambda_a(T)$ and again using the values of $\Delta\lambda_b(T)$, thus giving an independent check of the value of $\Delta\lambda_c(T)$. For samples C and D, however, the ratios of t/w for the probe field applied along the a-axis in both samples are small. Since the contribution to the measured penetration depth is as in Eqs.(5.6) and (5.7) the contribution to $\Delta\lambda_c(T)$ is also small. For the measurement field along the a-axis Sample C contains only $0.03\Delta\lambda_c(T)$ and Sample

D $0.05\Delta\lambda_c(T)$. Using this measurement orientation yields a statistically unsound $\Delta\lambda_c(T)$ based on a subtracted contribution of $0.02\Delta\lambda_c(T)$. With the field applied along the b-axis, a value based on a $0.2\Delta\lambda_c(T)$ contribution, ten times larger than in the other orientation, is yielded which is much more statistically sound.

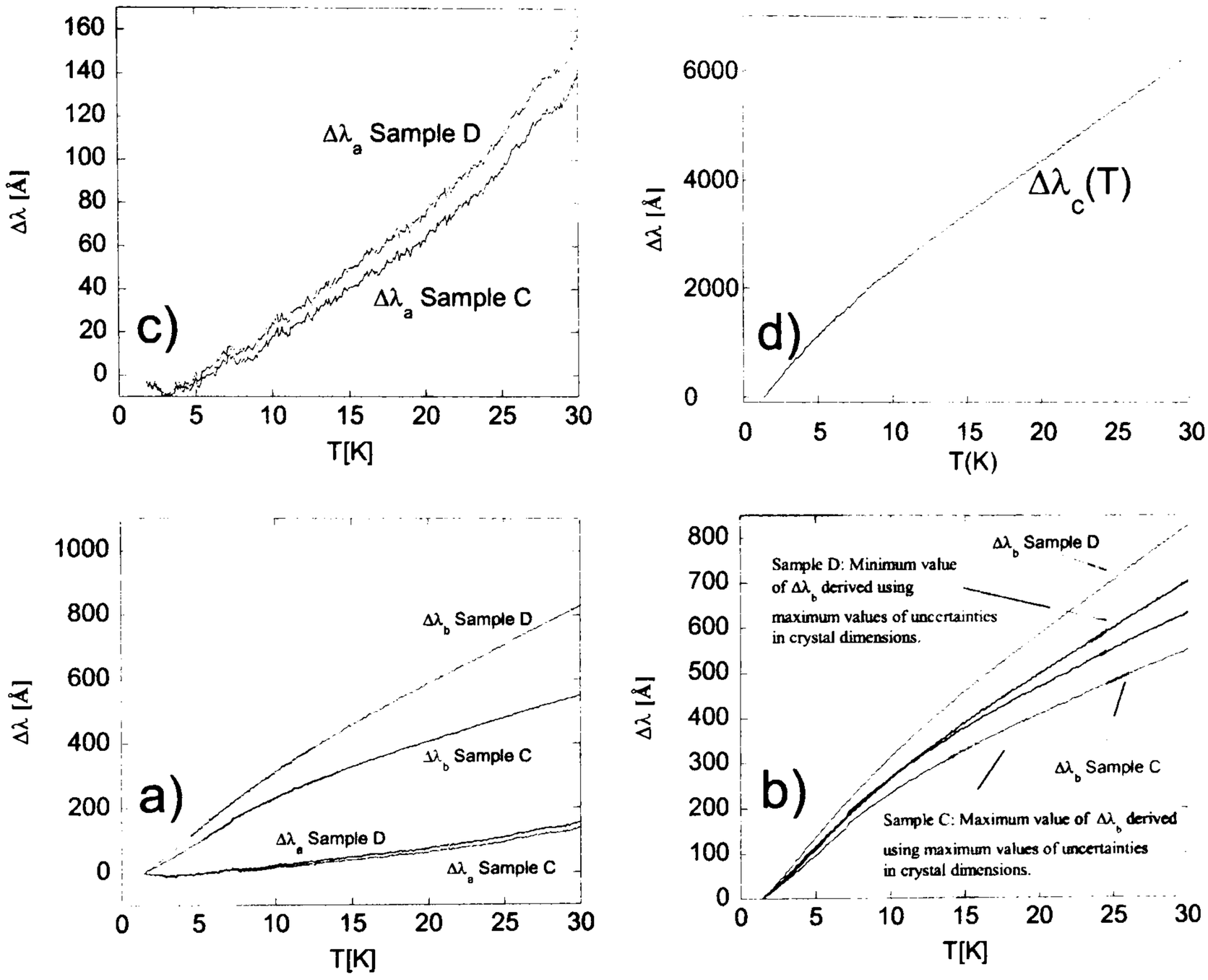

Figure 5.7: Values extracted for each component of the penetration depth using samples C and D. a) Shows $\Delta\lambda_b(T)$ for each sample. b) The maximum $\Delta\lambda_b(T)$ for sample C and the minimum $\Delta\lambda_b(T)$ for sample D using the maximum uncertainty in the sample dimensions. Both curves agree below $\sim$ 12 K. c) $\Delta\lambda_a(T)$ for each sample shows large amounts of curvature. d) $\Delta\lambda_c(T)$ also shows a downturn at low temperature.

Fig.5.7 shows the penetration depth components extracted via the method above. The values of $\Delta\lambda_b(T)$ given by each sample are quite different but agree within the experimental uncertainty of this method. This is illustrated in Fig.5.7b where $\Delta\lambda_b(T)$

is calculated for each sample and compared to values that can be obtained by recalculating each component with the uncertainties maximized. The two extracted values agree well up to $\sim$ 12 K but deviate at higher temperature. This shows that the two values differ in their temperature dependence by more than a scale factor. A possible reason for this is given below in terms of intrinsic differences between the two samples used for the analysis. Using the values of $\lambda_a(0) = 2000$ Å[89], $\lambda_b(0) = 800$ Å [89] and $\lambda_c(0) = 6150$ Å [132], the superfluid density can be calculated for each component as in Fig.5.8. The temperature dependence of $\Delta\lambda_a(T)$ shows a large degree of curvature. $d\lambda_a(T)/dT = 10.9$ Å/K for sample C and $d\lambda_a(T)/dT = 9.8$ Å/K for sample D. These values are approximately a factor two greater than for optimally doped Y123 (See Chapter 3). The small increase in the penetration depth at the lowest temperature is most likely an artifact of the component isolation process. The size of this upturn is well within the experimental uncertainty.

The results of Fig.5.8 are again in broad agreement qualitatively with those of Ref.[132]. Both ρ_b and ρ_c show an increase at low temperature. The overlap of ρ_b for Sample D and ρ_c is purely coincidental since different values of $\lambda(0)$ are used in the calculation of each component. A fit of $\rho_a(T)$ to the dirty d-wave formula [68] gives a value of $T^* \sim 15$ K for sample C and $T^* \sim 20$ K for sample D. Since $\rho_a(T)$ is attributed to the CuO_2 planes, this high value of T^* would imply a large impurity contribution to the penetration depth. Measurements by Bonn *et al.* showed that 0.31% Zn impurities in optimally doped Y123 resulted in a $T^* = 28$ K. This value is comparable to that measured here in Y124. Resistivity measurements on the same batch of samples [18] suggest that these crystals are very pure with an extrapolated chain residual resistivity of $\rho_0 = 0.5$ $\mu\Omega$cm. Hussey *et al.* argue that the chains represent a pseudo one dimensional system, with any disorder along the chains resulting in a large residual resistivity. If the superfluid densities for the chains and planes can be thought of as being independent, the results would imply that all impurities are localized to the CuO_2 planes with negligible amounts of disorder present within the CuO chains. An alternative view to this is that the T^2 behaviour in the

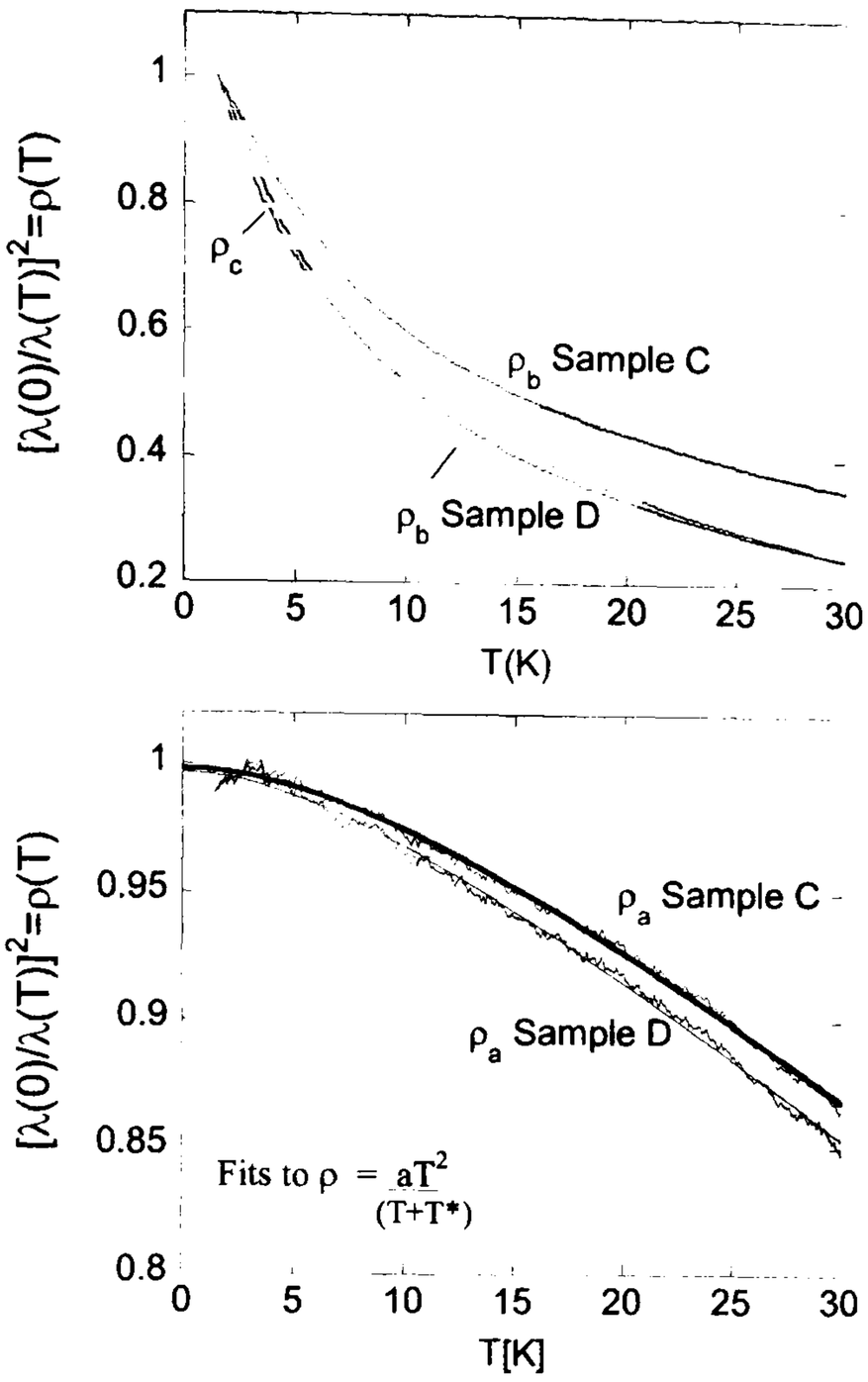

Figure 5.8: Superfluid densities derived from the penetration depth components in Fig.5.7. The anomalous decrease in ρ_a at low temperature is an artifact of the data subtraction and within experimental uncertainty.

a-axis superfluid density may suggest that plane-chain hybridization is not negligibly small as suggested by Xiang and Wheatley [90] since a linear in T superfluid density has never been categorically identified.

Although the method for the separation of the penetration depth components appears to be sound, most of the differences between the components derived from each sample may be due to intrinsic differences in the penetration depth response between samples. The total change in λ_b between base temperature and 30 K for the two samples shows $\Delta\lambda_b^{\mathrm{D}} = 1.5\Delta\lambda_b^{\mathrm{C}}$. This ratio is maintained for the probe field applied perpendicular to the sample plane where the calibration factors are

reached independently. If we take the extracted value of $\Delta\lambda_b(T)$ from the in-plane measurement and compare it with the averaged value of $\Delta\lambda_{ab}$ as given in Fig.5.3 we can see reasonable agreement in terms of the total change in penetration depth. These two components are plotted in Fig.5.9.

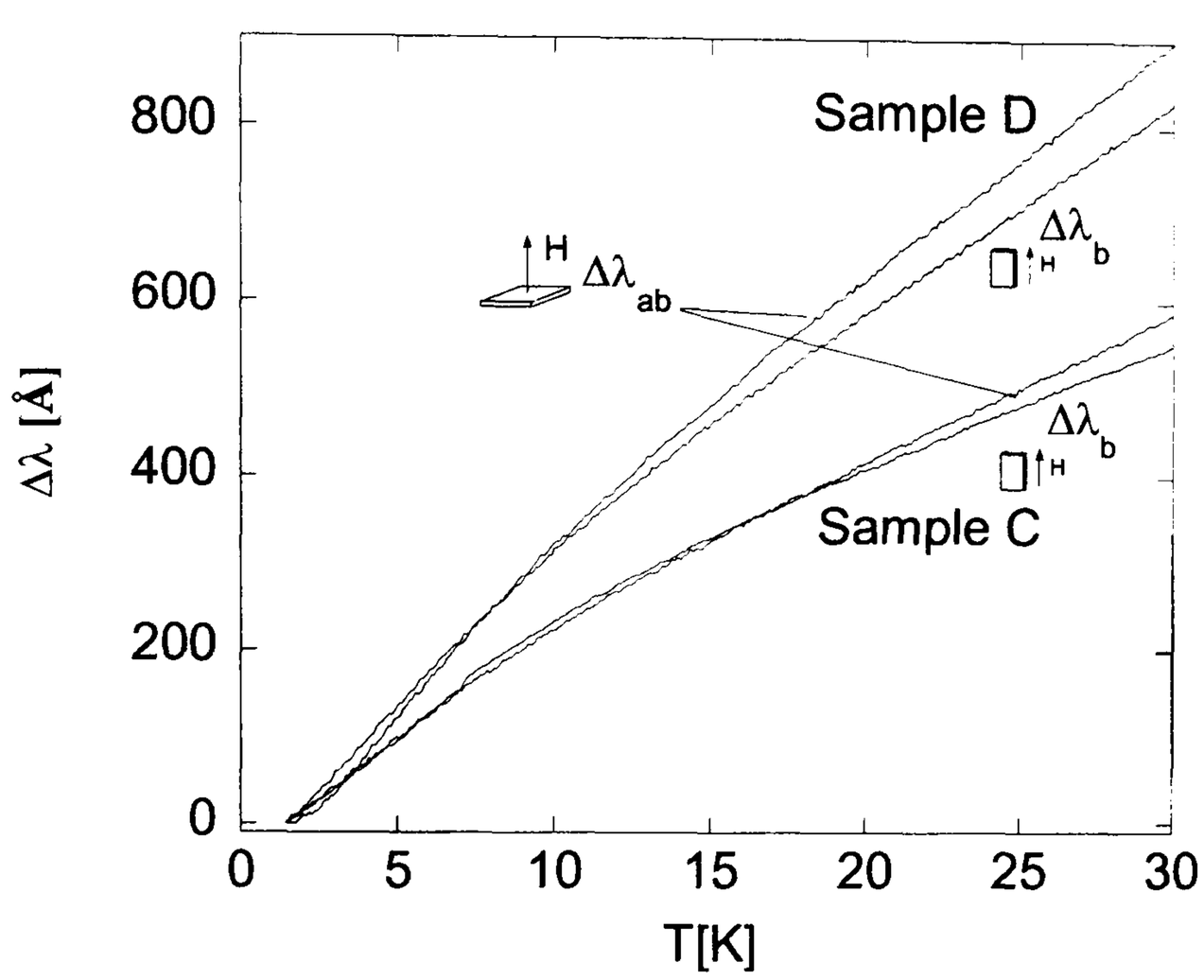

Figure 5.9: Comparison of the penetration depth as measured with the probe field perpendicular to the ab-plane ($\Delta\lambda_{ab}$) and field applied within the sample plane ($\Delta\lambda_b$).

Although the two orientations are very similar in terms of total shift, the detailed temperature dependence of the two are different. If the difference was merely a simple scale factor the difference might be indicative of a calibration error. The difference in the temperature dependence is to be expected as $\Delta\lambda_{ab}(T)$ contains some $\Delta\lambda_a(T)$ which is absent in the in-plane measurement.

An important factor in the separation of the penetration depth components is correctly knowing the axial directions of the crystals. Sample D is a needle-like crystal of the type used in resistivity measurements [18]. These measurements found that the b-axis extends along the long direction of the crystal. Sample C is rectangular rather than needle-like meaning that the crystal directions cannot be assumed directly. The

method by which the crystal axes were determined in Sample C was by solving the simultaneous equations (5.6) and (5.7) assuming one orientation and then repeating the process with the assumption reversed. The difference between the two assumptions is dramatic. The conclusion drawn is that the b-axis is again the longer axis of the crystal. By assuming the b-axis along the short axis leads to large inconsistencies between samples such as $\Delta\lambda_b(T) < \Delta\lambda_a(T)$ in Sample C and $\Delta\lambda_b(T) > \Delta\lambda_a(T)$ in Sample D. The behaviour of $\Delta\lambda_b(T)$ followed $T^{x>1}$ in Sample C and $T^{x<1}$ in Sample D. In order for the superfluid densities to agree values of $\lambda_b(0)$ must differ by a factor ~ 5.

5.4.3 Interpretation of Results

The penetration depth response of Y124 is very different to that of other cuprate superconductors. Optimally doped Y123 shows a largely linear in T dependence which can be shifted to T^2 in the presence of impurities. This power law temperature dependence is cited as direct evidence for the $d_{x^2-y^2}$ order parameter as the pairing mechanism in the cuprates. The low temperature increase in the superfluid density observed in both polycrystalline [132] and single crystal Y124 samples makes it distinct to the other cuprates. Measurements of $\Delta\lambda_b(T)$ in Y123 generally shows greater curvature than $\Delta\lambda_a(T)$ possibly indicating some CuO chain contribution to the penetration depth. The theory of Xiang and Wheatley [90], although originally formulated to describe the superfluid response of Y123, find a rapid increase in superfluid response in ρ_b and ρ_c at low temperature for single electron tunneling between chains, planes and layers. The results of Fig.5.8 appear to largely agree with Fig.5.1 which shows the calculated superfluid densities derived from the proximity model of Xiang and Wheatley [90]. The extra CuO chain present in the Y124 structure may facilitate this tunneling process leading to a different mechanism not available to Y123 due to a smaller amount of c-axis coupling. Stronger c-axis coupling in Y124 than in Y123 was implied in resistivity measurements [18]. Similar temperature dependence of $\Delta\lambda_b(T)$ and $\Delta\lambda_c(T)$ may suggest that they are intimately linked in Y124. The

larger amount of c-axis coupling may mean that Y124 cannot be well described as a 2 dimensional superconductor; a model ascribed to the other cuprates.

The application of a magnetic field suppresses the low temperature increase in superfluid density. The inactivity below 10 mT implies some critical field for proximity coupling. If the chain superconductivity is purely due to the proximity effect as previously suggested [132], a small magnetic field may suppress the chain superconductivity, reducing the difference in temperature dependence of the normalized superfluid densities along the a and b axes. The change in curvature of the penetration depth with field may also suggest that the superconductivity on the CuO chains and CuO_2 planes may have different critical currents. For small magnetic fields, the penetration depth response is due to both the CuO chains and CuO_2 planes. If the application of a magnetic field causes the chain critical current to be exceeded, the penetration depth response will be entirely due to the planes. The superfluid density becomes approximately linear in temperature, a result expected for a $d_{x^2-y^2}$ order parameter in the absence of impurities.

5.5 Summary

Five $YBa_2Cu_4O_8$ single crystals were measured with the goal of observing Andreev boundstates in a similar system to $YBa_2Cu_3O_7$. All five crystals were measured with the probe field applied perpendicular to the sample plane which is the measurement orientation associated with Andreev boundstate formation. No evidence for the presence of Andreev boundstates in this material is presented. The penetration depth was found to *decrease* at low temperature as previously observed in polycrystalline samples by Panagopoulos [132] *et al.* The data for all samples was compared to the $\sqrt{T}$ temperature dependence found by Panagopoulos *et al.* The data was fit to $\Delta\lambda(T) = a + bT^x$ and $\Delta\lambda(T) = a + b\sqrt{T}$. All samples were found to follow a $T^{0.7}$ temperature dependence rather than $\sqrt{T}$. The superfluid density in sample C was seen to increase at low temperature as $T^{0.2}$ rather than increasing linearly in temperature as expected for a $d_{x^2-y^2}$ order parameter. A low temperature enhancement in the superfluid density is predicted by Xiang and Wheatley [90] along the b and c axis, due to single electron tunneling between the CuO chains and CuO_2 planes. The presence of the extra chains in the $YBa_2Cu_4O_8$ system could facilitate this process in this material and be the reason that this effect is not observed in $YBa_2Cu_3O_7$.

The exponent that the low temperature decrease in the penetration depth follows, was seen to change as a function of applied magnetic field. For fields < 5 mT, the temperature dependence of the penetration depth remains unchanged. Above this field value the low temperature decrease in the penetration depth is progressively suppressed and the temperature dependence becomes more linear. For fields above 5 mT, the critical current of the superconductivity on the chains may be exceeded and the chain contribution to the superconductivity removed, leaving only the response due to CuO_2 planes. The superfluid density becomes increasingly more linear as the magnetic field is increased. The effect of fields up to 18 mT were studied as fields above this value result in irreversible behaviour in the temperature dependence of the penetration depth.

Samples C and D were also measured with the measurement field applied within

the *ab*-plane. In this orientation the measured penetration depth will contain contributions from $\Delta\lambda_c(T)$ as well as the in plane component. Using the results of samples C and D, an attempt to isolate the $\Delta\lambda_c(T)$ component was attempted. $\Delta\lambda_b(T)$ was seen to fall at low temperature and $\Delta\lambda_a(T)$ was seen to fit Hirschfeld and Goldenfeld's dirty *d*-wave expression with $T^* = 20$ K. Such a value in $YBa_2Cu_3O_7$ would correspond to a large penetration depth contribution due to impurity pair breaking. The temperature dependence of $\Delta\lambda_b(T)$ yielded by each sample was found to agree within the experimental uncertainty below ~12 K. The behaviour above this temperature does not agree well. The difference is attributed to differences between the temperature dependence between samples.

Chapter 6

Conclusions

The results presented in this thesis affect the general field of superconductivity in a number of ways. The results for optimally doped $YBa_2Cu_3O_7$ single crystals supplement the evidence for the $d_{x^2-y^2}$ order parameter in this material. Penetration depth measurements usually only give information regarding the magnitude of the superconducting gap. These results also provide phase sensitive information regarding the order parameter since the formation of Andreev boundstates at zero energy can only occur for an order parameter with a π-phase change around the Fermi surface. The penetration depth results presented here for MgB_2, the recently discovered superconductor, show convincing evidence that the order parameter has fully gapped pairing symmetry never before observed via penetration depth measurements. The observation of an exponential temperature dependence to the penetration depth agrees with the large body of other measurement techniques in implying s-wave superconductivity in MgB_2. The penetration depth results also allude to the presence of two weakly coupled superconducting gaps. The observation of a downturn in the penetration depth in $YBa_2Cu_4O_8$, in contrast to the linear temperature dependence expected for the $d_{x^2-y^2}$ order parameter has been previously observed [132]. The suppression of this downturn by small magnetic fields, as well as the temperature dependence of each of the penetration depth components, is unique to the work presented here. These findings imply that the CuO chains within the structure become superconducting

via a proximity mechanism. The superfluid components ρ_b and ρ_c show very similar temperature dependence suggesting that their behaviour may be intimately linked. The chapters where all of these results presented and discussed are summarized below.

Details of the design and calibration of a high stability LC-oscillator technique have been presented. The advantage of this high stability technique enables small single crystal high temperature superconductors (HTS) to be measured accurately. Some of the data presented in this thesis are taken on HTS samples which present a frequency shift of just 0.01 Hz/K from 1-30K which would not be measurable by many other techniques. The details of the preliminary measurements which have to be performed before measurements can be taken are also discussed. Attention is paid in particular to the differences between the two measurement configurations in terms of penetration depth components probed and calibration differences.

Measurements performed on optimally doped $YBa_2Cu_3O_7$ showed that the low temperature penetration depth deviates from the usual linear temperature dependence associated with *d*-wave superconductivity due to the formation of surface Andreev boundstates (ABS) at zero energy. Four $YBa_2Cu_3O_7$ crystals were measured with the probe field applied along the a, b and c crystal axes identifying $\Delta\lambda_b(T)$, $\Delta\lambda_a(T)$ and $\Delta\lambda_{ab}(T)$. The superfluid densities were calculated from $\Delta\lambda_a(T)$ and $\Delta\lambda_b(T)$ and fit to the dirty *d*-wave formula of Hirschfeld and Goldenfeld [68]. The values of T^* yielded for the crystals ranged between 0.7 K to 3.8 K for ρ_a and 1.5 K to 4.9 K for ρ_b indicative of high sample purity. The measurement orientation with the probe field applied along the *c*-axis of the crystal should measure a penetration depth contribution which is the average of $\Delta\lambda_a(T)$ and $\Delta\lambda_b(T)$. Instead of the highly linear behaviour associated with these components in the other measurement orientations, a low temperature increase in the penetration depth was observed in all four crystals. The low temperature increase in penetration depth is attributed to surface Andreev boundstates forming at zero energy. The ABS contribution is only observed for the measurement orientation whereby quasiparticles were confined to the *ab*-plane. ABS

form at zero energy due to constructive interference between electron and hole-like quasipartiles passing through a π-phase change in the order parameter. In this measurement orientation the quasiparticles can be specularly through reflected through adjacent lobes of the $d_{x^2-y^2}$ order parameter causing a delta peak in the quasiparticle density of states which introduces a $\sim 1/T$ dependence to the penetration depth. The magnitude of the ABS contribution to the penetration depth was seen to depend strongly on the shape of the crystal in a systematic way as predicted by the ABS theory of Barash *et al.* [79]. The ABS contribution can be modified by the presence of impurities which broadens the delta peak in the quasiparticle density of states. A fit to $c/(T+T^*)$ yielded T^*=0.8 K indicating only slight broadening of the boundstates due to impurities.

The ABS contribution to the penetration depth was seen to be strongly field dependent. Small dc magnetic fields were found to suppress the ABS contribution to with an applied field of $\sim$ 10 mT being sufficient to almost completely eliminate the ABS effect. The small field scale can be qualitatively explained in terms of the boundstates being Doppler shifted away from zero energy by an amount $\delta E = e\mathbf{v}_f \cdot \mathbf{A}$. The ABS theory of Barash *et al.* was used to fit field sweep data taken at constant temperature. The fits give values for the temperature dependent field scale associated with the suppression of the ABS. This field scale can be used to yield an experimentally derived value for the Fermi velocity v_f. The values yielded for the Fermi velocities in samples C and D are $v_f = (1.1 \pm 0.2) \times 10^5$ ms^{-1} and $v_f = (1.2 \pm 0.2) \times 10^5$ ms^{-1} respectively.

Evidence of ABS formation in another cuprate is also presented. A low temperature increase in the penetration depth was also observed for a slightly underdoped $Bi_2Sr_2CaCu_2O_8$ single crystal with the measurement field applied perpendicular to the *ab*-plane as in optimally doped $YBa_2Cu_3O_7$. The ABS contribution in this material was also seen to be suppressed by small magnetic fields. The combination of measurement orientation dependence and the small field scale associated with the suppression of the low temperature upturn points to zero energy ABS being source of

the low temperature penetration depth anomaly in the $Bi_2Sr_2CaCu_2O_8$ single crystal.

An underdoped $HgBa_2Ca_2Cu_3O_{(8+\delta)}$ single crystal ($T_c = 120$ K) also displayed a low temperature increase in penetration depth. This behaviour was not attributed to ABS since it was present in both measurement orientations and the application of large magnetic fields had minimal effect on the magnitude of the upturn. The most likely cause of the low temperature increase in penetration depth in this sample is an isotropic paramagnetic contribution due to sample degradation.

The penetration depth was measured in MgB_2 samples in order to study the symmetry of the superconducting order parameter in this material. Four different types of MgB_2 samples were measured with the temperature dependence of the penetration depth seen to follow exponential behaviour of the BCS form. The first sample measured was a dense polycrystallite. The measured penetration depth showed anomalous behaviour which disappeared following etching in ~0.5% HCl in ethanol. The temperature dependence of the penetration depth was fit to the BCS expression for the change in penetration depth due to thermally excited quasiparticles for a fully gapped superconductor. A value of $\Delta_0 = 33 \pm 2$ K was yielded by this fit. The second MgB_2 sample measured was made from commercially available MgB_2 cast into quick setting epoxy resin. An exponential temperature dependence was also seen which yielded a gap value of $\Delta_0 = 30 \pm 2$ K. A second epoxy sample was prepared again using commercially available MgB_2 powder in epoxy resin. This sample was made from sorted MgB_2 powder so that a value for $\lambda(0)$ could be estimated. The powder was ground and then sorted using a sedimentation technique to achieve particles of grain size $\lesssim 5\lambda$ allowing absolute values for the penetration depth to be derived. A value of $\lambda(0) = 1600 \pm 200$ Å was yielded by extrapolating the penetration depth to zero temperature. A value of $\Delta_0 = 30 \pm 2$ K for the gap was given by a fit to the BCS penetration depth. The value yielded from the sorted and non-sorted MgB_2 powder samples were the same. The effective penetration depth of the randomly oriented grains was estimated to be $\lambda(0) = 1.5\lambda_{ab}(0)$ giving a value of $\lambda_{ab}(0) = (1100 \pm 200)$ Å.

The final MgB_2 sample measured was a single crystal. The sample was measured

with the probe field applied within and perpendicular to the *ab*-plane of the sample. Again, the data was found to agree well with the BCS penetration depth behaviour yielding values of $\Delta_0 = (29 \pm 2)$ K for λ_{ab} and $\Delta_0 = (32 \pm 2)$ K for the probe field applied within the sample plane which yields a penetration depth with some *c*-axis contribution.

The superfluid densities for the single crystal and sorted powder MgB_2 samples were calculated using the value for $\lambda(0)$ yielded from the powder sample. A phenomenological model for the superconductivity in MgB_2 developed by Bouquet *et al.* [119] was discussed and used to analyze the the superfluid density data. The superfluid density data could be fit to a two gap model yielding values for each superconducting gap which agree well with data from other experiments fit either to the same phenomenological model and data where two gaps were measured directly.

An anisotropic *s*-wave theory by Haas and Maki [125] was also fit to the superfluid density data. This theory could be used to fit the experimental data but the values of $\lambda(0)$ implied were almost a factor two smaller than that yielded in the experiment and well outside of the experimental uncertainty. It was concluded that the anisotropic *s*-wave model did not accurately describe the data.

Following the identification of a contribution to the penetration depth from Andreev boundstates in optimally doped $YBa_2Cu_3O_7$, five $YBa_2Cu_4O_8$ single crystals were measured to see if Andreev boundstates modified the penetration depth in this material also. The samples were measured with the probe field applied perpendicular to the *ab*-plane which is the orientation associated with ABS formation. No evidence for the presence of Andreev boundstates in this material was found. The penetration depth was found to decrease at low temperature as previously observed in polycrystalline samples by Panagopoulos [132] *et al.* In the study of Panagopoulos *et al.*, the penetration depth was described as following a $\sqrt{T}$ temperature dependence. The data for the five crystals was fit to $\Delta\lambda(T) = a + bT^x$ and $\Delta\lambda(T) = a + b\sqrt{T}$. All samples were seen to fit $T^{0.7}$ temperature dependence rather than a pure $\sqrt{T}$. The superfluid density in sample C was found to increase as $T^{0.2}$ rather than increasing

linearly as expected for a $d_{x^2-y^2}$ order parameter. A low temperature enhancement in the superfluid density for a $d_{x^2-y^2}$ order parameter was predicted by Xiang and Wheatley [90], for the superfluid densities measured along the b and c axes of the crystal, due to single electron tunneling between the CuO chains and the CuO_2 planes. This effect may be present in the $YBa_2Cu_4O_8$ system and not $YBa_2Cu_3O_7$ due to the extra CuO chain in the unit cell facilitating c-axis coupling.

The low temperature decrease in penetration depth was also studied as a function of magnetic field. Applied magnetic fields below 5 mT was found not to affect the penetration depth behaviour. Fields above this value were found to gradually suppress the low temperature down turn with a magnetic field of 18 mT causing an essentially linear in T temperature dependence. Fields above 5 mT may cause the superconductivity on the CuO chains to be suppressed. If the CuO chains have a lower critical current than the CuO_2 planes, the superfluid enhancement due to the chains may be removed from the total response, leaving only the response due the to CuO_2 planes. Fields above 18 mT were found to cause irreversible behaviour in the temperature dependence of the penetration depth.

Samples C and D were also measured with the probe field applied along the a and b axes of the crystals. In these orientations the measured penetration depth contains some $\Delta\lambda_c(T)$ component determined by the ratio of sample dimensions. The results for samples C and D were used to try to isolate the $\Delta\lambda_c(T)$ component. $\Delta\lambda_b(T)$ was seen to fall at low temperature. $\Delta\lambda_a(T)$ was seen to have positive curvature. A fit to Hirschfeld and Goldenfeld's dirty d-wave expression [68] yielded a value for T^*=20 K. Such a value when related to $YBa_2Cu_3O_7$ would correspond to a large impurity contribution in the CuO_2 planes. The temperature dependence of $\Delta\lambda_b(T)$ yielded by each sample was found to agree within the experimental uncertainty below $\sim$ 12 K. The behaviour above this temperature does not agree well. This difference was attributed to a difference in the temperature dependence of the penetration depth from sample to sample.

Bibliography

[1] J. Magamatsu et al. *Nature*, 410:63, 2001.

[2] G. Bednorz and K. A. Müller. *Z. Phys. B*, 64:189, 1986.

[3] M. K. Wu. *Phys. Rev. Lett.*, 58:908, 1987.

[4] A.W. Tyler. *An Investigation into the Magnetotransport Properties of Layered Superconducting Perovskites.* PhD thesis, Cambridge, 1997.

[5] J.R. Cooper, S.D. Obertelli, A. Carrington, and J.W. Loram. *Phy. Rev. B*, 44:12086, 1991.

[6] R. Gagnon, C. Lupien, and L. Taillefer. *Phys. Rev. B*, 50:3458, 1994.

[7] D. A. Bonn. *Czech J. Phys.*, 46:3195, 1996.

[8] A. Carrington, R. W. Giannetta, and J. T. Kim J. Giapintzakis. *Phys. Rev. B.* 59:R14173, 1999.

[9] W. E. Pickett. *Rev. Mod. Phys.*, 61:433, 1989.

[10] H. Krakauer, W. E. Pickett, and R. E. Cohen. *J. Supercond.*, 1:111, 1988.

[11] H. Ehrenreich and D. Turnbull. *Solid State Physics: Advances in Research and Applications.* Academic Press Inc., London, 1989.

[12] J.G. Bednorz, K.A. Müller, and M. Takashige. *Science*, 236:73, 1987.

[13] F. Hermann, V. Kasowski, and W.Y. Hsu. *Phys. Rev. B*, 38:204, 1988.

[14] R.V. Kasowski, W.Y. Hsu, and F. Hermann. *Phys. Rev. B*, 38:6470, 1988.

[15] Y.S. Yao, W. Liu, Y.J. Su, Y.F. Xiong, W.J. Ma, G.H. Cao, G.T. Zou, and Z.X. Zhao. *Physica C*, 282:897, 1997.

[16] M. Gurvitch and A.T. Fiory. *Phys. Rev. Lett*, 59:1337, 1987.

[17] J.R. Waldram. *Superconductivity of Metals and Cuprates.* IOP, London. 1996.

[18] N.E. Hussey, K. Nowaza, H. Takagi, S. Adachi, and K. Tanabe. *Phys. Rev. B.* 56:R11423, 1997.

[19] H. Takagi et al. *Phys. Rev. B*, 40:2254, 1989.

[20] R.A. Klemm and S.H. Liu. *Phys. Rev. Lett*, 74:2343, 1995.

[21] R.C. Yu et al. *Phys. Rev. Lett*, 69:3529, 1992.

[22] T. Timusk and B. Statt. *Rep. Prog. Phys.*, 62:61, 1999.

[23] J. Halbritter. Pseudogap and transport in hts. *Journal of Superconductivity.* 14:9, 2001.

[24] Ch. Renner, B. Revaz, J-Y. Genoud, K. Kadawaki, and O Fischer. *Phys. Rev. Lett*, 80:149, 1998.

[25] J.M. Harris, A.G. Loesser, D.S. Marshall, M.C. Schabel, and Z-X. Shen. *Phys. Rev. B*, 54:R15665, 1996.

[26] M.R. Norman et al. *cond-matt/9710163*, 1997.

[27] R. Hackl, G. Krug, R. Nemetshcek, M. Opel, and B. Stadlober. *Spectroscopic Studies of Superconductors*, 5:194, 1996.

[28] Y. Itoh, T. Machi, A. Fukuoka, K. Tanabe, and H. Yasuoka. *J. Phys. Soc Japan.* 65:3751, 1996.

[29] J.V.M Williams, J.L. Tallon, E.M. Haines, Michalak R, and R. Dupree. *Phys. Rev. Lett*, 78:721, 1997.

[30] B. Bucher *et al. Phys. Rev. Lett.*, 70:2012, 1993.

[31] M. Bankay, M. Mali, J. Roos, and D. Brinkmann. *Phys. Rev. B*, 50:6416. 1994.

[32] G. Zheng, T. Odaguchi, Y. Kitaoka, K. Asayama, Y. Kodama, K. Mizuhasi. and S. Uchida. *Physica C*, 263:367, 1996.

[33] D. A. Bonn, S. Kamal, K. Z. Zhang, D. J. Baar, E. Klein, and W. N. Hardy. *Phys. Rev. B*, 50:4051, 1994.

[34] J. Bardeen, L. N. Cooper, and J. R. Schrieffer. *Phys. Rev*, 108:1175. 1957.

[35] J. F. Annett, N. Goldenfeld, and A. J. Leggett. *Physical Properties of High T erature Superconductors*, 2:375. 190.

[36] J. Hubbard. *Proc. Royal Society*, 243:336, 1957.

[37] S.R. White et al. *Phys. Rev. B*, 40:506, 1989.

[38] N.F. Berk and J.R. Schrieffer. *Phys. Rev. Lett*, 17:433, 1966.

[39] A. Millis, H. Monien, and D. Pines. *Phys. Rev. B*, 42:167, 1990.

[40] C. Pennington and C.P. Slichter. *Phys. Rev. Lett*, 66:381, 1991.

[41] T. Imai et al. *Phys. Rev. B*, 47:9158, 1993.

[42] D. Pines. *Physica C*, 235:113, 1994.

[43] J. Martindale et al. *Phys. Rev. B*, 47:9155, 1993.

[44] C. C. Tsuei and J. R. Kirtley. *Rev. Mod. Phys.*, 72:969. 2000.

[45] H. Ding, M. R. Norman, J. C. Campuzano, M. Randeria, A. F. Bellman. T. Yokoya, T. Takahasi, T. Mochiku, and K. Kadowaki. *Phys. Rev. B.* 54:R9678. 1996.

[46] D.R. Harshmann et al. *Phys. Rev. B*, 39:851, 1989.

[47] L. Kruisin-Elbaum et al. *Phys. Rev. Lett*, 62:217, 1989.

[48] W. N. Hardy, D. A. Bonn, D. C. Morgan, R. X. Liang, and K. Zhang. *Phys. Rev. Lett.*, 126:41–44, 1993.

[49] P. A. Lee. *Phys. Rev. Lett.*, 71:1887, 1993.

[50] L. Taillefer, B. Lussier, R. Gagnon, K. Behnia, and H. Aubin. *Phys. Rev. B.* 79:483, 1997.

[51] H. Aubin, K. Behnia, M. Ribault, R. Gagnon, and L. Taillefer. *Phys. Rev. Lett.*. 78:2624, 1997.

[52] G. E. Volovik. *JETP Lett*, 58:469, 1993.

[53] K. A. Moler, D. J. Baar, J. S. Urbach, R. Liang, W. N. Hardy, and A. Kapitulnik. *Phys. Rev. Lett.*, 73:2744, 1994.

[54] B. Revaz, J. Y. Genoud, A. Junod, K. Neumaier, A. Erb, and E. Walker. *Phys. Rev. Lett.*, 80:3364, 1998.

[55] S. H. Simon and P. A. Lee. *Phys. Rev. Lett.*, 78:1548, 1997.

[56] G. E. Volovik. *JETP Lett*, 65:491, 1997.

[57] D. J. Van Harligen. *Rev. Mod. Phys*, 67:515. 1995.

[58] D. A. Wollman, D. J. Van Harligen, W. C. Lee, D. M. Ginsberg, and A. J. Leggett. *Phys. Rev. Lett.*, 71:2134. 1993.

[59] F. London and H. London. *Proc. Roy. Soc.* A149:71. 1935.

[60] D. Xu, S. K. Yip, and J. A. Sauls. *Phys. Rev. B*, 51:16233. 1995.

[61] K. Kishio et al. *Physica C*, 235-240:2775, 1994.

[62] S. Chandrasekhar and D. Einzel. *Annalen der Physik*, 2:535. 1993.

[63] Z. Szotek, B.L. Gyorffy, and W.M. Temmerman. *Phys. Rev. B*, 62:3997. 2000.

[64] Michael Tinkham. *Introduction to Superconductivity 2nd Edition*. McGraw-Hill. 1996.

[65] A.B. Pippard. *Roy. Soc. Proc.*, A216:547, 1953.

[66] L.P. Gor'kov. *Sov. Phys. JETP*, 40:1155, 1985.

[67] K. Ueda and T.M. Rice. *Theory of Heavy Fermion and Valence Electrons*. Springer, Berlin, 1985.

[68] P. J. Hirschfeld and N. Goldenfeld. *Phys. Rev. B*, 48:4219, 1993.

[69] I. Kosztin and A. J. Leggett. *Phys. Rev. Lett.*, 79:135, 1997.

[70] J. Cooper. *Phys. Rev. B*, 54:R3753, 1996.

[71] C. T. Van Degrift. *Rev. Sci. Inst*, 46:599. 1975.

[72] D.I. Hoult and R.E. Richards. *Journal of Magnetic Resonance*. 24:71. 1976.

[73] R. A. Goldfarb, M. Lelental, and C. A. Thompson. *Susceptibility of Superconductors and Other Spin Systems*, page 49. Plenum, New York. 1991.

[74] D. Shoenberg. Cambridge University Press, Cambridge, England. 1952.

[75] R. Prozorov, R. W. Giannetta, A. Carrington, and F. M Araujo-Moreira. *Phys. Rev. B*, 62:115, 2000.

[76] J. Heubener et al. *Journal of Low Temperature Physics*, 6:275, 1972.

[77] A.F. Andreev. *Sov. Phys. JETP.*, 19:1228, 1964.

[78] T. Löfwander, V.S. Shumeiko, and G. Wendin. *Supercond. Sci. Technol.*, 14:R53, 2001.

[79] Y.S. Barash, M.S. Kalenkov, and J. Kurkij arvi. *Phys. Rev. B*, 65:6665, 2000.

[80] J.Y.T. Wei, N.C. Yeh, D.F. Garrigus, and M. Strasik. Ferromagnetic domains in thin Ni-Fe films. *Phys. Rev. Lett.*, 81:2542, 1998.

[81] I. Iguchi, W. Wang, M. Yamazaki, Y. Tanaka, and S. Kashiwaya. *Phys. Rev. B*, 62:R6131, 2000.

[82] M. Covington, M. Aprili, E. Paroanu, L.H. Greene, F. Xu, J. Zhu, and C.A. Mirkin. *Phys. Rev. Lett.*, 79:277, 1997.

[83] H. Walter, W. Prusseit R. Semerad, H. Kinder, W. Assmann, H. Huber, H. Burkhardt, D. Rainer, and J.A. Sauls. *Phys. Rev. Lett.*, 80:3598, 1998.

[84] J. Geerk, X.X. Xi, and G. Linker. *Z. Phys. B*, 73:329, 1988.

[85] C.R. Hu. *Phys. Rev. Lett.*, 72:1526, 1994.

[86] M. Fogelström, D. Rainer, and J.A. Sauls. *Phys. Rev. Lett.*, 79:281, 1997.

[87] S.K. Yip and J.A. Sauls. *Phys. Rev. Lett.*, 69:2264, 1992.

[88] S.E. Stupp and D.M Ginsberg. *Physical Properties of High Temperature Superconductors III.* World Scientific, Singapore, 1992.

[89] D.N. Basov, R. Liang, D.A. Bonn, W.N. Hardy, B. Dabrowski, M. Quijada, D.B. Tanner, J.P. Rice, D.M. Ginsberg, and T. Timusk. *Phys. Rev. Lett.*, 74:598, 1995.

[90] T. Xiang and J.M. Wheatley. *Phys. Rev. Lett.*, 76:134, 1996.

[91] L. Alff. *Phys. Rev. Lett.*, 83:2644, 1999.

[92] Y. Wang, B. Revaz, A. Erb, and A. Junod. *Phys. Rev. B*, 63:094508. 2001.

[93] M.C. Schabel, C.H. Park, A. Matsurra, Z.X. Shen, D.A. Bonn, R. Liand, and W.N. Hardy. *Phys. Rev. B*, 57:6090, 1998.

[94] A. Carrington, F. Manzano, R. Prozorov, and R.W. Giannetta. *Phys. Rev. Lett.*, 86:1074, 2000.

[95] A. Carrington, C. Marcenat, F. Bouquet, D. Colson, A. Bertinotti, J.F. Marucco, and J. Hammann. *Phys. Rev. B*, 55:R8674. 1997.

[96] C. Panagopoulos, J.R. Cooper, T. Xiang, G.B. Peacock, I.Gameson, P.P. Edwards, W. Schmidbauer, and J.W. Hodby. *Physica C*, 282-287:145. 1997.

[97] C. Buzea and T Yamashita. *Superconductor Science and Technology*, 2001.

[98] D. Mansk, C. Joas, I. Eremin, and K. H. Bennemann. *Phys. Rev. Lett.*. 97:334, 2001.

[99] J. Kortus, I.I. Mazin, K. D. Belashchenko, V. P. Antropov, and L. L. Boyer. *Phys. Rev. Lett.*, 86:4656, 2001.

[100] S. L. Bud'ko, G. Lapertot, C. E. Cunnigham, N. Anderson, and P. C. Canfield. *Phys. Rev. Lett.*, 86:1877, 2001.

[101] A.Y. Liu, I.I. Mazin, and J. Kortus. *Cond-matt/0103570*, 2001.

[102] O. F. de Lima, R. A. Ribiero, M. A. Avila, C. A. Cardoso, and A. A. Coelho. *Phys. Rev. Lett.*, 86:5974, 2001.

[103] S. Lee, H. Mori, T. Masui, Y. Eltsev, A. Yamamoto, and S. Tajima. 64, 2001.

[104] F. Bouquet, R. A. Fisher, N. E. Phillips, D. G. Hinks, and J. D. Jorgensen. *Phys. Rev. Lett.*, 87:047001, 2001.

[105] Y. Wang, T. Plackowski, and A. Junod. *Physica C*. 355:179. 2001.

[106] X.K Chen, M.J. Konstanovic, J.C. Irwin, D.D. Lawrie, and J.P. Franck. *Cond-matt/0104005*, 2001.

[107] J. W. Quilty, S. Lee, A. Yamamoto, and S. Tajima. *Cond-matt/0107216*, 2001.

[108] P. Sazbó, P. Samuely, J. Kacmarcik, T. Klein, J. Marcus, D. Fruchardt, S. Miraglia, C. Marcenat, and A.G.M. Jansen. *Cond-matt/0105598*, 2001.

[109] G.E Blonder, M. Tinkham, and T.M Klapwijk. *Phys. Rev. B*, 25:4515, 1982.

[110] X. H. Chen, Y. Y. Xue, R. L. Meng, and C. W. Chu. *Cond-matt/0103029*, 2001.

[111] C. Panagopoulos, B. D. Rainford, T. Xiang, C. A. Scott, M. Kambara, and I. H. Inoue. *Phys. Rev. B*, 64:094514, 2001.

[112] A. V. Pronin, A. Pimenov, A. Loidl, and S. I. Krasnosvobodtsev. *Phys. Rev. Lett.*, 61:1986–1987, 1992.

[113] A. Porch, J. R. Cooper, D. N. Zheng, J. R. Waldram, A. M. Campbell, and P. A. Freeman. *Physica C*, 214:350, 1993.

[114] N. Athanassopoulou. PhD thesis, University of Cambridge, 1994.

[115] D.K. Finnemore, J.E. Ostenson, S.L. Bud'ko, G. Lapertot, and P.C. Canfield. *Phys. Rev. Lett.*, 86:2420, 2001.

[116] A.M. Neminsky and P.N. Nikolaev. *Physica C*, 212:389, 1993.

[117] Y.A. Kufaev and E.B. Sonin. *Physica C*, 235:1813, 1994.

[118] Ch. Neidermayer, C. Bernhard, T. Holden, R.K. Kremer, and K. Ahn. *Preprint*, 2001.

[119] F. Bouquet, Y. Wang, R. A. Fisher, D. G. Hinks, J. D. Jorgensen, A. Junod, and N. E. Phillips. *Europhys. Letts.*, 88:L261–L266, 1990.

[120] H. Padamsee, J. E. Neighbor, and C. A. Shiffman. *J. Low Temp. Phys.*, 12:387. 2001.

[121] A. Junod, Y. Wang, F. Bouquet, and P. Toulemonde. *Studies of High Temperature Superconductors*, 38, 2001.

[122] S. Tsuda, T. Yokoyota, T. Kiss, Y. Takano, K. Togano, H. Kitou, H. Ihara, and S. Shin. *Cond-matt/0104574*, 2001.

[123] F. Giubileo, D. Roditchev, W. Sacks, R. Lamy, D.X. Thanh, S. Miraglia, D. Frutchard, J. Marcus, and P. Monod. *Cond-matt/0105592*. 2001.

[124] F. Laube, G. Goll, J. Hagel, H.V. Lohneysen, D. Ernst, and T. Wolf. *Cond-matt/0106407*, 2001.

[125] S. Haas and K. Maki. *Cond-matt/0104207*. 2001.

[126] N.E. Hussey, S.Nakamae, K. Behnia, H. Takagi, C. Urano, S. Adachi, and S. Tajima. *Phys. Rev. Lett.*, 85:4140, 2000.

[127] H.W. Zandbergen, R. Gronski, K. Wang, and G. Thomas. *Nature*, 336:596. 1988.

[128] S. Srinivas, A.K. Bhatnagar, S.B. Ogale, and R.D. Vispute. *Physica C*. 275:346. 1997.

[129] T. Miyake, S. Gotoh, N. Koshizuka, and S. Tanaka. *Nature*, 341:41, 1989.

[130] S. Adachi, K. Nakanishi, K. Tanabe, K. Nozawa, H. Takagi, W. Z. Hu, and M. Izumi. *Physica C*, 301:123, 1998.

[131] K. Behnia *et al. J. Low Temp. Phys.*, 117:1089, 1999.

[132] C. Panagopoulos, J.L. Tallon, and T. Xiang. *Phys. Rev. B*, 59:R6635, 1999.

[133] J.L. Tallon, C. Bernhard, U. Binningham, A. Hofer, G.V.M. Williams, E.J. Ansaldo, J.I. Budnick, and C. Neidermayer. *Phys. Rev. Lett.*, 74:1008, 1995.

[134] C. Bernhard, C. Neidermayer, U. Binninger, A. Hofer, C. Wenger. J.L. Tallon. G.V.M. Williams, E.J. Ansaldo, J.I. Budnick, C.E. Stronach, D.R. Noakes. and M.A. Blankson-Mills. *Phys. Rev. B*, 52:10488, 1995.

[135] M. Takigawa, P.C. Hammel, R.H. Heffner, and Z. Fisk. *Phys. Rev. B*, 39:7371. 1989.

[136] J.M. Wheatley, T.C. Hsu, and P.W. Anderson. *Phys. Rev. B*, 37:5897. 1988.

[137] K. Zhang, D.A. Bonn, s. Kamal, R. Liang, D.J. Baar, W.N. Hardy, D. Basov. and T. Timusk. *Phys. Rev. Lett.*, 73:2484, 1994.

[138] G.V.M. Williams, J.L. Tallon, R. Dupree, and R. Michalak. *Phys. Rev. B*, 54:9532, 1996.